University of Southampton PhD Thesis

Faculty of Engineering, Science & Mathematics
Graduate School of the Southampton Oceanography Centre

Rotating Exchange Flows Through Straits with Multiple Channels

by

Benjamin Rabe

Thesis for the degree of Doctor of Philosophy

September 2004

Southampton Oceanography Centre
UNIVERSITY OF SOUTHAMPTON AND
NATURAL ENVIRONMENT RESEARCH COUNCIL

Graduate School of the Southampton Oceanography Centre

This PhD dissertation by

Benjamin Rabe

has been produced under the supervision of the following persons

Supervisor/s:

Dr. David Smeed
Prof. Harry Bryden

Chair of Advisory Panel:

Prof. Jochem Marotzke

Member/s of Advisory Panel:

Dr. Jonathan Sharples

UNIVERSITY OF SOUTHAMPTON

ABSTRACT

FACULTY OF ENGINEERING, SCIENCE & MATHEMATICS

SCHOOL OF OCEAN & EARTH SCIENCES

SOUTHAMPTON OCEANOGRAPHY CENTRE

Doctor of Philosophy

ROTATING EXCHANGE FLOWS THROUGH STRAITS WITH MULTIPLE CHANNELS

by Benjamin Rabe

September, 2004

Ocean basins are connected by straits and passages geometrically limiting important heat and salt exchanges which in turn influence the global thermohaline circulation and climate. Such exchange can be modelled in an idealised way by taking into consideration the density-driven two-layer flow along the strait and the influence of rotation, in particular when the first mode baroclinic Rossby radius is of the same order or smaller than strait width. Some straits have complex bottom topography, such as the Strait of Sicily or the Straits of Hormuz. It is is the objective of this study to understand when and why this has to be taken into consideration.

We use a laboratory model of a lock exchange between two reservoirs of different density through a flat-bottom channel with a horizontal narrows, set up on two different platforms: a 1m diameter turntable, where density interface position was measured by dye attenuation, and the 14m diameter turntable at Coriolis/LEGI (Grenoble, France). On the latter, this type of experiment was carried out for the first time, measuring velocity using Correlation Imaging Velocimetry, a particle imaging technique. In all experiments, the influence of rotation is studied by varying a parameter, R_0, the ratio of the Rossby radius to the channel width at the narrows. In addition, the simple channel is modified by adding a central island to represent straits with non-uniform topography at the narrows.

Results show that the quasi-steady exchange flux for simple channels varies in a way similar to a theoretical prediction by Whitehead *et al.* (1974). When an island is introduced, the dimensional flux is larger than without an island for $R_0 \sim 1$. However, the total exchange is less than the sum of exchanges that would be expected from each individual channel. Furthermore, for $R_0 > 1$ the non-dimensional cross-channel slope at the narrows is shallower than predicted by Dalziel (1988)'s semi-geostrophic theory for simple channels. However, scaling R_0 using a reduced channel width in the island cases leads to a variation of these quantities with R_0 in accordance with theory. For $R_0 > 1$ two-layer flow persisted across the channel at the narrows with or without an island, but distinctly different flows occurred for lower R_0. One quasi-steady state with $R_0 \sim 0.7$ showed a 'split' regime with upper and lower layer currents passing on different sides of the island (left, looking downstream, respectively). A recirculation near the island tips was noticeable, particularly for $R_0 << 1$, where distinct jets circulated around the tips, opposing the flow of same density on the other side of the island. A similar phenomenon has been found in some oceanic strait flows. Flow at very low R_0 did not appear to reach a steady state but instead showed an oscillating current around the narrows associated with several, often barotropic, vortices. Instantaneous flow fields in those cases, however, still showed an exchange between the reservoirs, with one island case showing a flow split by the island and almost barotropic on either side. There, fluxes were twice as high as predicted by two-layer theory.

Our study showed that the combination of rotation and an island introduce significant 3-dimensional aspects to the flow, not present in non-rotating exchange flows.

To my grandparents

Martin, Manfred & Gretel

To my mother

Gundhild

Acknowledgements

Many thanks go to David Smeed and Harry Bryden for their patience with reading my manuscripts and their supervision throughout the PhD. Also thanks to Gregory Lane-Serff and Stuart Dalziel for collaboration at *Coriolis* and many useful comments. Many useful discussions also ensued with Uli Riemenschneider, Andy Hogg, Peter Killworth, Kate Stansfield and Mark Siddall, for which I am indebted to them.

Many thanks to the team at *Coriolis*, whose help during and after the collaborative experiments was invaluable. Thanks also go to John Hewitt and Ray Collins for help during the experiments at *SOC*.

My life at *SOC* and in Southampton has been made enjoyable by the many people in the postgraduate community, so thanks to all of you: Taro Hosoe & Ale, Alan Hughes, Martin Gutowski, Nils Cornelius, Florence Nedelec, Sara Benetti, Sara Sorhouet, Almudena Fontan, Sergio Capucci, Isabelle^2, Jörg Frommlet, Beth Greenaway, Ana Pirani, Riccardo Farnetti, Sinhue Torres, Sara Comelli, Francisco Benitez, Branco Bogunovic, Stefania Schinaia, the Italian Community, Los Mexicanos, Guillaume, Paula Alvarez, James Harle, Paula McLeoud, Phil Sexton, Charlie Thompson, the Brazilians and many others... Also thanks to my former housemates and friends Guy, Pete, Henry, Jenny, Marianne, Espen, Estelle, Dave, Stevedb as well as the Ninjitsu lot (you know who you are!).

A big thank you also goes to Adriana Huerta-Casas for her continued patience and personal support throughout.

Finally thanks to my mother, for her encouragement and support in undertaking a degree and research in oceanography, as well as the rest of my family.

The work at *Coriolis* was funded by the EU, Enhancing Access to Research Infrastructures action of the Improving Human Potential programme of FP5, under contract HPRI-1999-CT-0006. The PhD was partly funded by a Southampton Oceanography Centre studentship and the James Rennell Division.

List of symbols

- (RHS, LHS): the side of the channel with $(y < 0, y > 0)$
- $W(s, i)$: width of the channel at the narrows (simple channel width,reduced channel width)
- $W_{(R,L)}$: width of each side-channel (RHS,LHS) between island and side walls at the narrows
- H: total depth of water
- $h_{(1,2)}$: depth of layer (1,2), i.e. (light,dense)
- h_R: mean depth of layer 1 on RHS at narrows cross-section
- $V_{1,2}$: volume of reservoir (1,2)
- f: Coriolis frequency
- T: period of rotation
- t: time
- ρ $(\Delta\rho)$: density (difference between reservoirs)
- g': reduced gravity at the density interface
- $T_{L,SF,r,res,s}$: time scale (see details in section 4.1, p.80)
- q^*: dimensional volume exchange flux (absolute value of either layer)
- $\bar{q}$: non-dimensional volume exchange flux
- $\bar{q}_{whitehead}$: maximal theoretical, zero potential vorticity value of $\bar{q}$ by Whitehead *et al.* (1974)
- q_{nr}: non-rotating (dimensional) value of $\bar{q}$
- R: Rossby radius of deformation (based on inherent baroclinic gravity wave speed)
- R_0: Rossby number (based on R and W; also a form of the Burger number)
- $R_{0(s,i)}$: Rossby number based on $W_{(s,i)}$
- ν: kinematic (molecular) viscosity
- Ek: Ekman number (based on ν)
- Re: Reynolds number
- δ_{Ek} (δ_S): scale for Ekman (Stewartson) boundary layer thickness

Contents

List of Figures

List of Tables

Chapter 1

Introduction

The deep basins of the world's oceans are separated by ridges and coasts and connected by oceanic straits and passages. These are important for heat and salt fluxes between the basins and therefore the large-scale thermohaline circulation and climate (e.g. Mediterranean outflow, Bigg *et al.*, 2003). Dynamical processes in the straits are thought to control the exchange and are generally associated with constricting topography, such as narrows or sills.

Extrema in strait geometry may be associated with the process of hydraulic control giving a maximal bound on the steady exchange flux through the strait. Such control can be observed in flow over a weir which is dependent only on the depth of the water on the upstream side relative to the top of the weir. Any change in upstream conditions, such as water depth, is 'communicated' to the weir flow by small amplitude surface gravity waves and vice versa, but these waves cannot travel to the weir from directly downstream of it due to the speed of the flow there (super-critical). Waves are arrested at the weir, marking the control or "critical" condition. Further downstream, the super-critical flow is joined by a hydraulic jump to a sub-critical region, where gravity waves can travel in both directions. However, in straits the situation is usually modelled by one active layer with overlying passive or active layers, the waves now being internal ones, travelling on the density interface and influenced by the velocity in the layers above and below (Armi, 1986; Dalziel, 1991). In addition there may be multiple geometric extrema, such as a combination of sills and narrows, time variability, such as tides, and frictional effects.

An additional effect in wide straits is the cross-strait acceleration by the Coriolis force. Here wide means that the strait has a width similar to or greater than the baroclinic Rossby deformation radius. As we shall show, rotation also enhances the effect of non-uniform topography across the strait. Many straits have islands or ridges dividing the strait into multiple channels throughout all or part of the water depth. This can be seen in the Cretan Arc

Straits (e.g. Theocharis *et al.*, 1999), the Indonesian archipelago (e.g. Gordon *et al.*, 2003), the Straits of Hormuz (Johns *et al.*, 2003) or the Strait of Sicily, where complex interaction between Coriolis acceleration and topographic steering is observed (e.g. Stansfield *et al.*, 2001, 2003).

Despite the importance of oceanic straits, current ocean general circulation models (OGCMs) do not resolve the exchange processes and topography in many straits. On the other hand, theoretical treatment of exchanges has mostly been limited to one-layer or non-rotating inviscid two-layer exchange, often in channels with simplified cross-section geometry, for example rectangular or parabolic. Studies of specific straits by oceanic measurements and specialised process-modelling are often hampered by problems with synopticity, such as tides or seasonal variability, spatial resolution (see Dickson *et al.*, 1999) and parameterisation of the physical processes (e.g. Denmark strait overflow, Käse *et al.*, 2003), although several large programs exist to study such straits and their role in global climate (e.g. *http://www.clivar.org/science/atlantic.htm*). Further description of previous work on exchange flows is given in chapter 2 (p.24).

This study simulates rotating, two-layer lock-exchange flows in the laboratory. Some such studies have been undertaken on small platforms with channels of rectangular cross-section (Whitehead *et al.*, 1974; Dalziel, 1988), where exchange fluxes were measured and flow features qualitatively observed. In this work, a constant depth channel with symmetrically contracting walls (narrows) is used, which will be termed the 'simple channel' case. This is the first such study on a large rotating platform. In addition to this simple channel case, many oceanic straits have topographic complexities that separate all or part of the flow laterally across the strait. Therefore, an island is placed in the centre of our simple channel for some of the experiments, dividing the narrows cross-section of the channel into two passages. This will be termed the 'island' case. To the author's knowledge this is the first study to address this problem in a two-layer exchange. The focus is on the difference in the quasi-steady state between the simple channel and island cases as well as the influence of rotation on the exchange flow in general. The experiments were realised on both a small and a large platform. In general the split strait was symmetric in the across- and along-channel directions. A few cases of an island offset toward one of the channel walls were also studied, but those results will only be mentioned briefly in this thesis. The corresponding setup and measurement methods as well as the data processing are described in chapter 3 (p.42).

Time series of quantitative measurements of the two-layer density interface as well as the 2-dimensional velocity field at different depths within the channel are analysed with the aim of finding a quasi-steady state in chapter 4 (p.80). Chapter 5 (p.105) then analyses the resultant time-averaged fields with respect to the rotational influence and categorises the distinct flow regimes. The fluxes associated with different rotation rates and regimes are given in chapter 6 (p.133). That chapter will also deal with viscous effects, interfacial mixing and hydraulic control. A discussion of the results and wider-ranging issues is presented in chapter 7 (p.168) followed by conclusions and suggestions for future work in chapter 8 (p.183).

Chapter 2

Background on strait exchange and hydraulics

2.1 Hydraulic exchange and budget theory

2.1.1 Knudsen relations and hydraulic exchanges

One of the earlier works by Nielsen (1912) showed that a two-layer exchange flow can be determined by mass (salt) conservation between two basins. The upper- and lower- layer volume fluxes are respectively given by $q_1 = \frac{S_2 E}{S_2 - S_1}$ and $q_2 = -\frac{S_1 E}{S_2 - S_1}$, also known as the Knudsen relations, where S is the salinity in the upper (1) and lower (2) layer and E the net evaporation over the saltiest basin. An application of this is the Harzallah and Crepon (1993) prediction of exchange flows within the Mediterranean and between the Mediterranean and the Atlantic.

This alone is only a diagnostic method. Although applicable to any two-layered exchange flow dynamics and strait geometry this method requires knowledge of the often difficult to estimate basin evaporation parameter and either $S_{(1,2)}$ to calculate $q_{(1,2)}$ or vice versa from the conservation relations above. To fully determine the flux requires knowledge of the dynamics within the strait, such as the process of hydraulic control. Hydraulic control theory suggests that non-rotating multi-layer exchange flows are limited by the strait geometry, such as sill, narrows, and the layer density difference(s), that together constrain the flow and specify so-called control sections in the channel, entirely describing the flow. This incorporation of flow dynamics and topography determines the maximum possible exchange but may have to take into account forcing by reservoir conditions, such as a net flux, friction in long, narrow channels, rotation, especially in wide passages, and time variability, e.g. atmospheric pressure gradients and large tides as well as associated bores. Some examples of attempts to include these effects into hydraulic theory will be given in the rest of this chapter, but the main focus of this thesis is the quasi-steady state in a rotating, approximately inviscid exchange flow.

The geometric constraint in rectangular cross-section channels can be divided into horizontal (narrows) and vertical (sill) constrictions. Throughout this thesis, x (u) is defined as the along channel/strait coordinate (velocity) and y (v) the across-channel coordinate (velocity), unless otherwise stated. The across-strait section of minimum horizontal width will be called the 'narrows'.

2.1.2 Non-rotating hydraulics

The classical, non-rotating, hydraulics problem describes a single layer flow exiting a reservoir over a weir and can be found in many standard fluid dynamics textbooks (e.g. Henderson, 1966, p. 40). The appropriate non-dimensional parameter to describe the hydraulic state of such a flow, assuming a free fluid surface, is the Froude Number, $F = \frac{U}{\sqrt{gH}}$, (e.g. Tritton, 1988, p. 95), representing the importance of flow speed U to the surface gravity wave speed, $\sqrt{gH}$ determined by the depth H and gravity acceleration g. The two-layer or exchange version of this problem was introduced by Stommel and Farmer (1953), who investigated the two-layer dynamics in a rapidly narrowing channel, and was further developed by Long (1956, 1970, 1974). The internal hydraulics of the fluid can be described using a composite Froude number

$$G^2 = F_1^2 + F_2^2 = \frac{u_1^2}{g'h_1} + \frac{u_2^2}{g'h_2} = 1 + \frac{h_1 + h_2}{h_1 h_2 g'} c_1 c_2, \tag{2.1}$$

where subscripts $1(2)$ are referring to upper (lower) layer quantities. $u_{(1,2)}$ are the along-channel layer velocities, $h_{(1,2)}$ the layer depths, $F_{(1,2)}$ the layer Froude numbers, $g' = \frac{\Delta\rho}{\bar{\rho}}$ is the reduced gravity at the layer interface, $\bar{\rho}$ the mean density and $\Delta\rho$ the density difference between both layers, assumed to be much smaller than $\bar{\rho}$. $c_{(1,2)}$ are the phase velocities of the two small-amplitude, inter-facial gravity waves in the frame of reference of the channel and are given by $c_{(1,2)} = \frac{(H-h_2)u_1+h_2u_2}{H} \pm \sqrt{\frac{(H-h_2)h_2}{H} g'(1 - \frac{(u_1-u_2)^2}{Hg'})}$ (Dalziel, 1991). Here, the dynamics of both layers are deemed important for along-channel propagation of long internal gravity waves. Two super-critical states are given by $G^2 > 1$ when c_1 is of the same sign as c_2, so that waves can only travel in one direction along the channel. The sub-critical state is given by $G^2 < 1$ when $c_{(1,2)}$ are of opposite sign, so that waves can propagate in both directions. Further references can be found in Armi (1986) who used the G^2 parameter in describing the two-layer flow through channels with rectangular cross-section. He found that internal dynamics are independent of those at the surface if the density difference between both layers is small, i.e. $\Delta\rho << \rho$. This means that a free upper surface or rigid lid both have the same internal hydraulic controls. This assumption will be used throughout this thesis.

An approach different to the Froude Number analysis was introduced by Gill (1977) who related different geometric and flow parameters in the following theoretical framework:

1. The flow can be described in terms of a single dependent variable D, where the functional $J(H, W, ...; D) = constant$, i.e. the y dependence of D is entirely implicit in terms of the geometric variables H, W, etc.

2. The function J is multiple-valued, i.e. for a given range of h, w, ... there are several values of D. The surface $J = constant$ is also assumed to be smooth.

3. The geometry involves some sort of 'constriction' in the sense that $G = \frac{\partial J}{\partial H}\frac{\partial H}{\partial y} + \frac{\partial J}{\partial W}\frac{\partial W}{\partial y} + ...$ $= 0$, which reduces to $\frac{\partial H}{\partial y} = 0$ for a simple sill or $\frac{\partial W}{\partial y} = 0$ for a simple narrows.

The location where J is defined as described in 1 and where the conditions $\frac{\partial(H,W)}{\partial y} = 0$ and $\frac{\partial J}{\partial D} = 0$ are satisfied denotes the position of the control section (i.e. where the supercritical and sub-critical surfaces intersect). This approach was extended to two-layer non-rotating exchange flows by Dalziel (1991), who also related it to the G^2 criticality condition. Lane-Serff *et al.* (2000) further extended this functional approach to three-layer flows through a channel of rectangular cross-section with a single geometric constriction represented by a narrow and/or a shallow sill. The rotating version of the functional approach by Dalziel (1988) and Dalziel (1990) is explained in the context of rotating hydraulics in the next section. An example of the use of such a functional in hydraulic control analysis of our laboratory flows can be found in section 6.3.2 (p.152).

Armi (1986) showed that exchange flow through a narrows with specified upstream conditions leads to two possible flow solutions which are determined by conditions downstream with respect to each layer. In both cases, the control is located at the narrows. For all such flows, the narrows is felt by both layers equally. In contrast, a simple sill only directly influences the lower layer with a weak coupling to the upper layer. This leads to a splitting of the control into a real topographic one at the sill top and a virtual one, usually located at the foot of the sill, downstream of the sill crest with respect to the upper layer (Dalziel, 1991). Virtual in this context means that conditions at a particular location are such that $G^2 = 1$ without any topographic extremum at the same location. Virtual controls also occur if there is unequal flux in each layer, equivalent to barotropic forcing in an exchange flow (Armi, 1986). If the volume flux in the lower layer exceeds a certain threshold value, dependent on the ratio of the two layer speeds, the virtual control is no longer coincident with the real one (at the narrows) but becomes a virtual one upstream, in the direction where the net flow originates. If the flux in the slower layer has ~70% or less than the flux in the faster layer, the flow may be described by one active layer alone. This means that the latter assumption is valid if the net flux in an exchange flow is strong enough to make one layer almost stagnant. In rotating flows this threshold for the ratio of layer velocities is thought to be much lower (e.g. Borenas and Lundberg, 1990).

In controlled exchange flows in general, hydraulic jumps are thought to be responsible for isolating the sub-critical reservoirs from the supercritical region near the ends of the strait or channel. This is necessary in particular if the reservoir conditions are such that the interface is near the surface or bottom in dense and light reservoirs, respectively. However, jumps are usually assumed to be relatively weak in amplitude, so that momentum (but not energy) is conserved and no entrainment takes place across the density interface. Such weak hydraulic jumps were found by Armi (1986) to change the reservoir interface height in relation to the reservoir Froude numbers based on energy conservation between layers. Any internal jumps may only exist up to the maximum flow rate allowing sub-critical flow. If the matching of controlled flow to the reservoirs requires mass and/or momentum transfer between layers, e.g. entrainment, a so called "shear region" will form followed by a "classical internal hydraulic jump". This may occur if jumps form not only to join the interface associated with the supercritical flow inside the channel to the sub-critical one in the reservoirs but also due to friction (Dalziel, 1991). Jumps will be considered further in the following section on rotating hydraulics.

As in Farmer and Armi (1986)'s study, the flow in the aforementioned theories is generally assumed to be quasi-steady: any adjustments to internal hydraulics are considered rapid in relation to the forcing, e.g. winds, atmospheric pressure gradients or tides. This may not always be so, however, as has been shown for several straits by Helfrich (1995). He investigated the effects of time variable barotropic forcing on the hydraulics of two-layer exchange flows. The quasi-steady assumption is found to be invalid for situations where long internal waves cannot pass through the length of the strait on the timescale of the barotropic flow or when the time variability is of the same order as the spatial variability, i.e. $\frac{dv}{dt} \approx u\frac{dv}{dy}$. Two main parameters were identified to quantify this: the ratio of strait length to the distance any internal signal will propagate within one barotropic forcing period, and the magnitude of the barotropic transport normalised with respect to internal gravity wave speed. For example, Helfrich (1995) found for the Strait of Gibraltar that the inclusion of time dependence accounts for some of the differences between observations and the theoretical quasi-steady estimate without barotropic forcing (net flux). To get the average transport through the strait, not only the control sections, as for usual hydraulic control concepts, but the geometry of the whole of the strait is important. This would considerably complicate any parameterisation or simplification of strait exchange.

In addition to time variability, many environmental examples show considerable mixing across the density interface (e.g. the Bosporus Gregg and Özsoy, 2002) and vertical shear in the exchange flow. This is not easily incorporated into hydraulic theory, as the concept of internal waves simply travelling on the density interface cannot be applied. Non-rotating homogeneous but inviscid shear flows have been investigated by Garrett and Gerdes (2003) who found internal waves are still arrested at a point of hydraulic control. For non-rotating vertically sheared and stratified flows, Hogg *et al.* (2001b) showed that two principal internal wave modes can exist: a density mode, with a maximum amplitude centred on the region of strongest vertical density gradient; two other modes, called vortical modes, have their maxima on the vertical shear derivative maxima on the edges of the sheared region. The vortical mode waves are not arrested at the control section, but transform toward the reservoir in such a way that they get trapped in one layer, outside the mixed/sheared region. Hogg *et al.* (2001b) argue that this effectively prevents any information propagation from the reservoirs to the control regions with respect to baroclinic dynamics. The influence of mixing on the velocity and density fields and fluxes in non-rotating exchange flows was investigated by Hogg *et al.* (2001a) using numerical experiments. They found the hydraulic controls, if analysed with the inviscid criterion given by equation 2.1 (p.25), generally split into real and virtual ones, similar to the case where a barotropic flux is present. However, the findings by Hogg *et al.* (2001b) show the inviscid analysis is not fully applicable to determine hydraulic control in partially sheared and mixed flows if only the density mode waves are relevant to the interfacial dynamics. Hogg *et al.* (2001a) tested the limits set by two-layer hydraulic theory (e.g. Armi, 1986) and a turbulent mixed flow theory, termed the viscous advective diffusive (VAD) solution, where the exchange is dominated by turbulent eddy viscosity and diffusivity instead of advection. They described the variation of the modelled exchange flux in terms of a single parameter, $G_{rT}A^2$. G_{rT} is the turbulent Grashof number, measuring the ratio of viscous to buoyancy forces, and A the ratio of depth at the narrows to the length of the mixed region extending along the channel. They assume a turbulent Prandtl number of unity. This makes sense if turbulence is present, reducing the Prandtl number from it's usual value of 6 for water (p. 170 Tritton, 1988), based on kinematic molecular viscosity. Several environmental exchange flows were classified using an inferred value for $G_{rT}A^2$, showing the relative validity of the hydraulic and the VAD solutions. They found that volume and mass flux increase non-linearly with $G_{rT}A^2$, from a lower limit set by the VAD solution to an upper limit set by the hydraulic solution. Although this thesis will not analyse the propagation of internal waves as done by (Hogg *et al.*, 2001b) due to the lack of simultaneous density and velocity measurements, the $G_{rT}A^2$ parameter will be used for judging the experimental results of this thesis in section 7.3 (p.174).

2.1.3 Rotating hydraulics

In rotating flows, the additional influence on the flow is represented by the Coriolis parameter, $f = 2\omega sin\phi$, where ω is the angular rotation rate of the earth or a laboratory platform and ϕ the latitude. This causes the horizontal velocity to be accelerated perpendicular to it's direction, depending on the latitude in the ocean or the rotation of the experimental platform. Any density interface between two exchanging layers will thus be sloping not only along but also across the strait or channel. Rotating flow through a rectangular channel connecting two 'infinitely' deep reservoirs was first considered by Whitehead *et al.* (1974). This includes forced flow of a single reduced gravity ($1\frac{1}{2}$) layer and a two-layer lock-exchange. Whitehead *et al.* (1974)'s theory is based on the shallow water version of the Navier-Stokes equations, assuming homogeneous, inviscid layers and hydrostatic flow. In their semi-geostrophic approximation quantities, such as velocity, are expected to vary slowly along the channel, i.e. $\frac{d}{dy} << \frac{d}{dx}$ for geometric and interface height variations, and the flow to be approximately straight, i.e. $v >> u$, and in along-channel geostrophic balance. Assuming no relative vorticity in the "upstream" reservoir, the potential vorticity $\Pi = \frac{f}{H_u}$ ($\Pi = \frac{f}{D}$ in Whitehead *et al.*, 1974), based on the Coriolis parameter, f, and upstream depth, H_u. They further assume conservation of potential vorticity and $H_u \rightarrow \infty$ in the upstream reservoir, resulting in zero potential vorticity throughout the exchange flow. For $1\frac{1}{2}$ layer flow in the fast rotating limit, where the interface intersects the channel bottom, the flux is $q = \frac{g'h_u^2}{2f}$. This is equal to the maximal flux bound for free surface flows in rotating channels of arbitrary topography with non-negative potential vorticity found by Killworth and McDonald (1993), which suggests that potential vorticity, and thus the depth of the upstream basin, does not influence the flux to a great extent for most of the parameter range. This was also shown for two-layer flows by (Dalziel, 1988), hereafter referred to as D88.

Gill (1977) used his hydraulic functional approach, explained in the previous section, to describe a semi-geostrophic flow through a rectangular cross-section channel with a sill connecting two reservoirs. Width scales are based on the upstream Rossby radius, $R = \frac{\sqrt{gh_u}}{f}$, depth on h_u and velocity on $\sqrt{gh_u}$. Potential vorticity is assumed to be non-zero and constant ($\frac{\partial \Pi}{\partial x,y} = 0$) so that reservoirs are of finite depth but wide relative to R. As in non-rotating hydraulics long gravity wave phase speeds vanish at the control sections, although the nature of such waves is influenced by significant cross-channel variations due to rotation and the Rossby radius, i.e. Kelvin waves. Three parameters are given to determine the upstream reservoir condition: the sidewall boundary layer fluxes and the interior basin depth, e.g. a constant depth reservoir resulting in uniform Π. These are related such that specifying either the fluxes or the basin depth together with the channel geometry determines the remaining parameter(s) and thus fully describe the flow. Furthermore, if the channel is much wider than R or a sill of sufficient height is present, the current separates from the left hand boundary (for $f > 0$). In such a case, changes in width do not affect the flux that is only dependent on the ratio of sill height to upstream reservoir depth. This is similar for two-layer flows as will be shown below.

In the absence of single-layer hydraulic control, sub-critical flow may still be controlled geostrophically (e.g. Toulany and Garrett, 1984). First investigated theoretically and experimentally by Shen (1981), this phenomenon occurs if the downstream reservoir height is above the level of the sill. The free-surface height across the channel is then determined by the surface level difference between both reservoirs. This type of control is not possible in two-layer exchange flows. Further treatment of single layer rotating sill flows can be found in Pratt *et al.* (2000).

Although single (or reduced gravity) layer flows often occur in environmental settings, many cases require a multi-layer approach, as shown in the previous section for non-rotating flows. A theoretical treatment of two-layer hydraulics in channels of width much larger than the internal but smaller than the external Rossby radius is given in Pratt and Armi (1990). Here we are primarily interested in channels, where the external dynamics can be neglected, which in the rotating case not only requires $\Delta\rho << \rho$ but also the external Rossby radius to be much larger than the strait, so that the water surface is practically level. For a two-layer lock exchange in a rectangular channel Whitehead *et al.* (1974) found the dimensional flux through the lower layer to be

$$q_{whitehead} = \frac{1}{2}\sqrt{g'}H^{\frac{3}{2}}\frac{W}{2}(1-\frac{1}{3}\frac{W^2}{R^2});\ for\ \frac{W}{R} < 1 \tag{2.2}$$

at low rotation, with the interface intersecting both channel walls, and

$$q_{whitehead} = \frac{1}{6}\frac{g'h_0^2}{f};\ for\ \frac{W}{R} > 1 \tag{2.3}$$

at high rotation, with the interface intersecting both surface and bottom, where g' is reduced gravity, f the Coriolis parameter, H the channel depth, W the width and h_0 the layer thickness in the channel. The transition between these two states is continuous, where the interface spans from the left hand corner of the channel to the upper right hand wall. The exchange flow is reduced relative to the non-rotating value, by about $\frac{1}{3}$ for $W \sim R$. As in the single-layer case, q at high rotation is independent of W, but the maximal flux is now $\frac{1}{3}$ the value Whitehead *et al.* (1974) found for forced $1\frac{1}{2}$ layer flows.

An extension of the Gill (1977) functional approach was used by D88 and Dalziel (1990) to model hydraulic exchange flows both with and without rotation. The functional approach can principally be applied to any arbitrary channel geometry; however, the equations are greatly simplified by specifically considering rectangular and parabolic channel cross-sections with controlling narrows and sills of arbitrary height. Both the constant and zero potential vorticity constraints were investigated. The latter showed a maximal flux equivalent to the one found by Whitehead *et al.* (1974) and given in equations 2.3 (p.30) and 2.2 (p.30).

In accordance with previous authors, D88 found that the exchange is maximal for controlled flows, the same as in non-rotating channel flows. The fundamental difference between a sill and narrows in any two-layer system is also found in the rotating case (c.f Armi, 1986). The narrows equally influence both layers whereas a sill mainly affects the lower layer. D88 further notes that this asymmetry is reduced by rotation. As pointed out by Gill (1977) for single layer sill flows, if the upstream reservoir is wide, the only reservoir conditions needed for the hydraulic problem are the surface level in the reservoir interiors and the (arbitrary) fluxes in the side wall boundary layers; however, the latter cannot be arbitrarily defined for two-layer flows, meaning that flow between reservoirs of different interface depths has to pass through a hydraulic transition. Therefore, the case of a geostrophic control mentioned before is not realisable in two-layer exchange flows but is replaced by a partial control of the flow, where the control area is isolated from only one of the reservoirs with respect to long gravity wave disturbances (D88). This is associated with sub-maximal, but still controlled, exchange flux.

The ratio, b_c, of the channel width, W, to the Rossby radius, R, is used by D88 as a measure for the importance of rotation. In a rectangular constant depth channel with equal layer potential vorticity and $b_c \leq 1$, the exchange flow rate and the details of the flow are fairly independent of the actual value of potential vorticity. A summary of the shear interface position (active part of the flow) is shown in figure 2.1 (p.32). It shows the intersection of the interface with the walls and the channel floor and surface at different rotation rates; However, for $b_c > 1$ ($R_0 < 1$) this cannot be predicted exactly by theory. There, regions of stagnant fluid are thought to form on either side of the active flow crossing the channel. In the case of a constant depth channel with $b_c \sim 1$, there may be a single control or two controls. The latter are symmetrically located on either side of the narrows coinciding with a separation of the interface from the sidewalls and enclosing a region of sub-critical flow. Near this value of b_c, the theory breaks down for non-zero potential vorticity in channels of constant depth.

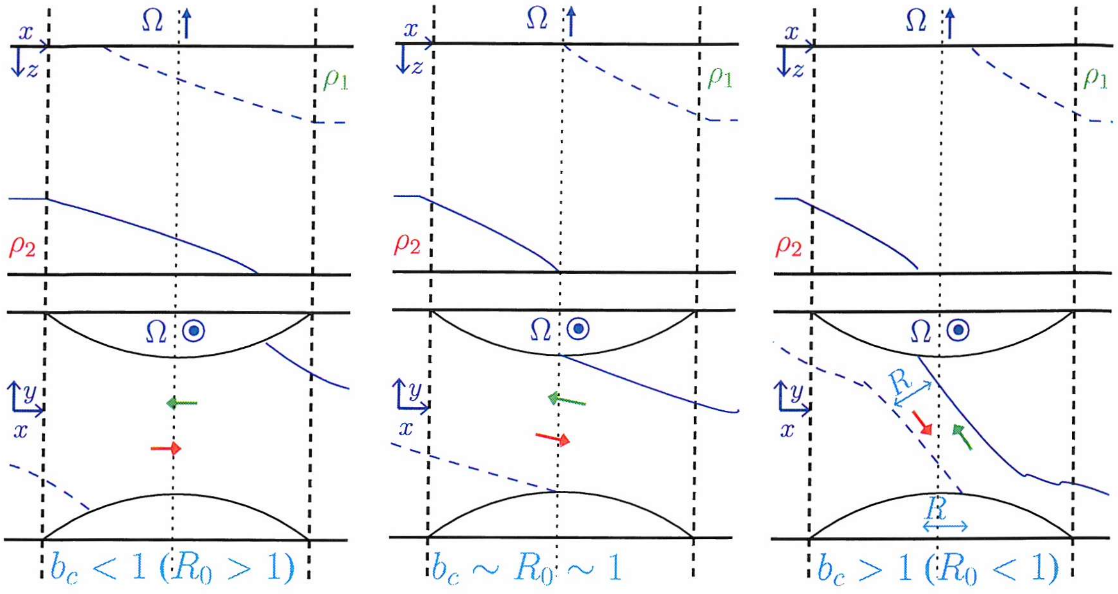

Figure 2.1: Position of the shear interface with changing b_c for lock-exchange flows (no net flow) in constant depth channels. Top panels show side view with dashed (solid) lines showing the interface at the RHS (LHS) wall of the channel. Bottom panels show plan view with dashed (solid) lines representing the interface intersection with the surface (bottom). Also shown is the R_0 parameter ($= b_c^{-1}$), which is also defined in section 3.1 (p.42). The interface intersections with the surface and bottom move toward the narrows as rotation is increased (b_c increased, R_0 lowered). D88 found that generally in this type of flow the control is at the narrows or near the channel ends ($b_c = R_0 = 1$). Note that for $b_c > 1$ ($R_0 < 1$) the exact position of the interface and channel crossing cannot be well predicted. However, D88 found in experiments that this crossing is usually around the narrows, oscillating along the channel in time with regions of stagnant fluids toward the walls.

Only with a symmetric vertical constriction does the theory show realisable flows with these parameters. In any geometry, the flow becomes separated for $b_c \gtrsim 1$ and the exchange flow rate is independent of channel width. This limit is slightly increased in finite potential vorticity flows and slightly reduced for sill flows due to the influence on the lower layer; for infinitely deep sills this is $b_c > 0.89416$ (Dalziel, 1990). The possibility of velocity reversal in the upper layer at both control sections would violate the basic assumptions of hydraulic theory, especially if there are closed streamlines (recirculations) away from the reservoirs. D88 overcame this problem by assuming a region of stagnant fluid, that may be formed by small viscosity acting over the long time period needed to attain a steady state. However, it is not clear where across the channel the interface should be located as it could be anywhere according to inviscid theory (c.f. channel crossing in section 2.2.1, p.34).

As in non-rotating hydraulics, barotropic forcing introduces an along-channel asymmetry to the flow and location of controls. It also changes rotational effects on the exchange flow rate: for no net flow, rotation decreases the exchange, whereas rotation increases it if larger barotropic forcing is present. If a simple sill is present, rotation decreases the asymmetry of the flow caused by the sill influence on the lower layer and changes the position of the virtual control (D88).

D88 noted that flow criticality in two-layer rotating flows may still be determined using a composite Froude number, similar to that in equation 2.1 (p.25), but now the definition is based on the hydraulic functional. Information is propagated via long, small amplitude internal Kelvin waves, whose amplitude varies across the channel. The importance of hydraulic controls and the fact that fully hydraulically controlled flows are always maximal has been emphasised by Killworth (1995). He showed for single layer and continuously stratified fluids that local flux maxima correspond to hydraulic controls and that all such controls, real or virtual, have to be specified to fully describe the flow. However, practical application of this theory to specific exchange flow cases was deemed impractical.

The problem of time variability in rotating hydraulics is still unsolved. Hydraulic jumps play an important part in this as they may travel in the form of a bore forced by changing flow conditions (e.g. tidal variation). This is possible since bores are not long gravity waves but represent a single or a group of solitary wave(s) that transmit the change in flow hydraulics (c.f. Lane-Serff and Woodward, 2001). The dynamics of rotating internal bores have not yet been satisfactorily described and details of the associated processes are beyond the scope of this thesis. However, even a stationary jump may influence the flow by changing its potential vorticity and facilitate mixing between fluid layers. D88 argued that hydraulic jumps may be assumed to be small if the interface height following the jump is "close to the level of the sub-critical solution associated with the controlled solution"; the location of such a jump will be near the control and thus be of small amplitude. There is likely to be little mixing in such a case (c.f. Armi, 1986) and potential vorticity will be unaltered if the reservoir is close to flooding the control. Thus the details of such a jump are unimportant with respect to the hydraulic control state which is only determined by the reservoir interface height, provided reservoir conditions have not been significantly altered.

Another unresolved topic are flows with non-constant potential vorticity. This problem is difficult to solve due to closed streamlines that do not enter the reservoirs. D88 suggests that the flow can still be viewed in the 'classical' sense considering contractions / sills and solution branch points / controls denoted by $G = 1$, where the specific energy at the sidewalls is at a local minimum. However, no detailed treatment of this has yet been given in the literature.

The following sections show some experimental and observational examples of rotating single layer overflows and multi-layer exchange flows. The environmental examples will show that many straits contain islands or submerged ridges that divide the flow giving rise to phenomena not observed in simple channels. However, previous experimental studies have all been concerned with simple channels.

2.2 Experimental and environmental example cases

2.2.1 Rotating hydraulic experiments

Whitehead *et al.* (1974) found good experimental agreement with semi-geostrophic theory both for attached (interface intersects both walls) and separated (interface intersects channel top and/or bottom) zero potential vorticity flows. In both $1\frac{1}{2}$ and two layer experiments at high rotation the interface sloped within approximately one Rossby radius from the right hand wall (looking downstream with respect to the lower layer) of the channel but did not intersect the top and/or bottom boundaries as predicted by theory. Instead a level region formed in the rest of the channel that was thought to return the viscous boundary layer transport to the inviscid interior via the sidewall boundary layer. Frictional effects were thought to be the cause of this which agrees with D88 who incorporated the thickness of, and transport in, viscous rotating boundary layers (Ekman and Stewartson layers) into his experimental analysis. This manifests itself in the form of levelling of the interface near the sidewalls due to horizontal shear layers and also shallowing of the interface overall toward mid-depth due to vertical boundary layers at the interface transporting fluid toward the wall. Such boundary layers do not occur in the same way in the oceans due to sloping boundaries and difference in horizontal, depth and viscosity scales. However, frictional boundary layers have been studied in the laboratory by Johnson and Ohlsen (1994). They simulated exchange through a semi-circular cross-section channel based on observations from the the Faeroe Bank channel, indicating that boundary layers can be significant in oceanic settings. Note that this is different to the rectangular cross-section channel used in the laboratory experiments in this thesis.

Further studies of single layer flow by Shen (1981) included a simultaneous sill and narrows located in a rectangular cross-section channel. The flow transport varies inversely with rotation rate and upstream potential vorticity, except for some special cases of channel floor topography (c.f. section 2.3). The experimental results agree well with semi-geostrophic theory, except when supercritical separation (high f) occurs at the control section. This agrees with numerical model results by Pratt *et al.* (2000) who also found that such separation does not occur at the narrows for hydraulically controlled flows, even though theory predicts this. Separation is also difficult to predict theoretically in two-layer rotating hydraulics, as it is not possible to restrict hydraulic control to a specific location in the channel if the two-layer flow is separated from both walls at the narrows (D88).

D88's experimental work showed that in a constant depth narrowing channel without barotropic forcing the interface slope for $R > W$ compares well with semi-geostrophic two-layer theory with the viscous adjustment mentioned above. He also found strong evidence for zones of stagnation mentioned in section 2.1.3. This concept agreed with the observed exchange flow rates but uncertainty remains as it contradicts the constant potential vorticity constraint used in his theory.

D88 also showed that the flow in each layer crossed the channel in the region of the narrows. This crossing occurred at a length scale governed by the channel width for $b_c < 1$. For wider channels, the width did not seem to influence the flow and the flow crossed at a length comparable to one Rossby radius. This is also supported by Gill (1976)'s Rossby adjustment problem, although the mechanisms of transition from a growing fluid intrusion to a steady controlled flow are not yet known. In the laboratory this refers to the adjustment of the dam break flow at the location of the barrier to the controlled flow at the geometric constriction, i.e. the narrows. The along channel location of the crossing seemed to oscillate at frequencies proportional to f, but in the presence of a sill was fixed to the geometric contraction. In such separated flows, D88 proposed that this channel crossing hydraulically controls the flow. It is associated with the formation of Margules-type fronts, where frontal waves replace the internal Kelvin waves on the density interface (see also Nof, 1986).

2.2.2 Representative environmental exchanges

The different exchange configurations of channels connecting two basins can be found in environmental flows. Rotation is not found to be relevant to straits much narrower than the baroclinic Rossby radius, such as the Red Sea outflow. There, very simple conditions may be used at the exit together with a model of the basin (e.g. Grimm and Maxworthy, 1999), although more than two layers (Smeed, 2000) and seasonal variability Siddall *et al.* (2002) can add additional complications. For channels much wider than the baroclinic Rossby radius (and close to the barotropic one), such as Drake Passage, the theory by Pratt and Armi (1990) mentioned in section 2.1.3 may be suitable. The rotating hydraulic control theory presented in section 2.1.3 (p.29) is thought to be most applicable for straits of width in between these two extremes.

First we will consider basin connections slightly wider than but close to the internal Rossby radius. Borenas and Lundberg (1990) discussed hydrographic data from the Faeroe Bank Channel deep-water flow in the context of rotating hydraulic $1\frac{1}{2}$ layer theory. Single layer infinite upstream depth models (e.g. Whitehead *et al.*, 1974; Borenas and Lundberg, 1988) were found to be accurate to "lowest-order" and previous theoretical maximal flux estimates agreed well with observations. When incorporating finite upstream depth models to account for bidirectional velocities in the upper basin, the lower layer was well described. However, the interface height and the magnitude of the velocity variations in the lower layer were different from the observed. Although the lower layer was observed to have velocities at least three times that of the upper layer, i.e. there was a significant net flux, the upper layer showed large fluctuations and even velocity reversal, rendering the assumption of a stationary and quiescent upper layer invalid. This may be due to the fact that the Rossby radius is smaller than the channel width. However, classification of the Faeroe Bank Channel with respect to it's width is complicated by the fact that the cross-channel topography is not rectangular and does not extend to the surface due to the adjacent shelf areas. Therefore some authors consider it to be of similar width to the Rossby radius (Johnson and Ohlsen, 1994) and some as a "wide" channel (Borenas and Lundberg, 1990). Note that recirculation would not occur in the non-rotating case without some topographic forcing, so that the quiescent layer assumption is valid more often (c.f. Armi, 1986). This represents one reason to study the rotating two-layer case, even in the context of ocean strait overflows.

The Gibraltar Strait represents another interesting case. It consists of a series of sills and narrows, where the strait width at each of these locations is narrower than the internal Rossby radius. This complicated situation has largely been modelled using non-rotating hydraulic control theory (Armi and Farmer, 1988), although additional processes have been identified associated with this exchange; for example, basin conditions (Bryden and Kinder, 1991) and tidal variability (Helfrich, 1995). The latter can cause the exchange to be sub-maximal for part of the time, even when using a quasi-steady model (Garrett, 1996; Astraldi *et al.*, 1999). D88 also modelled the flow through the Strait of Gibraltar using his semi-geostrophic theory and found that rotation does not change the exchange to a great extent, relative to the non-rotating model. He additionally varied the parameter f to model the exchange to a hypothetical strait of width greater than is actually the case. However, he found the situation difficult to model when $R_0 < 1$, as the case for a separate sill and narrows is not as well known as the non-rotating equivalent (see section 2.1.2, p.25). An attempt to resolve this dilemma of control section location (and thus a well defined topographic control) has recently been made by Laanearu and Lundberg (2000) who used the Bornholm channel as an example to calculate an upper bound for the transport by the deep water flow. However, their stationary upper layer assumption is found to be valid only to lowest order (c.f. Faeroe Bank channel Borenas and Lundberg, 1990).

The above examples may account for along channel variations but all assume that all the flow passes through a single channel. This may not always be the case as can be seen in the Cretan Arc Straits (e.g. Theocharis *et al.*, 1999) where topography is highly variable resulting in complex layered hydrography around islands and submerged ridges. Other examples include the Indonesian archipelago (e.g. Nof, 1995; Potemra *et al.*, 2003; Gordon *et al.*, 2003), where the detailed processes of topographic influence on the exchange through the various straits are still not fully understood, and the Straits of Hormuz, where the outflow in a deep channel bifurcates at an island (Johns *et al.*, 2003).

The Strait of Sicily has two deep (below shelf level) channels connecting the Eastern and the Western Mediterranean Seas (see figure 2.2). Stansfield *et al.* (2003) show that this leads to a more complicated path of the deep flow from the former to the latter basin through the strait than would likely be the case with a single passage. The main flow in the intermediate density layer (Levantine Intermediate Water) generally steers toward the right (North-east of the strait) but is separated in two by the ridge. The flow to the left of the ridge keeps close to this obstacle and circumvents it, flowing back in to join the flow through the much narrower channel to its right, as shown by velocity, salinity and temperature measurements from different instrumental platforms (see also Stansfield *et al.*, 2001). Similar flows are observed in the experiments with multiple channels described in this thesis. A review of theoretical and experimental findings relevant to such geometries is given in section 2.3 (p.39).

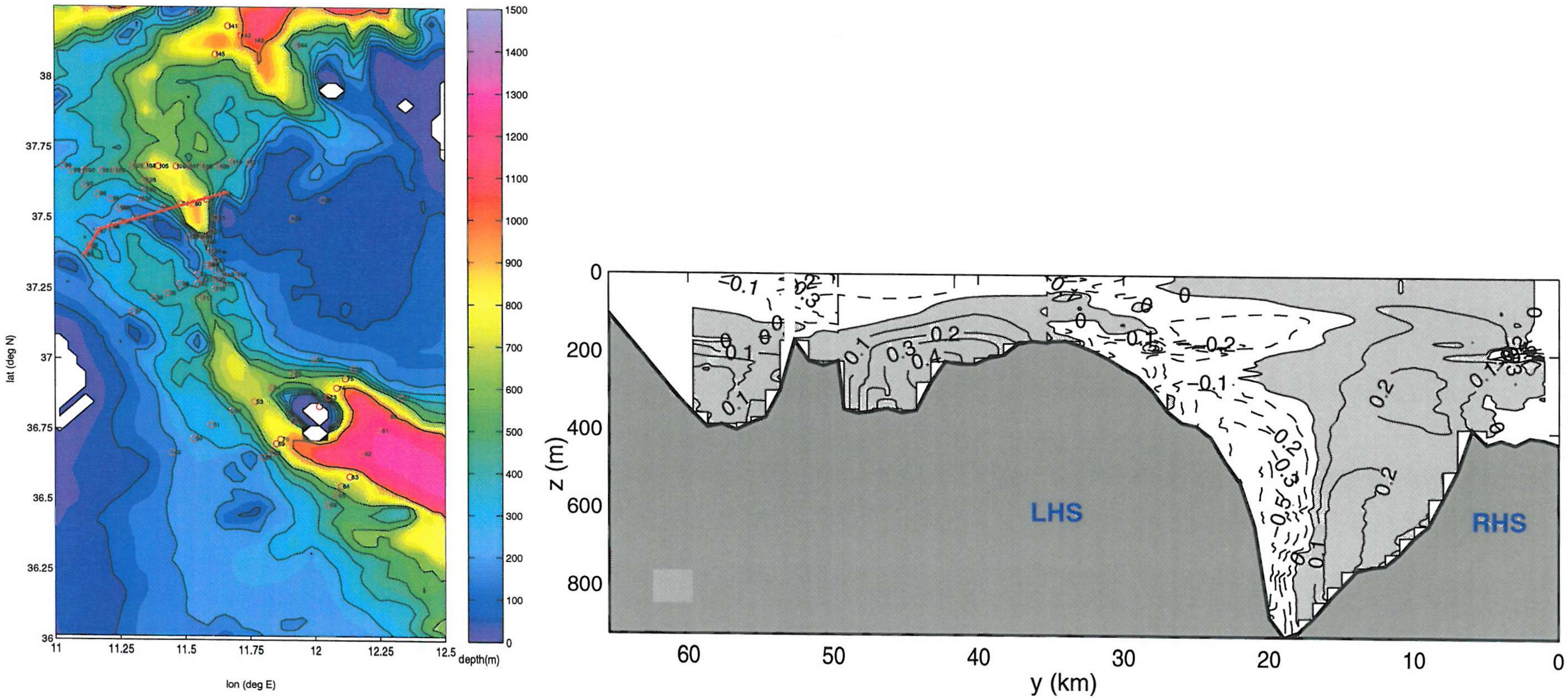

Figure 2.2: Topography of the Strait of Sicily in the vicinity of the Sicily channel (plot on left). The region of the sills is divided by a ridge submerged to about the level of the bordering shelf. The location of a hydrographic cross-section of velocity is shown by the thick red line, located at the North-western end of the ridge. This cross-section represents Lowered Accoustic Doppler Current Profiler (LADCP) data merged with ADCP measurements from an autonomous underwater vehicle, AUTOSUB, all taken in May, 2000 (Stansfield *et al.*, 2001) and is shown in the plot on the right. Velocity is given in ms^{-1}, where positive (shaded) contours represent flow into the western basin. The figure is modified from Stansfield *et al.* (2003). The deep flow from the Eastern to the Western Mediterranean can be seen on both sides of the ridge. However, a reverse flow occurs in the left side of the right-hand channel. This has been shown to originate in the left-hand part of the section and to circumvent the ridge in the form of a jet (Stansfield *et al.*, 2003).

2.3 Channel dividing obstacles

One of the main aims of this thesis is to understand the effect of flow-dividing obstacles on the hydraulics of the flow with particular focus on the case of an island. In the non-rotating case, this can be observed in single-layer flow around bridge piles or piers. Henderson (1966) reviewed several different cases of such flows, where the reservoir level downstream of the piles may be used to compute upstream levels. This was related empirically to the Froude Number downstream as well as the pier shape and dimensions. Henderson (1966) also mentioned a limiting value of distance between the piles, a function of the Froude Number, that determines if the flow is critically controlled between the piles or sub-critical everywhere. Furthermore, energy loss due to drag was related to flow velocity and the drag coefficient. Longer (non-cylindrical) piers and large angles of pier offset from the along-channel direction increase this coefficient and thus the difference in reservoir heights.

Apart from small vortices at the downstream end of the piles (or on the sides for an offset pier) and two additional friction-related boundary layers this case is the same as that of a simple narrows in non-rotating flows. However, when rotation is introduced, surface or interface height as well as velocity vary across the channel. An island centred at the narrows will provide an additional wall that the flow can "lean on", particularly if the flow crosses the channel at high rotation rates. Such a situation is therefore likely to modify the cross-channel asymmetry in the flow and the interface slope. This has been investigated theoretically by Whitehead (2002), who used single, reduced gravity, layer theory to investigate the flow through a rectangular channel divided by an infinitely thin island. Whitehead (2002) argued that if the upstream Bernoulli function (energy) is approximately the same, the flux will be approximately the same in each channel half. Therefore, the sum of the flux through the channels would be twice the maximal flux for the whole channel without an island. One could imagine this argument being extended to the two-layer exchange flow case. However, the work of Killworth and McDonald (1993) suggests that there is an upper bound on overflow of a reduced gravity flow that is independent of the number of channels. Resolving this question is a major objective of this thesis.

The Strait of Sicily example, presented in the last section, shows the complex flow path that can be caused by a submerged ridge separating the deep and intermediate exchange flows. Such processes will be one focus of this study, in particular if they influence the baroclinic coupling between the two flowing layers.

Unfortunately the theoretical and experimental treatment of exchanges with such topography has received little attention in literature so far. Some work on single layer rotating zero potential vorticity flow through non-uniform channel cross-sections has been undertaken by

Shen (1981). He defined the case of flow separation to occur if the interface lies below the mean cross-channel depth somewhere within any cross-section. This investigation mainly considered inclines of constant cross-channel slope. The transport was predicted to increase to a maximum at some moderate rotation rates if the floor slopes in the same direction as the water surface but to otherwise decrease with rotation. For the case of concurrent slopes the transport was also predicted to be larger than for opposite slopes. The experimental results for non-separated flows agreed well with the semi-geostrophic theory for all cross-channel slopes, but the separated case generally did not. In the latter case a stagnant region near the (upstream) entrance (c.f. Borenäs and Whitehead, 1998) was observed to break down a short distance further down the channel despite its predicted existence there.

Many studies have examined flow around islands and ridge topography usually in homogeneous or continuously stratified fluids (see review by Boyer and Davies, 2000) and often turbulent flow, for example studying generation of lee wakes (e.g. Alessio *et al.*, 1992) and vortices (e.g. Longhetto *et al.*, 1996). This is relevant to many environmental settings, such as atmospheric flows over orography, but none of these have specifically considered exchange flows.

The Rossby adjustment problem mentioned before (for linear and non-linear studies see Gill, 1976; Helfrich *et al.*, 1999, respectively), although not bound by the semi-geostrophic assumption, is only partially useful as it does not include any hydraulic control and information about the steady state is limited. Studies that do attempt to treat a wide range of hydraulically controlled flows includes theory by Killworth (1995) that describes certain features inherent in any hydraulic flow. For non-uniform sill cross-sections flow control is not necessarily uniform across the channel, so that $G = 1$ can no longer be used as an along-channel varying parameter. However, no application of this theory to environmental flows is made as a very complex topography would likely have an infinite amount of virtual controls, which makes a hydraulic model impractical.

To my knowledge, no work other than Whitehead (2002) has been published regarding the effect of an island on the exchange flow hydraulics through a rotating channel. Detailed prediction of the expected flow pattern cannot be made since suitable hydraulic theory does not exist and no adjustment of previous theory to this situation is attempted. However, the theoretical fully hydraulically controlled (maximal) flux with zero potential vorticity will be used as a comparison to the simple channel and island cases under study. As the island represents a cross-channel discontinuity, some of the basic assumptions of existing semi-geostrophic theory are likely to be broken. This includes the assumptions of slow along channel variations and no significant cross-channel flow. In particular regions near the ends of the island may introduce significant changes in the flow pattern not present in a simple channel, that may change the baroclinic interdependence of each half of the whole channel cross-section and the paths each layer in the exchange flow will take. The next chapter will describe the setup and method for the laboratory experiments in this thesis.

Chapter 3

Laboratory methods

3.1 Schematic layout and non-dimensionalisation

A simplified version of the situation in an oceanic strait can be represented in the laboratory as shown in figures 3.1(a) (p.43) and 3.1(b) (p.43). The channel is bounded on either side by large reservoirs with water of different density, separated by a lock-gate. This thesis studies the lock-exchange flow that ensues once this gate is raised. The right hand side of the channel looking toward positive y will be denoted as RHS and the left side LHS throughout this thesis. This will be facing downstream with respect to the lower (dense) layer, looking into the light reservoir. When otherwise denoting the flow direction, however, we will use *right* and *left* with respect to the principal along-channel direction of the flow in that layer. This means that "the upper layer flow turns to the right" could actually be the flow turning to the LHS of the channel, as by our definition above.

Reduced gravity at the layer interface is defined as $g' = g\frac{\Delta\rho}{\bar{\rho}}$, where $\Delta\rho$ is the density difference between the two layers and $\bar{\rho}$ the mean density. The Rossby radius for our purposes is defined as $R = \frac{\sqrt{g'H}}{f}$ and in non-dimensional form $R_0 = \frac{R}{W}$. Subscripts will be used when the differences in R_0 defined by the different channel cross-sections (island and simple channel) are highlighted: i denotes the island case, R_{0i} and W_i, and similarly s the simple channel and (R, L) the individual channels on each side of the island. However, wherever R_0 and W are used they refer to the corresponding value for the experiment, e.g. in an island experiment $R_0 = R_{0i}$ unless otherwise stated (that this is indeed the appropriate scaling in the island cases and not $R_0 = R_{0s}$, as in the simple channel cases, will be shown in the analysis in sections 5.2.1, p.108 and 6.1, p.133). The definition of the internal Rossby radius differs somewhat from the strict definition of the 1st mode baroclinic Rossby radius as it does not account for the interface depth. However, the interface is sloping significantly across the

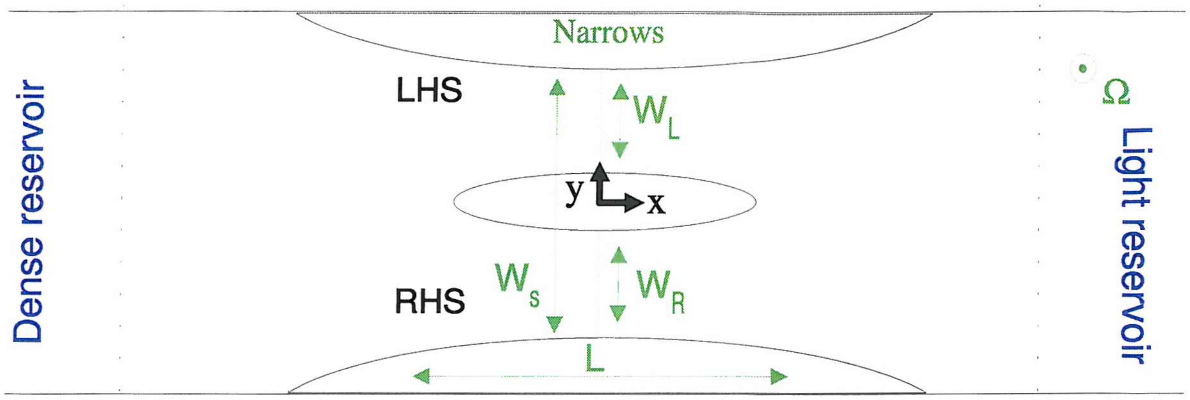

(a) Plan view.

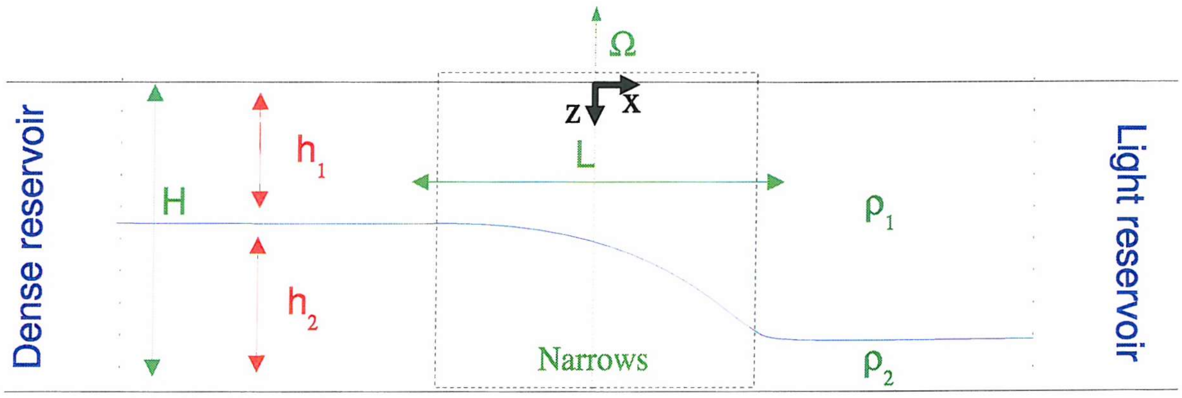

(b) Side view (from RHS).

Figure 3.1: Principal geometry and important parameters for hydraulic investigation. The coordinate origin is in the centre of the channel at the surface with y increasing along to the right, x across to the channel left and z vertically downward. $h_{1(2)}$ and $\rho_{1(2)}$ are the upper (lower) layer depth and density, respectively, and H the total water depth. $W_{(R,L)}$ is the channel width on the RHS (LHS) of the island, W_s the total channel width from "coast to coast" and $W_i = W_R + W_L$, i.e. the whole channel width less the island. Ω is the rotational vector, where the Coriolis parameter, $f = 2\Omega$. Note the barrier is not marked in the figures. It is on the $y < 0$ (dense reservoir) side of the island in most cases, except experiments 703 and 15. The exact location also differs between the two platforms.

channel, so that the only constant height parameter is H. The non-dimensional number R_0 is a type of Rossby number, based on a velocity scale of $\sqrt{g'H}$ instead of the velocity of the actual flow. In that sense, R_0^2 is also a Burger number in a two-layer stratified fluid. An earlier study by D88 used the non-dimensional channel width as the main parameter, which is the inverse of our R_0.

The non-dimensionalisation of variables is chosen as shown in table 3.1 (p.45). (x, y) and all variables incorporating length units have been non-dimensionalised with respect to the channel dimensions. This choice has been made as it agrees with the concept of R_0 and highlights the similarity to the non-rotating case at low rotation / high R_0.

Measured or derived quantity	Non-dimensionalisation
Horizontal distance (x, y)	$\frac{(x,y)}{W}$
Vertical distance (z)	$\frac{z}{H}$
Time (t)	$t \cdot f$
Horizontal velocity $(u*, v*)$	$\frac{(u,v)}{(g'H)^{\frac{1}{2}}}$
Narrows exchange flux $(\overline{q})$	$\frac{q}{(g'H)^{\frac{1}{2}}HW} = \frac{q}{q_{nr}}$
Vertical divergent flux (q_{div})	$\frac{q_{div}}{q}$

Table 3.1: Non-dimensionalisation of variables. The symbol used for the non-dimensional variable is given in the first column, whereas the dimensional one is given together with the non-dimensionalisation in the second column. Note where both symbols coincide, the non-dimensional version will be used throughout this thesis. Unless stated otherwise, q_{nr} denotes the scale of the maximal inviscid two-layer exchange flux in a constant-depth channel with horizontal narrows as given by Armi (1986).

The following sections will explain how these experiments were conducted on two different platforms: a small, $1m$ diameter turntable at the Southampton Oceanography Centre (from now on termed *SOC* platform) and the large $14m$ diameter table at the CORIOLIS/LEGI laboratory in Grenoble, France (*Coriolis* platform). The different measurement techniques, errors and details of each platform's setup will be detailed in this chapter.

3.2 *SOC* platform

3.2.1 Layout and setup

The experiments were realised in a perspex tank (wall thickness $\sim 1.2cm$) measuring $(H * W * L)$ $30 * 56 * 87cm^3$ with the according maximum volume of $146l$ mounted on a rotating table. Taps were fitted in the tank bottom for drainage. The overall setup can be seen in figure 3.2.

The tank is divided into two reservoirs with a connecting channel $(H * W * L) 200 * 200 * 294mm^3$ (c.f. D88 experiments using a $100 * 100 * 300mm^3$ channel without island). The shape is relatively long and thin, but also wide enough to allow for $R_0 < 1$, even for experiments with an island. Curved inserts, fitted to the channel sides, vary smoothly over $240mm$ along the channel to reduce its width by $50mm$ at the narrows and give an overall shape as shown in the sketch in figure 3.1(a) (p.43). The island dividing the full depth of the channel has an approximately elliptical plan section, is $120mm$ long and $\sim 27mm$ thick.

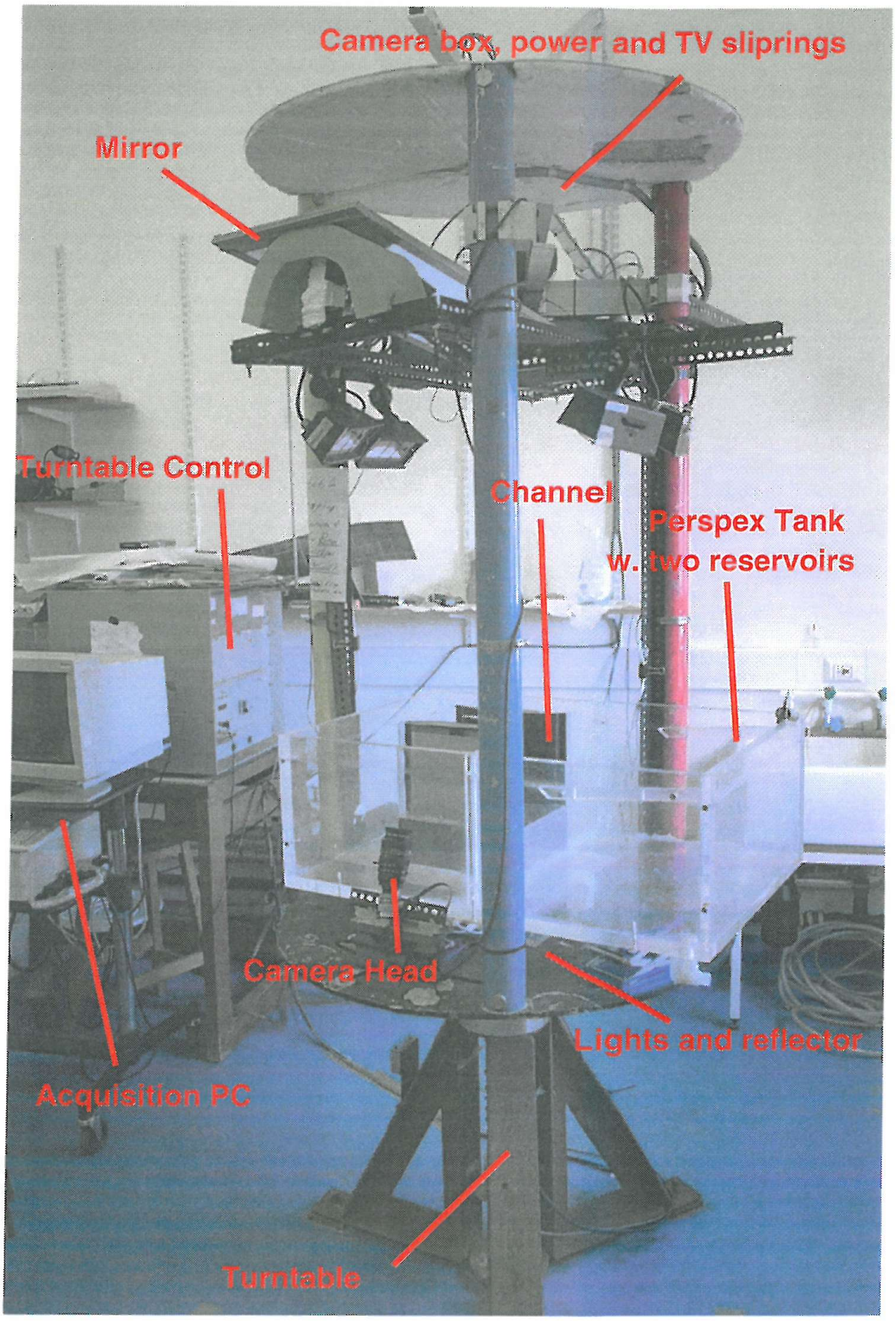

Figure 3.2: Overview of *SOC* setup. The channel, camera and other major components are indicated in the image. Please note that in our experiments the channel floor was at approximately the same level as the reservoirs, as opposed to this image taken from a previous setup. The halogen lights (same as can be seen mounted on the table in this picture) were positioned underneath the tank at each channel end to indirectly light the channel bottom via upward reflecting plastic-covered cardboard facing each set of lights at an angle.

Here, a compromise is made between a slowly varying island, i.e. relatively long, and the ability to observe flow around the island tips still within the channel, i.e. short island. The setup leads to a reduction width of $(8.8, 6.7)cm$ (simple channel,island) at the narrows, which is sufficient to investigate values of $R_0 < 1$. The barrier was generally located at the dense reservoir end of the channel, except in experiment 703, where it was at the light reservoir end (see also table 3.6, p.79).

Care was taken in levelling the channel connecting the reservoirs and the turntable using a spirit level accurate to $1\frac{mm}{m}$ horizontal slope. When mounting the rectangular tank on the rotating table counterweights were used to move the centre of mass to the axis of rotation. On the horizontally levelled table (equivalent to the Earth's poles) $f = 2|\Omega| = \frac{4\pi}{T}$, where T is the period of turntable rotation (steady to within $\pm1\%$). Practicable Coriolis parameters are $\frac{4\pi}{5} \leq f \leq \frac{4\pi}{40}s^{-1}$ allowing for reasonably steady rotation at low f and easy accessibility of the table at large f, for example when raising barrier.

Density interface depth measurements were made by dyeing one, usually the lower, layer and recording the images using a COHU 4980 camera with a remote head positioned as shown in figure 3.3(b) (p.48). This is a non-intrusive method best suited to the small dimensions of the platform (see section 3.2.3 for further details of method). This gave a plan (top) camera view of the channel by use of a mirror mounted $\sim 70cm$ above the tank and maximised the path length between the camera lens and the channel to avoid distortion at wide lens aperture. The flow was lit by two sets of $2 * 500W$ halogen floodlights that point onto a piece of plastic covered cardboard at an angle to reflect directly upward through the channel bottom (see figure 3.3(a), p.48). The cardboard was shaped in this way to give continuous illumination in the vicinity of the narrows, so that two lines visible on either along-channel side of the narrows represent the joins between the three differently angled cardboard surfaces. Care was also taken to vent the lights with two small electric fans to avoid heating the water in the tank above. The intense illumination was necessary due to the use of a coloured filter mounted in front of the camera lens (see section 3.2.3) which significantly reduced the intensity recorded by the camera. The camera was directly connected (via the turntable's slip rings) to a frame grabber in a 90MHZ Pentium PC to avoid non-linear response associated with using a VCR and video tape. The frame grabber gave an image of $512x512$ pixels, which is close to the actual resolution of the camera. The camera's gamma correction and automatic gain were switched off at all times. This remote measurement of the flow did not disturb the flow, which is particularly important on a small platform.

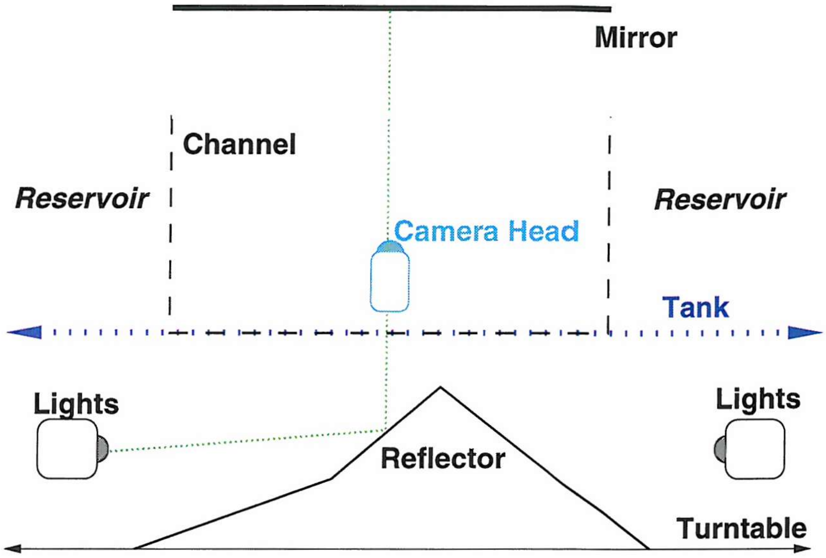

(a) Along-channel view (from camera)

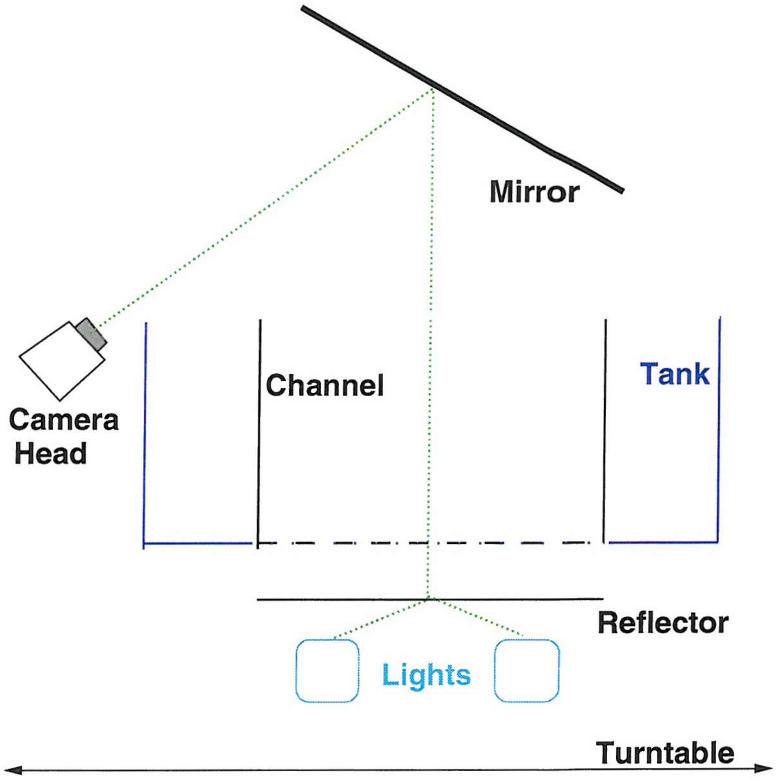

(b) Across-channel view (from lights)

Figure 3.3: Sketch of *SOC* setup. The channel, camera and other major components are indicated in the image. Note each sketch is in one vertical plane except the cyan-coloured component, which is located out of the page. The lights at each channel end illuminate the perspex channel via the reflector. The camera records plan view images of the flow via the mirror above the channel.

3.2.2 Density and fluxes

The time-mean exchange flux over the whole of a lock-exchange experiment can be calculated from density measurements of the (well mixed) reservoirs before the barrier is removed and after it has been replaced. The exchange flux is given by

$$q^* = \frac{|\Delta\rho_m|V}{t\Delta\rho}, \tag{3.1}$$

where V is the volume and $|\Delta\rho_m|$ the difference in initial and final density of reservoir m. $\Delta\rho$ is the initial density difference between both reservoirs 1 and 2 (Whitehead *et al.*, 1974). This only requires three measurements of ρ, i.e. the final ρ is only required for reservoir m. Using both $m = (1, 2)$ gives two different values of q^* that should be equal, the difference being a measure of the experimental error. Inferred values of q^*, the average of these two different values, will be presented as part of the flux analysis in chapter 6 (p.133).

To calculate q^* and to constrain the parameter regime for the experiments, reservoir density was measured at the time of the experiments using hydrometers. However, these only allowed $\Delta\rho$ to be determined to $5 \cdot 10^{-4} gcm^{-3}$ accuracy, leading to errors in q^* of $\sim 12\%$. Therefore, water samples were taken from each of the reservoirs and at a later date analysed in an Autosal salinometer allowing an accuracy of $0.01PSU$, lower than the usual instrument specification due to the large range of salinities in the samples (Ocean Scientific International representative, pers. comm.). A calibrated temperature probe was used to measure temperature to within $\sim 0.1^oC$ at the time the samples were taken. These temperature and salinity measurements gave a density value accurate to $2.3 * 10^{-5} gcm^{-3}$ (see table 3.2), i.e. an order of magnitude better than the hydrometer measurements.

The density difference, $\Delta\rho$, was chosen to allow a suitable range of Rossby numbers around unity, representing the theoretical transition from attached to separated flow at the narrows. Further considerations included viscous effects (see also Re discussion in section 3.4, p.73) associated with low $\Delta\rho$ (and similarly g') that lead to a very diffuse interface and thus invalidate the two-layer assumption. Another constraint was the camera image acquisition speed: to observe the flow a sufficiently low flow velocity, scaled by $\sqrt{g'H}$, was required. Past experiments showed a practicable range of $0.003 \le \Delta\rho \le 0.05 gcm^{-3}$ in the laboratory (min. from D88 and max. from Smeed (1988); Munday (2000)). With the above considerations and the measurement accuracy in mind the following fixed parameters were chosen: $\Delta\rho = 0.003 gcm^{-3}$, $H = 14.5cm$, resulting in $g' \sim 3cms^{-2}$ and possible $3 \le R \le 22cm$ (for range of f given in section 3.1, p.42). Similar considerations were made for the *Coriolis* platform with parameters given in section 3.3.1 (p.54).

3.2.3 Dye concentration and interface height

As mentioned in section 3.2.1 (p.45), the *SOC* setup used plan images of the channel with the (usually) lower layer dyed to infer the position of the density interface between the two layers. Images were acquired using the camera system directly connected to the PCs frame grabber as the alteration of intensity may be highly nonlinear if recorded on video tape due to adjustment by and noise from the VCR electronics and tape response (Holford and Dalziel, 1996). The frame grabber was controlled using DigiImage V1.5, available from DL Research Partners, Cambridge. This software allowed images to be acquired at user-specified times. Subsequent processing to infer density interface depth was done using Matlab v.6 by Mathworks Inc. The intensity measurement of the camera system was calibrated to be representative of the absolute light intensity, I.

Red food colouring was used as dye in the dense fluid to visualise the interface between the two layers. The lower layer thickness, h, could be estimated by assuming an exponential attenuation of the light passing through the fluid from channel bottom (Holford and Dalziel, 1996). The attenuation coefficient in a uniformly dyed fluid is

$$k = \frac{-1}{h} ln(\frac{I}{I_0}), \tag{3.2}$$

where I is the light intensity past the fluid, I_0 the incident (background) intensity and h the path length of the light through the fluid (see also p. 517 Apel, 1987). Unfortunately the coefficient k is not constant across the light spectrum. In addition, it varies with dye concentration. Therefore a colour filter (green, Hoya X1) is used to select that part of the spectrum where k changes linearly with dye concentration. In this case the absorptivity function of the dye may be approximated to $k(c) = Ac + b$, where A and b are constants and c the dye concentration. However, b is assumed to be negligible, so that only c influences $k(c)$. The dye at the concentration used in the experiments has maximum absorbance at a wavelength of $\lambda \sim 480nm$. The filter actually transmits most light at $\lambda \sim 480nm$ (approximately Gaussian transmittance curve with $< 10\%$ transmitted at $\lambda > 600nm$, which was the most suitable commercially available at the time).

Using the attenuation approximation a relation between c, background corrected absolute light intensity ($\frac{I}{I_0}$, where I_0 is the background light intensity) and layer thickness (h) can be obtained

$$\frac{I}{I_0} = e^{-Ach} \Rightarrow c = \frac{-1}{Ah} ln(\frac{I}{I_0}) \tag{3.3}$$

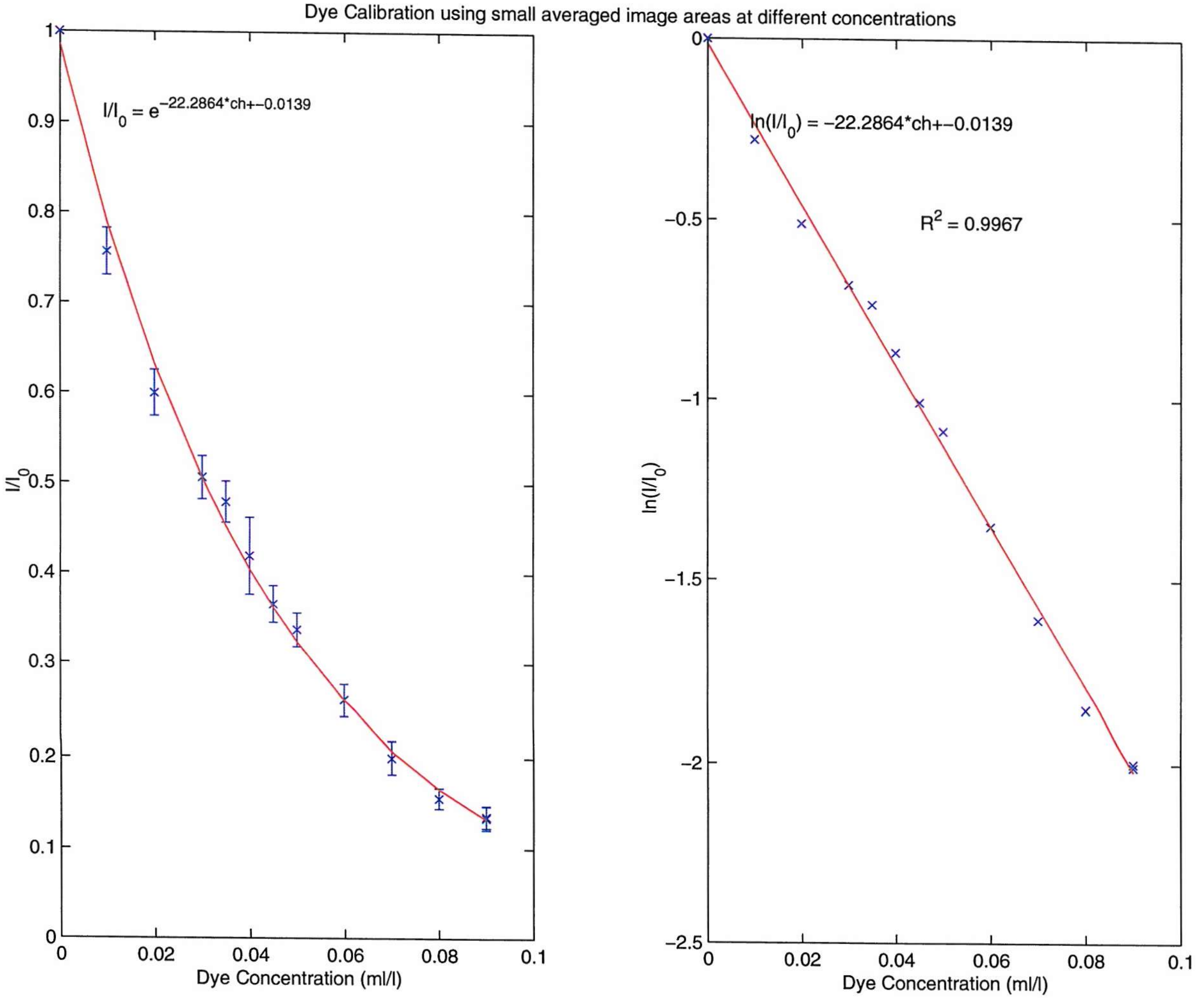

Figure 3.4: Dye concentration vs. background removed absolute light intensity as viewed from above the fluid ($\frac{I}{I_0}$). Note the steep slope at high intensities, which gives a large error when inferring c from $\frac{I}{I_0}$.

This relation was calibrated using the background image (I_0) of a beaker of constant-depth salt solution and images with different amounts of dye added (I). As can be seen in figure 3.4 (p.51) such a calibration of $\frac{I}{I_0}$ vs. c has an error in c that is biased toward the low intensities. Therefore a range of c was chosen where this relationship is more linear to give an approximately constant error in c. The maximum $c = c_p$ has been suggested by Holford and Dalziel (1996) to be where the tangent of $c = f(\frac{I}{I_0})$ is four times that at $c = 0$; this gave $c_p = 0.039\frac{ml}{l}$ for the channel depth in our experiments. This leads to the new relation

$$h = \frac{-1}{Ac_p} ln(\frac{I}{I_0}). \tag{3.4}$$

h was directly calibrated using a slanting container with a uniformly dyed fluid, which gave a horizontal variation in h by geometric considerations. This effectively gave a value for $\frac{-1}{Ac_p}$ from the calibration curves shown in figure 3.5 (p.53) and allows h to be accurately measured to within 7% of channel depth (see table 3.2). Parallax was ignored as it was found to be within the measurement error when recording a uniform dye field.

Potential shortcomings of the method are mixing of the two fluids causing a diffuse interface and filling up of regions in the initial, unsteady phase that are stagnant and/or isolated during the steady exchange, thus giving a false impression of the active part of the flow. Any scattering effects are included in the dye attenuation and are considered to be negligible.

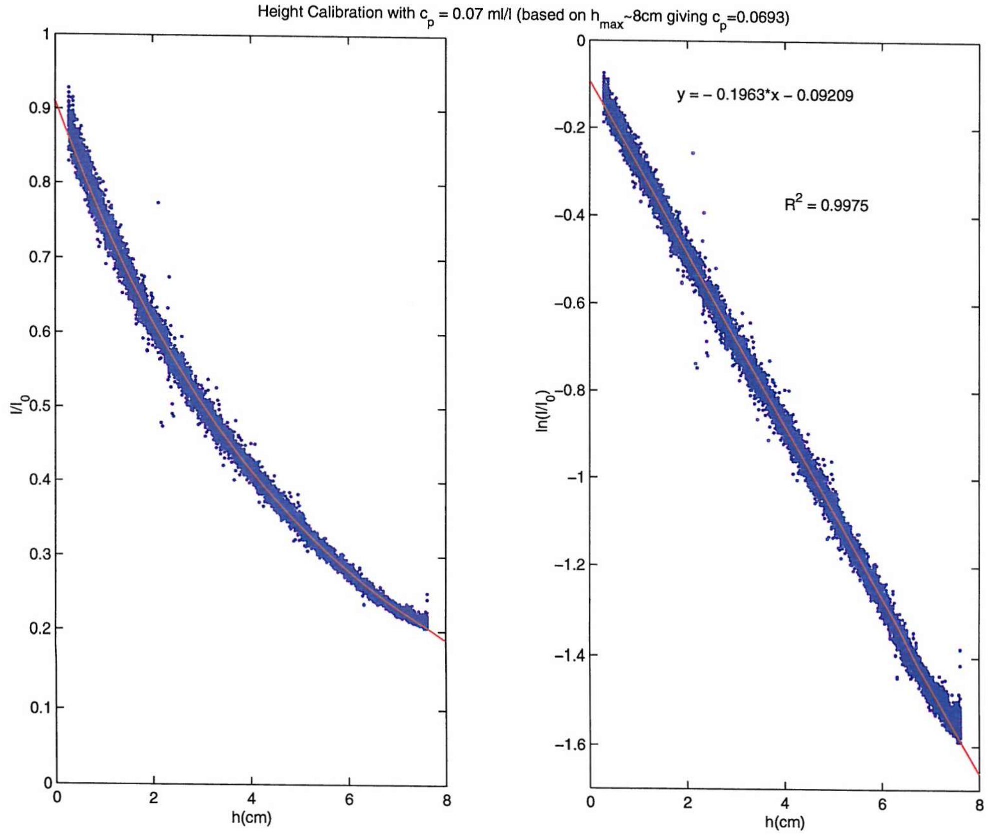

Figure 3.5: Direct calibration of h vs. $ln(\frac{I}{I_0})$ at constant dye concentration c_p, using a vertically slanting container with a uniformly dyed fluid (ρ of similar magnitude as in the experiments). This gives a horizontal variation in h by geometric considerations.

3.3 *Coriolis* platform

Two-layer rotating exchange flow experiments were carried out on the large rotating platform at CORIOLIS/LEGI in Grenoble, France, as part of a collaborative project. It is the first time such experiments were performed on such a large scale. The work in Grenoble was funded by the EU, Enhancing Access to Research Infrastructures action of the Improving Human Potential programme of FP5, under contract HPRI-1999-CT-0006.

The author of this thesis was part of a team carrying out the experiments in October and November, 2002. The other team members were David Smeed (SOC, Southampton), Gregory Lane-Serff (UMIST, Manchester) and Stuart Dalziel (DAMTP, Cambridge University). The work was planned in advance together with the staff at *Coriolis*, who gave support throughout the time in Grenoble as well as during the subsequent data-processing stage. The setup was prepared during the first week in Grenoble after which experiments were conducted for four weeks. Details about this setup and the measurements made are given in the following sections. An overview of the experimental results is published in Rabe *et al.* (2003).

3.3.1 Layout and setup

The $13m$ diameter turntable tank was modified to allow the study of two-layer exchange flows through a flat-bottom, horizontally contracting channel connecting two reservoirs of differing density. A picture of the setup and facility is given in figure 3.6 (p.55) and a plan-view sketch of the setup in figure 3.7 (p.56). A movable island was placed in the channel centre for some experiments. Experiments offset toward each sidewall were also performed but only density fluxes are presented in this thesis. The reader is referred to Smeed (2004) for further results. On this platform, velocity was inferred using plan view camera images of particles suspended in the water, illuminated by a laser (see image processing method in section 3.3.3, p.58). Therefore, all walls and the island were made of perspex sheets, reinforced with wood, to allow passing through of the laser light. The removable barrier, separating the reservoirs initially, was located just outside the field of view of the camera, between the narrows and the reservoir opposite the laser (see figure 3.7, p.56). This was done to shorten the initial adjustment, from Rossby adjustment at the barrier to flow presumably centred around the narrows, and thus reduced experiment running time.

The digital camera was fitted so as to obtain a view of a large part of the channel while retaining sufficient resolution to observe important features in the flow. The camera used was an SMD/DALSA 1M60 with a $14x14mm^2$ CCD chip providing 12bit digital output

Figure 3.6: Elevated view of the setup in the *Coriolis* rotating tank. The scanning laser head and mirror were fitted inside the grey box fixed to the tank rim with a steel bar. The observation bridge held the actual laser (connected to the laser head below) and computer acquisition equipment, connected to the camera located above the centre of the channel below. The channel was connecting the two large reservoirs and had a removeable island and barrier.

at a resolution of $1024x1024$ pixels. The camera was fitted with a $25mm$ Schneider lens and mounted $4.3m$ above the standard water surface ($0.60m$ above bottom) near the channel centre with a slight along-channel offset toward the laser due to light attenuation problems. The field of view was approximately $2.5x2.5m^2$ ($2.41m^2$ at surface; calibration at mid-depth and channel centre gave $2.55m^2$). The configuration program for the SMD was set to acquire frames at $30Hz$ with *Gain* = 4, *anti-bloom=off* and a *varying DC* = *off* to get optimal black level for each experiment. Near the barrier end, where the light had passed through the perspex more than once, absorption was found to be too great for particles to be picked up by the SMD. The laser was located outside the channel opposite the barrier end and set to illuminate a plan surface consecutively at different discrete depths. The rays enter the water through a submerged glass plate, which had to be regularly swept clear of bubbles before experiments. The light sheet covered a vertical scanning distance of approximately 6 to $54cm$ above the bottom. The horizontal scan of the laser was synced to the SMD camera and illuminated most of the SMD field of view at the laser's standard setting (*Amplitude* = 4.7; *offset* = 0), with slightly better coverage in RHS part of the channel, as this allowed better observation of the dense current leaving the channel near the wall. The laser was set to consecutively scan 9 discrete horizontal levels (3 in experiment 1, 5 in experiment 2), evenly spaced in the vertical. One whole set of levels (i.e. the whole channel volume) could be scanned in approximately $15s$. The levels were adjusted several times to correct horizontal slant and limits near the surface and bottom of the water (motor was blocked to avoid reflection off the mirror bottom or top). The sheet was $4mm$ thick in experiments 1 to 4 and adjusted to $10mm$ for experiments 5 to 8 and 14 to 15. The thicker sheet was found to

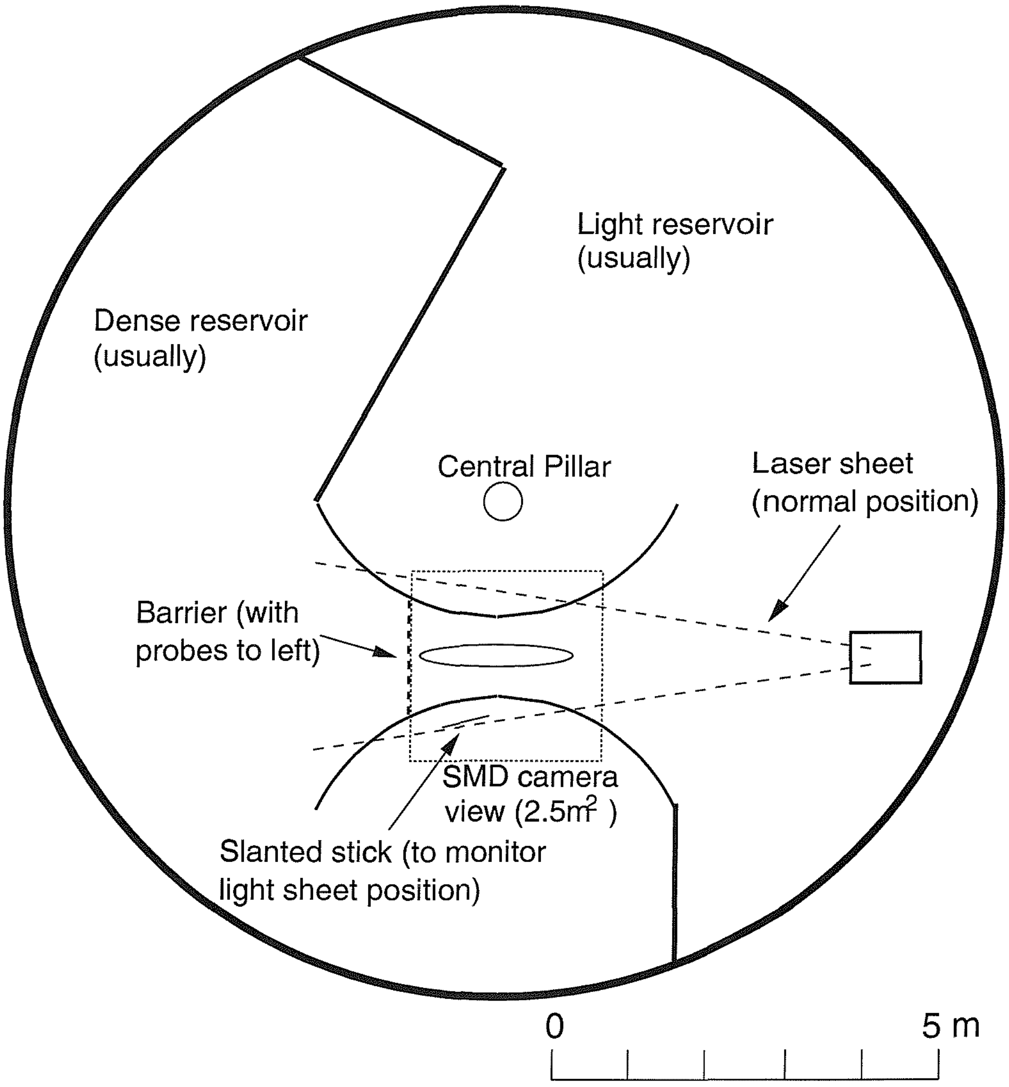

Figure 3.7: Plan view schematic of setup in the *Coriolis* rotating tank. The camera field of view is centred in an across-channel direction but offset slightly from the channel centre toward the laser. The barrier is located just to the left of this field. Note the field of view varied slightly with depth (see section 3.3.4, p.67) and some shading occured near the island and the walls on the channel half opposite to the laser.

reduce the effect of particles vertically moving in and out of the light sheet, which can lead to false velocity values in the image processing technique outlined in section 3.3.3 (p.58).

Measurements were undertaken at the barrier end of the channel using conductivity and temperature probes mounted on a profiling mechanism as well as a set of fixed probes; however, these turned out to be difficult to calibrate for the density difference used in our experiments, which is why they are not presented here.

A slanted stick was fixed just outside channel centre (to right of barrier) to allow laser sheet level monitoring in the field of view of the SMD camera. White tape on black background was attached to the barrier to function as a barrier raising monitor ($25cm$ spaced white marks along initial tape position). To avoid wind-induced motion, plastic sheets were added from experiment 6, covering approximately $\frac{1}{2}$ of reservoir surfaces and left there for subsequent experiments.

3.3.2 Water modification and density sampling

Two mixers driven by electric motors, each with a volume throughput of $20\frac{m^3}{hour}$, were mounted on the tank rim one in each reservoir to allow mixing up of the reservoirs to uniform density in between experiments. This could be achieved within two to three hours (volume of one reservoir is $\sim 40m^3$). Brine was added using a hose near the water surface (near the mixer in the non-laser reservoir, near the centre in the laser reservoir), connected to the central pillar water tank (total volume $0.4m^3$). Fresh water was added using either 'drains' at the bottom of the tank (connected to a separate storage tank) or a freshwater hose at the surface near mixer (in non-laser reservoir at tank wall side of channel). Our intended density difference was $10^{-3}gcm^3$, determined using similar considerations as given in section 3.2.2 (p.49) for the *SOC* platform and the feasibility of keeping constant temperature in the large tank. In practice, this value was changed by up to $\pm 20\%$ between experiments due to inaccuracy in volume measurement of the water input and leakage between the reservoirs during the mixing process. The latter was only relevant immediately after the freshwater addition / water removal when the surface height differences between the reservoirs equilibrated and did not occur during the running of the experiments.

$0.1 - 0.2mm$ diameter particles (pliolite DF01) were added to the water and the quantity (i.e. particle density in the water) was increased before experiment 3. The tank bottom was swept with a broom before the experiments, usually during spin-up to allow decay of motion before the experiment.

The water surface level was measured using a thin metal rod with measurement ruler, calibrated to the tank bottom (accuracy $1mm$) and usually located in the light reservoir (to allow surface adjustment with freshwater addition). The water was changed twice, before experiments 7 and 13. In addition, chlorine tablets were added when necessary to bleach out fluorescene, which was used in some experiments to visualise the flow but which also absorbs the laser light. It was also found that varnish on the wooden part of the channel clouded the water in the tank with time, which was eventually alleviated by over painting the wood with waterproof black paint.

Reservoir densities were measured using a hydrometer (range 1.02 to $1.03 gcm^{-3}$) read to an accuracy of approximately $0.5 * 10^{-4} gcm^{-3}$, better than the hydrometer available for the *SOC* platform. Pre- and post experiment water samples were taken from the mixed reservoirs in small (app. $30ml$) bottles to allow more accurate densities with a densitometer in DAMTP (Cambridge). However, the sample bottles, although convenient for transport back to the UK, turned out to the insufficient to preserve the original density of the water, due to partial evaporation of the relatively small sample volume.

3.3.3 Correlation Imaging Velocimetry

As mentioned in section 3.3.1 (p.54) the main measurements on the *Coriolis* platform were images of particles suspended in the water. These were used to obtain horizontal velocity using an image-processing technique called Correlation Imaging Velocity (CIV). During the experiments, the camera images were acquired using the software CIVIT v. 3, available from Fincham and Spedding at the *Coriolis* facility, which allowed fast consecutive images to be acquired at each discrete vertical level. The software allowed the user to specify both the timing of these images and the acquisition at each level synchronously with the movement of the laser light sheet. Subsequent to acquisition, these raw images as well as the configuration and log files were copied from the SMD camera acquisition computer to another partition on the *Coriolis* network where the images were converted to PNG format to allow further processing with the CIV software suite developed at *Coriolis*/LEGI and the "uvmat" utility by Joel Sommeria. These two software packages are a combination of binaries (now available for Windows and Linux), a controlling HTML/Pearl/cgi interface and a matlab program (uvmat). The packages were used in conjunction during the CIV process. Before such processing, the median (background) of sets of 20 images was removed to better visualise particle movement in regions of laser light reflection, bottom particle deposits and badly illuminated regions.

CIV is a particle imaging velocimetry (PIV) technique that utilises pattern correlation in consecutive images (Fincham and Spedding, 1997; Fincham and Delerce, 2000). Here the images are sets of horizontal fast-repetition images taken at the same depth to estimate veloc-

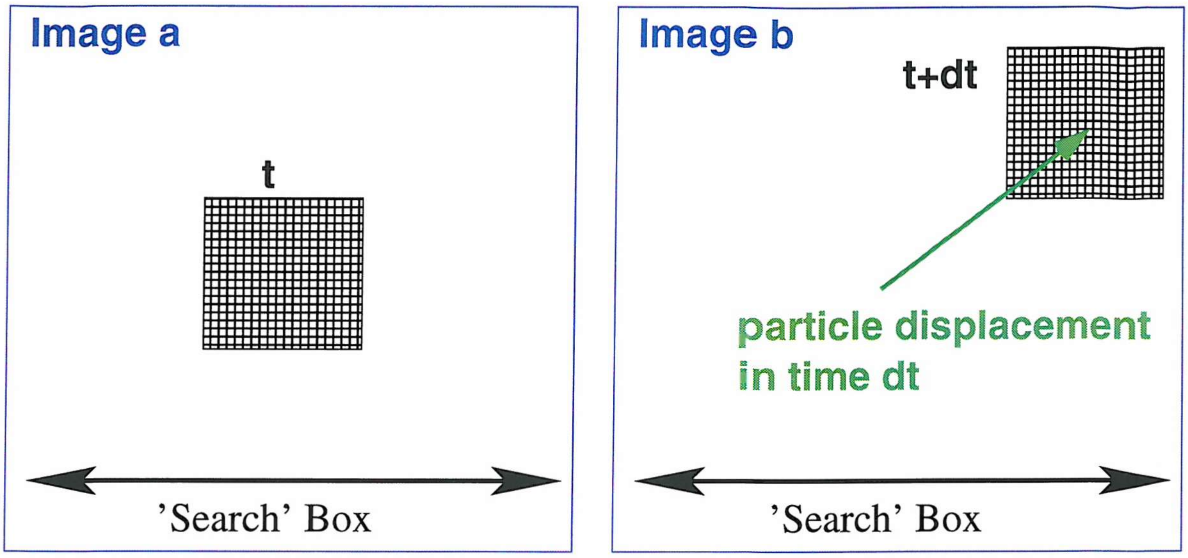

Figure 3.8: Schematic of CIV process after Fincham and Spedding (1997). The pattern box in image *a* is correlated to the same size box moved within a search distance (search box) in image *b*. The centre of each pattern box in the latter image gives a displacement relative to the centre point of the search box. The displacement with the highest correlation is the actual pixel displacement within the time *dt* between the images.

ity. CIV works by specifying pattern boxes of size (bx, by) centred on a predefined regular pixel grid in an image and correlating the pixel intensity pattern with that in a box of the same size in a consecutive image. The way to get local displacements is by allowing the pattern box in the second image to move within a certain search box of size (sx, sy), also centred on the grid (see figure 3.8, p.59) and calculate the correlation coefficient as a function of displacement. The displacement with the highest correlation is taken to be the actual displacement. This method, however, would in principle only yield displacements accurate to 1 pixel. To achieve sub-pixel resolution in the displacement estimates, it is not sufficient to simply take the correlation maximum of the pattern boxes in the two image pairs. Instead, the correlation curve is interpolated using a thin-plate smoothing spline approximation (Spedding and Rignot, 1993) of the correlation values. This gives a sub-pixel displacement associated with the correlation maximum of this splined curve.

The smoothing spline approximation, F, is a combination of a least squares fit to and a pure spline approximation of the x or y displacement data points, U, within an array box containing 400 pixels, equal to about 100 data grid points.

In the CIV software, the degree of smoothing is determined by a parameter φ , effectively weighting the spline part of equation 3.5. This means that $\varphi \to 0$ represents the limit where F is closest to the original values of U and $\varphi \to \infty$ represents the pure spline (maximum smoothing of U). For example U can be represented by the minimisation of the following functional:

$$l_{\varphi}(U) = \int\limits_{\Re^2} |\nabla^2 U|^2 + \frac{4\pi}{\varphi} \sum_{n}^{k=1} |U_k - F_k|^2, \tag{3.5}$$

where the first term represents the spline and the second is the sum of the squares of the residuals (k is the number of data points in U). $\Re^2$ denotes the set of numbers over which equation 3.5 is applicable, here real numbers in two dimensions. The weighting of the second term, i.e. how close F is to U, is represented by φ. For details of solutions to $l_{\varphi}(u)$ see Spedding and Rignot (1993). The spline is used for two different purposes during processing: interpolating the correlation curve and smoothing the vector fields themselves, where the corresponding smoothing parameters are termed φ_{CIV} and φ_{patch}. The different processing stages and methods are described below.

There is a further problem with spurious correlation peaks, which is remedied by comparing correlation fields at neighbouring grid points and eliminating those peaks from both fields. This method is termed "Hart" (Hart, 1998) and is illustrated in figure 3.9 (p.64). It is only used in the first CIV pass, as it actually increases the problem of peak-locking, explained later. However, it gives a valuable estimate for subsequent CIV passes at grid points that would otherwise have less accurate or absent velocity.

To allow more accurate processing, a 2nd CIV pass (CIV 2) is usually performed. This utilises the results from the first CIV pass (CIV 1) in the following way: the displacement field is scrutinised using various criteria, such as output from Hart and the CIV algorithm, specifying the reliability of each displacement estimate. This can include correlation maxima near the edge of the search box, low correlation coefficient, or simply an out-of-the-ordinary vector (caused by bad lighting, vertical particle movement between images etc.). The latter can be selected ("flagged") either by visually considering some prior knowledge of the flow dynamics or by some algorithm that determines the expected spatial variability in velocity and local deviations from it. Due to the large volume of data the former option is found to be impractical. Instead, the "Fix_Vel" option in the 'uvmat' utility is used, which not only selects vectors by CIV flags, such as the search-box being too small, but also uses the difference between the CIV vector field and a suitably smooth interpolation with a threshold value (typically $|CIVfield - Smoothinterpolation| > 1pixel$) to select false vectors. "Fix_Vel" using these two groups of criteria will be referred to as "FIX 1" and "FIX 2", respectively. "Fix_Vel" was rigorously applied despite the risk of flagging vectors as "bad" that may actually have been coherent. However, subsequent interpolation gave sufficiently similar displacement values in areas of low spatial variability. Where variability is high, strong shear is likely to be present which can in any case not be adequately resolved by the image resolution. The same applies to velocity calculation close to the walls.

The same spline routine (equation 3.5, p.60) as used for the correlation curves is then used to interpolate ("Patch") and fill in gaps (e.g. from "bad" flagged vectors) in the displacement field from CIV 1. To use the CIV to patch differences in FIX 2 above, this interpolation is applied twice. The smoothed displacement field is then used as an estimate to limit the search boxes for each pattern box in a 2nd CIV pass (CIV 2), a process named "Decimal Shift".

As mentioned above, the spline interpolator smooths the correlation curve to give a good estimate of the displacement at correlation maximum. In practice, however, there is still a mean-bias toward integer pixel displacements, termed "peak-locking". Such a mean-bias error is inherent to all PIV methods (Fincham and Spedding, 1997) and results in an error dependent on displacement in addition to a random error. It is even enhanced by the Hart method, which is why this is used only in CIV 1. Peak-locking is remedied by rigorously applying Patch and using the smoothed estimate in subsequent CIV passes. This effectively smooths out the peak-locking error, which is periodic in nature and depends on the magnitude of particular pixel displacements. The smoothing parameter in the spline interpolation, φ_{patch}, has to be carefully adjusted depending on the physical size of flow features, such as vorticity, in order to avoid eliminating significant flow features. The criterion for selection is based on the mean differences between the smooth ($\varphi_{patch} > 0$) and un-smoothed ($\varphi_{patch} = 0$) Patch fields; if the RMS of this difference is very low (e.g. < 0.05 pixels) , φ_{patch} needs to be increased. For practical purposes, a minimum difference of 0.1 pixels is chosen. The resulting smooth field then reduces peak-locking by giving a displacement limit for CIV 2 (Decimal Shift).

In principle, one could also adjust φ_{CIV} when interpolating the correlation curves during the actual CIV process. This would effectively randomise the phase of the (periodic) peak-locking error (Fincham and Spedding, 1997). In practice, however, there is no clear guideline available. Trials on our own data did not yield significant differences in velocity fields or peak-locking error estimates. Therefore this parameter was not altered. Note that this should not be confused with the φ_{patch} used in Patch.

The random (RMS) error component, on the other hand, is reduced by a deformation algorithm, that takes into account the local strain of the velocity field acting to deform the pattern box between different images (Fincham and Delerce, 2000). This is usually applied in a 3rd CIV pass (CIV 3) together with the aforementioned Decimal Shift, as CIV 2 provides a mostly peak-locking free estimate for CIV 3.

For time-averaged fields we have a method to estimate the peak-locking error. This utilises all vectors used to calculate this average field, giving a large set of samples to eliminate the random component of the error. This leaves only the mean-bias (peak-locking) error. An overall estimate of the peak-locking error can then be computed, as outlined in appendix A (p.186), by assuming the mean-bias to be periodic in pixel displacement space (Joel Sommeria, pers. comm.). In general this error is $\sim 0.1 pixels$ or less, which gives a velocity error around $0.1 cms^{-1}$. The peak-locking error may not be important when analysing the pure velocity fields or integrated quantities, such as fluxes. However, difference quantities, such as vorticity and divergence, are very sensitive to peak-locking errors, and it is thus desirable to reduce the error to a minimum instead of sacrificing spatial resolution (which would increase the differences). This is important in particular for the flows under study in this thesis, as the two-layer nature of the exchange leads to regions with low velocity variability in either horizontal direction (as opposed to more vortical flows, where large gradients in velocity make the peak-locking error less significant). Therefore calculations involving velocity differences have largely been avoided.

The actual CIV processing procedure used is illustrated in figure 3.10 (p.65) and listed as follows:

- Pre-processing: The median (background) is removed from sets of images (20 images) in each experiment. This reduces problems with reflection of the laser light and badly illuminated areas.
- CIV 1: Correlate pattern box in image a, centred on search box, with pattern box in image b, maximised to a location within search box. Run Hart as part of CIV 1 to eliminate spurious correlation – flag 'bad' vectors (black)
- Fix 1: Flag some general vector field vectors as 'bad' (criteria from CIV 1 process)
- Patch: Interpolate grid points onto regular grid using thin shell spline including smoothing (φ optimised for physical measurement domain!), resulting in interp1 (just interpolated) and filter1 (smoothed) fields – this 'fills' the gaps left by 'magenta' flagged vectors
- Fix 2: Flag using the difference between the smooth (Patch) and un-smooth (CIV 1) fields as a threshold
- Patch : Same as above.
- CIV 2: Perform second CIV pass using previous guess ('Decimal shift'), possibly with different image pairs in CIV 1 and CIV 2 (may get better slow velocity, but also bad

vectors) – this should reduce peak-locking. Choose $\varphi_{CIV} = 1$ as no clear guideline for adjusting this is available.

- Fix 1: Flag some general vector field vectors as 'bad' (criteria from CIV 2 process)
- Patch : Same as above, but this time interpolate / smooth the CIV 2 field, using the same φ_{patch} as before.
- Fix 2: Flag using the difference between the smooth (Patch) and un-smooth (CIV 2) fields as a threshold.
- Patch : Same as previous patch.
- CIV 3: Reiterate the CIV 2 process, this time using decimal shift (using high resolution CIV 2 fields as previous pass) and accounting for 'Deformation' of the pattern box; the deformation algorithm reduces the 'rms' (random) error.
- Fix 1: Flag some general vector field vectors as 'bad' (criteria from CIV 3 process)
- Patch: Interpolate onto regular grid for further use (e.g. fluxes, vorticity..). φ_{patch} same as before.

This procedure leads to plan velocity fields at different depths (depending on the laser levels scanned) and different times (relative to the opening of the barrier, i.e. when it just leaves the water). Note that any velocity fields that belong to the same volume scanned by the laser, i.e. from images taken consecutively at different depths, are assumed to be at the time the mid-depth level images were acquired, which will subsequently be referred to as the 'instantaneous' time. The actual time of acquisition is a maximum of $\pm 7.5s$ (the whole volume is scanned in $15s$) different from this, which is not expected to be significant in analysing the exchange flow except during the initial adjustment and in the very fast-rotating cases.

Overall, velocity fields yield less error when images are pre-processed with background removal and the CIV process described above rigorously applied. Note that the time-series in experiment 3, as presented in chapter 4 (p.80), has only been processed to CIV 2 without background removal, as the full process is very time-consuming. All time-averaged fields and the time-series in other experiments are processed fully as described above. Advantages of hierarchical processing scheme and background removal can be seen in an example in figure 3.11 (p.66). At the time of processing parallax correction was not included in the CIV software which is why it is applied afterwards as described in the next section.

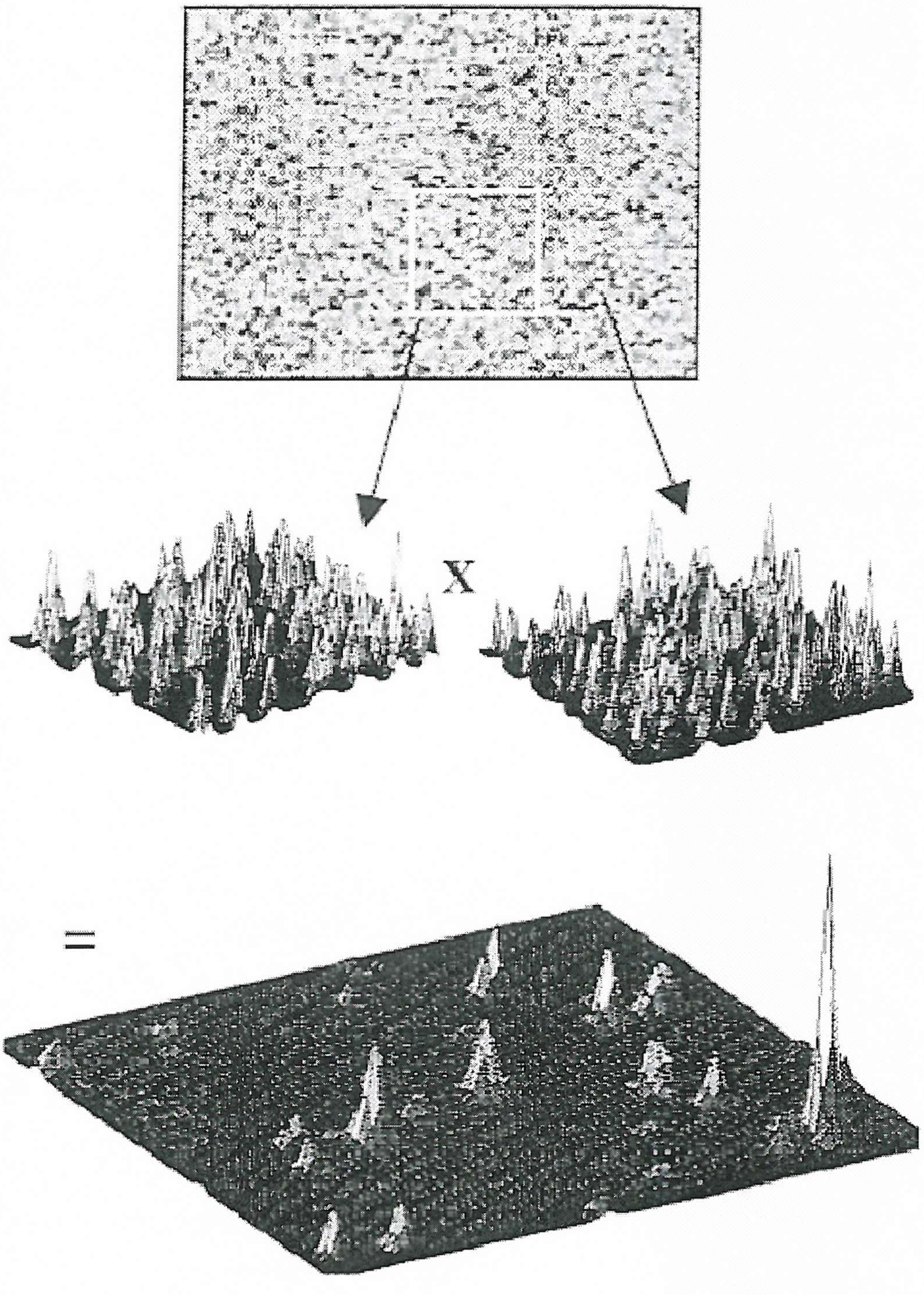

Figure 3.9: Schematic of Hart process after Hart (1998). Correlation fields at neighbouring grid points are multiplied to eliminate spurious correlation peaks within the search box.

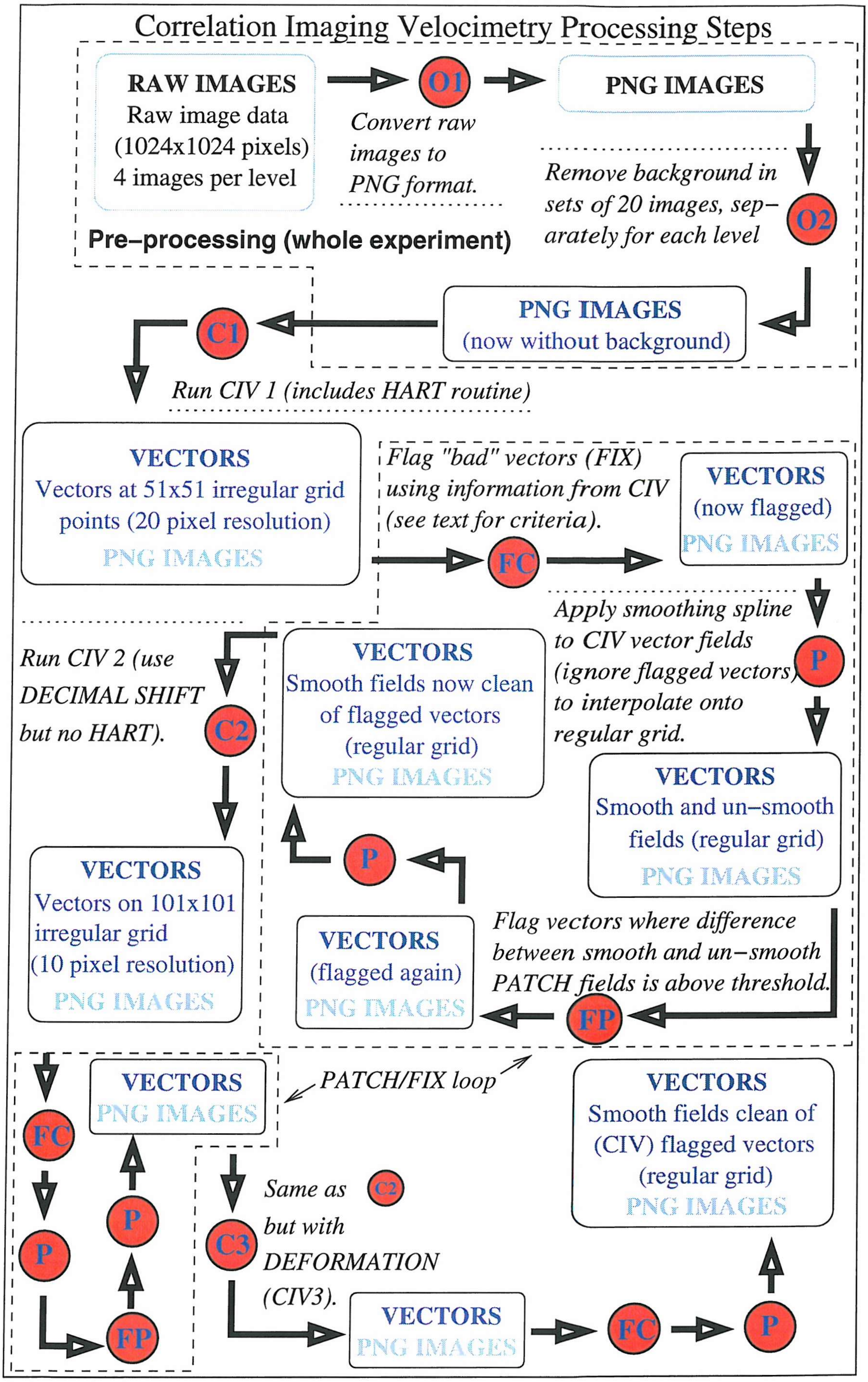

Figure 3.10: CIV processing procedure using the steps described in this section.

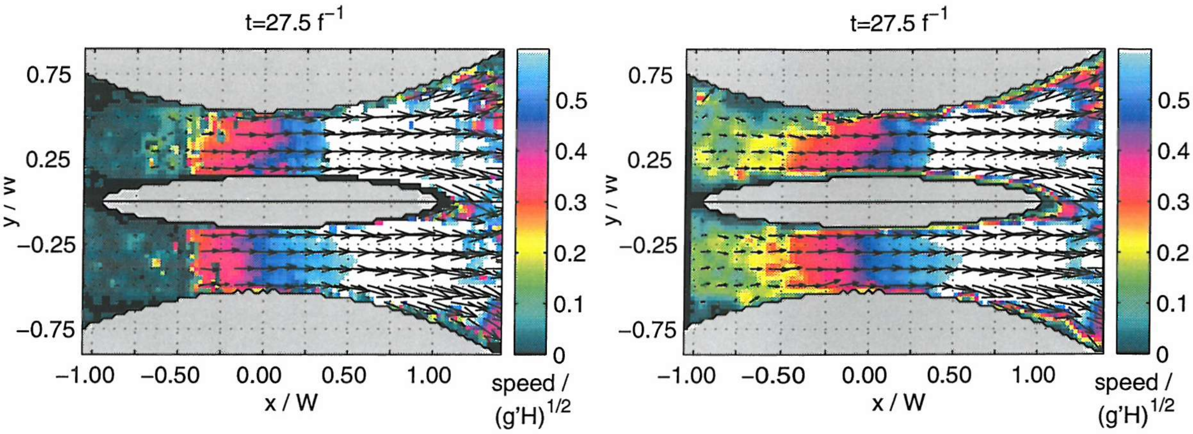

Figure 3.11: Comparison of instantaneous velocity fields on the near-bottom level (9) in experiment 6 on the *Coriolis* platform. The data is from background-removed images and processing to the CIV3/patch stage (on right) and unprocessed images with CIV to stage 2 / patch (on left). Note that the main difference in the velocity fields can be seen near the dense reservoir ($x < 0$). Here the laser light has been absorbed both horizontally (from laser to particles) and vertically (from particles to camera) by the particle-laden water, so that the images yield no useful signal for the particles.

3.3.4 Parallax correction

When calculating velocities and comparing vector fields at different laser levels, we need to account for parallax. One way to achieve this is to calibrate the camera view at each laser level using an object of known length. However, this would have been very time consuming, as the laser levels varied slightly between experiments. Furthermore, such calibration would not improve the error greatly, as the internal density interface does refract the laser sheet to a limited extent, $\lesssim 2cm$ with maximum around mid-depth and no refraction at near-surface or near-bottom levels. Instead, the camera was calibrated once at mid-depth, coincident with the laser sheet there. We can then approximate the parallax effect by considering the distance of the camera from the water surface and the depth of each laser level, incorporating the effect of the refraction at the air-water interface (figure 3.12, p.68). From Snell's Law we know

$$n_2 sin(\alpha) = n_1 sin(\beta), \tag{3.6}$$

where the index of refraction for air is $n_1 \approx 1$ and for fresh water is $n_2 = 1.33$; the effect of salinity is ignored, which was not constant between experiments, but only changes this index to a maximum of 1.34 at $20°C$ (Apel, 1987, p. 528). Using the small angle approximation $sin(\alpha) \approx \alpha$ and similarly for β we can write

$$\frac{\alpha}{\beta} = \frac{n_1}{n_2} \tag{3.7}$$

Assuming a flat, horizontal surface it can be shown by geometric arguments (Tipler, 1991, p. 1022 pp.) that the real (z_r) and apparent (z_v) depths of an object below the surface (as viewed from above) are related by

$$\frac{n_2}{z_r} = \frac{n_1}{z_v} = \frac{1}{z_v} \Rightarrow z_v = \frac{z_r}{n_2}. \tag{3.8}$$

Thus the normal parallax effect (the field of view of the camera increases linearly with distance from the lens) can be corrected for the refraction at the water surface (figure 3.12) to give the width of the camera field of view, $L(z)$, at depth z:

$$L(z) = \frac{l}{m}(D + \frac{z}{n_1}), \tag{3.9}$$

where m is the focal length of the camera lens and l the square CCD chip length. This gives a factor for the apparent length $L(z)$ of any object relative to L_0:

$$N_z(z) = \frac{L(z)}{L_0(H - H_{calib})} \tag{3.10}$$

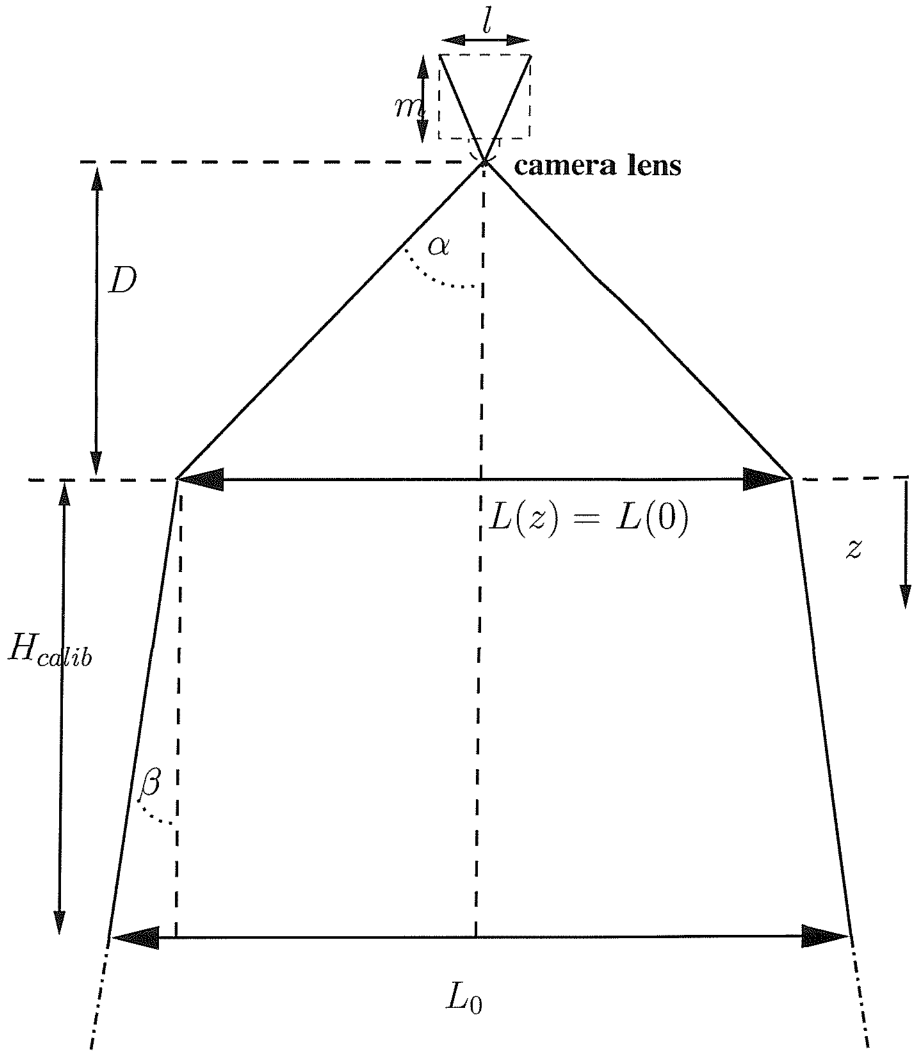

Figure 3.12: Schematic of parallax in the *Coriolis* setup. $L(0)$ is the length of the object as perceived by the camera if raised to the water surface ($z = 0$), i.e. if the whole field of view is considered, the camera actually sees less horizontal distance near the surface than near the bottom. Through simple geometry and some approximation, a factor is applied to the horizontal grid at each laser level to correct for this.

Note that we do not actually need either l or m for this relation. As the water surface (H) changes slightly between experiments, it is actually more accurate to use D and n_1, rather than the calibration length of L_0:

$$N_z(z) = \frac{D + \frac{z}{n_1}}{D + \frac{H - H_{calib}}{n_1}}. \tag{3.11}$$

We can then multiply the grid at each level by $\frac{1}{N_z(z)}$, which is 1 at mid-depth, < 1 above this and > 1 below. The same factor applies to velocity.

As the CIV software did not include such correction at the time of processing, this correction has been applied after iterative CIV processing to the final velocity fields as well as the grid point positions. The data was interpolated onto a regular grid after this correction. It was found that this correction significantly improved the estimates of along-channel flux at the narrows by reducing the spurious net flux.

3.3.5 Interface depth

To have a measure of the interface between the two exchanging layers from velocity alone, we need to rely on the vertical profiles of velocity. The shear maximum should in principal give the interface position; however, as shear may be large in other parts of the water column, especially if one layer is very thin, we look instead for the near-zero isotach (speed ~ 0 within a threshold of $0.1cms^{-1}$).

The complete algorithm is summarised in figure 3.13 (p.70). The initial 3-d velocity field is interpolated vertically at each horizontal grid-point. The height of the zero-velocity isotach ("shear" interface) is then determined from the interpolated profiles. The resultant horizontal interface depth (h_{raw}) field is filtered using a $7x7$ moving window with a median filter resulting in the filtered field, h_{filt}. The RMS of the difference between the filtered and unfiltered points in each window is also calculated. If this RMS is above a factor 4, the centre-point of the window is marked as an outlier. Such outliers are then repeatedly set to their original value in h_{raw} and the median filter again applied. After three iterations of this process all final outliers are marked as bad. However, a record of their location is kept to distinguish them from other bad data due to missing velocity values.

As we have a discrete number of laser sheets throughout the depth of the channel, an interpolation of the velocity has been performed for each individual vertical profile at each horizontal grid point. Figure 3.14 shows an example of a typical profile together with smoother profiles using different interpolants. The piecewise cubic hermite polynomial interpolant (matlab implementation; for algorithm see Fritsch and Carlson, 1980; Kahaner *et al.*, 1988)

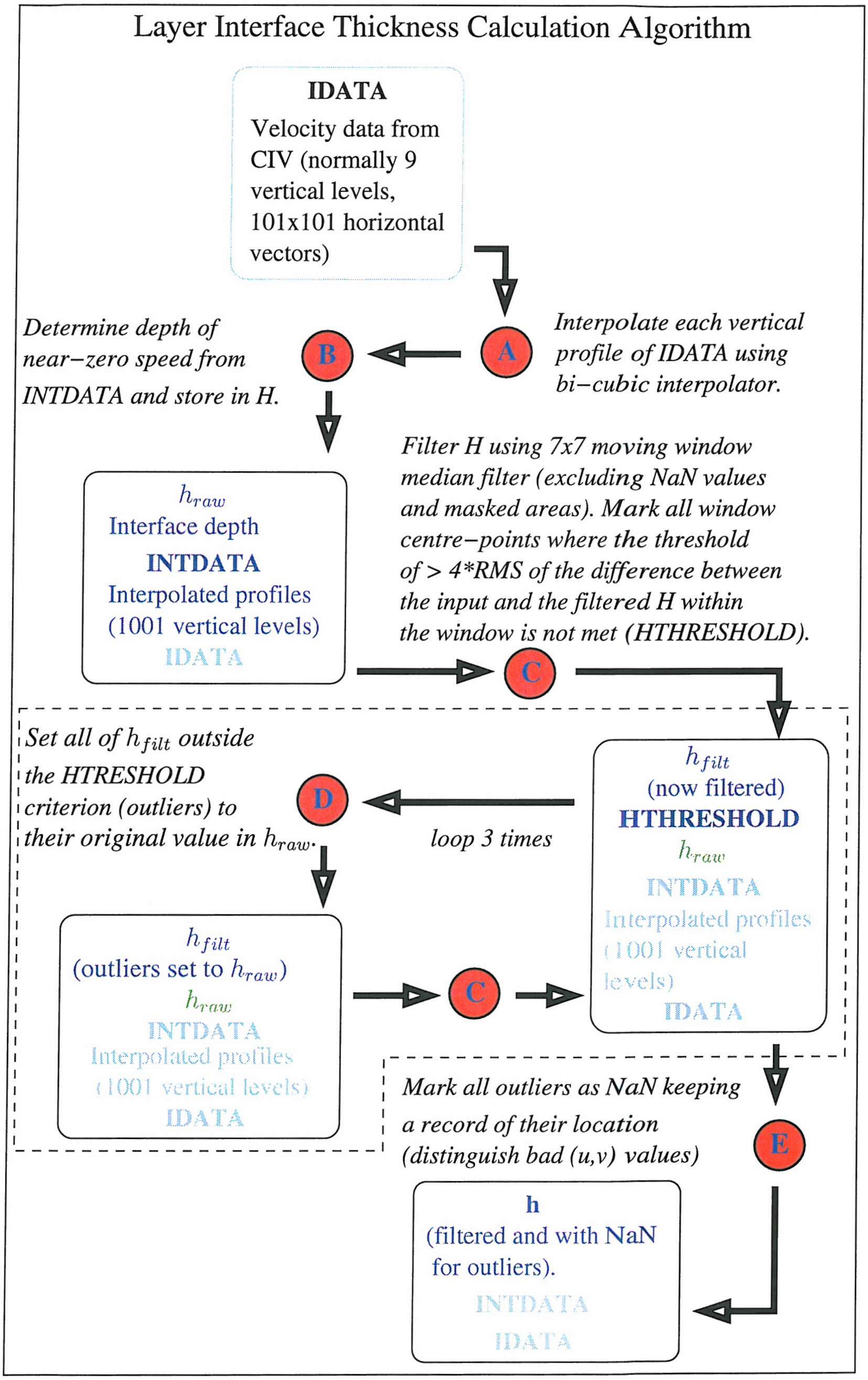

Figure 3.13: Outline of algorithm for layer (zero-velocity / "shear") interface calculation. Note the processes inside the dashed line are applied three times.

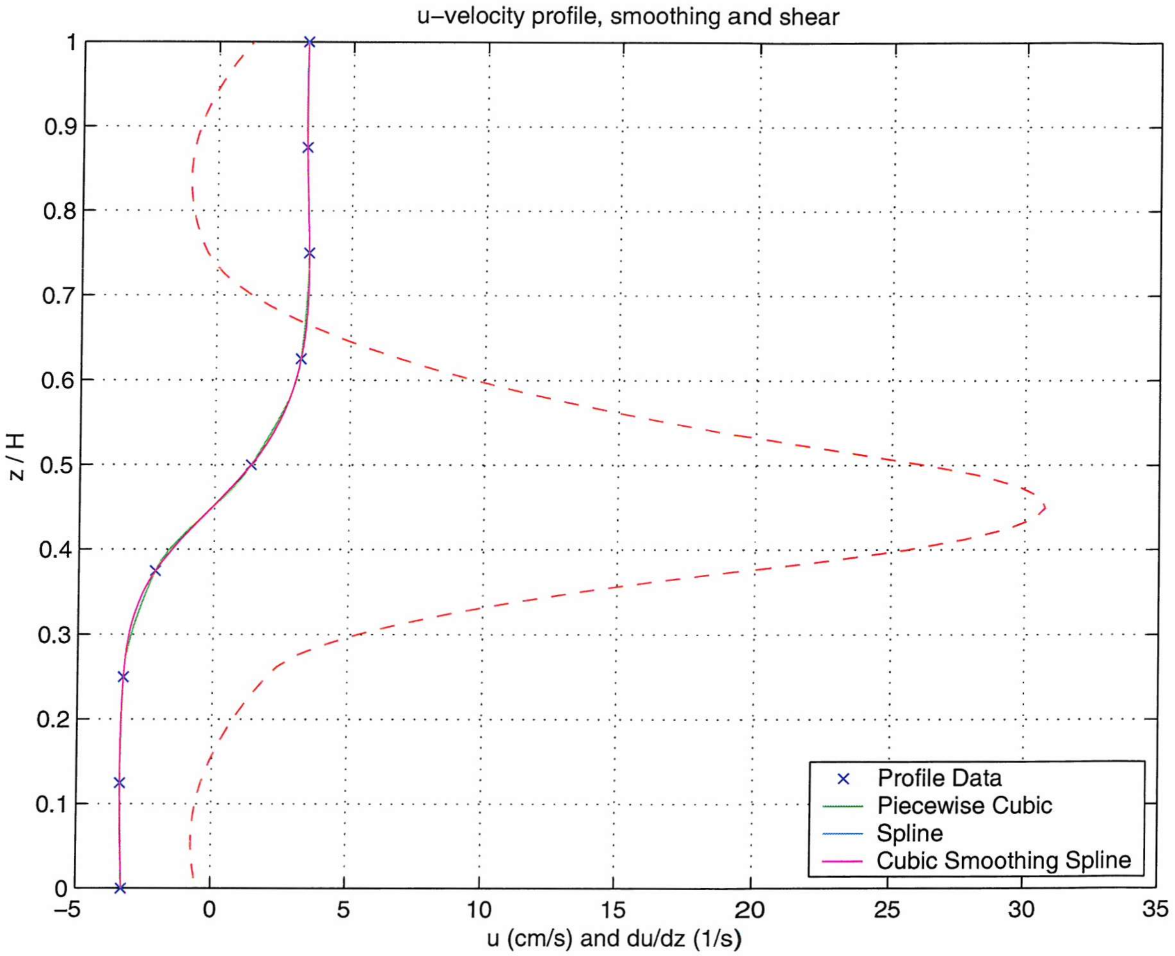

Figure 3.14: Example of different interpolation schemes to determine the depth of the zero isotach (interface). The solid lines represent the different interpolants used on the u-velocity profile and the dashed line the local shear from the cubic spline profile.

was found to give the best representation of a two-layer profile while keeping edge effects near the surface and channel bottom to a minimum. Note the cubic spline profile in figure 3.14, which similar to the interpolant mentioned above, but requires the second derivative in the interpolated data profiles (e.g. $\frac{d^2u}{dz^2}$) to be always continuous. Due to this condition, the spline actually gives a smoother representation around mid-depth and thus possibly a better indication of the interface position. However, edge effects were found to distort profiles near the surface and bottom boundaries, making depth-mean velocity within each layer difficult to determine. This method was found to break down in cases of higher rotation, $R_0 < 1$ (or $T < 150$), with barotropic vortices that showed no clear baroclinic interface and in cases of less vertical laser levels, where this approach is difficult to apply. Thus interface depth and layer properties are only presented for experiments 4, 6, 7, 14 and 15.

3.4 Viscosity and boundary layers

In non-rotating flows viscous effects are commonly described by the Reynolds number (Re), describing the ratio of inertial to viscous effects (see also p. 22 Tritton, 1988):

$$Re = \frac{UL}{\nu}, \tag{3.12}$$

where ν is the molecular kinematic viscosity, U the scale for the along-channel flow velocity and L the flow's length scale.

In the non-rotating island cases, the island naturally sets the scale $L = 2m$. Further considering $U \sim \sqrt{g'H}$ (reduced gravity wave speed)and ν (the total viscosity equal to the kinematic viscosity $\nu \sim 10^{-2} cm^2 s^{-1}$) gives $Re \sim 10^5$ for the *Coriolis* platform. This suggests that the majority of the flow is only little affected by viscosity and at the same time the flow should be still laminar; see p.31 Tritton (1988) for a discussion on flow states and Reynolds numbers.

In a rotating fluid, such viscosity is additionally constrained by f, giving rise to Ekman boundary layers at the surface, bottom and the density interface and Stewartson shear layers at the horizontal boundaries. The appropriate parameter in the rotating case is the Ekman number (Ek):

$$Ek = \frac{\nu}{\Omega H^2} = \frac{2\nu}{fH^2} \tag{3.13}$$

This together with the fluid depth is the scale for the vertical (Ekman) boundary layer (e.g. p. 228 Tritton, 1988):

$$\delta_{Ek} = Ek^{\frac{1}{2}} H. \tag{3.14}$$

Note that δ_{Ek} is therefore only dependent on rotation and viscosity, not the depth or the density of the water. At the sloping interface the Ekman layer may be slightly thicker than at the channel floor due to drag exerted by the different layer velocities.

For the experiments on the *SOC* platform $1 \leq \delta_{Ek} \leq 2mm$ and for *Coriolis* $2 \leq \delta_{Ek} \leq 11mm$, assuming laminar flow, showing that generally $\delta_{Ek} << H$ (i.e. $< 2\%$ in all experiments on both platforms). This can also be seen in figure 3.15 (p.74), where $\frac{\delta_{Ek}}{H} = E^{\frac{1}{2}}$, the non-dimensional vertical boundary layer thickness, is given. In other words, where a layer of approximately unidirectional velocity, assumed to be similar to a layer of constant density, is $\sim 0.5H$ thick, total flux in such layers will not be affected much by slower velocities

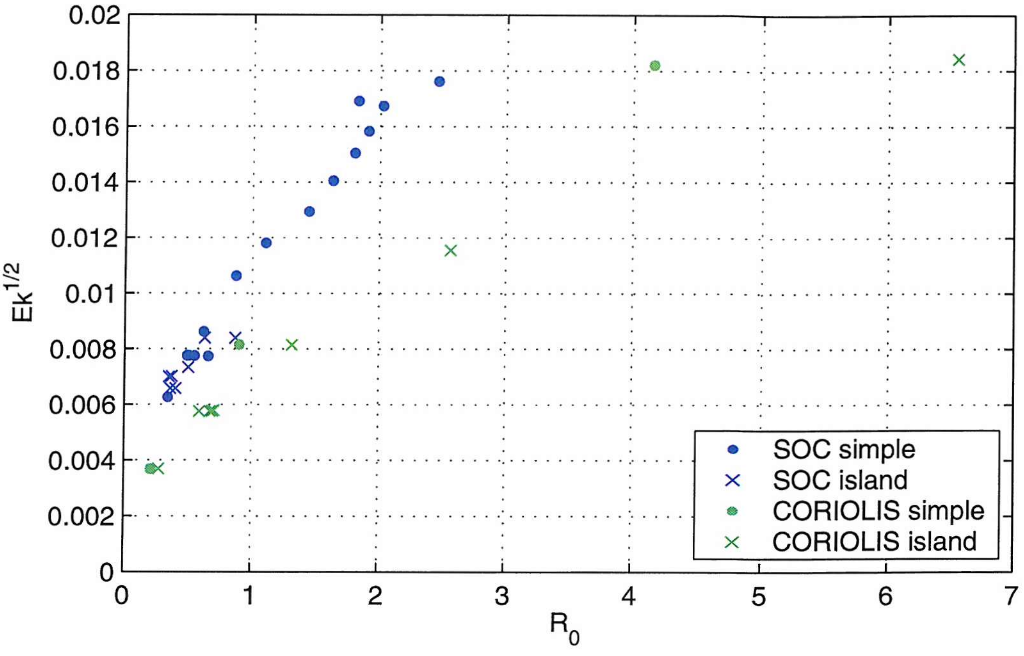

(a) Ekman layer thickness ($\frac{\delta_{Ek}}{H} = Ek^{\frac{1}{2}}$)

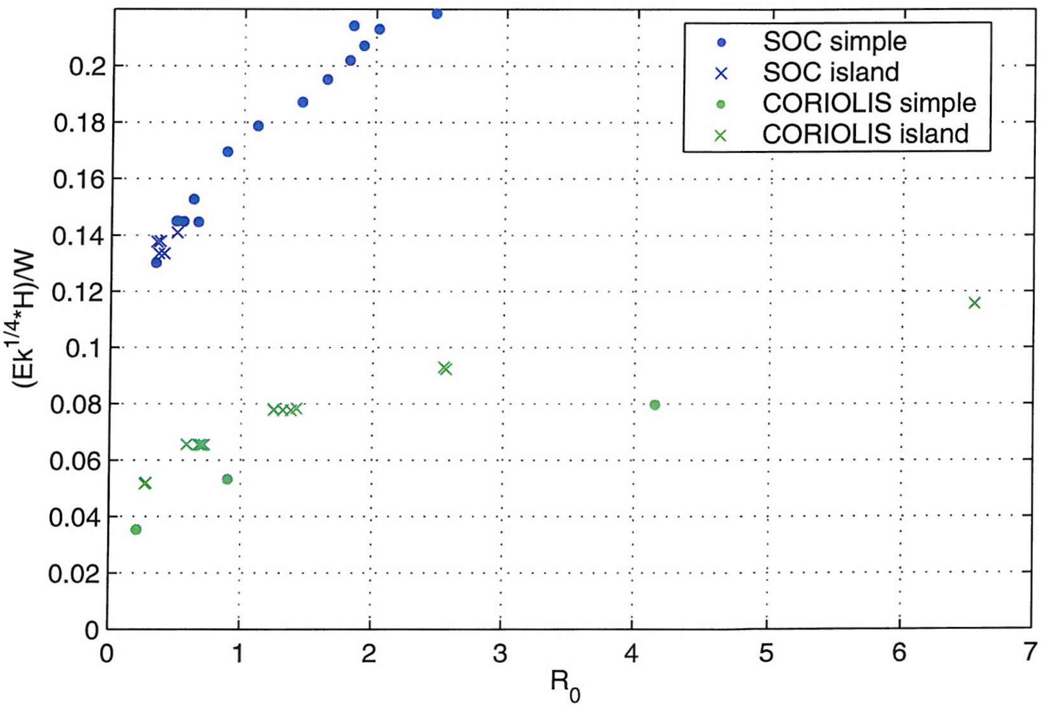

(b) Stewartson layer thickness ($\frac{\delta_S}{W} = Ek^{\frac{1}{4}}\frac{H}{W}$)

Figure 3.15: Non-dimensional viscous boundary layer thickness vs. R_0 for both platforms. Note that the Ekman layer is an order of magnitude smaller than the Stewartson one. *Coriolis* values are generally lower than *SOC* ones. Note the Stewartson layer here is the one responsible for the non-slip sidewall condition on along-channel flow and the cross-channel flux, i.e. the $Ek^{\frac{1}{4}}$ layer.

inside the Ekman layer at the adjacent boundary. This issue will be revisited in the context of velocity extrapolation near the surface and bottom boundaries in section 6.2.1 (p.144).

Along the sidewalls and the island, Stewartson layers carry the flow between the interior and the Ekman layers. They have sometimes been found to be of significant thickness relative to the channel width, W. The boundary layer responsible for the non-slip sidewall condition on along-channel flow and the cross-channel flux has width

$$\delta_S = Ek^{\frac{1}{4}}H \tag{3.15}$$

(pp 30 and 97 Greenspan, 1968, D88), leading to $1.1 \leq \delta_S \leq 1.9cm$ (i.e. 13 to 32% of W_i) for the *SOC* platform and $3.5 \leq \delta_S \leq 8cm$ (i.e. 3.5 to 11.5% of W_i) for *Coriolis*, which is an order of magnitude higher than δ_{Ek}. This can also be found in figure 3.15 (p.74), where the non-dimensional quantity is now $\frac{\delta_S}{W} = Ek^{\frac{1}{4}}\frac{H}{W}$. A thinner boundary layer (replace $\frac{1}{4}$ exponent by $\frac{1}{3}$) also exists at the sidewalls to match the vertical velocity boundary condition. These boundary layers cause the interface to flatten near both sidewalls, especially at low f, and are associated with significant horizontal shear. This needs to be borne in mind when investigating interface height and velocity distributions since it decreases the channel cross-section available to the exchange flow. Note however that the effective reduction is less than the δ_S as the velocity inside the boundary layers is not zero. As the CIV data showed some problems with resolving velocity close to the boundaries, no detailed analysis of the shear boundary layers will be attempted. However, the magnitudes of δ_S and δ_{Ek} will be referred to when appropriate.

3.5 Measurement errors

Measurement errors, as mentioned in previous sections, are summarised in this section for both the *Coriolis* (table 3.3, p.77) and the *SOC* platform (table 3.2, p.76). The main differences between both platforms are in the accuracy of T, which is better on the *Coriolis* platform due to very precise turntable control, and $\Delta\rho$, which is better on the *SOC* platform due to use of water samples and salinometer. However, for $\Delta\rho$ on the *Coriolis* platform, a better measurement device would not likely have improved the estimate as temperature variations inside the reservoirs were too great to allow higher accuracy. It should also be noted that the error in the non-dimensional flux, $\bar{q}$, on the *Coriolis* platform is greatly increased by the dependence on $\Delta\rho$ (g') due to the non-dimensionalisation, i.e. division by $\sqrt{g'}H^{\frac{3}{2}}W$.

Quantity	Device / Primary quantity	Accuracy (absolute)	Nominal Value (min / max)	Accuracy (%)
t	video timer	$1s$	$60s$	1.7%
$T\ (f)$	analog optical turntable drive	$0.052s\ (0.024s^{-1})$	$5.23s\ (2.4s^{-1})$	1%
V_{res}	ruler; bucket	$(0.4cm)^3$	$(17cm)^3$	2.4%
$(x, y), W\ (H)$	ruler	$10^{-3}\ (10^{-3})\ m$	$0.061\ (0.145)\ m$	0.7% (1.6%)
$Temp$	digital thermometer	0.1^oC	15^oC	0.7%
Sal	salinometer	$0.01PSU$	$35PSU$	0.3%
$\rho_h\ (\Delta rho_h)$	hydrometer	$5{\cdot}10^{-4}gcm^{-4}$	$1\ (3{\cdot}10^{-3})\ gcm^{-3}$	0.05% (17%)
$\rho_s\ (\Delta rho_s)$	$Temp$,Sal	$6{\cdot}10^{-5}gcm^{-3}$	$1\ (3{\cdot}10^{-3})\ gcm^{-3}$	$6{\cdot}10^{-3}$% (2%)
g'_s (g'_h)	g,$\Delta\rho_s\ (\Delta\rho_h)$ g,$\Delta\rho_s\ (\Delta\rho_h)$	$5.9 \cdot 10^{-4}ms^{-2}$ $(4.9 \cdot 10^{-3}ms^{-2})$	$3 \cdot 10^{-2}ms^{-2}$	2% (16%)
R	H,f, $g'_s\ (g'_h)$	$0.15\ (0.57)\ cm$	$3\ cm$	5% (19%)
R_0	H,f,W, $g'_s\ (g'_h)$	0.017 (0.65)	0.34	5% (19%)
$\bar{q}$	H,V_{res},t,g'_S,$\Delta\rho_s$ (g'_h,$\Delta\rho_h$)	0.0035 (0.011)	0.05	7% (22%)
dye weight	scales	$0.01g$	$2.1g\ (2.1ml)$	0.48%
c_p	dye weight, V_res	$0.002mll^{-1}$	$0.07mll^{-1}$	2.9%
h,z	h calibration	$1cm$	$14.5cm$	7%
$\frac{dz}{W}$	h,W	0.07	0.1	70%

Table 3.2: Errors and associated quantities or measurement devices for the *SOC* experiments. The percent-age accuracy is also given. In some cases of derived quantities, this carries forward, so that the absolute error given is just this percent-age of the nominal value; in cases where the absolute error is constant over all ranges of nominal values the percent-age error is in cyan and vice versa. In case of primary (directly measured) quantities the nominal value is the smallest or biggest one occurring, so that the percent-age error is greatest. Note that the error in $\bar{q}$ is a pure measurement-derived error and does not include effects of unsteady flow during the experiments due to initial or reservoir adjustment.

Quantity	Device / Primary quantity	Accuracy (absolute)	Nominal Value (min / max)	Accuracy (%)
Temp	Mercury thermometer	0.1^oC	20^oC	0.5%
$t\ (\Delta t)$	stopwatch	$1s$	$1700s$	0.06%
T (f)	turntable drive	$0.01s\ (1260s^{-1})$	$30s\ (0.419s^{-1})$	0.03%
$(x, y), W\ (H)$	ruler (metal rod)	$10^{-3}\ (10^{-3})\ m$	$0.695\ (0.6)\ m$	0.14% (0.17%)
$\rho\ (\Delta rho)$	hydrometer	$10^{-4}gcm^{-3}$	$1\ (10^{-3})\ gcm^{-3}$	0.01% (10%)
g'	$\Delta\rho$,g	$9.81 \cdot 10^{-4}ms^{-2}$	$9.81 \cdot 10^{-3}ms^{-2}$	10%
$R\ (R_0)$	g',H,f (W)	0.02 (0.02)	0.22 (0.21)	10% (10%)
(u, v)	CIV / Camera	$0.1pix\ (0.12cms^{-1})$	$5cms^{-1}$	2.5%
$\bar{q}$	g',H,W,t, u $(\Delta\rho)$	0.005	0.20	12.5% (10%)
h,z	laser refraction	$0.02m$	$0.6m$	3%
$\frac{dz}{W}$	h,W	0.02	0.06	33%

Table 3.3: Errors and associated quantities or measurement devices for the *Coriolis* experiments. Percentage accuracy etc. given in the same way as in table 3.2 (p.76). Note the percent-age error carries forward from $\Delta\rho$ to g', R, R_0 and $\bar{q}$. The dimensional version of the latter has a similar error as u but is not used in the analysis, as any theoretical prediction will include g'. The flux based on $\Delta\rho$ will be considerably less accurate in practice, as the flow is unsteady throughout some of the experiment running time and the reservoir volumes were not calculated to great accuracy.

Experiment	W (cm)	"f" (s^{-1})	"g'" (ms^{-2})	Running Time (s)	R (cm)	R_0	Volume Flux (dm^3s^{-1})
709	8.8	2.4	3.7	228	3.02	0.34	0.04
703++	8.8	1.6	3.3	171	4.35	0.49	0.05
701	8.8	1.6	3.4	171	4.46	0.51	0.05
711*	8.8	1.6	5.9	101	5.8	0.6	NaN
702	8.8	1.6	4.1	171	4.84	0.55	0.17
708	8.8	1.3	3.4	124	5.49	0.62	0.07
707	8.8	0.84	2.9	81	7.7	0.87	0.11
706	8.8	0.68	3	64	9.72	1.1	0.02
705	8.8	0.57	3.6	61	12.7	1.4	0.49
710	8.8	0.48	3.3	65	14.4	1.6	0.13
715	8.8	0.42	3.1	60	15.9	1.8	0.21
713	8.8	0.33	2	60	16.1	1.8	0.12
712	8.8	0.38	2.8	61	16.8	1.9	0.15
704	8.8	0.34	2.5	51	17.8	2	0.14
714	8.8	0.31	3	60	21.7	2.5	0.11
801	6.1	1.9	2.5	122	3.09	0.51	0.17
802++	6.1	1.9	2.8	122	3.2	0.54	0.05
805++	6.1	2.2	4.1	151	3.29	0.58	0.49
804*++	6.1	2.2	3.4	151	3.56	0.5	0.14
803++	6.1	1.8	4.2	125	4.43	0.72	0.05
806*++	6.1	1.4	3.9	155	5.56	0.9	NaN
807*	6.1	1.4	7.4	150	7.67	1.2	NaN

Table 3.4: List of *SOC* experiments with parameters and flux measurements from reservoir density and running time. Note that experiments 711, 804, 805 and 806 have only hydrometer measurements with an error of $5 * 10^{-4} gcm^{-3}$, i.e. one order of magnitude higher than density error from salt samples.

*Inaccurate, as only hydrometer densities: 711, 804, 805, 806
++reservoir ρ reversed

3.6 Experiments and parameter variations

The experiments on the *SOC* platform were carried out by the author between April and September, 2002 and are listed in table 3.4 (p.78). An overview of these is also published in Rabe and Smeed (2002). The experiments on the *Coriolis* platform were carried out during five weeks in October and November, 2002, as part of a collaborative project and are listed in table 3.6 (p.79). The preliminary results from these experiments are published in Rabe *et al.* (2003).

Note that in cases where the reservoir densities are reversed, (x, y) are inverted (transposed to $(-x, -y)$). This is the case in experiments 802 to 806, 15 and 703 and also means in the latter two that the barrier is effectively at the other end of the channel, so that initial conditions are different with respect to the x-coordinate. Running time for each experiment was chosen to allow the flow to adjust to a quasi-steady state but also to minimise the effect of adjusting reservoir conditions. These time scales are presented later in the context of time averaging in section 4.1 (p.80).

Expt.	T (s)	H (cm)	W (m)	drho (*10^-4 g cm^-3)	drhof (*10^-4 g cm^-3)	g' (m s^-2)	Flux (dm^3 s^-1)	Flux Volume (m^3)	Running Time (s)	R (m)	R_0	Island
1	150.00	60.0	1.02	10.0	6.0	0.0098	4.6	8.0	1720	0.92	0.90	N
2	150.00	60.0	0.72	10.0	5.0	0.0098	5.8	10.0	1720	0.92	1.28	C
3	75.00	60.0	0.72	11.0	8.0	0.0108	2.7	5.4	2040	0.48	0.67	C
4	300.00	59.8	0.72	9.5	2.0	0.0093	8.0	15.7	1970	1.78	2.49	C
5	30.00	59.2	0.72	11.0	9.8	0.0108	1.2	2.3	1823	0.19	0.27	C
6	750.00	59.3	0.72	10.0	2.0	0.0098	5.5	15.9	2883	4.55	6.37	C
7	750.00	60.0	1.02	8.5	0.0	0.0083	7.2	19.9	2780	4.22	4.16	N
8	30.00	59.4	1.02	14.0	8.0	0.0137	1.6	8.5	5460	0.22	0.21	N
14	Inf	60.0	0.72	6.0	NaN	0.0059	NaN	NaN	NaN	Inf	Inf	C
15	150.00	60.0	0.72	-9.0	-4.5	-0.0088	5.0	10.0	1972	0.87	1.22	C*

Reservoir volumes: 39.8 m^3 *reservoir densities reversed

Table 3.5: List of *Coriolis* experiments with parameters and flux measurements from reservoir density and running time.

Chapter 4

Transient phenomena in experiments and steadiness

The primary objective of this thesis is to look at the quasi-steady state, as this allows comparison to previous studies. However, selecting this state from the data in each experiment requires a look at the transient behaviour. For this purpose, the time scales expected in a two-layer lock-exchange flow are identified and compared to visual observations during the experiments. The following sections then identify the time variability and quasi-steady periods in the data in the light of these time scales. This is followed by a brief description of the establishment of the exchange flow by the initial transients. Time series of the velocity fields in the the fast rotating cases ($R_0 < 1$) are then shown, since in those cases either a steady state does not exist at all or multiple quasi-steady states can be identified. Throughout this chapter and the remainder of this thesis, non-dimensional units will be used as summarised in section 3.2.1 (p.45).

4.1 Time scales and criteria for steady flow

4.1.1 Start-up of experiment

To decide on the time interval of an approximately steady state in the exchange flows under study, we have to consider the timescales involved, as previously mentioned in section 3. Such timescales involve the setup of the exchange flow by the initial transients and the adjustment near the end of the experiment. (see also Helfrich, 1995, for a study of time-variability in non-rotating exchange flows).

Initially, the barrier lifting, or 'dam break', leads to gravity currents intruding into the other density fluid as part of a Rossby-type adjustment. These currents will initially behave like the non-rotating equivalent but will slump toward the right with respect to the along-channel flow direction within approximately f^{-1}, the time it takes the flow to fully feel the effect of rotation. The time for the gravity current passing $\frac{1}{2}$ of the channel is given by

$$T_L = \frac{L}{2 * (g'H)^{\frac{1}{2}}}, \tag{4.1}$$

where L is the channel length.

The front formed during the initial adjustment eventually moves along the channel to the narrows, which will not only depend on the speed of the gravity current but also the actual flux, filling part of the channel with dense fluid (light fluid in some cases on the small platform, where the channel was initially filled with dense fluid and the barrier removed at the light reservoir exit). This is represented by the time to fill $\frac{1}{2}$ channel with dense (light in reverse reservoir density experiments) fluid:

$$T_{SF} \approx \frac{WLH}{q_{whitehead}}, \tag{4.2}$$

where W is the channel width, H the full channel depth and $q_{whitehead}$ the theoretical flux as defined in equations 2.2 (p.30) and 2.3 (p.30).

A stage of approximately steady exchange would thus be expected when the mid-interface has centred around the narrows or, in other words, the flow is approximately symmetric around each diagonal (axis at 45 ^{o} to the along and across channel axes) at mid-depth.

Another scale to be considered is the spin-up time for a homogeneous fluid, given by

$$T_s = Ek^{-\frac{1}{2}} f^{-1}, \tag{4.3}$$

where

$$Ek = \frac{\nu}{\Omega H^2} = \frac{2\nu}{fH^2} \tag{4.4}$$

is the Ekman number. This will be significant in the formation of Ekman and Stewartson shear boundary layers (see also 3.4, p.73).

In practise we found that T_S for the slowly rotating experiments was significantly larger than the experiment running time, limited by the finite reservoir volumes. Thus, we are not always able to study the flow with fully developed boundary layers. In addition to this, the velocity near the boundaries is not always well resolved by CIV on the *Coriolis* platform. The same applies to the interface depth in the *SOC* experiments, here due to the sidewalls or island obscuring the background lighting. Note that the actual spin-up may take longer due to the two-layer fluid; however, efforts were made to run the experiments for longer than T_s, which was possible in the $R_0 < 1$ cases.

However, if we assume such boundary layers to be small relative to the channel width and approximately stable, we only need to look at the averaged velocity field to determine their influence on the exchange flux and the R_0 scaling.

Bearing this in mind, one approach to represent the quasi-steady state would be to average the velocity or interface height fields between the end of the initial adjustment and the return of the initial gravity currents into the channel, altering the exchange flow near the narrows. These events can be observed in the time series in section 4.2 (p.85) and overall variability in section 4.3 (p.96) and can be combined with our preliminary information about inherent timescales.

Some of these timescales are visually observed during the experiments on the *Coriolis* platform. These are given together with the theoretical values in table 4.1 (p.83); note experiments not otherwise presented in this thesis are also shown. It can be seen that T_{SF} is of similar magnitude as T_L at high R_0; however, for low R_0 (< 1) this adjustment process can take considerable time as the gravity current is followed by propagating fronts. The velocity fields need to be therefore checked to see not only at what time the gravity current reaches the end of the channel or the field of view but also when the adjustment / channel crossing region reaches the narrows. However, as the 3-dimensional nature of a rotating gravity current leads to a non-uniform velocity and density channel cross-section, our best criterion for determining a quasi-steady state in the exchange are the conditions at the narrows.

4.1.2 End of experiment

Near the end of the experiment, gravity currents may return after having circumvented the reservoirs. Theoretically, this is given by

$$T_r = \pi \frac{X}{(g'H)^{\frac{1}{2}}}, \tag{4.5}$$

where X is the tank radius. These currents should be to some extent delayed by hydraulic jumps forming near the channel exits. However, if they are of significantly large amplitude, they may propagate into the channel in the form of internal bores. This is important as it can change the state of the exchange, so it is no longer steady, and can, in addition, cause significant mixing that renders the inviscid two-layer approximation less valid. Another way to think of this adjustment is the finite volume of the reservoirs being filled by the steady

		Gravity Current Time					T_S	T_{res}		T_{SF}		Qwhitehead	
	T	Observed Return		Derived				(Whitehead)		(Whitehead)		Theoretical Fluxes	
Expt.	(s)	Dense	Light	(T_r+T_L)	T_r	T_L		$R_0>1$	$R_0<1$	$R_0>1$	$R_0<1$	$R_0>1$	$R_0<1$
1	150.00	NaN	NaN	28	22	5	123	484	475	31	30	0.15	0.15
2	150.00	NaN	NaN	30	22	8	123	516	475	23	21	0.20	0.22
3	75.00	NaN	NaN	58	43	15	174	*2635*	1727	*115*	75	*0.08*	0.12
4	300.00	NaN	NaN	15	11	4	87	226	*125*	10	*5*	0.24	*0.43*
5	30.00	NaN	NaN	145	107	38	271	*-585*	10937	*-26*	484	*-0.86*	0.05
6	750.00	NaN	NaN	6	4	2	54	85	*19*	4	*1*	0.25	*1.09*
7	750.00	24.13	NaN	6	5	1	55	63	*22*	4	*1*	0.25	*0.69*
8	30.00	NaN	1457.7	118	95	23	272	*-190*	8564	*-12*	551	*-1.60*	0.04
9	150.00	90.48	90.48	29	21	8	122	483	433	21	19	0.21	0.23
10	30.00	653.45	NaN	141	104	37	275	*-613*	10322	*-27*	450	*-0.79*	0.05
11	75.00	110.58	NaN	55	41	14	174	*2107*	1580	*92*	69	*0.09*	0.12
12	75.00	NaN	NaN	67	50	18	174	*22360*	2370	*974*	103	*0.01*	0.10
13	75.00	NaN	NaN	59	44	15	174	*3031*	1809	*132*	79	*0.07*	0.11
14	Inf	NaN	NaN	NaN	NaN	NaN	NaN	1530	NaN	67	Inf	0.25	NaN
15	150.00	120.64	140.74	32	24	8	123	559	528	24	23	0.20	0.21
16	150.00	75.4	130.69	32	23	8	123	558	527	24	23	0.20	0.21
17	300.00	62.83	NaN	16	12	4	88	228	*127*	10	*6*	0.24	*0.42*
18	150.00	98.02	85.45	28	21	7	124	463	408	20	18	0.21	0.24
19	75.00	341.81	NaN	56	42	15	173	*2351*	1654	*103*	72	*0.08*	0.12

Table 4.1: Comparison of observed and theoretical timescales for experiments. The observed return of the gravity current would theoretically be the same as $T_r + T_L$. Note that all times are in units of f^{-1}, except T (s) and those for experiment 14 $(\frac{2*\sqrt{g'H}}{L})$. Those numbers in *italics* are outside the valid range of the formula. Note times for experiments 9 to 13 and 16 to 19 are only shown for comparison to the experiments with similar R_0 otherwise presented in this thesis (i.e. experiments 1 to 8, 14 and 15).

exchange flux and thus altering the reservoir interface conditions. The according time scale can be approximated by assuming Whitehead *et al.* (1974)'s maximal flux:

Reservoir draining time:

$$T_{res} = \frac{V_{basin}}{q_{whitehead}}, \tag{4.6}$$

where V_{basin} is the reservoir volume (approximated to $\frac{1}{2}$ the total tank volume) and $q_{whitehead}$ the exchange flux as given in equations 2.2 (p.30) and 2.3 (p.30). The internal bores are just the means to propagate this change in the reservoir interfaces (i.e. not near either the surface or the bottom) to the channel interior in a two-layer exchange.

Table 4.1 (p.83) shows the theoretical and observed gravity current propagation times. Note that experiments not otherwise presented in this thesis (9 to13 and 16 to 19) are also shown for comparison (e.g. similar R_0), as gravity current observations are not available for all experiments. The times of the gravity currents propagating around the basins and returning to the channel are much slower than would be expected from a full-depth rotating gravity current (given by $T_r + T_L$); this was also observed in the experiments on the small platform (times not shown). This is generally expected as they are much shallower than the total depth H and some mixing with the reservoir fluids may occur reducing their density. T_{res} is generally much larger than running time apart from experiments 6 and 7. Any significant change in reservoir conditions will be visible in the flux time series in section 4.2.1 (p.85).

One needs to bear in mind, however, that both timescales assume immiscible fluids. If there were sufficient mixing inside each reservoir the source water for the corresponding layer in the exchange flow could change its density, giving rise to a smaller $\Delta\rho$ and thus a reduction in R and R_0. This process would not require an internal bore to propagate through the strait. However, both of these scenarios are really equivalent with respect to fluxes, as the effect on R due to a change in H (difference in interface depth in either reservoir) is the same as due to a change in $\Delta\rho$. Thus both cases would reduce the exchange fluxes, assuming $\bar{q} \propto R$. However, the cross-channel interface slope would steepen in the case of uniform mixing, as this would reduce R_0. It would shallow in the case of a change in reservoir layer depths transmitted via a gravity current or an internal bore. We will assume the latter case to be predominant, as the flow is not likely to be significantly turbulent to fully mix the fluid in each reservoir with an intruding gravity current. Indeed such gravity currents were observed to visibly circumvent each reservoir along the boundaries. Change in fluxes and interface depth at the narrows will be considered in the next two sections to identify the quasi-steady state in each experiment, bearing in mind the initial timescales presented in the previous section.

We need to be aware of the main difference in measuring time-variability using the h time series from the *SOC* experiments and the flux time series used with the *Coriolis* platform: we cannot easily see the drop-off in the $h(t)$ record near the end of the high R_0 experiments, for example in figure 4.1, p.86. This is due to the running time being kept low as reflections of internal bores from the rectangular tank wall are likely and reservoir conditions are expected to change earlier due to limited volume of the *SOC* tank. Thus we have to identify the first quasi-steady period and assume this will be representative of the steady two-layer exchange flow. Such periods are marked in the $h(t)$ figures. They may be before any peaks near the end of the experiments as those may represent internal bores passing through the channel. However, they must be after the initial adjustment, which can be seen by a noticeable decrease in the slope of $h(t)$.

4.2 Time series of properties at the narrows

4.2.1 CIV fluxes (*Coriolis* platform)

To have a first look at the general variability of the flow, it is useful to consider the time-dependent exchange fluxes ($\bar{q}$) through a section across the channel at the narrows. Note that the range of t in each experiment differs due to the non-dimensionalisation which in most cases does not allow several experiments to be shown in the same figure. $t = 0$ starts when the barrier just leaves the water, so that some dense flow is able to propagate toward the narrows beforehand. Only a selection of experiments is shown here and the remainder in appendix B (p.189).

The time scales in 4.1 (p.80) suggest that an average over most of the experiment, after the initial adjustment but before the return of any internal bores, is likely to give the best estimate of the quasi-steady two-layer exchange flow. The remainder of this section will show that this is indeed the case for $R_0 \gtrsim 1$ with and without an island, but not necessarily for lower values.

Experiment 7 ($R_0 = 4.16$, simple channel) is chosen as an example for flux time variability as it shows both the initial adjustment, a quasi-steady period and signatures of returning bores and changing reservoir conditions. The remaining experiments with $R_0 \gtrsim 1$ showed a similar pattern of exchange fluxes in time and the main differences will be described briefly. Note that time in all the rotating experiments is non-dimensionalised by f^{-1}. Figure 4.1 (p.86) shows that the initial increase in fluxes occurs within $t \sim f^{-1}$ followed by a small peak, likely caused by the unsteady flow associated with the gravity current and the initial adjustment. This is followed by a period of almost constant fluxes between $5f^{-1} \lesssim t <\lesssim 15f^{-1}$. The following increase in variability coincides with visual observations of a gravity

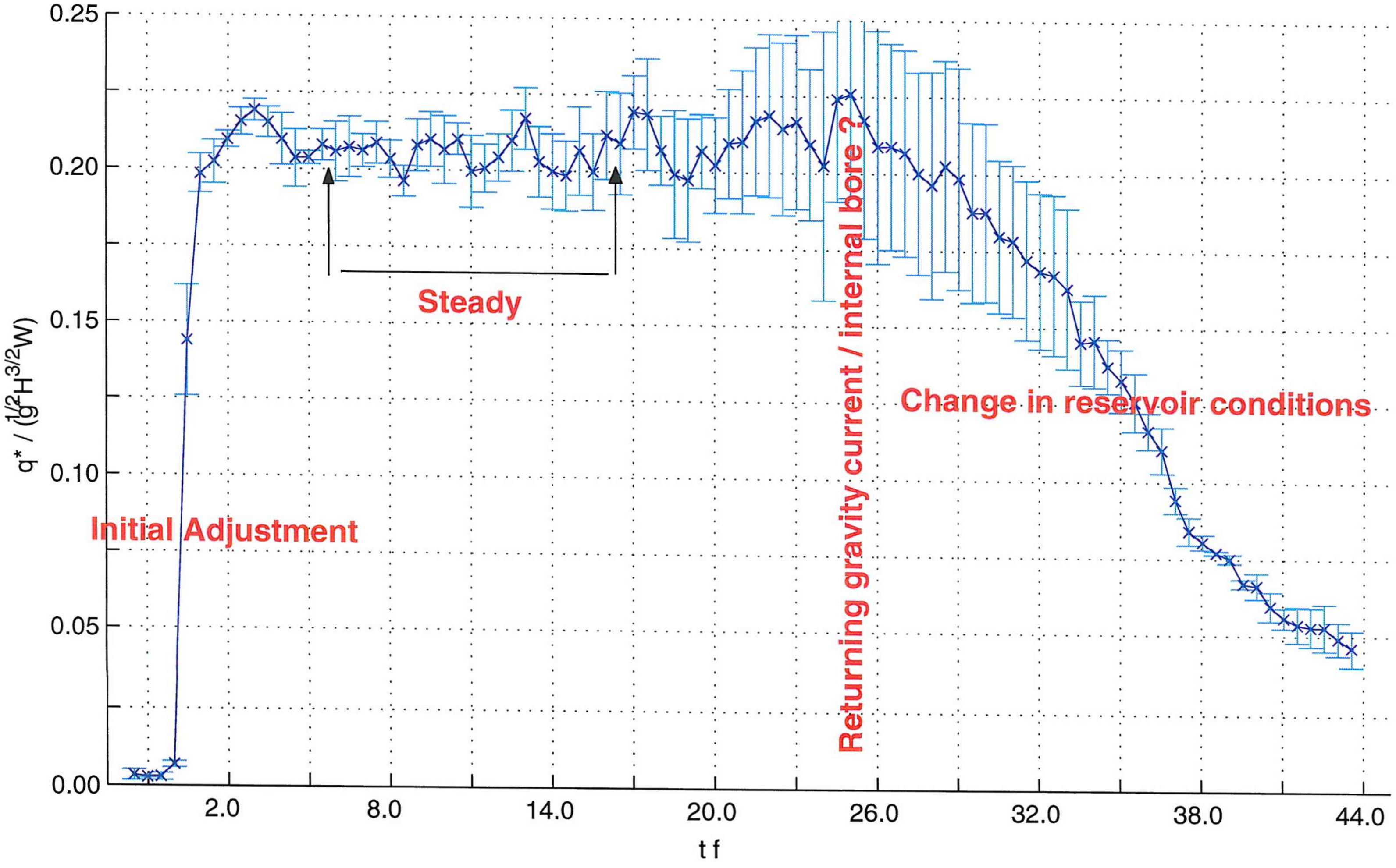

Figure 4.1: Time series of flux ($\bar{q}$) for experiment 7 (simple channel, $R_0 = 6, 37$). Error bars and flux non-dimensionalisation as in figure B.1 (p.190). Time is non-dimensionalised by f^{-1}. Note the initial adjustment within $t \sim f^{-1}$. A period of almost constant $\bar{q}$ then persists before the peak around $t = 24.5f^{-1}$ and the following gradual decrease due to changing reservoir conditions. The increased error from the middle of the experiment toward the end is caused by bad and missing data in the surface laser level.

current returning from the dense reservoir, probably communicating the change in reservoir conditions to the exchange flow in the channel in the form of an internal bore. This is marked by a flux peak around $t = 24.5f^{-1}$ and a following decrease in exchange fluxes, indicating that the channel exchange is no longer isolated from one or both reservoirs. Also shown are arrows, denoting the beginning and end of the quasi-steady period, over which time-averages were calculated. The latter are the basis for the quasi-steady analysis in the next chapter.

Experiment 6 ($R_0 = 6.37$, island) showed a similar flux peak but a slower and less continuous flux decrease near the end, suggesting that the island influences the interaction of internal bores with the flow inside the channel. This was also evident in a faster rotating island case, experiment 4 (island, $R_0 = 2.49$). Here, less variability and smaller error was seen which was a trend generally observed as R_0 approached unity (see figure 4.2, p.88 for experiments 4 and 2, the latter with $R_0 = 1.28$).

The final adjustment in experiments with $R_0 \sim 1$ (experiments 2, 15 and 1) could not be observed within the experiment running time due to lower fluxes. This generally lead to longer periods of quasi-steady exchange, although the period near the end of the experiment was often chosen as this was the most steady. In addition, the spin-up time, T_S, was close to the end of these experiments or earlier. This also applies to experiments with lower R_0. Therefore any time-averages should include fully developed boundary layers, as described in section 3.4 (p.73). This was not possible for experiments 4, 7 and 6, which must be kept in mind when comparing exchange fluxes to the inviscid theoretical prediction in section 6 (p.133). However, this does not significantly influence the qualitative observations of the exchange and differing flow regimes treated in the next chapter.

A further decrease in R_0 still leads to quasi-steady flow. However, here it occurs in the form of several different regimes during the course of the experiments. Experiment 3 (island, $R_0 = 0.67$) shows two periods, around $t = 60f^{-1}$ and near the end, of distinctly steady fluxes of similar magnitude (see figure 4.3, p.89). These can be identified to belong to a similar flow regime, where both layers are 'split' between either side of the island, so that baroclinic exchange (vertically layered currents) no longer occurs at the narrows. Another period at $t \sim 130f^{-1}$ shows a slightly decreasing trend in fluxes, but does show two exchanging layers in both island side-channels, which is why this is termed the 'dual' regime. The latter is similar to the baroclinic exchange found for the island cases with higher R_0. Velocity fields for these regimes can be found in chapter 5 (p.105).

$R_0 << 1$ leads to long period oscillations of similar amplitude to the mean magnitude of fluxes during the experiment. Figure 4.4 (p.90) shows this variability for both the simple channel ($R_0 = 0.21$, experiment 8) and the island ($R_0 = 0.27$, experiment 5) cases. Both show that the initial adjustment is slower than for higher R_0 and occurs in several stages.

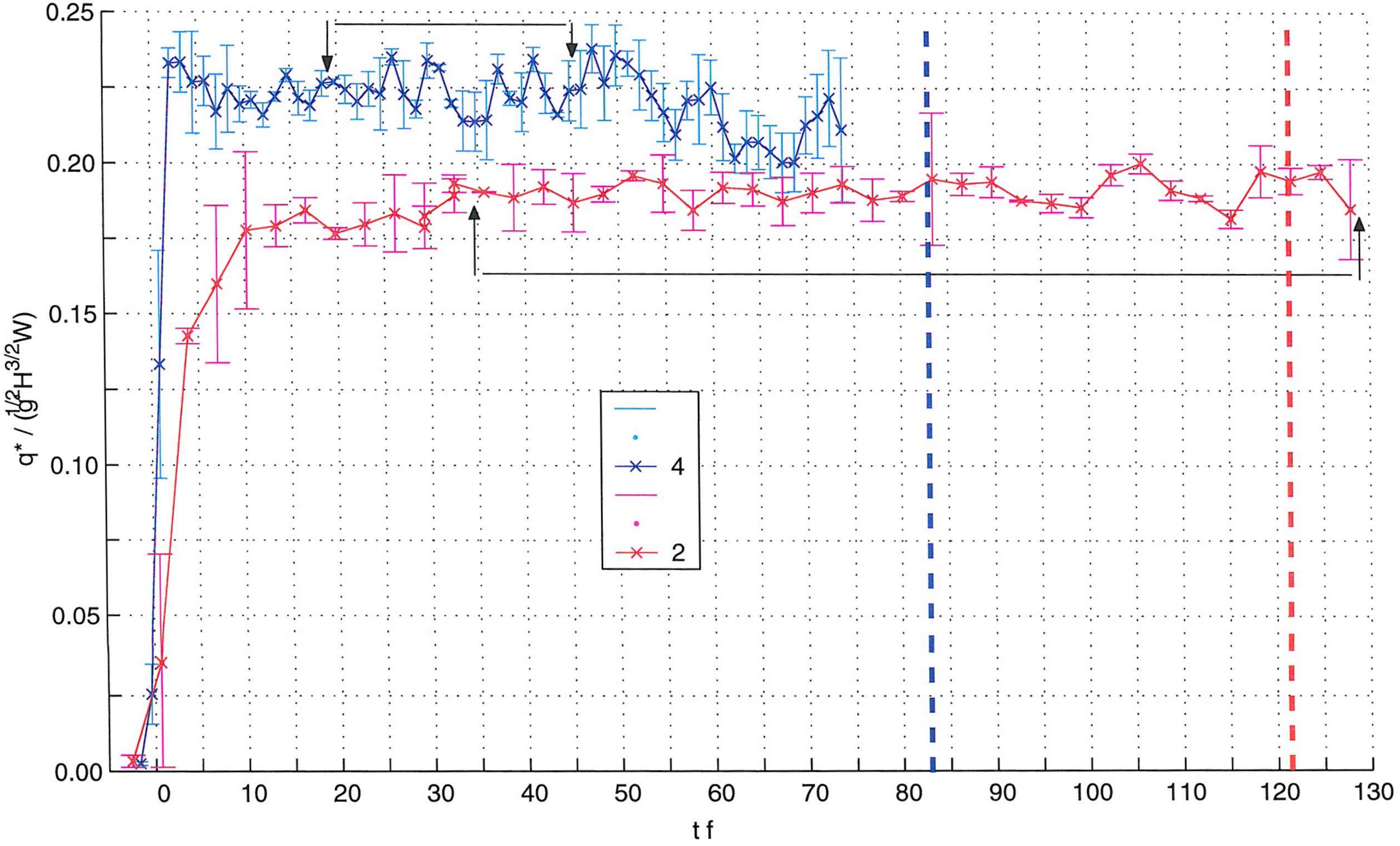

Figure 4.2: Time series of $\bar{q}$ as in figure 4.1 (p.86) for experiments 2 and 4 (island, $R_0 = 1.28$ and 2.49, respectively). Note the initial adjustment is less rapid in the lower R_0 case and missing the initial strong peak. This case does not show the signs of adjustment near the end of the experiment due to changing reservoir conditions, which are visible in experiment 4. Spin-up time denoted by thick vertical dashed lines.

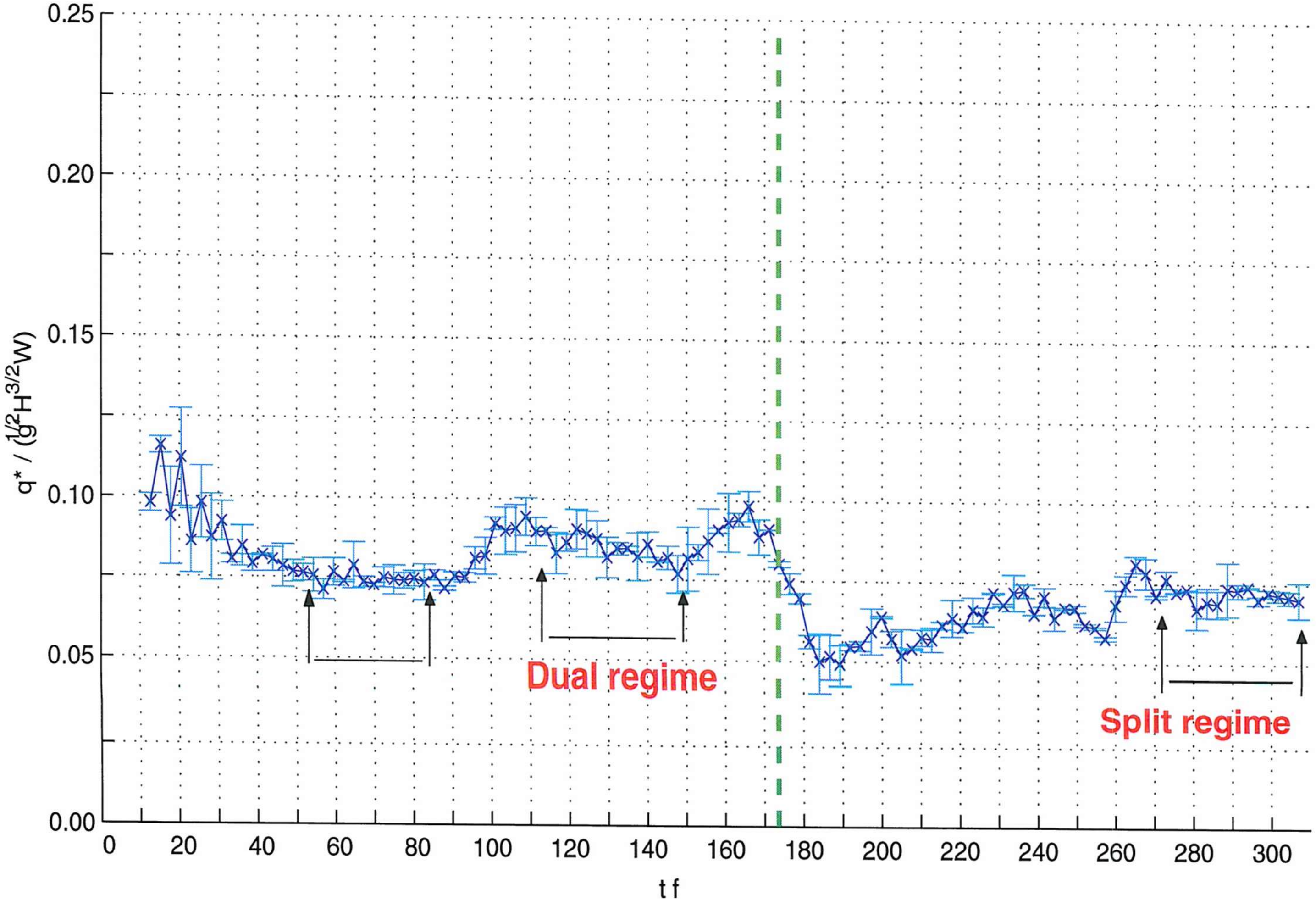

Figure 4.3: Time series of $\bar{q}$ as in figure 4.1 (p.86) for experiments 3 (island, $R_0 = 0.67$). Note the very steady periods near just after the initial adjustment and at the end of the experiment showing almost the same flux magnitudes. Slightly higher fluxes are present around $t = 130 f^{-1}$. From instantaneous velocity fields (not shown) we found this period to be associated with a difference in flow regime. Spin-up time denoted by thick vertical dashed line.

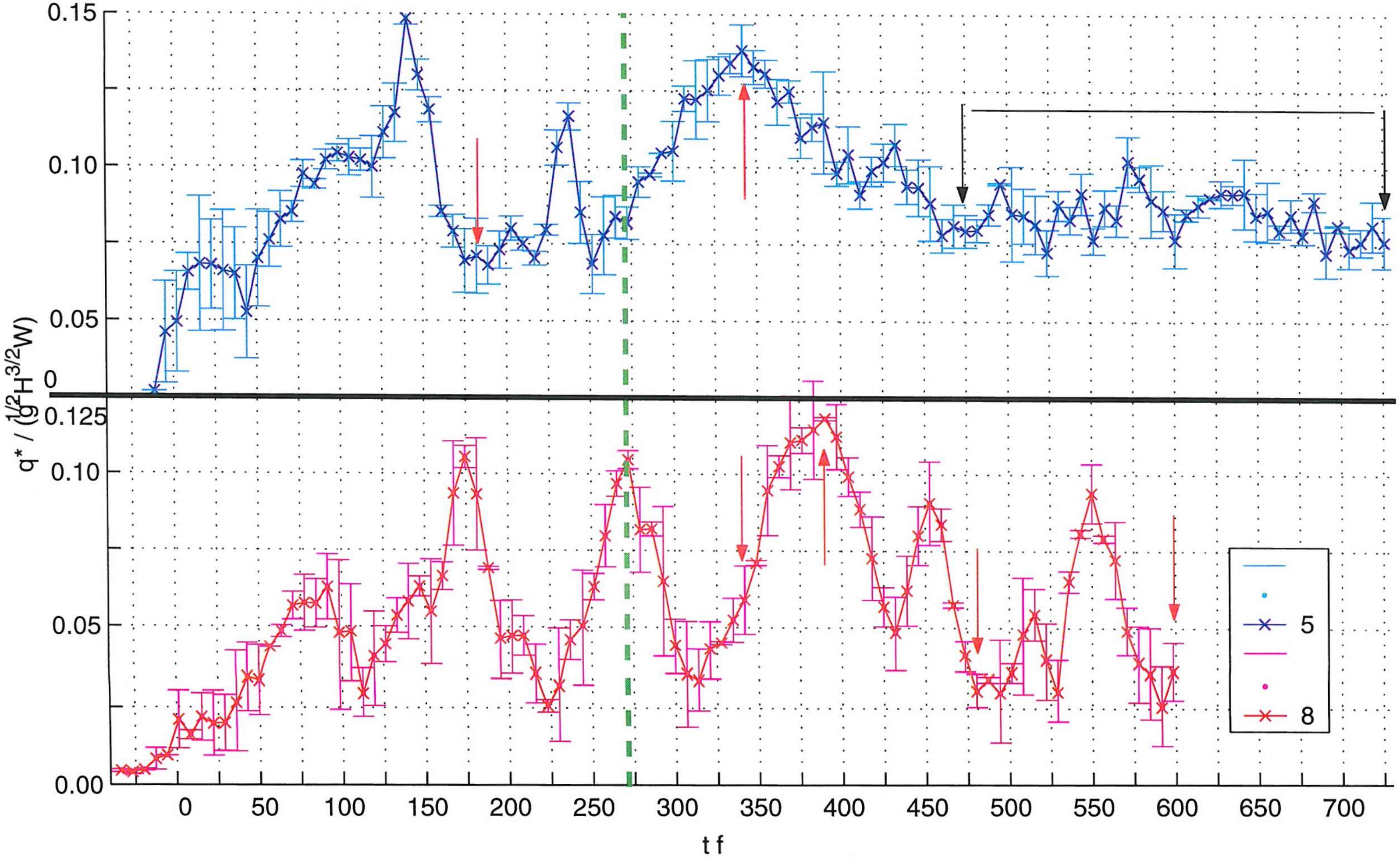

Figure 4.4: Time series of $\bar{q}$ as in figure 4.1 (p.86) for experiments 5 (island, $R_0 = 0.27$) and 8 (simple channel, $R_0 = 0.21$). Fluxes for experiment 5 are vertically offset by $0.125 q_{nr}$. Red arrows denote the instantaneous velocity fields used in subsequent analysis. Note the approximately regular oscillations during most of experiment 8 and the less regular (but similar amplitude) oscillations in experiment 5 followed by almost constant flux. Spin-up time denoted by thick vertical dashed line.

This is due to the step-like nature of the adjusting gravity current and following fronts (see section 4.3.1, p.96). In experiment 8 this is followed from $t \sim 180f^{-1}$ onward by more or less regular oscillations of similar amplitude ($\sim 0.1q_{nr}$). Oscillation periods appear to be around 80 and $120f^{-1}$ corresponding to frequencies of $\sim 10^{-2}f$, which is confirmed by Fourier analysis. Due to the fast rotation, inertial oscillations may be expected. However, their period is $2 \cdot \pi f^{-1}$ (angular frequency $= f$) which cannot be detected in the velocity record as it is smaller than the sampling interval. Oscillations at the inertial frequencies may not occur in any case, as experimental findings related to the movement of the current crossing region by D88 show. We would assume movement of the crossing region to be one reason for this oscillation as it is likely associated with the movement of vortices, shown in section 4.3.2, p.99.

Experiment 5 also shows oscillations with a similar period but much less regularity and a more constant flux in the final $\frac{1}{3}$ of the experiment. This indicates that different flow regimes occur in the island case compared to the simple channel one, although they are less steady than those found in experiment 3. Velocity fields in such flow regimes will be studied in chapter 5 (p.105).

These results show that it is easier in the cases with $R_0 \gtrsim 1$ to determine the quasi-steady time period, as the oscillations in the narrows exchange flux are mostly of very small amplitude, relative to the error. The existence of such steadiness for a significant time period in these experiments is indeed encouraging and the quasi-steady time period has therefore been chosen as denoted by the arrows in figures 4.1 (p.86) and 4.2 (p.88) and those for other experiments in appendix B (p.189). The same applies to figure 4.3 (p.89), but here three time periods have been identified, corresponding to different regimes. The latter will described in chapter 5 (p.105).

The actual time-mean exchange fluxes will be presented in section 6.1, including the overall error from both standard deviation and the measured net flux (assumed to be zero).

Flow at $R_0 << 1$ evidently requires a further examination of the instantaneous velocity fields to determine any distinguishable, if unsteady, states. In particular vortices propagating through the narrows may be a cause of the high amplitude flux oscillations. The latter are not representative of an exchange flow between either reservoir, as some of the streamlines are closed within the channel. In other words, not all the water passing through the narrows actually originates and/or ends up in either reservoir. If such propagating vortices moved a core of fluid from one reservoir to the other they could still effectively contribute to the exchange flux. However, due to the lack of concurrent density and velocity measurements, such analysis is beyond the scope of this thesis.

4.2.2 Local interface height (*SOC* platform)

We use a similar time series approach as in section 4.2.1 (p.85) to look for interesting points in time and determine if and when a quasi-steady state exists in the experiments on the *SOC* platform. As we do not have velocity measurement, we use the local interface height field at the narrows, as inferred from dye measurements (see section 3.2.3, p.50). This quantity (h_R) is the average over half the channel at the narrows (RHS; $-0.455 < y < 0$). This method differs from the flux time series in the last section as it does not show a change in reservoir conditions in the non-rotating case, if concurrent in both reservoirs, as the interface would still be near mid-depth at the narrows, even if the flux significantly reduces. However, in the rotating case a change in reservoir interface depth effectively corresponds to a change in velocity $u \sim \sqrt{g' n_H H}$, where $n_H H$ is the vertical distance between the interface positions in both reservoirs. If the flow is approximately semi-geostrophic, i.e. $|fu| \sim g'|\frac{dh_R}{W}|$, where dh_R is the vertical extent of the interface, $n_H < 1$ implies a decrease in cross-channel slope proportional to $\sqrt{n_H}$. Note that our assumption for the two-layer exchange is $n_H = 1$ if reservoir conditions are not altered.

Most of the h_R time series can be found in appendix B (p.189), and only the fast rotating cases will be presented here. Overall it is found that the adjustment of h_R becomes less rapid as $R_0 \rightarrow 1$ (where $R_0 < 1$) , similar to the flux records in the previous section. A distinct drop near the end (representative of changing reservoir conditions) can again only be seen in experiments with sufficiently high R_0 (> 1.9). As before the quasi-steady period is between the initial adjustment and the distinct drop or just the end of the experiment. For cases with lower R_0, the time series show a more complex (staircase-like) adjustment and several quasi-steady periods (regimes) thereafter, as on the *Coriolis* platform (experiment 3, with island).

In figure 4.5 (p.93) we can see the distinct change in the time variability around $R_0 \sim 0.5$ (experiment 701). Here, the initial adjustment is much slower and separated into distinct steps with oscillations in local interface height visible throughout the experiment. The record is not continuous due to data recording limitations but the various well resolved time periods show high frequency oscillations overlying longer term variability. Even though these are below the stated measurement error in amplitude, it should be noted that they do not occur near the end of the experiment nor for higher R_0. For $R_0 = 0.34$ (experiment 709), we can see very fast, high amplitude oscillations around a general mean trend throughout the experiment. From the middle, where the oscillations have maximum amplitude, to the end there is a slow but constant increase in h_R. Notable is that the high amplitude and long period oscillations do not occur as in the flux records (experiment 8). This is likely due to

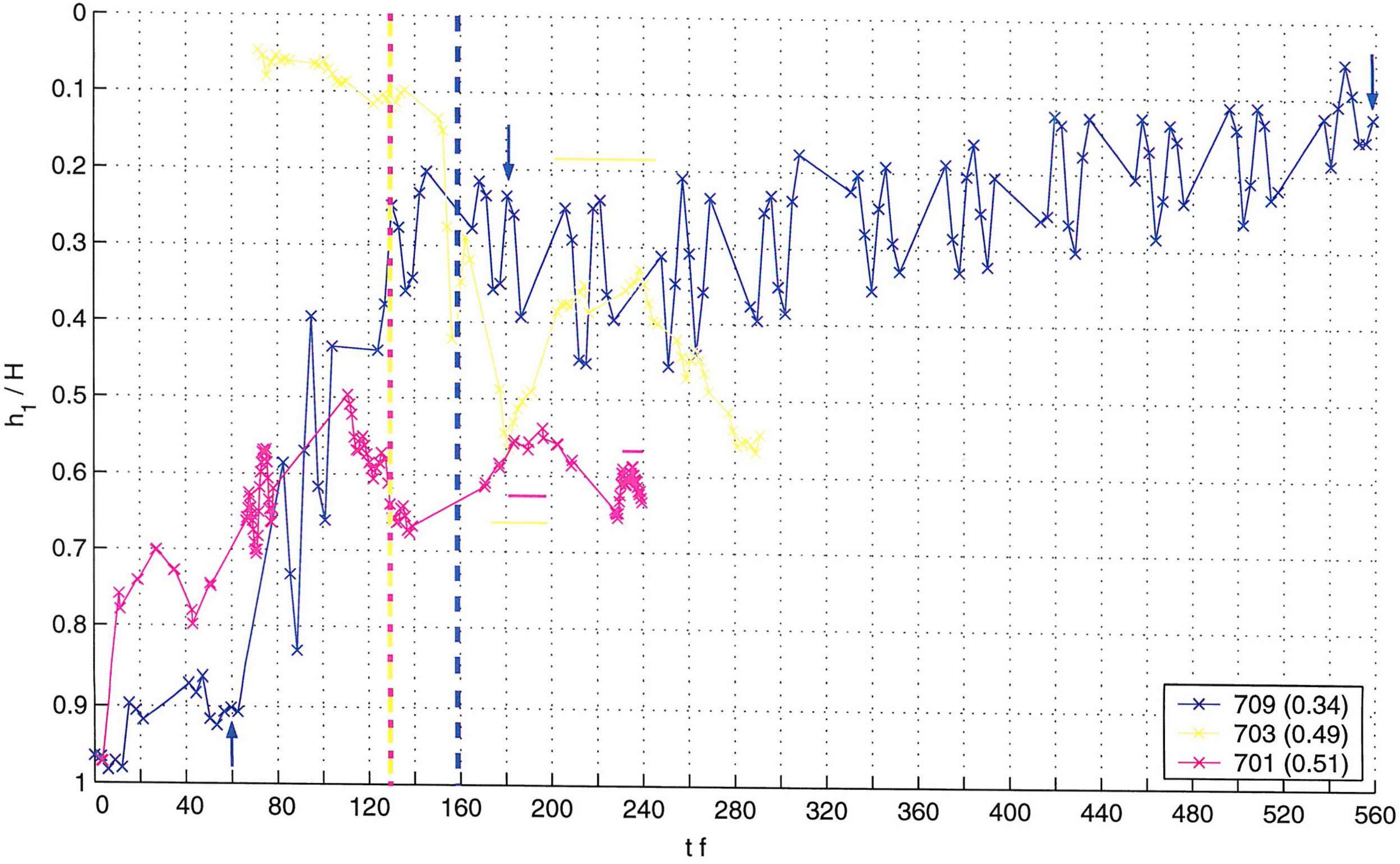

Figure 4.5: Time series of interface height on RHS near narrows for experiments 709, 703 and 701 with corresponding $R_0 = 0.34$, 0.49 and 0.51. Measurement error is 7% as shown. Also shown are the times chosen for averaging, marked by solid horizontal lines corresponding to experiment time series of same colour. Where no quasi-steady period could easily be identified in the time-series, the instantaneous times of interest are marked by coloured arrows. Spin-up time denoted by thick vertical dashed lines.

the fact that vortices intersecting the narrows lead to a false impression of volume exchange flux between the reservoirs but not as significant a change in the interface position. If such vortices are baroclinic, they will indeed only lead to minor interface curvature. In other words, baroclinic vortices do not cause h_R to oscillate with an amplitude of similar order as the mean value, as opposed to $\bar{q}$, where oscillations are of similar amplitude as the mean.

On the *SOC* platform, experiments with an island only cover the parameter range $R_0 \lesssim 1$. Note that the averaging area is now reduced to the range $0.284W < y < 0.455W$ to avoid the island but is still on the RHS of the channel. The experiments with $R_0 > 0.7$ adjust to overall lower levels in h_R which are again consistent (figure 4.6, p.95). The slower adjustment for $R_0 = 1.3$ is due to the fact that the channel was filled with dense water but not dyed, so that the light instead of the dense gravity current passed through the channel but the lower layer adjusted in a similar way as the upper one does in the other experiments. For $R_0 = 0.72$ we can see similarly distinct states as for the *Coriolis* platform (experiment 3). The four experiments with $R_0 \sim 0.5$ (experiments 801, 802, 804 and 805) are found to follow a similar adjustment pattern and to reach an approximate equilibrium in the last third of the experiment, similar to the simple channel case with $R_0 \sim 0.3$. This may again be due to the fact that not all of the lower layer may be active and that vortices, leading to different flow regimes and fluctuations in exchange fluxes, are not necessarily visible in h_R. Nevertheless, the similarity of $h_R(t)$ in most experiments with $R_0 \sim 0.5$ is encouraging suggesting a reproducibility of experiments independent of the exact initial adjustment conditions, such as barrier lifting.

With the exception of experiment 807 (channel filled with dense fluid) and where R_0 values were very close between experiments, the adjustment time roughly decreases with increasing R_0. This is due to faster, less 3-dimensional flow structures following the gravity current. In other words, the initial flow is close to a non-rotating gravity current as opposed to cases with $R_0 \lesssim 1$ where several cross-channel fronts offset along the channel follow the gravity current head toward the narrows. The difference in adjustment time is amplified by the time scaling of f. In the context of this, the velocity and h fields during initial adjustment are briefly described in the next section. This is followed by a closer look at cases with $R_0 << 1$ in section 4.3.2 (p.99), where the same approach as in the *Coriolis* flux records will be used in choosing several extreme or transition points in the highly variable $h_R(t)$ record and to examine the instantaneous h fields.

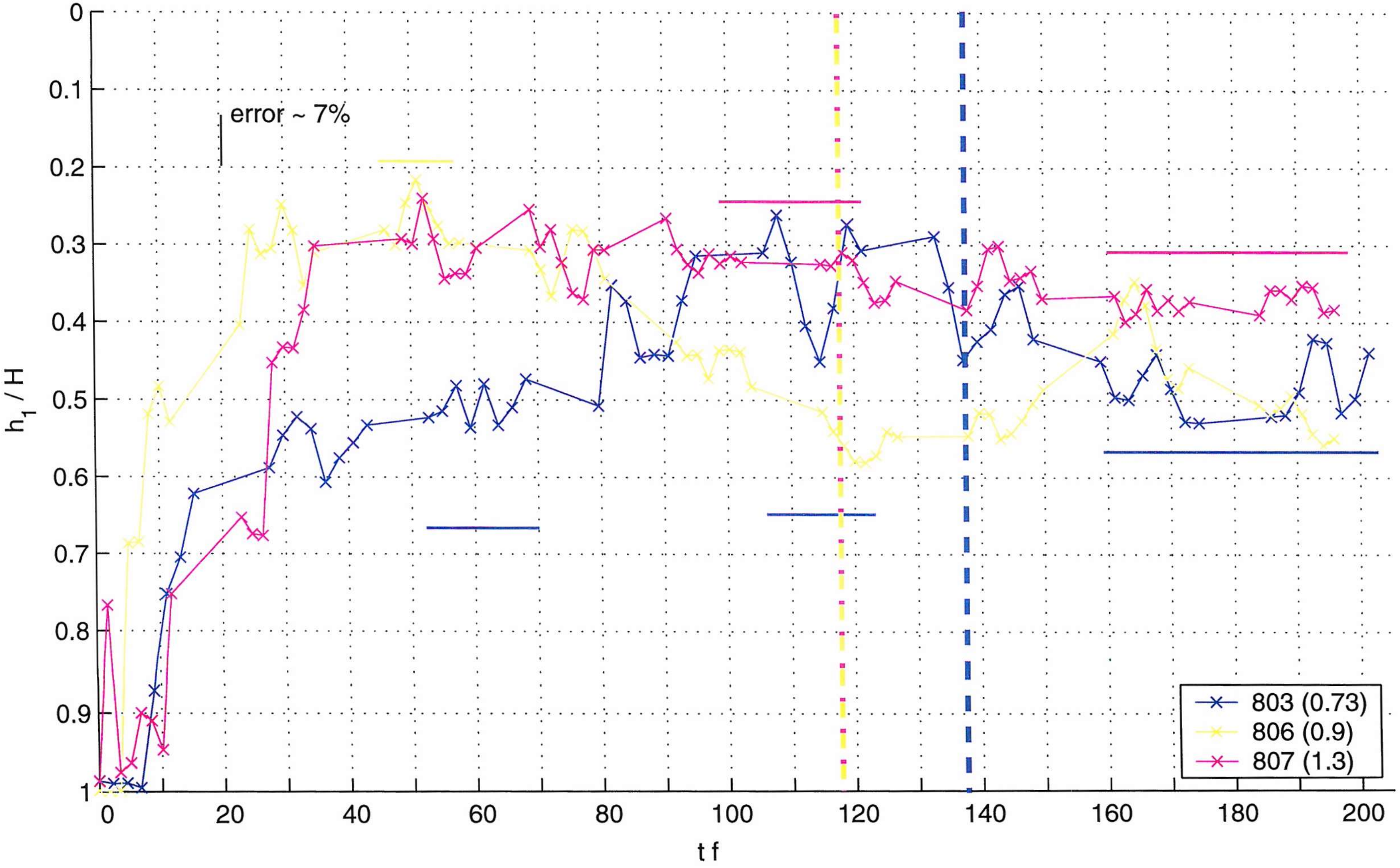

Figure 4.6: Time series of interface height on LHS (RHS) near narrows for experiments 803, 806 and 807 with corresponding $R_0 = 0.73$, 0.9 and 1.3. Measurement error is 7% as shown. Also shown are the times chosen for averaging (solid horizontal lines corresponding to experiment time series of same colour) and the instantaneous times of interest (coloured arrows) where no quasi-steady period could easily be identified in the time series. Spin-up time denoted by thick vertical dashed lines.

4.3 Velocity and interface height evolution

4.3.1 Initial adjustment and establishment of the exchange flow

Having seen the time series in section 4.2 (p.85) it is worthwhile to briefly look at the form of the initial gravity current intrusion into the channel and the Rossby-style adjustment taking place (see Lane-Serff *et al.*, 1995; Hacker and Linden, 2002, for treatment of non-rotating and rotating gravity currents, respectively). As in a non-rotating flow, the rotating lock-exchange is initially associated with a dense gravity current (the light one moves outside the field of view) that moves along the channel. In a constant cross-section channel (i.e. no narrows or sills) this adjustment would lead to a an exchange with the control located in the vicinity of the lock. However, in the case under study the adjusting currents fill the channel with dense fluid and eventually set up the exchange in the vicinity of the narrows (if the lock was located at the narrows this process would be faster). Details of this process are not yet well understood but it is clear from the experiments that the adjustment becomes considerably slower with increasing rotation (decreasing R_0). Here this adjustment is briefly presented to give an idea of the time dependence expected in a lock-exchange flow and possibilities for a change in the exchange flow regime later on in an experiment.

Examples for $R_0 \gtrsim 1$ can be seen in figure 4.7 (p.97), where the flow initially behaves like a non-rotating gravity current but 'feels' the effect of rotation after a time of $\sim f$ (figures 4.7(a), p.97 and 4.7(c), p.97). Both velocity (*Coriolis* platform) and interface depth (*SOC* platform) are shown. The current moves along the RHS wall with several 'step-like' horizontal fronts propagating toward the narrows, as can be seen for $R_0 = 0.9$ (figures 4.7(b), p.97 and 4.7(d), p.97). This presumably represents the adjustment to an exchange flow centred around the narrows. In the island case this process is quite different: the gravity current splits between both island side-channels where the part propagating on the RHS wall is deeper and faster than on the LHS of the island (see figures 4.7(e), p.97 and 4.7(f), p.97). The latter turns around the tip, filling the gap between the other current and the island with dense water before joining with the other part of the gravity current. This will be important to remember for the analysis of the quasi-steady exchange in section 5.4 (p.125), as a separation region forms there.

$R_0 \lesssim 1$ leads to a gravity current almost entirely confined to a thin region near the RHS wall but with a distinct 'bulge' or vortex in the LHS half of the channel (see figure 4.8(a), p.98 and 4.8(c), p.98). This vortex is initially separated from the gravity current within the field of view but later advances toward the narrows together with the flow joining it and the one on the RHS wall. This was also found in numerical experiments of non-linear Rossby

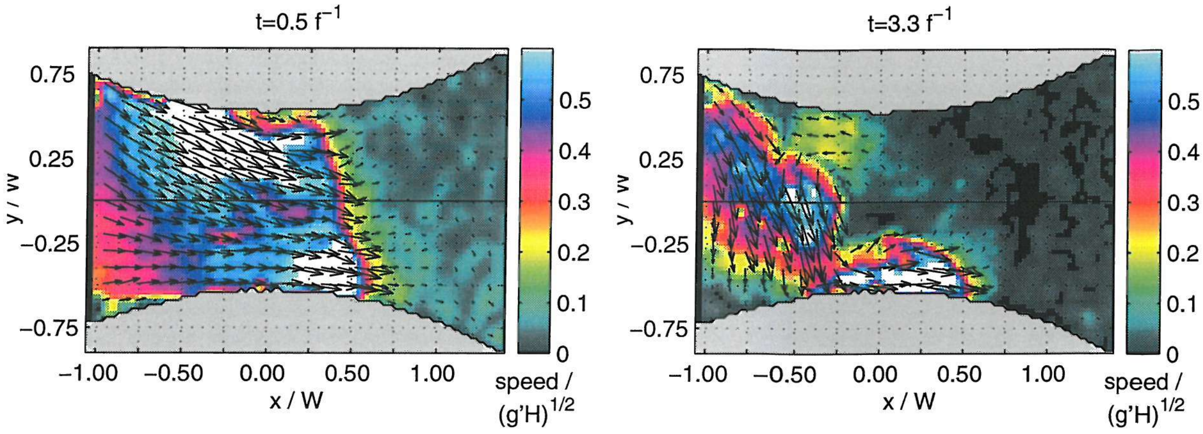

(a) $\underline{u}$ and $|u|$ in expt. 7 (simple channel, $R_0 = 4.16$).

(b) $\underline{u}$ and $|u|$ in expt. 1 (simple channel, $R_0 = 0.90$).

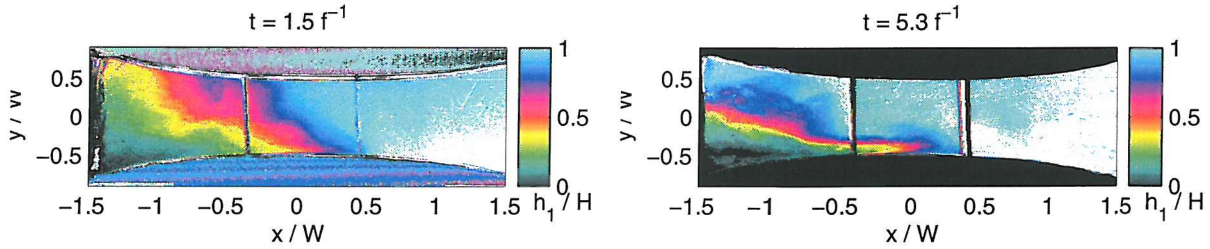

(c) h in expt. 714 (simple channel, $R_0 = 2.5$).

(d) h in expt. 707 (simple channel, $R_0 = 0.87$).

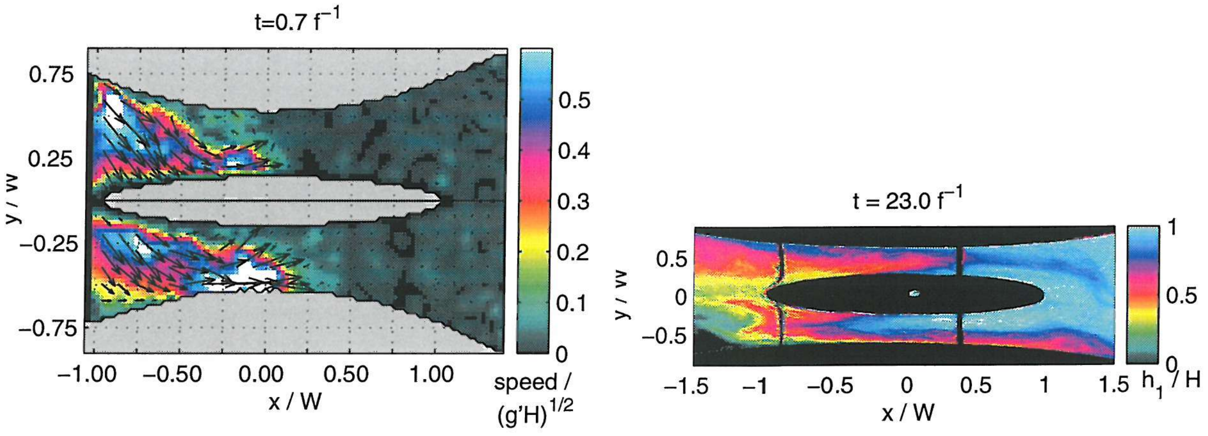

(e) $\underline{u}$ and $|u|$ in expt. 2 (island, $R_0 = 1.28$).

(f) h in expt. 807 (island, $R_0 = 1.2$).

Figure 4.7: Gravity current intrusion represented by velocity fields near the channel bottom (*Coriolis* platform) and interface depth (*SOC* platform, small plots) for $R_0 \gtrsim 1$. Both examples with and without an island are shown. Times after barrier opening are given. Note the intrusion becomes more variable across the channel with decreasing R_0, ranging from an almost uniform front to several step-like ones propagating toward the light reservoir end. Velocity is highly variable near the propagating fronts.

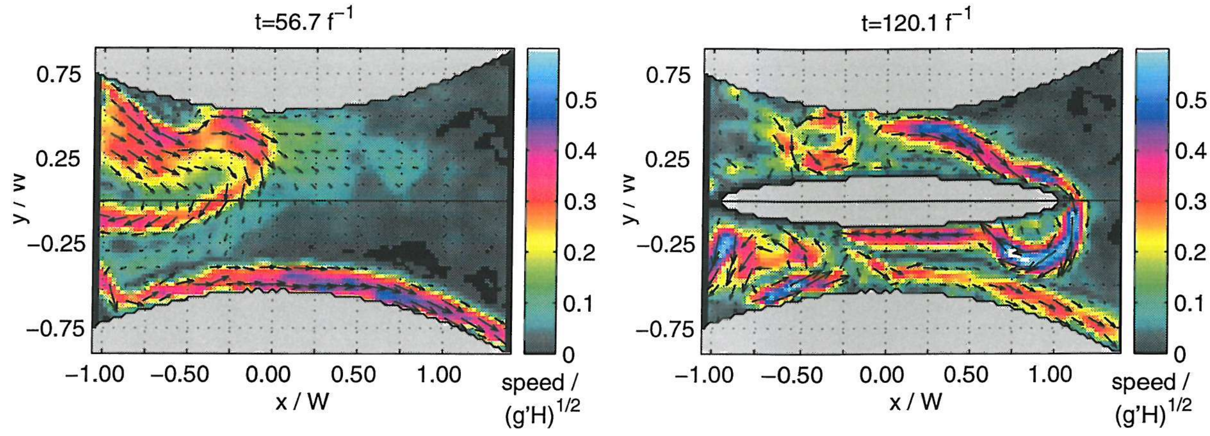

(a) Velocity and speed in experiment 8 (R_0 = 0.21).

(b) Velocity and speed in experiment 5 (R_0 = 0.27).

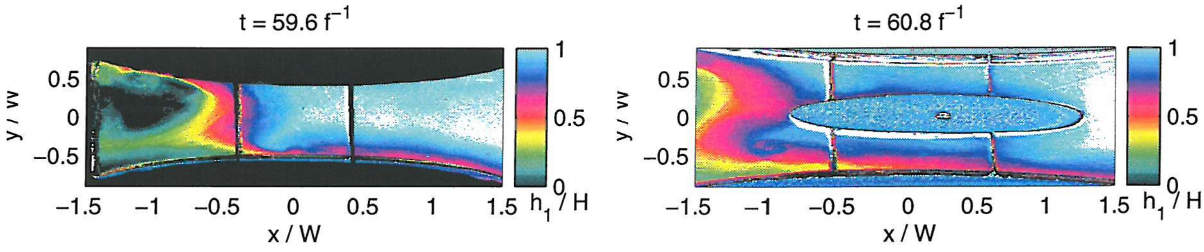

(c) Interface depth in experiment 709 ($R_0 = 0.34$).

(d) Interface depth in experiment 801 ($R_0 = 0.51$).

Figure 4.8: Gravity current intrusion as in figure 4.7 (p.97) but for $R_0 \lesssim 1$. Note the bulge on the LHS half of the channel and the separate gravity current propagating close to the RHS wall. With an island this situation leads to the same split gravity current as before but the one on the LHS circumvents the island tip and actually recirculates back toward the dense reservoir. This means that an exchange of some sort may already start to set up on the RHS of the island while the LHS is still in the initial adjustment stage, i.e. the initial intrusion front is still propagating along the channel toward the light reservoir.

adjustment in a rectangular channel by Helfrich *et al.* (1999) and has been studied for single layers by Hermann *et al.* (1989). The latter explained this phenomenon as a propagating potential vorticity front, where the intrusion on the RHS is much faster than on the LHS and both are separated from each other, even leading to enclosure of ambient fluid in between. Kelvin waves would only allow propagation in the same direction along one wall. Hermann *et al.* (1989) found that the non-linear effects associated with the advection of vorticity allows this propagation along both walls, which they suggest is an intermediate stage to set up the steady, hydraulically controlled flow. In a two-layer fluid, one could imagine similar processes allowing the propagation of fluid along both walls in each layer alone and thus leading to the observed 'bulge'.

In this observed 'bulge', the difference between the island and the simple channel again becomes evident: the vortex interacts with the island, depending on R_0 and the ratio of horizontal channel geometry (i.e. island to channel length and width near the island tip), causing the gravity current to eventually propagate on the LHS of the island (see figures 4.8(b), p.98 and 4.8(d), p.98). This may happen considerably later than on the RHS, which differs in the high R_0 cases. It may not occur at all, if $R < \frac{W(x_{tip})}{2}$, where $W(x_{tip})$ is the width of the channel at the island tip, or $R < \frac{1}{2}L_{channel} - L_{island}$, where $L_{channel,island}$ are the lengths of the channel and the island, respectively. The latter condition means that R is smaller than the distance between the reservoirs and the corresponding island tips. This leads to a change in different quasi-steady exchange flow regimes for $R_0 \lesssim 1$ if an island is present (see sections 5.2.2, p.114 and 5.4.2, p.130).

The next section deals with the variability present for $R_0 << 1$, where the interface depth and flux time series show significant variability even after the initial adjustment. This will identify some instantaneous velocity fields suitable for analysis in the next chapter.

4.3.2 Non-steady flows ($R_0 << 1$)

The time periods thought to represent the quasi-steady exchange flow also show little variability in the horizontal fields with the same principal flow structures and exhibit a fairly constant flux and interface depth at the narrows. Thus a quasi-steady exchange is expected to occur, even if several distinct regimes exist within one experiment. For very high rotation (low R_0) a quasi-steady time period no longer exists but some temporary flow states, represented by one instantaneous snapshot of the flow, can be identified to represent an exchange flow with a channel-crossing current in both the upper and lower flows in the vicinity of the narrows.

Figure 4.9 (p.100) shows some of such instantaneous fields for the simple channel case

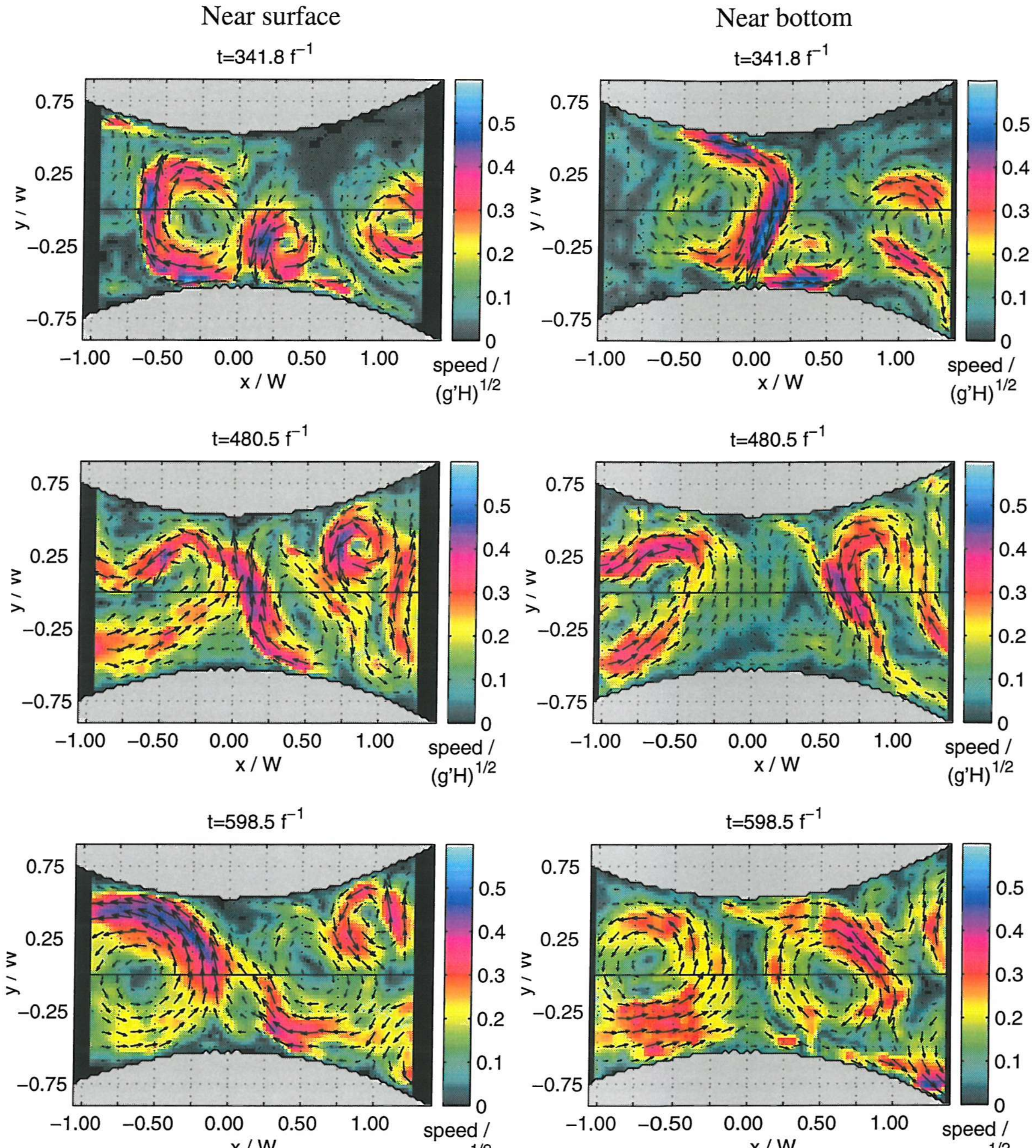

Figure 4.9: Selected instantaneous horizontal velocity fields in experiment 8 (simple channel, $R_0 = 0.21$) at times shown in figure 4.4 (p.90). Data from levels 1 (near-surface) and 9 (near-bottom) shown in the left and right columns, respectively. Absolute velocity is shown in colour. The initially dense reservoir is on the left and the light one on the right. Note the slightly barotropic nature of the flow with near-surface and near-bottom flows not horizontally coincident, i.e. less baroclinic.

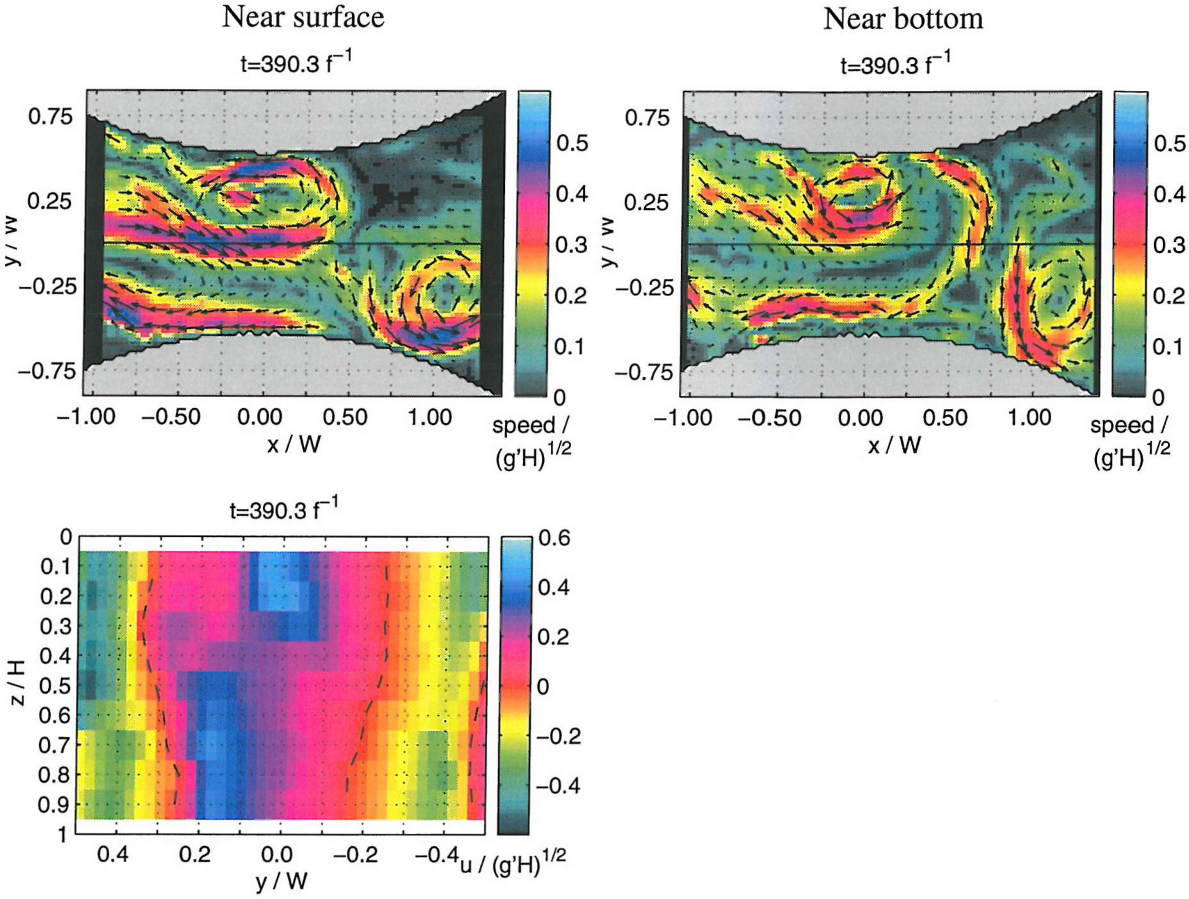
Near surface

Near bottom

Figure 4.10: Velocity field as in figure 4.9 (p.100) near the surface and bottom. Also shown is the along-channel velocity at the narrows cross-section. Note the vortex present at the narrows leading to the impression of strong flow in both directions through the corresponding cross-section. Such periods cannot be identified in the flux time series presented earlier in this chapter but only in the horizontal velocity fields. Vortices at the narrows are avoided in the exchange flux analysis in chapter 6.1 (p.133) as part of the flow is recirculating inside the channel and not passing between the reservoirs.

with $R_0 = 0.21$. At $t \sim 340f^{-1}$ the vortex formed during the initial gravity current has reached the narrows and the near-bottom flow crosses the channel, visible there as a velocity core at the edge of the vortex before banking against the RHS wall at $x > 0$. Near the surface the flow also crosses, though in a more complicated pattern. It appears that here the water actually flowing from one reservoir to the other is much less than the along-channel volume flux at the narrows suggests. This is seen in the speed at the edge of the vortices, e.g. at the narrows, which is more than twice that away from those flows.

Throughout the experiment, the channel-crossing of the currents is $\sim R$ wide (with adjacent vortices making an accurate measurement of width difficult) and oscillates with time in an along-channel direction in the vicinity of the narrows. This agrees with experimental results by D88. However, the currents in figure 4.9 (p.100) also show undulations in other parts of the channel steered by the two large and other smaller vortices. This signifies the partly barotropic nature of the flow, as opposed to an almost entirely baroclinic flow for $R_0 > 1$. Furthermore, the crossing is at times more sluggish and wider, for example near-bottom at $t = 480f^{-1}$. Figure 4.10 (p.101) also shows that vortices, largely barotropic and intersecting the narrows, can significantly distort the magnitude of the exchange where some of the flow recirculates around the narrows instead of transporting water between both reservoirs. Visual observation during these experiments showed vortices travelling from near the channel-ends toward the narrows, suggesting that they are generated within the reservoirs. However, the vortices may also be generated by horizontal shear within the channel. The origin of the vortices cannot be determine with certainty, as their density structure is not known.

Overall the flow structures in figure 4.9 (p.100) appear more ordered near the end of the experiment with two large vortices residing on either side of the narrows along the channel. This region of current crossing was also found by D88 to occur around the narrows, although oscillating with frequencies not obviously linked to f (see section 4.2.1, p.85). Note that there is no a-priori theoretical reason for this in inviscid theory.

In the island case for $R_0 < 1$, not only the initial adjustment but also the subsequent evolution of the flow is different from the simple channel experiment. Figure 4.11 (p.103) shows for $R_0 = 0.27$ (experiment 5) that vortices are of the scale of either island side-channel (i.e. W_R and W_L) as opposed to the simple channel case where the only geometric limitation was given by the channel walls (i.e. W_s). The flow path changes significantly throughout the experiments from thin meandering currents (e.g. $t \sim 180f^{-1}$) to almost unidirectional flow on either island side at $t \sim 340f^{-1}$. The latter shows strong velocities and narrows exchange fluxes (figure 4.4, p.90) but appears to be mostly free of vortices or recirculation, much different from the corresponding simple channel case (experiment 8). Near the end of the experiment when fluxes are more steady the flow field is found to be still changing and

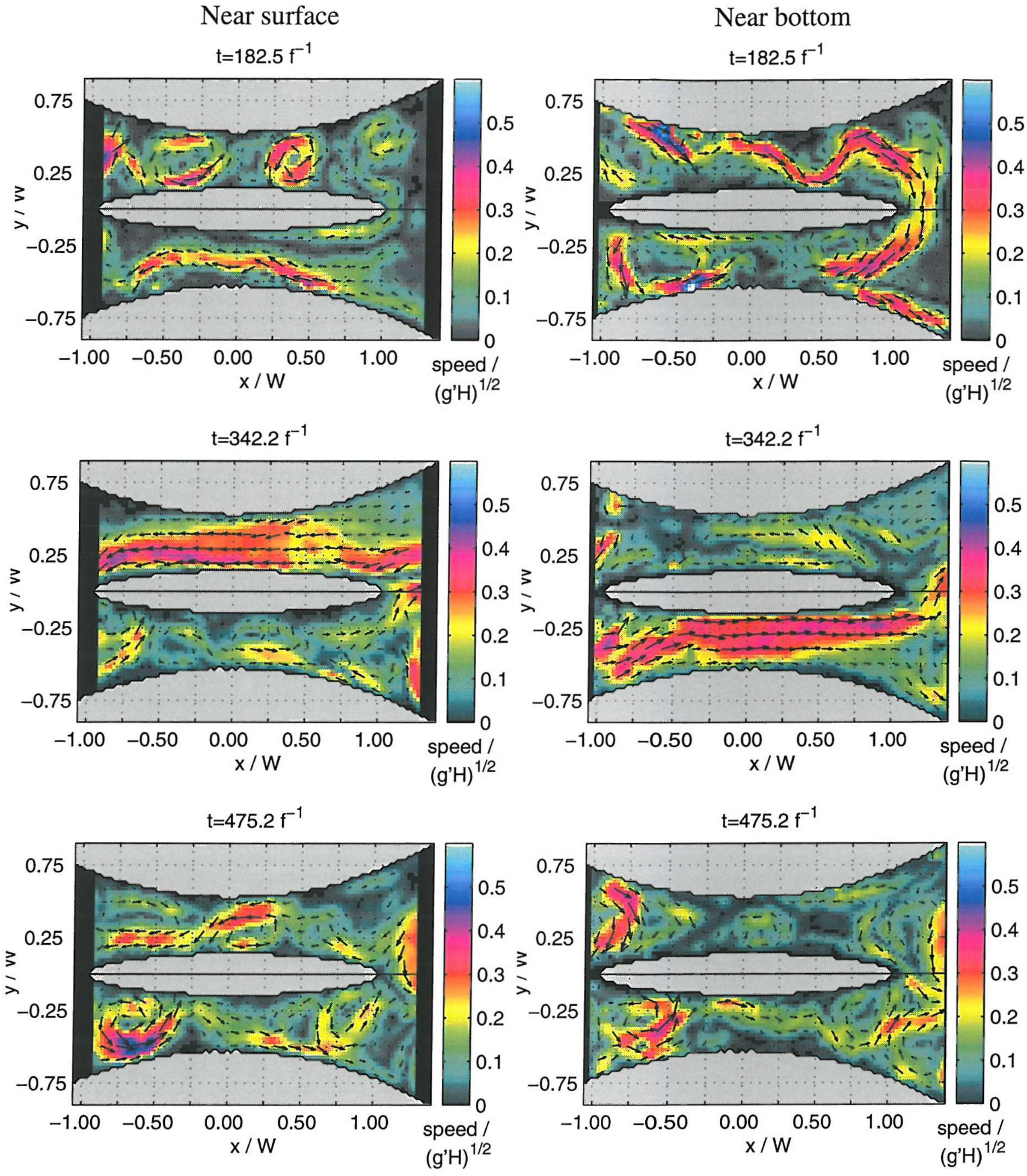

Figure 4.11: Selected instantaneous horizontal velocity fields in experiment 5 (island, $R_0 = 0.27$) arranged in the same way as figure 4.9 (p.100). Note the meandering nature of the currents near the surface (left column) and the bottom (right column), except at $t \sim 340f^{-1}$, where the flow on either island side is practically uni-directional and barotropic.

difficult to trace between the reservoirs.

In both experiments 5 and 8 where $R_0 < 1$ a time-mean flow field over most of the running time does not yield a velocity field coherent with an exchange flow. However, despite the variability described in this section several distinct instantaneous flow states can be distinguished, where no barotropic vortices are present at the narrows and part of the flow can be traced along the channel between both reservoirs. Such flow states will be analysed in chapter 5 (p.105) and are associated with different flux values as presented in figure 4.4 (p.90).

4.4 Summary

This chapter identified quasi-steady flow fields by analysing the time variability of interface depth and exchange fluxes at the narrows. The variability agrees with expected lock-exchange sequence: the initial transient (gravity current and following frontal adjustment), the steady state exchange (near-constant flux and interface depth with no significant changes in velocity and h fields) and the returning gravity current due to significantly changed reservoir conditions. Despite the variability found in the experiments, it is possible to identify one or more quasi-steady time periods in most cases.

For $R_0 \lesssim 1$ a series of quasi-steady regimes was found, interrupted by transient periods. It will be shown in chapter 5.3 (p.119) that on the *Coriolis* platform these regimes are associated with distinct flow paths. For $R_0 \sim 0.2$, no steady state could be discerned, but some instantaneous velocity fields show clear characteristics of an exchange flow with both layers crossing at the same x-location. With an island a 'split' regime was also identified, where the flow on either island side is almost barotropic. Low R_0 also showed persistent large scale variability in the flow: cyclonic and anti-cyclonic vortices (often barotropic and either quasi-stationary or travelling in from the reservoir) and vortices formed within the channel (e.g. separation regions) that are likely due to mixed barotropic/baroclinic instability, as both horizontal and vertical shear are considerable.

All of the quasi-steady regimes and some instantaneous flow fields for $R_0 << 1$ will be used in the remainder of this thesis to study variation with R_0. This includes an analysis of the flow fields, separation, fluxes and hydraulic control.

Chapter 5

Quasi-steady and instantaneous flow fields

The primary objective of this work is to look at the exchange flow through a channel with and without an island. We will concentrate on the quasi-steady state(s) after the initial adjustment, as many oceanic exchange flows are assumed to be quasi-steady. As seen in chapter 2 (p.24) much previous work makes this assumption. In this chapter, the appropriate time averages determined in chapter 4.2 (p.85) will be analysed with respect to different exchange flow patterns. It will be shown that at the narrows, all flows for $R_0 \gtrsim 1$ behave in a manner expected from simple channel rotating two-layer exchange flow theory if the reduction in channel width is taken into account in the island cases. For $R_0 \lesssim 1$ significant differences between the flow regimes in island and simple channel cases can be found. Furthermore, these two cases show differences in flow separation and current crossing away from the narrows for all R_0.

5.1 Non-rotating exchange

In an inviscid, non-rotating two-layer exchange the interface is expected to slope in an along-channel direction and be fairly flat across, except near the boundaries. If the flow through a constant-depth channel is hydraulically controlled, theory predicts $h = 0.5H$ at the narrows, mid-depth with the flow being vertically symmetric (Armi, 1986; Dalziel, 1991). The u-velocity cross-section at $x = 0$ shown in figure 5.1(a) (p.106) shows this, but with a vertical offset $\sim 0.05H$ toward the surface. The interface is reasonably flat across the channel, and the small cross-channel difference of ~ 0.01 may be attributable to variability in the channel floor geometry.

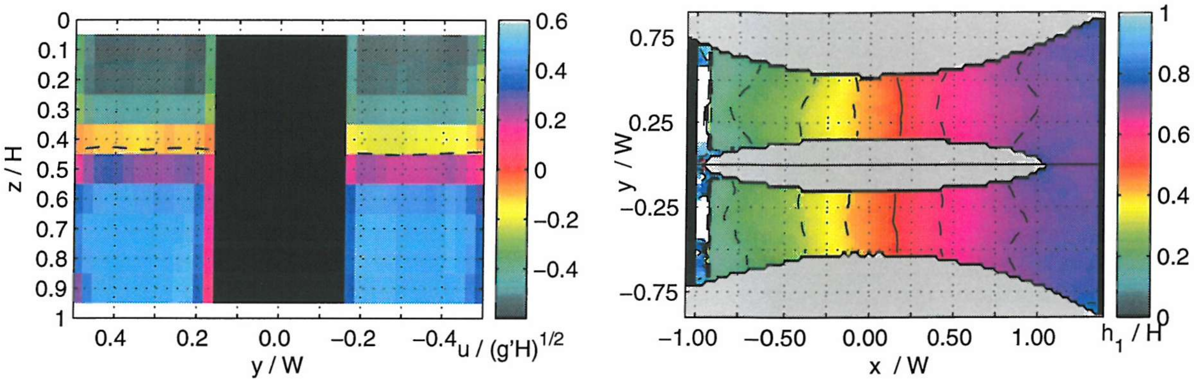

(a) Velocity cross-section for experiment 14 at the narrows. The lower layer flows into the page toward light reservoir. Note that CIV velocity near the walls and the island may not be accurate, which is why no measure of the boundary layers there is given.

(b) Shear interface depth (h_1) field for experiment 14; contours are drawn at $0.1H$ intervals with the solid one representing mid-depth.

Figure 5.1: Steady non-dimensional along-channel velocity and shear interface depth for the non-rotating cases with island on the *Coriolis* platform. Time-average taken for $7.2\frac{2*L}{\sqrt{g'H}} < t < 36\frac{2*L}{\sqrt{g'H}}$. The 2-d field of h_1 is also shown. Both plots show that there is generally little cross-channel variability and a degree of symmetry in the vertical at the narrows. Frictional effects at the bottom are thought to be responsible for the small shift in interface depth, along the channel in figure 5.1(b) and toward the surface in figure 5.1(b).

The horizontal h field (figure 5.1(b), p.106), calculated as shown in section 3.3.5 using the zero isotach, accordingly shows a shift of the mid-depth contour toward the light reservoir. This may be due to frictional effects near the solid bottom boundary, which slows velocity in the bottom layer and thickens it near the light reservoir, downstream with respect to flow direction. Such frictional effects were investigated by Zaremba *et al.* (2003) using a numerical model of two-layer exchange in a flat-bottom, horizontally contracting channel, the equivalent of our simple channel (see Pratt, 1986, for a treatment of the single layer case using a reduced gravity model). They found that setting surface friction to zero, but keeping internal, bottom and side wall boundary friction, causes an upward offset in the interface at the narrows: the $h = 0.5H$ point moves toward the light reservoir, downstream with respect to the lower layer. They found a parameter to determine the effect of friction, $\alpha = f_b\frac{L}{H}$, where the non-dimensional parameter for bottom friction is a type of drag-coefficient, $f_b = \frac{16}{Re}$; the latter relationship is used in laminar flows and is consistent with work by Anati *et al.* (1977). However, a suitable Reynolds number is difficult to determine in our experiments. It may be noted, that Zaremba *et al.* (2003) for values of $\alpha = 0.25$ that the upper layer near the dense reservoir is approximately $\frac{3}{4}$ as thick as the lower layer near the light reservoir; this ratio is only slightly higher than in our experiments. However, Zaremba *et al.* (2003) did not show a noticeable vertical offset of the interface at the narrows for $\alpha < 1$, even though we observed this. This suggests that, regardless of the actual value of α, further calculations using this approach with our data is not likely going to lead to further insight of the problem of bottom friction.

Figure 5.1(a) (p.106) also shows that the shear interface is approximately 0.2 to $0.3H$ thick, bounded by regions of nearly constant velocity above and below, but may be vertically offset from the density interface away from the narrows due to internal mixing at the interface. This would lead to a shallowing of the shear interface relative to mid-depth, so that the density interface (mean-density isopycnal) would be nearer to the surface (bottom) near the dense (light) reservoir than the shear interface (Hogg *et al.*, 2001a; Stenström, 2003; Winters and Seim, 2000). However, this difference is assumed to be only significant near the reservoir ends of the channel, where the flow is almost stagnant throughout with a thin shear layer near the surface or bottom. Significant here means with respect to the accuracy of vertical position from the laser light sheet sheet on the *Coriolis* platform and dye attenuation on the *SOC* platform. Further discussion of the sharpness of the shear interface and mixing in the context of previous studies is given in section 7.3 (p.174).

Overall, the non-rotating results in both experimental setups, with and without an island, agree with the concept of a fully hydraulically controlled, i.e. maximal, exchange (Armi, 1986; Dalziel, 1991), where the strongly sloping interface at the narrows is isolated from linear (small) disturbances in either reservoir. Note that a submaximal flow would have an interface with a small, changing along-channel slope and a minimum depth at the narrows if it is not hydraulically controlled or an interface much closer to mid-depth near one channel end than the other if it is partially controlled (Dalziel, 1991). Frictional effects near the bottom are small and agree with the vertical offset of the interface as found by Zaremba *et al.* (2003). The agreement of non-rotating results with theoretical studies is encouraging and gives us confidence in the rotating cases. This will be confirmed in the remainder of this thesis when comparing the experiments to inviscid, semi-geostrophic hydraulic exchange theory for simple channels. When rotation is introduced we can still look at the narrows cross-section as will be shown in the next two sections. Later we will consider the flow field in the whole channel to study flow separation and effects unique to the island cases.

5.2 Width of current at the Narrows

5.2.1 Attached flow ($R_0 \gtrsim 1$)

For rotating flows, the simple channel case has been treated theoretically by D88 and Dalziel (1990). In cases of fast rotation, $R_0 \lesssim 1$, and with an island in particular, the theory is limited and flows in the experiments of this study are found to be more complex. Therefore we will first consider cases with slow rotation, $R_0 \gtrsim 1$. This section will show that at the narrows, flows with an island may still be viewed in a similar manner to the simple channel cases if the island width is accounted for in the calculation of W and thus R_0. For this purpose the subscripts (s, i) will be used, so that the whole (simple) channel width is represented by W_s and the reduced width available to the flow in the island cases is represented by W_i; similarly, $R_{0(s,i)} = \frac{R}{W(s,i)}$. Whenever W or R_0 is referred to in this thesis without the subscripts, the corresponding appropriate values are used (e.g. $W = W_i$ in the island case).

The flow has two boundaries to lean on in the island cases. One question arising out of this cross-channel geometry is whether the island 'spreads' the flow over a larger portion of the cross-section than a simple channel. Further points of interest include the sensitivity to initial conditions and the role of viscous effects. The latter will be treated in section 6.4 (p.160).

To answer the above questions using the quasi-steady velocity fields it is simplest to view the cross-section velocity at the narrows, as this is where the exchange flow is normally expected to be hydraulically controlled. We will do this from high to low R_0 sequentially, regardless of the platform or channel geometry used. However, if R_0 is similar we will still try to treat the simple channel cases first as the island can be viewed as an increased degree of complexity to this. When we look at separation and flow paths in the next section, we will again treat the simple channel and island cases separately, as there are significant differences between them, in particular away from the narrows.

From previous studies, we expect the span of the interface, i.e. the vertical distance between sidewall attachment points, dz, to be a function of R_0 for $R_0 \geq 1$, i.e. slowly rotating flows (D88, Dalziel, 1990; Whitehead *et al.*, 1974). In a zero potential vorticity flow the interface would theoretically span the whole channel depth if the channel was of same width as the Rossby radius, i.e. R_0 wide, so that $dz = H$ and $\frac{dz}{W_s} = 1$. On the other hand, in a non-rotating flow the interface would not slope across the channel at all, i.e. as $R_0 \rightarrow \infty$, $dz = 0$ and $\frac{dz}{W_s} = 0$. Making these assumptions, the linear relationship we expect for the

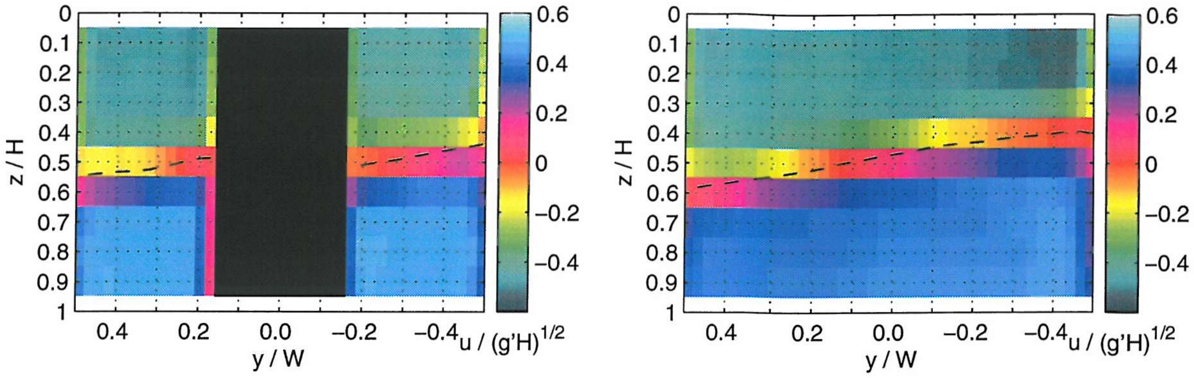

(a) Experiment 6 ($R_0 = 6.37$, island) (b) Experiment 7 ($R_0 = 4.16$, simple channel)

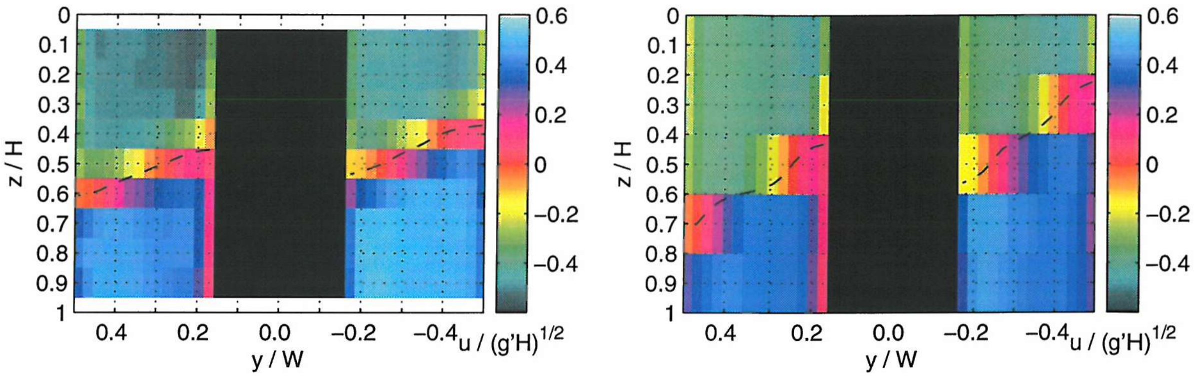

(c) Experiment 4 ($R_0 = 2.49$, island) (d) Experiment 2 ($R_0 = 1.28$, island)

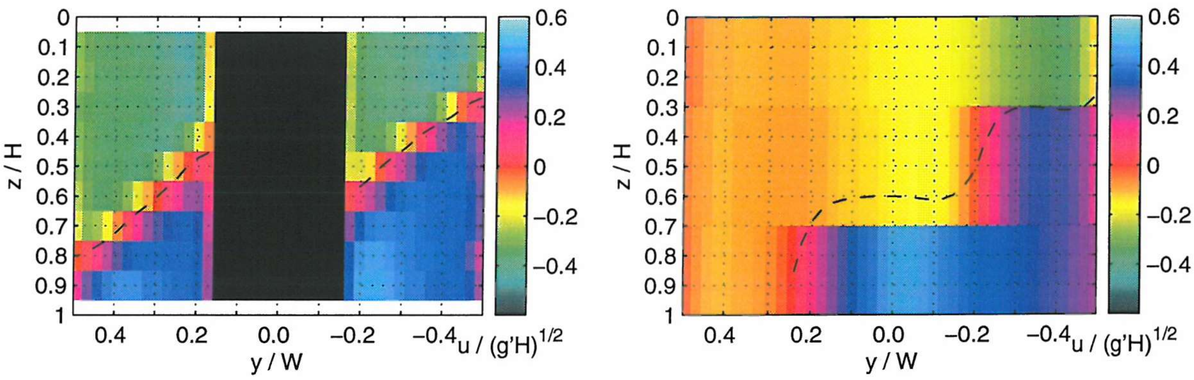

(e) Experiment 15 ($R_0 = 1.22$, island) (f) Experiment 1 ($R_0 = 0.90$, simple channel)

Figure 5.2: Along-channel velocity and contours of the zero velocity interface at the narrows cross-section for $R_0 \geq 0.9$ during the quasi-steady period (corresponding averaging times listed in appendix D, p.201). View is downstream with respect to lower layer. The y-coordinate is reversed for experiment 15 as reservoir ρ was reversed. Note the increase in interface slope with decreasing R_0 (except experiment 1, showing asymmetry) and the different overall depth of the interface on either side of the island. The offset toward the surface over the whole section is due to the difference in surface and bottom boundary conditions.

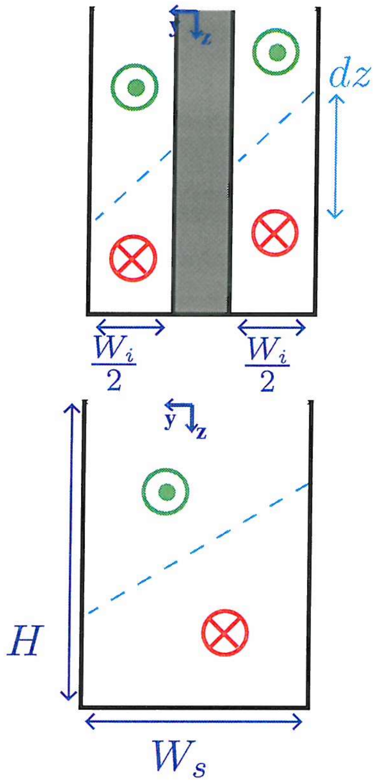

Figure 5.3: Schematic of the principal conditions at the narrows in experiments with $R_0 \gtrsim 1$, where baroclinic flow occupies the whole cross-section. The red and green circles represent flow from the dense and light reservoir ends of the channel, respectively. The blue dashed line indicates the distinct shear interface. The results show that for similar R_0 the island ($R_0 = R_{0i}$) and simple channel ($R_0 = R_{0s}$) cases show the same cross-channel slope, represented by $dz_{W_{(i,s)}} = \frac{dz}{W_{(i,s)}}$ and given in equation 5.2 (p.110).

simple channel case is

$$R_{0s} = \frac{R}{W_s^*} \approx \left(\frac{W_s^*}{H^*}\right)\frac{dz^*}{W_s^*} = \frac{1}{dz} \Rightarrow dz_{W_s} \approx \frac{1}{R_{0s}}, \tag{5.1}$$

where the * variables are dimensional, as before and R the dimensional Rossby radius. The expected cross-channel slope, dz_{W_s}, can thus be calculated from the measured R_{0s} and vice versa. Note that in dimensional terms this means that dz^* occupies the same fraction of the channel depth, H^*, as R of the width, W_s^*. Therefore, $\frac{dz^*}{W_s^*}$ needs to be multiplied by the term in brackets, $(\frac{W_s^*}{H^*})$, in equation 5.1 (p.110), since R_{0s} is independent of the ratio of $\frac{W_s^*}{H^*}$. Despite the applicability of equation 5.1 (p.110) to simple channel exchange with $R_0 > 1$, the results in this section will show that dz_{W_s} overestimates the cross-channel slope in the island cases, if we use W_s as a measure for W. Here it is necessary to use the reduced quantity, W_i, so replacing all the s subscripts in equation 5.1 (p.110) by i. This leads to the generally applicable relationship

$$\frac{dz}{W_{(i,s)}} = dz_{W_{(i,s)}} \approx \frac{1}{R_{0(i,s)}} \tag{5.2}$$

Note that using R_{0s} in the island cases would over predict the value of dz by a factor W_i^2 and the one for dz_W by a factor of W_i, i.e. the ratio $\frac{W_i^*}{W_s^*}$. This assumption is tested in the observed data as subsequently described.

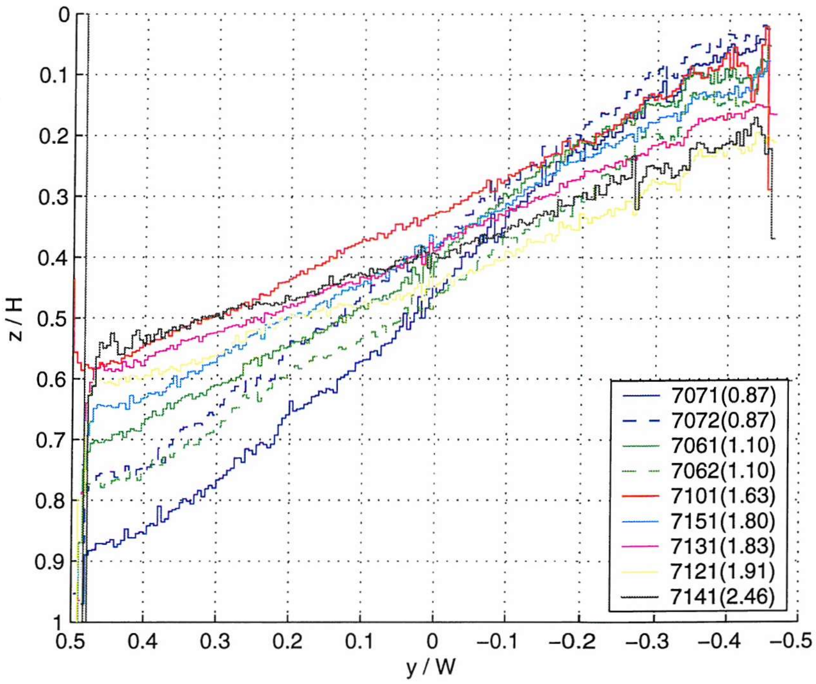

Figure 5.4: Cross-sections of non-dimensional interface depth at the narrows from simple channel experiments on the *SOC* platform ($R_0 \gtrsim 0.9$), averaged over suitable time-periods as given in section 4.2 (p.85). The first three digits in the legend give the experiment (R_0 given in brackets) while consecutive multiple averaging periods for the same experiment are denoted by the final digit. View is downstream with respect to the lower layer. Note the banking up of the lower layer on the RHS. Cross-channel slope generally increases with decreasing R_0 but width of the sloping part of the interface decreases for $R_0 \lesssim 1$. Some vertical offset, more on the LHS wall, represents the viscous effects present on this platform.

For high R_0 ($= 4.16$), experiment 7 (simple channel; see figure 5.2(d), p.109) shows that the cross-section slope covers only $dz = 0.2H$ around $z = 0.5H$, which is slightly smaller than the expected value of $dz \sim \frac{1}{4}H$ from equation 5.2 (p.110). Conversely, this suggests that R_0 is actually more similar to a value of 5. This could be due to viscous effects near the sidewalls in cases with $R_0 >> 1$ (see section 6.4, p.160).

In experiment 6 ($R_0 = 6.37$) dz is even less than in experiment 7 (see figure 5.2(a) (p.109)), even though the Rossby radius (R) is approximately the same, highlighting the applicability of equation 5.2 (p.110). We can also find a similar cross-section structure for $R_0 \sim 2.5$ (figure 5.2(c), p.109) but with an increased dz. In comparison, experiment 710 (and similarly 715) from the *SOC* platform has a value of $R_0 = 1.6$ which would suggest a steeper sloping interface than that observed, covering approximately $0.6H$. The same can be said for experiment 712 which spans $\sim 0.1H$ less depth than expected and even less for experiment 713.

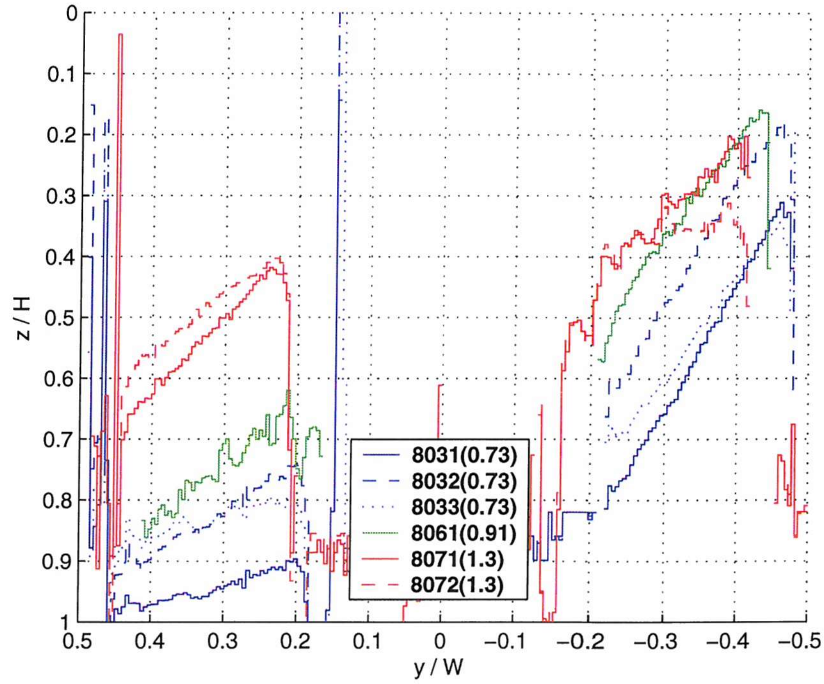

(a) $R_0 \gtrsim 0.7$

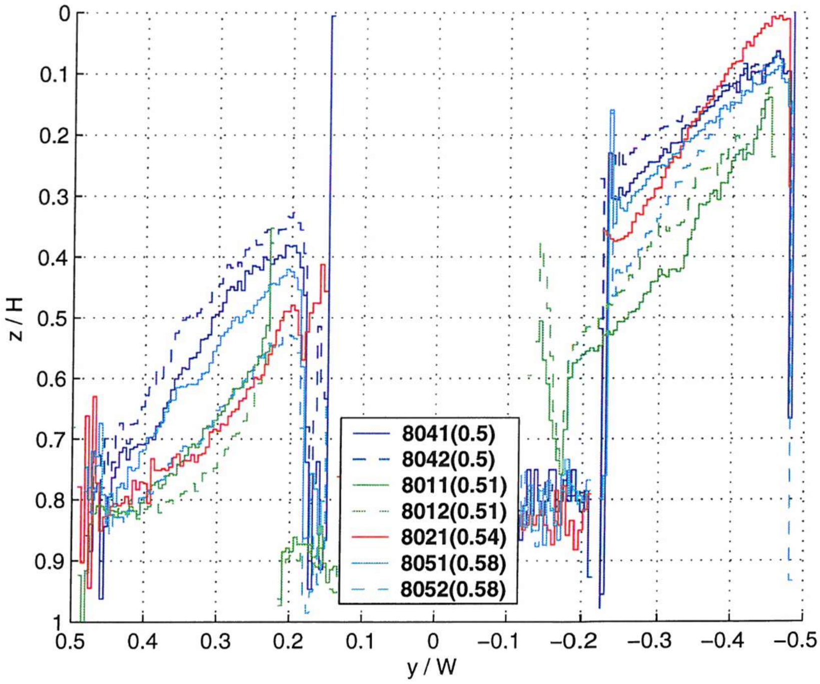

(b) $R_0 \sim 0.5$

Figure 5.5: Cross-sections of non-dimensional interface depth as in figure 5.4 for island experiments on the *SOC* platform. y is reversed for experiments 802 to 806 as reservoir densities reversed. Regions near the walls and the island are obscured, leading to erroneous data there. Note that the lower layer (as displayed) is generally banking up on the RHS wall or the island, with some vertical offset on either island side. Variation in interface position between the different time periods is evident.

For $R_0 \sim 1$ (simple channel), experiment 706 from the *SOC* platform shows a slightly reduced slope on the LHS of the cross-section of the density interface at the narrows (see green line in figure 5.4, p.111). With an island at similar R_0 (experiment 807, red line in figure 5.5(a), p.112) the flatter slope is on the RHS instead. On the *Coriolis* platform, we have two experiments again showing an increase in interface slope, experiment 15 (figure 5.2(b), p.109) and experiment 2 (figure 5.2(e), p.109). Experiment 2 has a reduced number of sampling levels which gives some bias in z toward these levels, which makes the interface slope appear overall smaller (see figure 5.2(e), p.109). Nevertheless, fluxes were found to be of similar accuracy in both experiments, as mentioned in section 4.2.1 (p.85). The presence across the whole cross-section of both density and shear layers in all five experiments described in the last paragraph also occurs in the simple channel and island cases for $R_0 \sim 0.9$ on the *SOC* platform (simple channel experiment 707, blue line in figure 5.4, p.111 and island experiment 806, green line in figure 5.5(a), p.112) but differs significantly from the corresponding simple channel case on the *Coriolis* platform. The latter case, experiment 1 ($R_0 = 0.9$, see figure 5.2(f), p.109), shows a distinctly asymmetric velocity distribution with the interface intersecting the channel floor. Note the zero-velocity contour here shows a strong bias toward the three measurement levels and is only supposed to highlight the attachment points of the shear interface at the boundaries. Therefore no value of dz can be given for this experiment.

A summary of the measured values of dz_W and R_0 for all experiments $R_0 \gtrsim 1$ is given in figure 5.6 (p.114). The application of equation 5.2 (p.110) to the relevant experiments in the form of the calculated (inferred) values of dz_W and R_0 overall confirms the relationship. With respect to the original question, this means that the island does effectively spread the flow across the channel, relative to the simple channel case with the same R_{0s}. This effectively means that an island of infinitesimal width, i.e. a flat plate in the channel centre, would not change the simple channel conditions at the narrows for $R_0 > 1$. Note that this may not be the case for $R_0 < 1$. For a finite width island, however, the interface actually attaches at different depths on each island side, leading to a steeper slope than dz_W within each 'side-channel'. The two 'channels' separated by the island are similar in the sense that inverting the z-coordinate and reversing the velocity directions on one side would give approximately the same image in both channel halves. Therefore it may at first appear as if there was one exchange flow in each side-channel separated by the island, which would require the relationship in equation 5.1 (p.110) to hold for each island side-channel separately. However, it will be shown in section 7.1.1 (p.168) that this is not the case and that the flow on both island sides is not independent for the range of R_0 analysed in this section.

In addition to the increase in dz_W with decreasing R_0, i.e. increasing rotation, there is

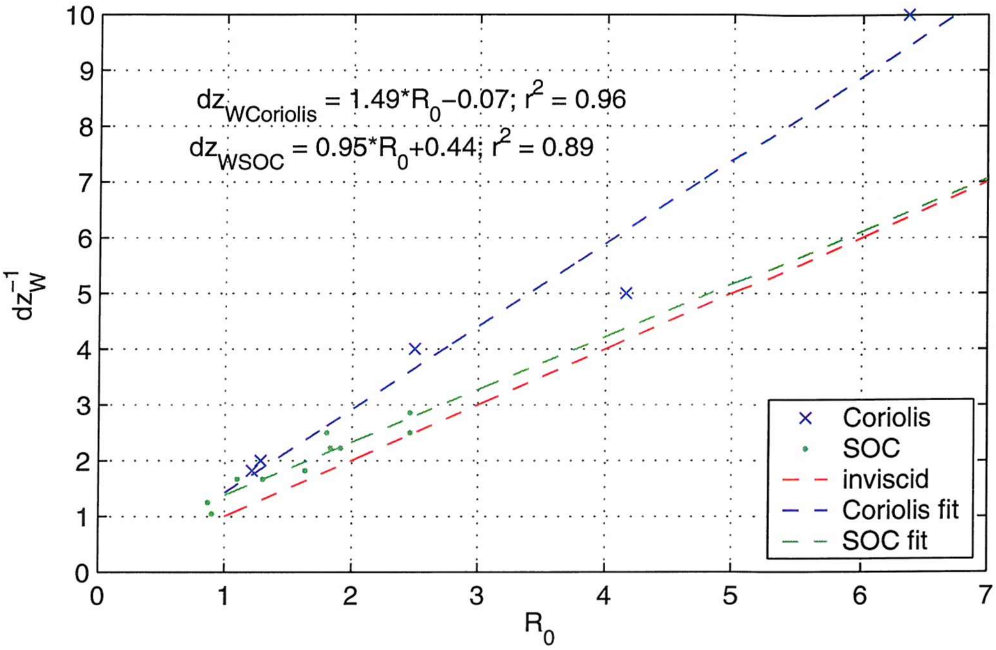

Figure 5.6: The inverse of cross-channel slope at the narrows, $dz_W^{-1} = \frac{W}{dz}$, vs. R_0. The values of dz_W^{-1} from the interface position at the narrows as presented in the figures in this section are shown as well as the theoretical (inviscid) values, expected from equation 5.2 (p.110). A reverse calculation, using the measured dz_W, can be found in table D.1 (p.203). The values generally agree with the inviscid prediction, except for $R_0 >> 1$, where viscous effects cause the interface to flatten near the sidewalls. This effect is enhanced in the island cases, which is the reason for the greater agreement of the *SOC* results (largely simple channel) with the inviscid prediction (viscous boundary layers were actually less significant on the *Coriolis* platform overall, as shown in section 3.4, p.73).

an overall decrease in along-channel velocity, u, as shown in figure 5.2 (p.109). The only exception is the island case with $R_0 \sim 2.5$, experiment 4. This change in u is associated with the variation in exchange fluxes, which will be analysed in section 6.1 (p.133). The narrows cross-section in cases with $R_0 \lesssim 1$ is studied in the next section.

5.2.2 Partially stagnant or separated flow ($R_0 \lesssim 1$)

Different regimes within each experiment can be identified, either quasi-steady or instantaneous, associated with distinct flow paths and fluxes as shown in section 4.2, p.85. This is possible despite the fact that cases with $R_0 < 1$, in particular on the *Coriolis*-platform, show much time variability and $R_0 << 1$ does not show any steady state. $R_0 < 1$ means that $R < W$ and thus the parameter dz_W is no longer practical, as the flow here may be banked onto one side or even meander horizontally. The interface in the former case may still be largely confined to a distance $\sim R$ from the wall but attaches at the wall below the surface, so that the slope is lower than an application of equation 5.2, p.110 would predict. Dalziel (1990) suggests that the relationship is still linear but the slope $\frac{dz_W}{\frac{1}{R_0}} = dz_W \cdot R_0 < 1$. However, we do not find enough similarity in the interface at the narrows for different R_0 to derive such a relationship. In this section some examples are given to illustrate the differing nature of the sloping interface comparison to the cases in the previous section. The following sections will then study the flow paths and different regimes in more detail, taking into account the flow in the whole of the channel.

Simple channel examples of the narrows cross-section for $R_0 \lesssim 0.6$ are given in figure 5.8 (p.118) for the *SOC* platform. We will term the fairly straight, strongly sloping part of the interface the "active" part from now on since the flow in other parts, at least in the lower layer, is likely to be sluggish or stagnant. It can be seen that overall the active part spans less of the channel width as R_0 decreases and is often attached to the RHS wall with an almost horizontal interface toward the LHS. The latter is due to viscous effects described in section 6.4 (p.160). This again agrees with experimental findings by D88. In the island cases, we found that this effect is reduced, with the interface more straight for similar R_0, although with a different slope on either island side; for example, experiment 803 in figure 5.5(a) (p.112) and also the edge of the core current, $u \sim \pm 0.1 cms^{-1}$ in experiment 3, figures 5.7(a) (p.116) and 5.7(b) (p.116). This can be compared to $R_0 \sim 0.5$ in figure 5.5(b) (p.112), where the interface on either island side shows an "active" and fairly flat part, similar to the whole cross-section in the simple channel cases. All these cases show differences in interface slope on either island side. This is in contrast to cases with $R_0 \gtrsim 1$, where the more baroclinic flow is associated with a similar interface slope on either island side. These cases also show more symmetry in the sense that rotating one half of the cross-section by 180^o would give a similar interface as the other half; for example, experiment 807, where this is at $\sim 0.45H$ and the schematic in figure 5.3 (p.110).

The active part of the interface widens toward the LHS in the simple channel cases during later time periods, denoted by final digits of 2 and 3 in the experiments (figure 5.8, p.118). Assuming that the lower layer current edge is represented by the density interface and current width does not change significantly in time, the cross-channel interface movement indicates that the current in the lower layer is not necessarily attached to the RHS wall. This is confirmed by the narrows current structure in experiment 8 (figure 4.9, p.100 and section 4.3.2, p.99). Changes in current paths at the narrows have been found in previous experiments by D88, who found that the lateral channel-crossing of the current oscillates along the channel in the vicinity of the narrows. Such oscillation is not found in experiments with $R_0 > 1$ as the crossing is fixed to the narrows in the simple channel cases since the flow is attached to both walls there.

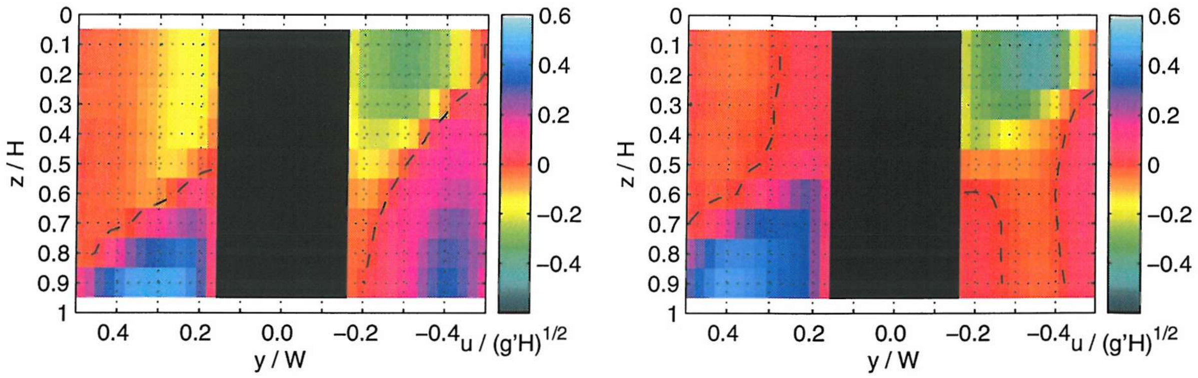

(a) Experiment 3, 'dual' regime ($R_0 = 0.67, 114 < t < 148f^{-1}$)

(b) Experiment 3 'split' regime ($R_0 = 0.67, 272 < t < 307f^{-1}$)

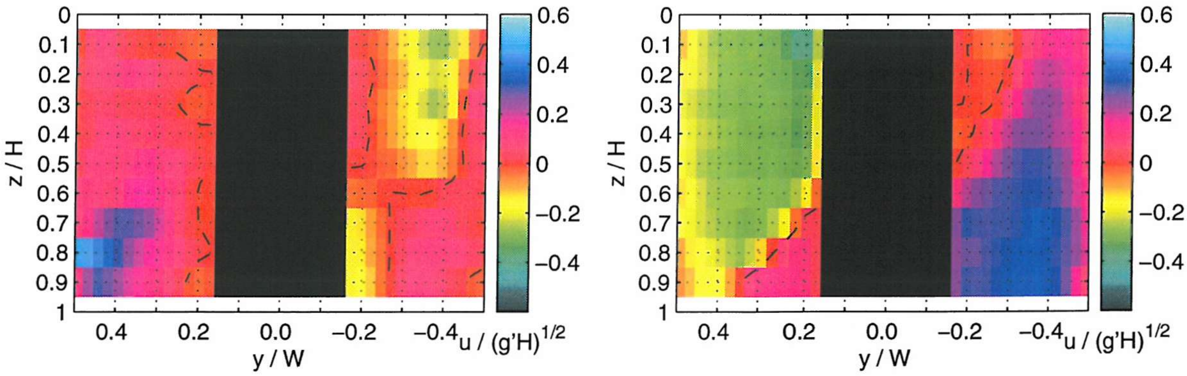

(c) Experiment 5 ($R_0 = 0.27, t = 180f^{-1}$)

(d) Experiment 5 ($R_0 = 0.27, t = 342f^{-1}$)

Figure 5.7: Along-channel velocity and zero velocity interface at the narrows cross-section during quasi-steady and instantaneous regimes for island experiments with $R_0 \lesssim 0.7$ View is downstream with respect to lower layer.Note the 'split' and 'dual' regimes in experiment 3. Experiment 5 also shows an almost split regime in both instantaneous cross-sections, but with velocities at $t = 342f^{-1}$ on the opposite island side compared to experiment 3. The shear interface is seen to deviate significantly from the edge of the current core in some cases.

In the island cases, changes in interface position are more obviously associated with changes in current paths and can be more easily identified when some velocity data is available. On the *Coriolis* platform the case with $R_0 = 0.67$ (experiment 3) shows a period of unidirectional flow on either side of the island ('split' regime) and one with more baroclinic flow on either side ('dual' regime, similar to the cases with higher R_0) in figures 5.7(b) (p.116) and 5.7(a) (p.116), respectively. The edge of the current core ($u \sim \pm 0.1 cms^{-1}$) in either case is fairly straight, spanning a similar depth range on either side of the island and being more flat in the 'split' regime than the 'dual' one. The shear interface in either case is not necessarily close to this edge, as sluggish flow leads to deviation of the interface in parts of the cross-section Note that this is different to flows with $R_0 > 1$. Experiment 803 with $R_0 = 0.73$ (figure 5.5(a), p.112) shows the interface changing position between the different time periods. The flow regime is likely to be more baroclinic on the RHS, as the interface there is steeper, which is the case in experiment 3 during the 'dual' regime. The LHS shows a steep interface only during the second time period (803_2), so that a baroclinic flow is more likely there. Variability in interface shape and slope can also be seen for $R_0 \sim 0.5$ (figure 5.5(b), p.112), although it is less obvious what the associated currents are. This variability may partly be due to the difference in the position of the interface and the edge of the core current, as also shown before in experiment 3. This becomes clearer on the *Coriolis* platform for lower R_0, as will be shown below.

Not only the interface but also the current structure becomes more irregular as R_0 decreases. Experiment 8 ($R_0 = 0.21$) shows several different types of currents crossing the channel (figure 4.9, p.100). Even without the presence of vortices, such flow could lead to a density interface as seen in experiment 709 ($R_0 = 0.34$) during the later two time periods (dashed and dotted blue lines in figure 5.8, p.118). If two layered currents cross in a thin region of the cross-section (e.g. $\sim R$ wide) the interface may be sloping in this dynamically active two-layer region. However, as in experiment 8, other parts of the cross-section may be stagnant or recirculating and not directly part of the exchange between the reservoirs, leading to an overall unevenly varying interface. On the other hand the current at times crosses in an "S"-shape, as in experiment 8 at $t \sim 340 f^{-1}$, leading to two dynamically active parts in the cross-section which may also be associated with an irregularly varying density interface slope as in experiment 709.

The island case with similarly low R_0, experiment 5 ($R_0 = 0.27$), also shows this, as can be seen in figure 5.7(c) (p.116). Near the beginning of the experiment, just after the adjustment, the flow divides similar to the split regime in experiment 3 but with some penetration of the current on the RHS (LHS) toward the bottom (surface). It can be seen that not all of the cross-section is taken up by the flow. In the middle of the experiment a flow regime

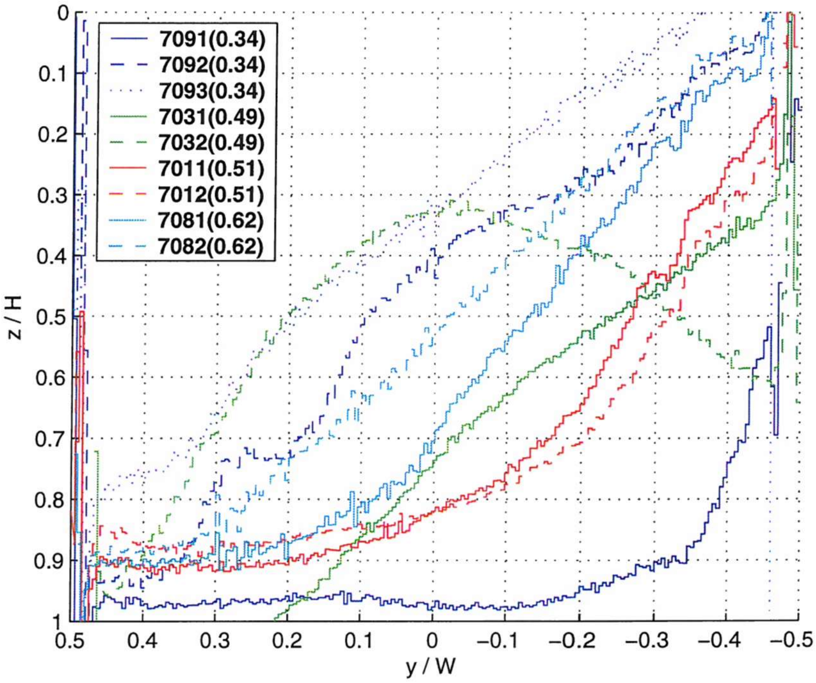

Figure 5.8: Cross-sections of non-dimensional interface depth at the narrows as in figure 5.4 for simple channel experiments with $R_0 \lesssim 0.5$. Note that 7091 is during the initial adjustment stage. The upper layer is dyed in experiment 703 instead of the lower one (all other experiments). However, this should give the density interface position in the same way as the experiments with the lower layer dyed. The initial conditions in experiment 703 are different in that the barrier is positioned at the other channel end, leading to an intruding light, upper layer gravity current. Note the interface generally "leans" on the RHS wall with the cross-channel extent of the strongly sloping part reducing with R_0, where irregularities in experiment 703 are likely due to movement of both currents and dye mixing. The differing extent of the upper layer in experiments 701 and 703 ($R_0 \sim 0.5$), suggests that initial conditions have some influence on the quasi-steady state of the flow. The different interface positions in experiment 709 are likely to be associated with across-channel movement of the exchange currents, as observed in experiment 8.

occurs that is not found in the simple channel case: it is also a 'split' regime but with mainly barotropic flow on either island side (figure 5.7(d), p.116). In contrast to experiment 3, the currents now choose the wall they would naturally lean on without an island.

5.3 Flow regimes

Having identified the conditions at the narrows for different R_0, this section briefly describes the conditions over the whole channel. To consider the whole channel volume it is convenient to use the vertically interpolated (see section 6.2.1, p.144) horizontal velocity fields and plot the absolute velocity (speed) in colour. We plot this in three vertical and horizontal slices, respectively, to make the across and along-channel variability of the shear interface as well as stagnant regions visible. To see actual horizontal flow direction we also plot a subsample of our vector fields on these slices, every fourth grid point horizontally and the nine vertical levels of the non-interpolated data.

The principal flow regime for $R_0 > 1$ is similar not only at the narrows but also throughout the rest of the channel. For example, experiment 7 ($R_0 = 4.16$) in figure 5.9 (p.120) shows the same shear interface position at the narrows as in figure 5.2(d) (p.109). However, the corresponding velocity cross-section is now vertically interpolated. Near $x = |1|$ the shear interface is close to the upper or lower boundaries and is diffused by the vertical shear in the thinner layer. The 3-d view of the shear interface in figure 5.9(b) (p.120) illustrates the two-layer nature of the flow more continuously along the whole channel. In the island case this is similar, but with the interface vertically offset, as seen in the previous sections. This is shown for $R_0 = 1.22$ in figure 5.10 (p.121). Note that 3-d figures of experiments 4, 6 and the first time-average of experiment 3 are shown in appendix C (p.197).

All the cases with $R_0 > 1$ show baroclinic flow in most parts of the channel, although some differences between the island and simple channel cases will be shown in section 5.4 (p.125). For $R_0 < 1$ the different regimes that occur during each experiment are associated with flow structures very different to the cases with higher R_0. This section describes the different regimes for experiments 3 and 5, summarised schematically in figure 5.13 (p.124).

Experiment 3 shows an alteration between a 'dual' regime and a 'split' one, where the upper and lower layers flow along the channel on opposite sides of the island. During the dual regime (figure 5.11, p.122), the main deep current is located on the LHS but a weaker current is present on the other island side, later joining near the light reservoir island tip. In this way it is more similar to the exchange at higher R_0 with both upper and lower layers coupled via the baroclinic interface.

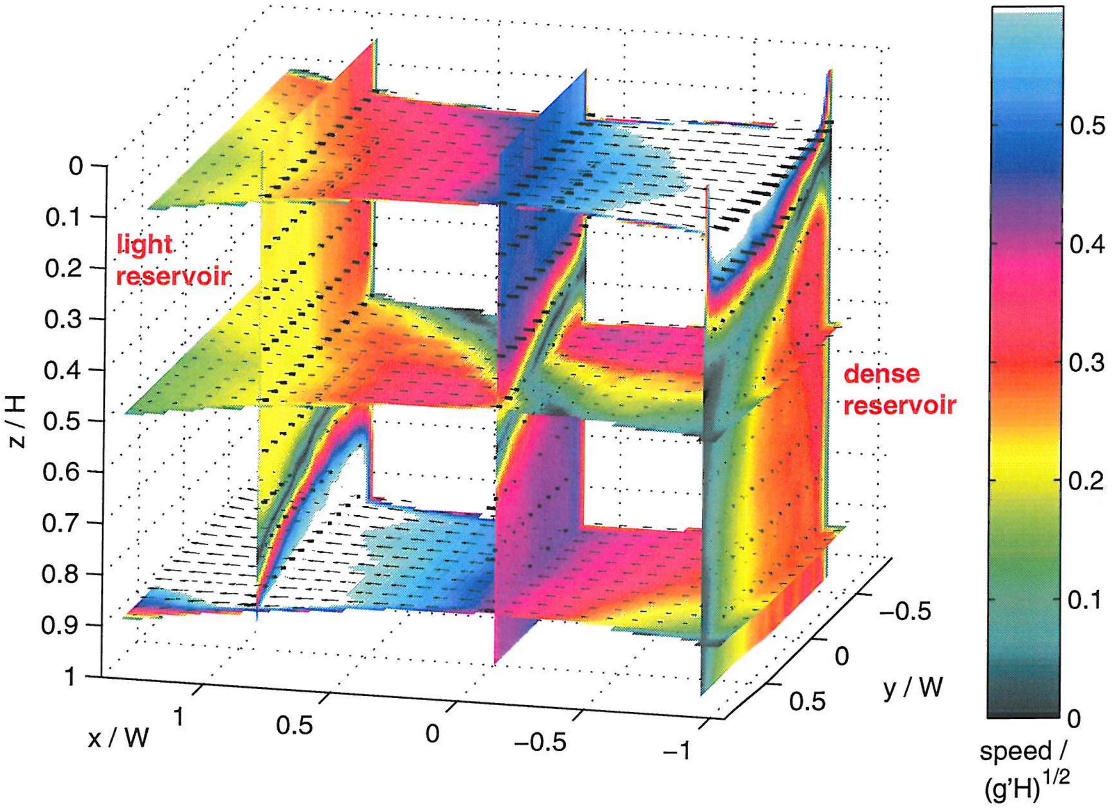

(a) Velocity vectors and speed

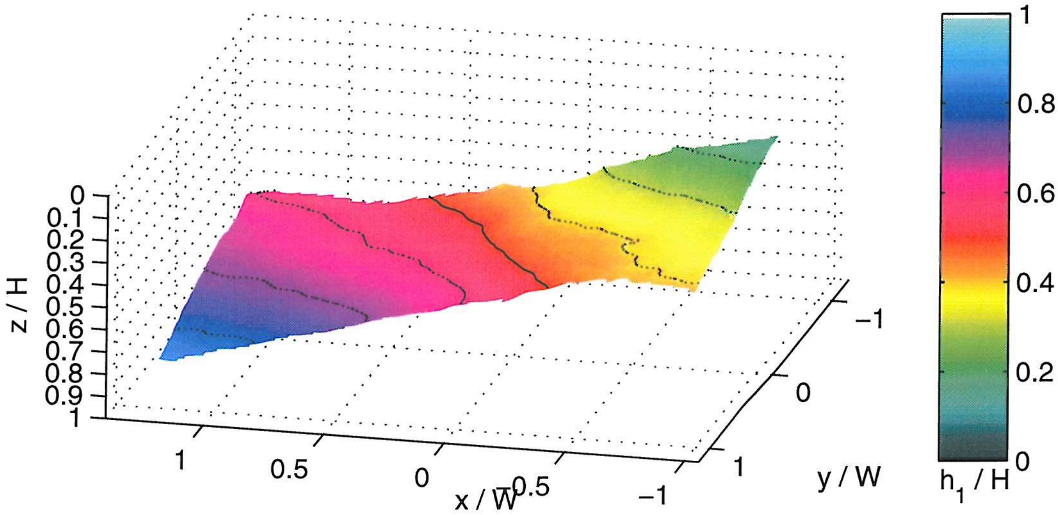

(b) Interface depth

Figure 5.9: 3-D view (from LHS, dense reservoir) of horizontal velocity vectors, speed and shear interface position for experiment 7 ($R_0 = 4.16$, simple channel) during the quasi-steady period. Note the shear interface slopes approximately linearly at the narrows and is near the top (bottom) near the dense (light) reservoir. Although velocity is still primarily in an along-channel direction there is considerable cross-channel shear near mid-depth, not present in the non-rotating case.

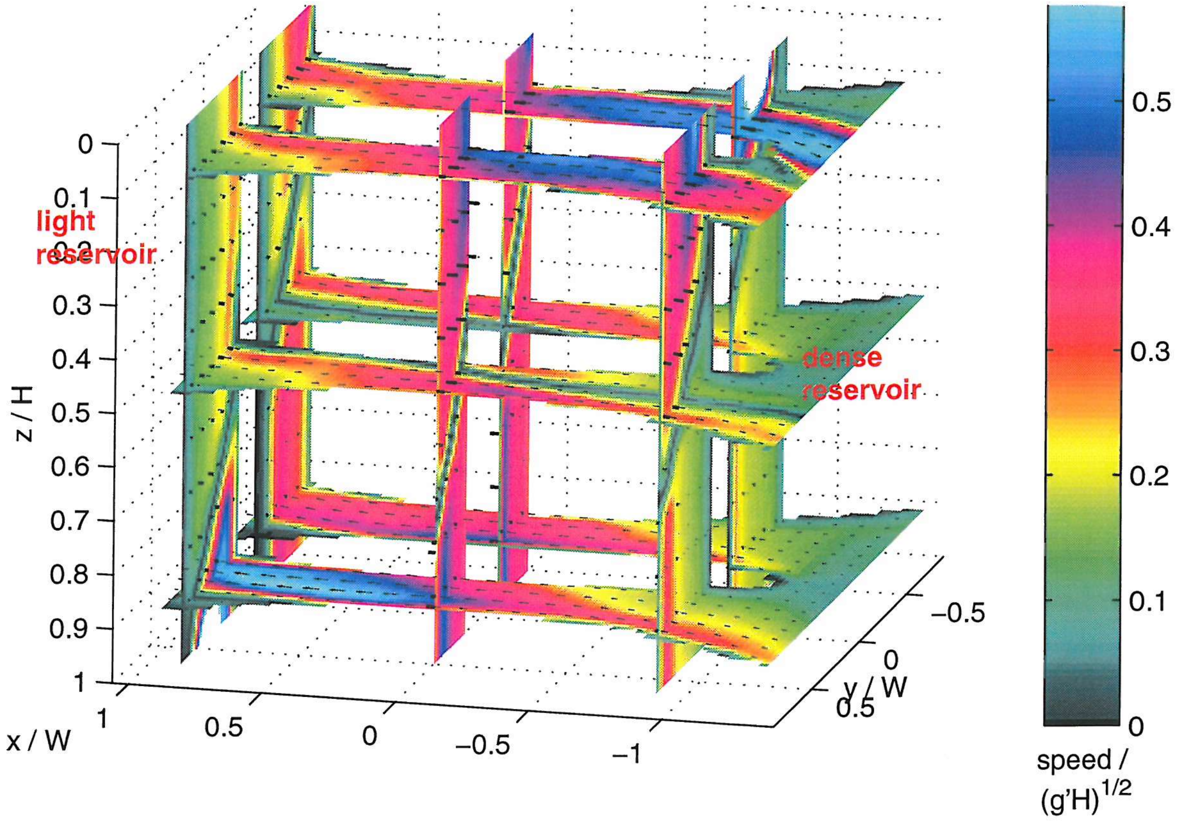

(a) Velocity vectors and speed

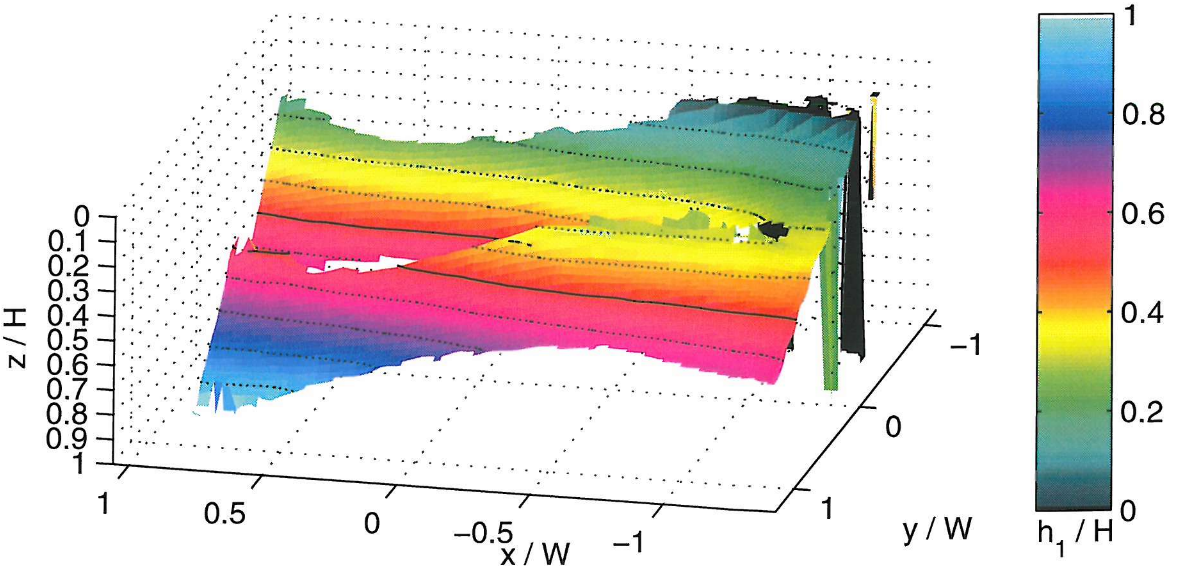

(b) Interface depth

Figure 5.10: Horizontal velocity vectors, speed and shear interface position as in figure 5.9 for experiment 15 ($R_0 = 1.22$, island) during the quasi-steady period. Note that the horizontal coordinates have been inverted as reservoir densities are reversed. Cross-channel slope of h is strong and the currents flowing out of the channel near the bottom separate from the wall to their left. However, nowhere is the flow entirely separated and stagnant throughout the whole water column.

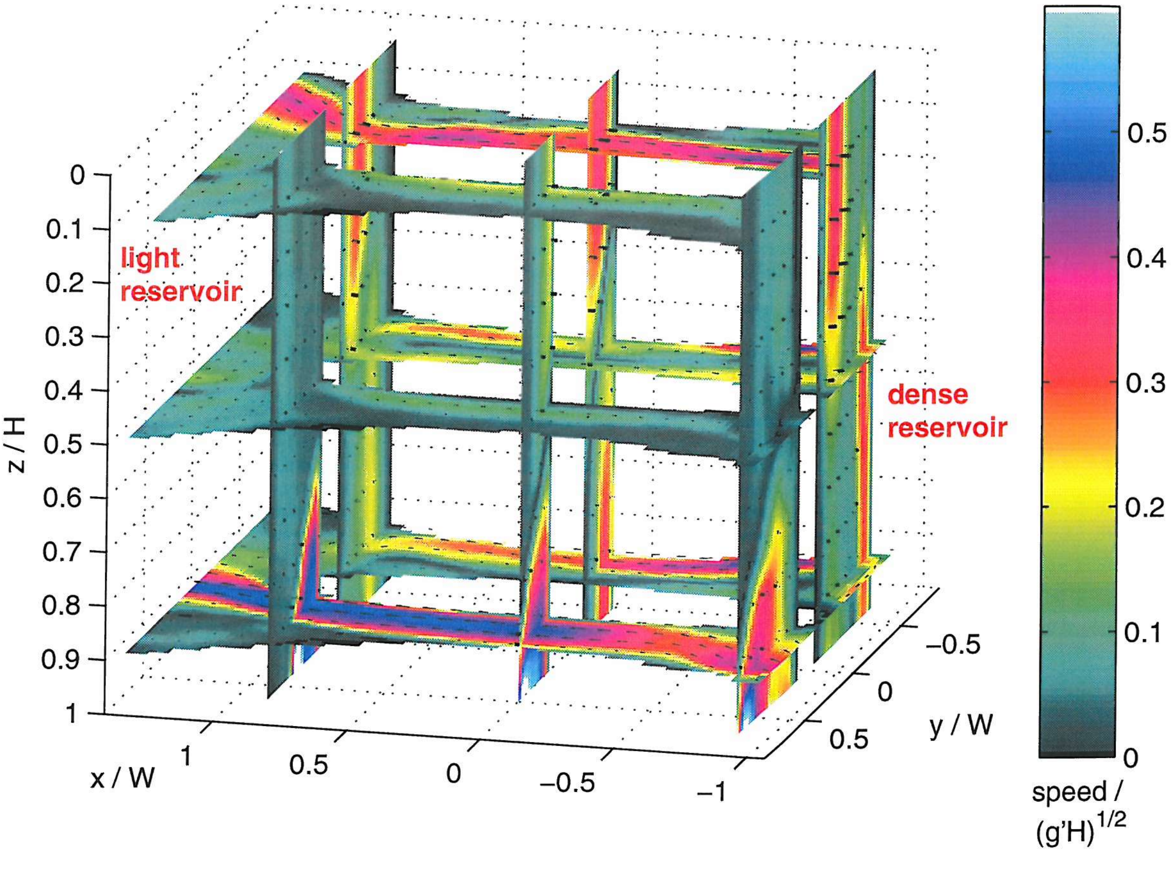

Figure 5.11: Horizontal velocity vectors and speed as in figure 5.9 for experiment 3 ($R_0 = 0.67$, island) during the quasi-steady 'dual' regime (figure 5.13(d), p.124). The shear interface is visible throughout most of the channel (black areas) with a clear two-layer flow on the RHS and a deep current with a sluggish return flow on the LHS.

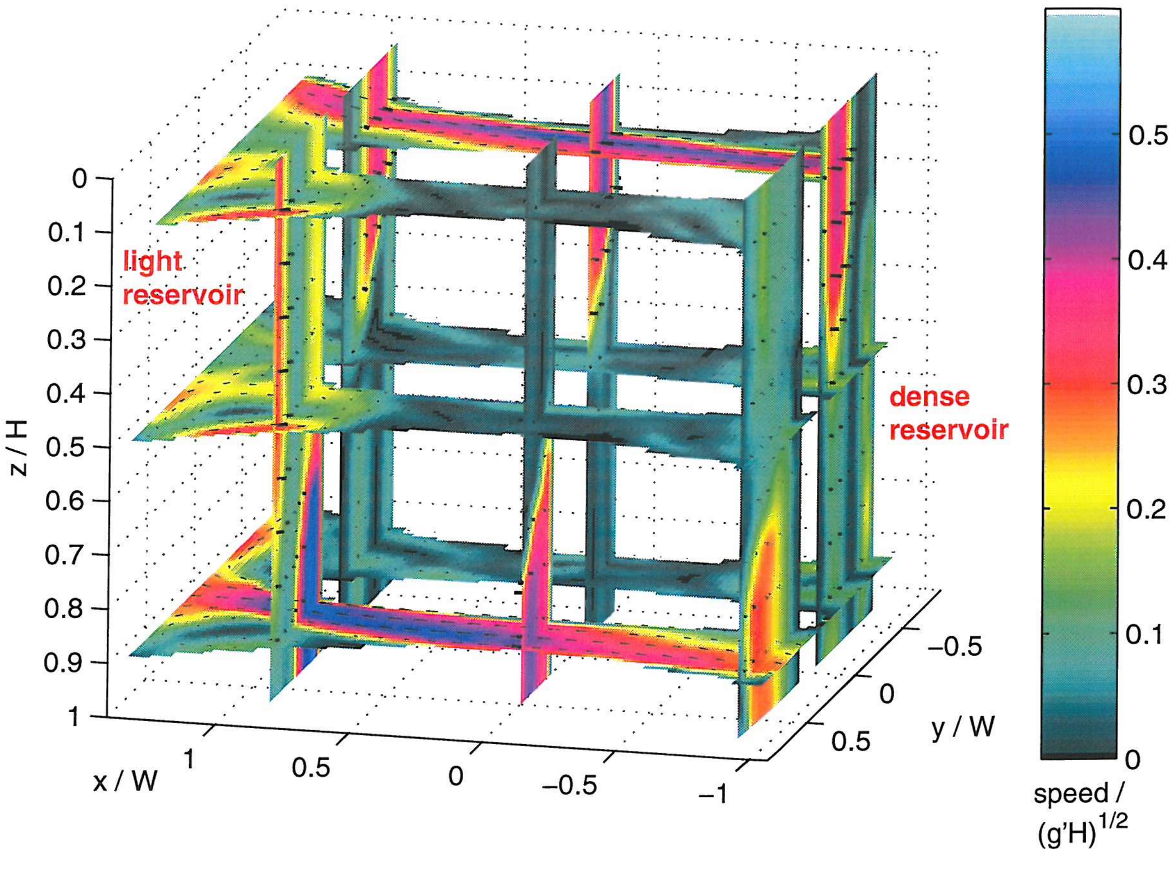

Figure 5.12: Horizontal velocity vectors and speed as in figure 5.9 for experiment 3 ($R_0 = 0.67$, island) during the quasi-steady 'split' regime (figure 5.13(c), p.124). The shear interface is not visible throughout most of the channel and the exchange flow is split between both channels.

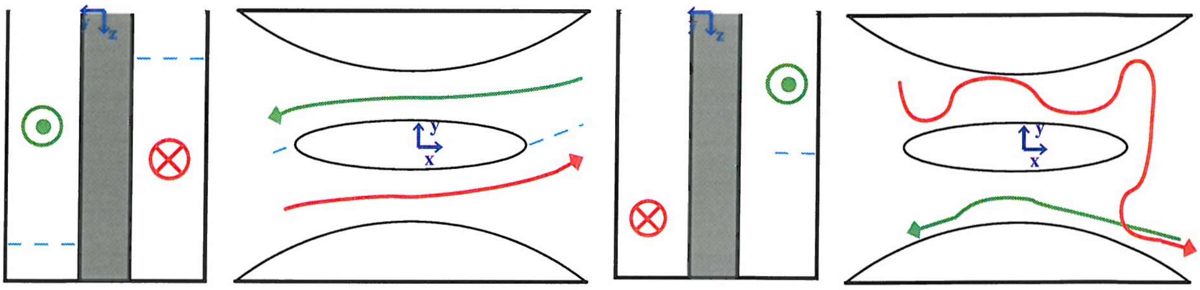

(a) Experiment 5 ($R_0 = 0.27$, $t = 342f^{-1}$), barotropic split regime

(b) Experiment 5 ($R_0 = 0.27$, $t = 180f^{-1}$), baroclinic split regime

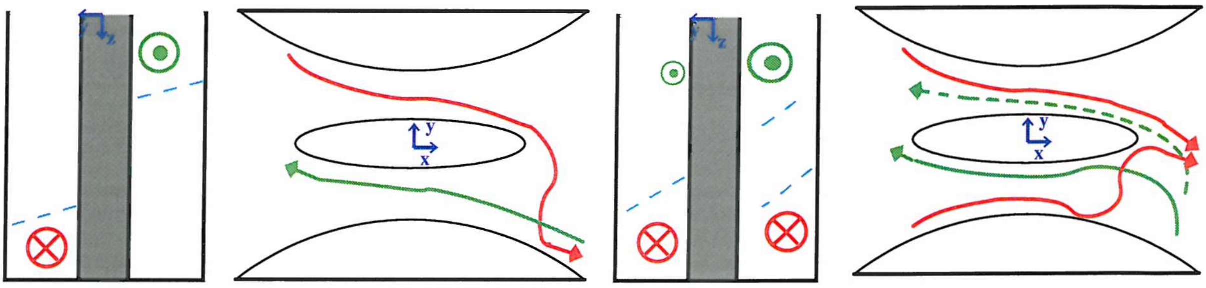

(c) Experiment 3 ($R_0 = 0.67, 272 < t < 307f^{-1}$), split regime

(d) Experiment 3 ($R_0 = 0.67, 114 < t < 148f^{-1}$), dual regime

Figure 5.13: Schematic of distinct regimes in island experiments 3 ($R_0 = 0.67$) and 5 ($R_0 = 0.27$). The red and green lines represent flow from the dense and light reservoir ends of the channel, respectively. The blue dashed line indicates a distinct shear interface or edge of the current core. Both plan views of the channel and narrows cross-sections are shown. The schematics for experiment 5 were drawn from velocity fields at all vertical levels, such as the velocity fields near the bottom and the surface in figure 4.11 (p.103). Note only the dual regime with $R_0 = 0.67$ shows a bidirectional flow on both island sides that is traceable along the whole channel (the dashed green line indicates a relatively weak flow).

The split regime is characteristic of almost entirely isolated currents on either island side, not only at the narrows but also near the island ends (figure 5.12, p.123). At least within the field of view we cannot see any baroclinic coupling (i.e. vertically overlapping, opposing currents with a clear shear interface) between the exchanging currents.

As mentioned in section 5.2 (p.108) 'split' regimes can also be seen in instantaneous velocity fields for $R_0 = 0.27$. The currents can be found either in baroclinic form, as shown at $t = 182f^{-1}$ in figure 4.11 (p.103), similar to experiment 3, or in a more barotropic form at $t = 342f^{-1}$ by choosing the other side of the island and occupying almost the entire corresponding half of the channel for all x. In the latter form, a shear region separates the largely barotropic flow between the island and the reservoirs. This barotropic split regime is entirely different to any exchange found in the simple channel for similar R_0, i.e. experiment 8. This can be attributed to the fact that for such low R_0 the current is confined to a width less than that of one island side-channel ($W_{(L,R)}$). Thus virtually none of the water would enter the channel half on the side opposite to the one initially entered, e.g. a dense current entering on the LHS may not enter the channel on the RHS. The crossing is still associated with the narrows which suggests that any hydraulic control would be located there. The current path upon entry into the channel is likely associated with reservoir conditions, but this is beyond the scope of the observations in this thesis. Associated with this regime is an exchange flux much higher than expected at such R_0, as shown in the flux time series in figure 4.4, p.90 and also the analysis in chapter 6.1 (p.133).

The occurrence of different quasi-steady states or instantaneous flow regimes for $R_0 < 1$ may be due to changing conditions near the channel ends, for example the current width relative to the distance between the island tip and the sidewall or current separation from the wall. Thus a small part of the current may be diverted onto the other island side (opposite to the one near the current entry into the channel). The change in this process initiating a switch between regimes may occur by the propagation of an internal bore but details of the transient nature of this process are beyond the scope of this thesis.

5.4 Flow separation and paths

We showed that with decreasing R_0 or increasing rotation the cross-channel variation of both the interface and velocity increases. Some trends in this behaviour were evident in the flow, in particular for $R_0 \gtrsim 1$ in a simple channel as well as with an island, the latter largely influenced by the fact that the island reduces W from W_s to W_i and accordingly $R_0 = R_{0i}$ was found to be appropriate in those cases. In this section it will be shown that away from the narrows the flow for any R_0 differs considerably between the island and simple channel cases. This manifests itself in the paths of the exchanging currents, the joining of the flow near the island tips (in the context of interdependence of both channel halves) and separation and recirculation (in the context of existing hydraulics theory). First the simple channel cases will be investigated with respect to where the flow in each along-channel direction crosses the channel and if the corresponding velocity cores are passing on top of each other (baroclinically) or side-by-side (barotropically). Then flow separation will be identified near the sidewalls. In particular, separation in the vicinity of the narrows is interesting as existing theory fails to adequately describe the flow path and channel crossing of the currents and the interface position in such separated flows (D88). Later we will discover how the answers to these questions differ in island and simple channel cases and how the island tips have a unique influence on the flow in the (cross-)channel centre.

5.4.1 Simple channel

Channel-crossing

The flow for high R_0 shown in figure 5.9(a) (p.120) shows little cross-channel velocity, where each of the two currents flowing out of the channel toward the corresponding reservoir is fairly evenly distributed across the channel. When entering the channel from the reservoir the core of the lower layer current is on the wall to its right, with respect to flow direction, whereas the upper layer entering from the other reservoir is on the wall to its left. In both cases this is the RHS wall and it is more distinct in the lower layer. It is likely that the lower layer current is actually closer to the LHS wall nearer the dense reservoir and is in the process of crossing at the edge of the field of view ($x \sim -W$).

As $R_0 \Rightarrow 1$ the crossing of the lower layer moves toward the narrows with the current core still attached to the LHS wall at $x \sim -W$, as can be seen in experiment 1 (figure 5.14(a), p.127). The upper layer current, on the other hand, now hugs the RHS wall along the whole channel and is thus overlying the lower layer on the light reservoir end of the channel but not on the opposite one (figure 5.14(b), p.127). This suggests that this current, if it crosses at all does so closer to the dense reservoir. As the barrier in this experiment is located between the field of view and the dense reservoir, both currents would then cross close to the location of the initial Rossby adjustment, i.e. the steady state would be dependent on the initial conditions. Note that once the barrier was raised on the *Coriolis* platform, this location had no significant obstruction that could represent a geometric extremum, such as the narrows or the island tips. Such dependence on initial conditions is also supported by experiments 701 and 703 in figure 5.8 (p.118).

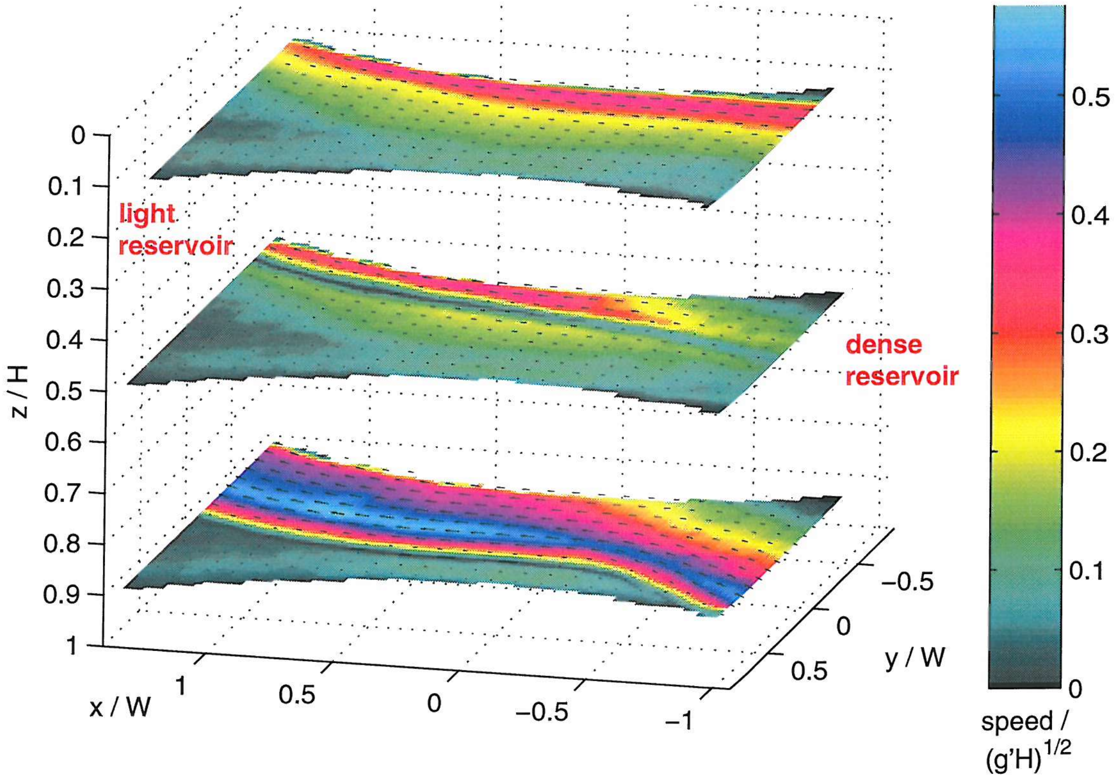

(a) Velocity field

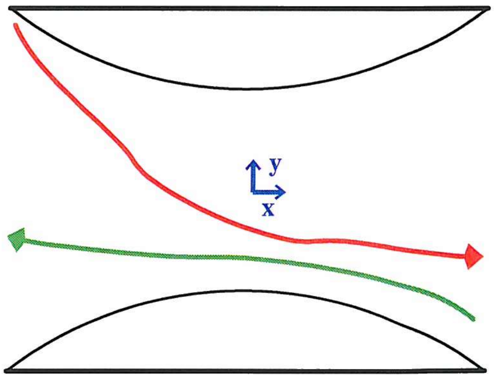

(b) Schematic

Figure 5.14: Horizontal velocity vectors and speed as in figure 5.9 for experiment 1 ($R_0 = 0.90$, simple channel) during the quasi-steady period. No vertical slices have been plotted as only three depth levels were sampled. A schematic of the core of the upper (lower) layer flow is also shown as a green (red) line. Note the asymmetric nature of the lower layer, crossing the channel near the dense reservoir and keeping to the RHS wall from there on. The remainder of the channel is occupied by upper layer flow in the dense reservoir direction with its core also located along this wall.

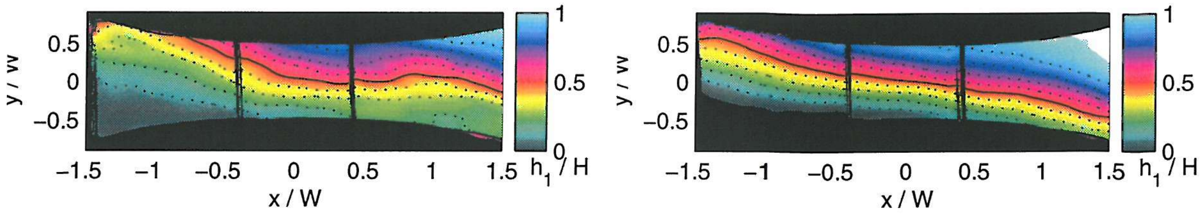

(a) Experiment 706 ($R_0 = 1.1$, $23.2f^{-1} < t < 28f^{-1}$)

(b) Experiment 707 ($R_0 = 0.87$, $23.6f^{-1} < t < 31.2f^{-1}$)

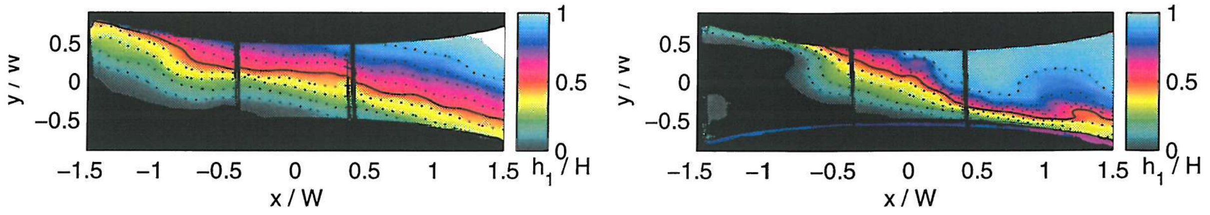

(c) Experiment 707 ($R_0 = 0.87$, $36.3f^{-1} < t < 43.0f^{-1}$)

(d) Experiment 709 ($R_0 = 0.34$, $437f^{-1} < t < 440f^{-1}$)

Figure 5.15: Time-averaged density interface depth for simple channel experiments on the *SOC* platform for $R_0 \lesssim 1$ during the quasi-steady periods. The data has been filtered with a $15x15$ grid point ($\sim 0.105x0.075W^2$) moving window median smoother to eliminate small-scale error and the parallax error but still give adequate (effective) resolution to allow comparison to the *Coriolis* experiments. Note that flow from the dense reservoir ($x < 0$) banks up on the RHS wall as it crosses the narrows.

$R_0 << 1$ lead to much thinner currents and much more meandering flow paths. This can be seen in figure 4.9, p.100 for experiment 8 ($R_0 = 0.21$), where the crossing is not necessarily in the form of just one current. Even if the near-surface and near-bottom currents both cross at the narrows they may do so with opposite cross-channel velocity, such as both crossing from RHS to LHS at $t = 598.5f^{-1}$. The current in the upper layer is $\sim R$ wide, in agreement with previous work (D88) and the crossing occurs over a distance of approximately three Rossby radii (three times the width suggested by D88). Similar R_0 on the *SOC* platform shows an interface depth field in agreement with such flow crossing in the vicinity of the narrows. The mid-depth interface contour in experiment 709 with $R_0 = 0.34$ (figure 5.15(d), p.128) crosses the channel around the narrows, which is likely representative of the current direction there if the flow is separated from the wall.

Separation

The current paths described above are associated with regions of separation, where the flow near the wall is stagnant. For $R_0 >> 1$ the only evidence of near-stagnation is close to the channel bottom at the RHS wall, dense reservoir end. The $R_0 = 0.9$ case, however, shows separation of lower layer current leading to a practically stagnant region next to this wall near the channel floor and throughout depth near the light reservoir. Almost stagnant conditions exist next to the LHS wall, from mid-depth downward at the dense reservoir end. The separated regions at the wall near either reservoir are more evident on the *SOC* platform, where the whole channel is within the field of view. Here the likely change in the size of such separated regions is indicated by the position of the attachment point of the $h = \{0.1, 0.9\}$ density interface contours: these points move toward the narrows as R_0 decreases, for example experiment 706 with $R_0 = 1.1$ (figure 5.15(a), p.128) shows the $h = 0.9$ contour at the LHS wall to be around $x = 1$ whereas it is near $x = 0.5$ in experiment 707 with $R_0 = 0.87$ (figure 5.15(b), p.128). Separation near the reservoirs is not only dependent on R_0 but also the channel shape, e.g. wall curvature, and may occur even for $R_0 > 1$. This would be in agreement with findings by D88 .

Lower R_0 leads not only to stagnation but also recirculation and vortices on the edge of meandering currents. For example the velocity field in experiment 8 at $t = 598.5f^{-1}$ shown in figure 4.9 (p.100) has two large vortices on either side of the narrows with near-surface and near-bottom currents both crossing in between. Separation and stagnation can be seen near the surface on either side of the crossing current. The density interface for similar R_0 in experiment 709 (figures 5.15(d), p.128) shows features that are indicative of the existence of such flow separation or vortices, for example the bulge at the RHS wall near the light reservoir (separation) and the circular streaks near the light reservoir (vortex).

Summary

The results in this section show that the currents from either reservoir become narrower with decreasing R_0, eventually leading to separation in the vicinity of the narrows for $R_0 \sim 1$ and leading to recirculations and vortices for $R_0 << 1$. To date semi-geostrophic hydraulics theory for the rotating two-layer exchange has assumed that the regions not occupied by the exchanging current are stagnant, because closed or recirculating streamlines would make the hydraulic concept invalid (D88). The flow expected from such theory does approximately occur in our experiments with $R_0 >> 1$ but there are significant differences in cases with lower R_0. The stagnant assumption may not be realistic for exchange flows occurring in the ocean, although such flows may show exchange fluxes of similar magnitude as the theory.

The channel-crossing of the currents for $R_0 << 1$ is found in our experiments to occur in the vicinity of the narrows, which is in agreement with experimental findings by D88. However, there is no a-priori theoretical reason for this in inviscid theory which may explain why the current crossing in experiment 1 with $R_0 = 0.9$ occurs near the initial barrier position and is thus influenced by the initial conditions.

5.4.2 Channel with island

When we look at separation and flow paths in channels with an island we have not only the sidewalls to consider but also separation from the island, in particular the tips. Therefore we separate these two cases in this thesis as they are inherently different: the walls are continuous and smoothly varying while the island tips represent discontinuities to the along-channel flow. Thus some separation would naturally occur there in non-rotating flows if there was flow only on one of the island sides (see Serra *et al.* (2002); Sadoux *et al.* (2000); Cenedese and Whitehead (2000)). Separation near either the side walls or the island leading to stagnant region near the narrows or recirculation may be relevant to the exchange with respect to wave propagation, hydraulic control and viscous effects.

Channel-crossing

For $R_0 > 1$ the current principally moves from the boundary to its left to the one on the right. Cross-channel velocity is generally low at the narrows where the walls and the island are approximately aligned along the channel, so that the overall crossing is forced by the channel geometry around the narrows. However, near the island tips the current from the left side of the island, with respect to flow direction, crosses to join the current to its right. The crossing appears more centred around the narrows in the island cases than the simple channel ones, where the crossing appeared to be closer to the initial Rossby adjustment, i.e. the barrier. For lower R_0 the crossing is not necessarily linked to the narrows. During the 'split' regime in experiment 3 ($R_0 = 0.67$) the crossing occurs around the narrows; in contrast, in the 'dual' regime the crossing is instead associated with the discontinuity of the island tips. This can be seen in figure 5.11 (p.122) where both the deep and the near-surface currents on the LHS and RHS, respectively, are separated from the sidewalls. $R_0 = 0.27$ (experiment 5) shows no obvious current crossing but a meandering current during the more baroclinic 'split' regime. Even during the barotropic 'split' regime, where the flow near-surface and near-bottom fills all of one channel half, the only crossing occurs near the channel ends, outside the side-channels formed by the island, due to the discontinuity of the island tips. Overall, the crossing is more abrupt in the sense that the distance between separation points with flow attached at the narrows decreases with decreasing R_0. If the flow at the narrows is separated, the separation points are moving further apart the more R_0 is decreased (i.e. the distance the flow is not attached to either wall increases). The findings suggests that for $R_0 < 1$ the location of the channel-crossing current in an inviscid rotating exchange is not predictable for most of the quasi-steady regimes and for all the unsteady regimes that occur.

Separation

In association with the narrows crossing, the point of flow separation from the sidewalls moves toward the narrows in a similar way as in the simple channel cases as $R_0 \rightarrow 1$. This is also shown in the theory schematic in figure 2.1 (p.32). However, the separation points are closer to the narrows for the same R_0 as the channel effectively widens more quickly with an island. For $|x| > 0$ the island increases the channel width relative to the narrows in addition to the side walls. For $R_0 < 1$, the separation regions close to the island and around the narrows are associated with an over- or under-lying current whereas the regions near the channel ends are generally barotropic. The latter regions sometimes show vortices, for example for $R_0 = 0.67$ during the split regime (experiment 3, figure 5.12, p.123) the region where the near-bottom current on the LHS near the tip is separated from the side wall shows a weak vortex that becomes stronger toward the surface. In this case the vortex may be barotropised through vertical current shear by the recirculating current passing over the stagnant region near the bottom. Vorticity may also be generated at the point of separation (e.g. Blanchonette, 1998). The implications of the channel crossing position and separation for hydraulic control of the flow will be treated in section 6.3 (p.150).

5.5 Summary

Quasi-steady (time-averaged) or unsteady (instantaneous) velocity fields of rotating lock-exchange flows have been presented in this chapter. In general, flows with $R_0 > 1$ showed regular behaviour while flows with lower R_0, higher rotation, were more difficult to interpret.

For $R_0 > 1$, cross-channel shear and interface slope increased with decreasing R_0 while separation of currents from sidewalls and the island near the surface and bottom occurred closer to the narrows. Conditions at the narrows were found to give a good representation of the exchange for $R_0 > 1$, as the flow and channel crossing of the current were centred around this location. The cross-section slope of the shear or density interface at the narrows showed a linear variation with R_0 in the simple channel cases, as predicted for fully hydraulically controlled flows by semi-geostrophic theory. However, the linear relationship was found to apply to the island cases only if taking into account the reduced width, W_i, to calculate the parameter R_{0i}. It shows that our island, on both platforms, was not only wide but also long enough in relation to R and channel dimensions to influence the exchange flow for $R_0 > 1$.

For lower R_0, such relationship was no longer appropriate, as the flow at the narrows was often separated from at least one wall. For $0.5 < R_0 < 1$, the different regimes represent the quasi-steady flow with distinct positions of the channel-crossing current. These regimes occurred in between the transient movement of the current and the interface across the channel. Unique regimes were found with an island, one where the current was split in unidirectional (but still baroclinic) flow on either island side (split regime) and one where bidirectional baroclinic flow existed in both channel halves (dual regime). These did not occur in the simple channel cases. It is interesting to note that the dual regime showed currents separated from the boundary to their left along the whole channel (e.g. from the island for the deep flow on the RHS), which is one possible reason that the main crossing occurred near the island tips, as the currents could not 'feel' the narrows on both sides. During the split regime the currents were attached to both walls at the narrows and the crossing occurred around there. This may have implications for hydraulic control, for example the control could have been located near the island tips in the dual regime. Further analysis and discussion is in section 6.3.3, p.156.

Besides a baroclinic regime, similar to the 'split' regime above, flows with $R_0 << 1$ also show a barotropic split regime, where almost barotropic unidirectional flow existed on either island side. This could be attributed to the choice of current path near the island tips, where the current near the narrows is then confined to one channel side.

For all cases with $R_0 < 1$ the flow dynamics are difficult to interpret with steady two-layer hydraulic theory. In addition, the island introduces a constraint to flow paths not present in a simple channel. This suggests the dynamics, in particular for $R_0 << 1$, can only be fully understood by studying these flows using the full non-linear equations of motion to analyse simultaneous velocity and density fields. Such simultaneous fields would also allow the study of internal wave propagation, hydraulic control and eddy dynamics in fast rotating flows using instability theory. However, despite this the following chapter shows that the exchange fluxes at the narrows show regular behaviour with the appropriate R_0 not only for $R_0 > 1$ but also for some of the unique regimes with $R_0 < 1$.

Chapter 6

Fluxes and hydraulic control

In the previous chapter the focus was on various aspects of our exchange flow utilising horizontal velocity fields at different depths within the channel. So far, this involved no assumption about the two-layer nature of the flow, except when considering shear interface height fields. It was evident that the narrows region appears representative of a two-layer exchange under the influence of rotation at most R_0 studied here. Therefore this chapter will first focus on the exchange flux as measured by the initial and final reservoir densities over each experiment's running time and as calculated from our velocity fields at the narrows cross section. This will also allow comparison of fluxes from both platforms. It will be shown that these results agree well with existing theory, bar some viscous effects, mixing and error, provided R_{0s} and R_{0i} are used in the simple channel and island cases, respectively. An exception is the very high flux during a barotropic split regime only occurring in the island case with $R_0 \sim 0.3$. The whole-channel nature of the exchange even if an island is introduced will be confirmed by analysis of the net fluxes on each island side. Further, layer quantities for the *Coriolis* experiments with $R_0 > 1$ will be used to determine the effect of mixing between the two layers and to analyse hydraulic control. Viscous effects and the influence of initial conditions are also analysed and put in the context of previous studies.

6.1 Fluxes

6.1.1 Variation with rotation

Now that time variability and various quasi-steady states have been described in the previous chapter, it is worth considering the time-averaged fluxes associated with each experiment. The theoretical estimate by Whitehead *et al.* (1974) is for the simple channel, zero potential vorticity case, where reservoirs are infinitely deep relative to the channel (section 2.1.3, p.29). In terms of R_0, this is given by

$$\bar{q} = \bar{q}_{whitehead} = \begin{cases} \frac{1}{4}(1 - \frac{1}{3}\frac{1}{R_0^2})\, for R_0 > 1 \\ \frac{1}{6}R_0\, for R_0 < 1 \end{cases}, \tag{6.1}$$

which is the non-dimensional version of equations 2.2 (p.30) and 2.3 (p.30).

Note that if the R_0 scaling in the island cases ($R_0 = R_{0i}$) is correct, this theory for simple channels should hold even for the island cases, meaning that the measured value of $\bar{q}$ should be similar to the theoretical one for a particular value of R_0, regardless if an island is present or not. The theoretical $\bar{q}_{whitehead}$ is plotted vs. R_0 in figures 6.1 (p.137) and 6.3 (p.139) together with the measured exchange fluxes from the experiments under study. Note that $\bar{q}$ is the exchange flux non-dimensionalised by 4 times the maximal non-rotating flux, giving $\bar{q} = \frac{1}{4}$ for the inviscid, non-rotating exchange (see also 3.2.1, p.45). For the *SOC* platform, all measurements are time averages for the whole experiment from reservoir density measurements. On the *Coriolis* platform, various CIV velocity fluxes are also shown, selected according to the various quasi-steady flow regimes identified in chapter 5.3 (p.119).

Non-dimensional fluxes in series 700 (simple channel, *SOC* platform) show an approximately linear increase, except for a flattening of slope around $1 < R_0 \leq 2$. Fluxes from the *Coriolis* platform show similar linearity but the flattening occurs at higher R_0. Except for $R_0 \sim 2.5$, values always stay below the predicted maximal flux of 0.25, which is equivalent to the non-rotating, inviscid, two-layer exchange flux through a flat-bottom, horizontally contracting channel (Armi, 1986; Dalziel, 1991). However, the averages over the whole of the experiments from density measurements may include significant periods of adjustment and changing reservoir conditions, as described in section 4.1, p.80. This may differ in relation to experiment running time between platforms. The influence of adjustment fluxes during the experiment on density is supported by the fact that almost all *Coriolis* fluxes using CIV velocity fields are higher than the corresponding density based estimates, except $R_0 \sim 2.5$. Experiments with an island (series 800) have measurements with $R_0 \lesssim 1$, high rotation, that mostly show fluxes similar to or slightly lower than the simple channel case.

Comparison of simple-channel to island cases on each platform separately shows a similar behaviour versus R_0, if R_{0i} and R_{0s} are used for the island and simple channel cases, respectively. This means that the R_0 scaling with a modified channel width due to the island (W_i) is indeed appropriate, as shown for cross-channel interface slope in section 5.2.1 (p.108). Note that such correction influences both R_0 and the non-dimensionalisation $\bar{q}$ in the same way. Notable is that for $R_0 > 1$, density-based estimates of the non-dimensional flux for an exchange with a laterally offset island show equal or lower flux than the corresponding cases with a central island or simple channel. This is the case for offset toward either the RHS or the LHS, represented by grey and black circles in figures 6.3, p.139 and 6.1, p.137, respectively. For lower R_0, however, the offset island fluxes appear to be equal or higher. Here this difference may merely be noted as an additional influence the island has on the flow and the reader is referred to Lane-Serff (2004) for further analysis. In dimensional terms we find that the island increases the exchange flux, at least for $R_0 \sim 1$, which can be seen in figure 6.2 (p.138). Higher R_0 do not show this likely due to viscous effects.

The slight decrease in fluxes for $R_0 \geq 2.5$ is likely due to increased viscous effects near the sidewalls for this rotation rate, which will be treated further in section 6.4 (p.160), 7.3 (p.174) and put into the oceanic context in 7.4 (p.177).

For very low R_0 ($<< 1$) a series of quasi-steady states were chosen throughout each experiment. However, the smaller R_0 the more similar are the density-based estimates on both platforms to the theoretical prediction by Whitehead *et al.* (1974), even though the flow at $R_0 << 1$ is often found to significantly deviate from the one expected in a two-layer exchange flow at the narrows, for example experiment 8 shown in section 4.3.2, p.99 and chapter 5, p.105. As shown in section 5.2 (p.108), the baroclinic exchange concept may not be appropriate at very fast rotation as the flow is dominated by moving barotropic vortices. Indeed, the CIV flux averages over the whole running time of the experiment after the initial adjustment are much larger than the theoretical limit and fall out of the generally observed relation of fluxes with R_0 at lower rotation. For this reason we use the different instantaneous or quasi-steady states presented in chapter 5 (p.105) where such vortices are not present at the narrows. This can be seen in figure 6.3 (p.139), where the region $R_0 < 1$ has been enlarged. For most fluxes, regardless of calculation method and platform, the values are below the theoretical prediction. Small differences between regimes be seen around $R_0 = 0.7$, where the dual one shows a slightly higher flux than the split, but still baroclinic, regime. Noticeable is the much higher flux during the split (barotropic) regime near $R_0 = 0.3$ (green cross with $\bar{q} \sim 1$). This is a true exchange flux with the velocity fields showing clearly that the flow passes between the ends of the field of view. It is conceivable that recirculation between the opposing currents occurs outside the latter but before the reservoirs. However, this information is not available and thus for now it is assumed that it is a true exchange between the reservoirs. This result indicates that the flux limit only applies when the flow in each island side-channel is more baroclinic, even if unidirectional with stagnant water above or below the current core. The barotropic case is also found not to occur in the simple channel case with similar R_0, indicating that the island can increase the flux considerably above the theoretical semi-geostrophic limit, albeit in a temporary, not entirely steady, state.

D88's semi-geostrophic theory also considers finite potential vorticity, provided it is constant everywhere and equal in both layers. Raising potential vorticity from zero to some positive finite value slightly decreases the flux for $R_0 \gtrsim 1$, but only by up to 3.5%. For constant depth (simple) channels the theoretical Rossby number limit at which flows with zero potential vorticity separate at the narrows and fluxes vary linearly with rotation or R_0 is given by $R_{0sep} \sim 1$. For finite potential vorticity this limit is non-linearly lowered to a minimum of $R_{0sep} \sim 0.6$ in flows with unity non-dimensional potential vorticity. However, for such cases, the theory breaks down for a certain set of values around $R_0 = 1$, the lower bound of this set given by R_{0sep}. Only if either potential vorticity is unity or R_0 is considerably less than unity, slightly closer to unity than R_{0sep}, does the theory show fluxes for realisable, but separated, flows again. In those cases non-zero potential vorticity was found to considerably decrease the flux by up to 15% with unity potential vorticity, where the flux is still dependent on rotation but now independent of the channel width. Overall it can be said that finite potential vorticity, as is certainly present in the experiments under study due to reservoir depths being the same as in the channel, may decrease the flux for $R_0 << 1$ and could be responsible for some of the reduction found in fluxes there. This reduction is relative to the zero potential vorticity limit given by equation 6.1 (p.134). The relatively low fluxes on the *SOC* platform may thus be due to higher potential vorticity in the exchange flows than on the *Coriolis* platform, although no a-priori reason for such a potential vorticity difference is obvious, as both platforms had reservoirs at the same level as the channel bottom. However, viscosity is likely to play a greater role than potential vorticity for $R_0 \gtrsim 1$. Furthermore, comparison of the specific case where the flux was found to be much higher (experiment 5, split barotropic regime) may not be valid as the exchange shows a fundamentally different flow regime, probably due to the island (see chapter 5, p.105), that may alter the semi-geostrophic assumption and the types of hydraulic control in maximal exchange as presented in D88 and Dalziel (1990).

Thus far it was found that the island-width-corrected R_0 scaling, R_{0i} in the island cases, gave a coherent variation of $\bar{q}$ with this parameter, that is fluxes are similar to $\bar{q}_{whitehead}$, bar some differences likely due to viscous effects, mixing, problems with near-boundary velocity estimates or finite potential vorticity. For $R_0 < 1$ there were distinct regimes during the corresponding experiments, where one split regime in the island case with mostly barotropic flow along the whole channel showed fluxes approximately twice as high as during the more baroclinic regimes. This shows that despite the scaling of R_0 used, there are regimes present with an island that show higher fluxes than would be the case in the corresponding simple channel case.

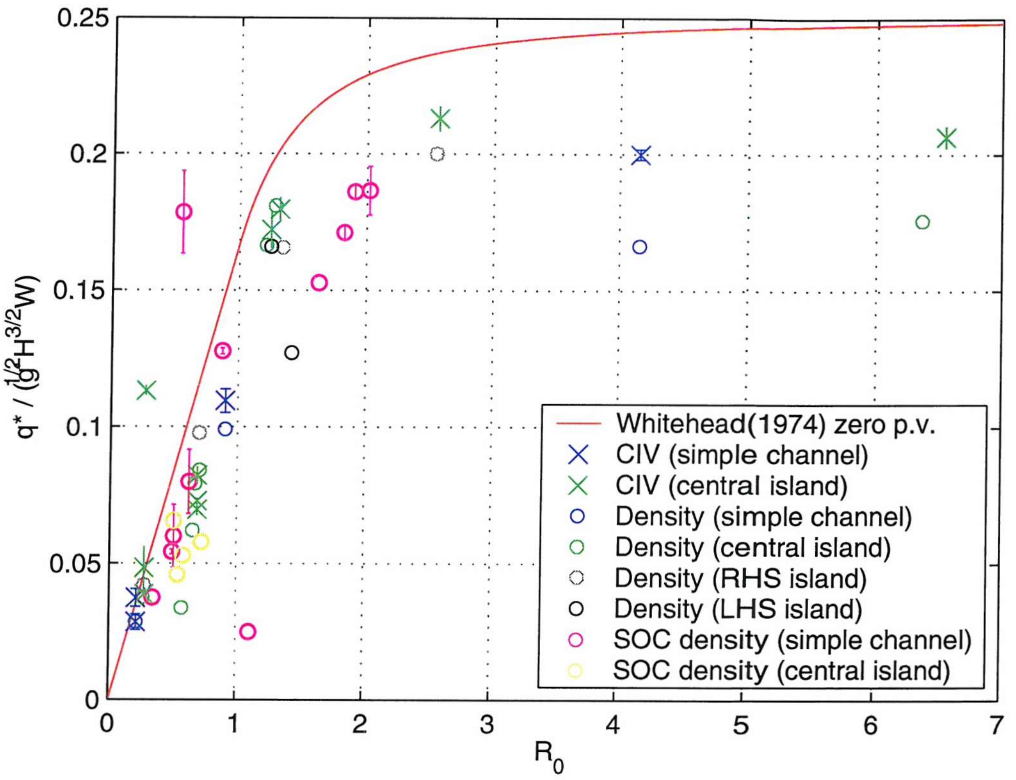

Figure 6.1: Time-averaged exchange fluxes ($\bar{q} = \frac{q^*}{g'^{\frac{1}{2}} H^{\frac{3}{2}} W}$) vs. R_0 for experiments on both platforms. Averaging periods for *Coriolis* velocity (CIV) based estimates used as outlined in section 4.1 (p.80) and presented in chapter 5 (p.105). Other estimates are from density measurements of the reservoirs before and after the experiments (both platforms). Error bars as shown; fluxes from density measurements without error bars are hydrometer-based estimates with an error $\sim 50\%$ (*SOC*) and $\sim 10\%$ (*Coriolis*) of $\bar{q}$. Note the generally linear relationship between R_0 and $\bar{q}$ for $R_0 \lesssim 1$ and the flattening of the slope for higher R_0. The CIV fluxes are generally lower than those from density and the *SOC* simple channel fluxes show lower values for $R_0 > 1$. Also shown are density fluxes for the cases where the island was shifted nearer to one channel wall (both RHS and LHS cases shown). The correction of W ($= W_i$) for the island cases is generally coherent. Inviscid hydraulically controlled, maximal exchange flux with zero potential vorticity (p.v.) after Whitehead *et al.* (1974) is also shown ($\bar{q}_{whitehead}$). This is equivalent to the extended semi-geostrophic theory by D88 and Dalziel (1990) in the zero p.v. limit.

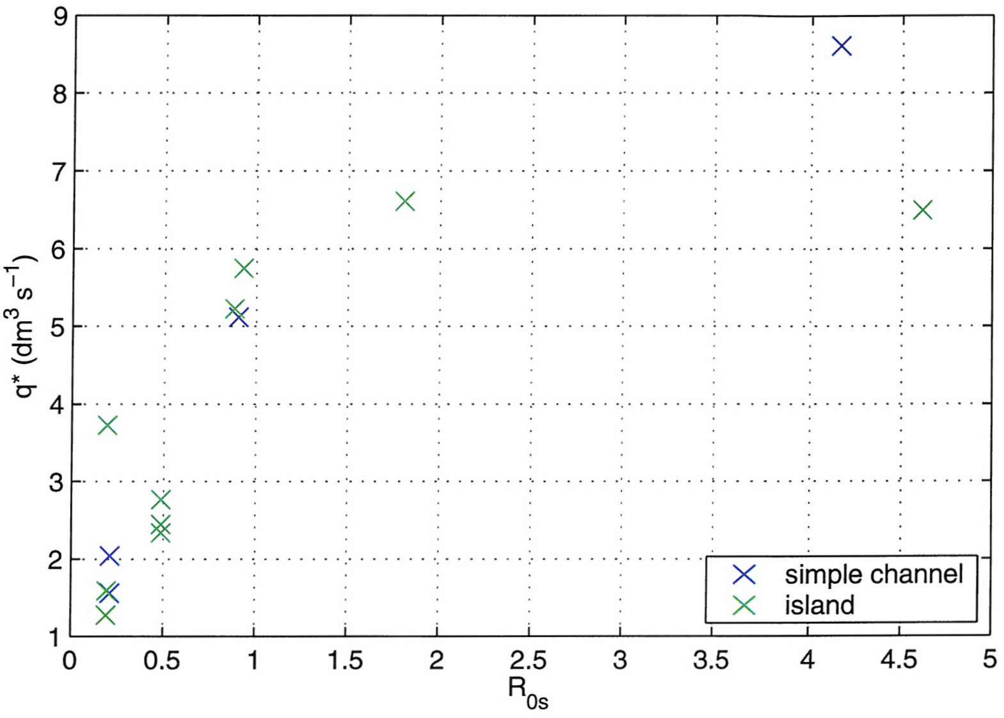

Figure 6.2: Time-averaged dimensional exchange fluxes ($\bar{q}*$) from CIV velocity on the *Coriolis* platform. Note that for the same R_{0s} fluxes are higher in the island cases than the simple channel ones, except for $R_{0s} >> 1$ due to viscous effects. The parameter R_{0s} represents mainly the influence of rotation but also includes small variations in reduced gravity, g', between experiments. R_{0s} is independent of the presence of an island, which is useful for comparing the dimensional fluxes. It can be seen that the dimensional flux with an island is higher for $R_{0s} \sim 1$ than the simple channel case. This is reversed for $R_0 >> 1$, likely due to additional viscous effects at the island.

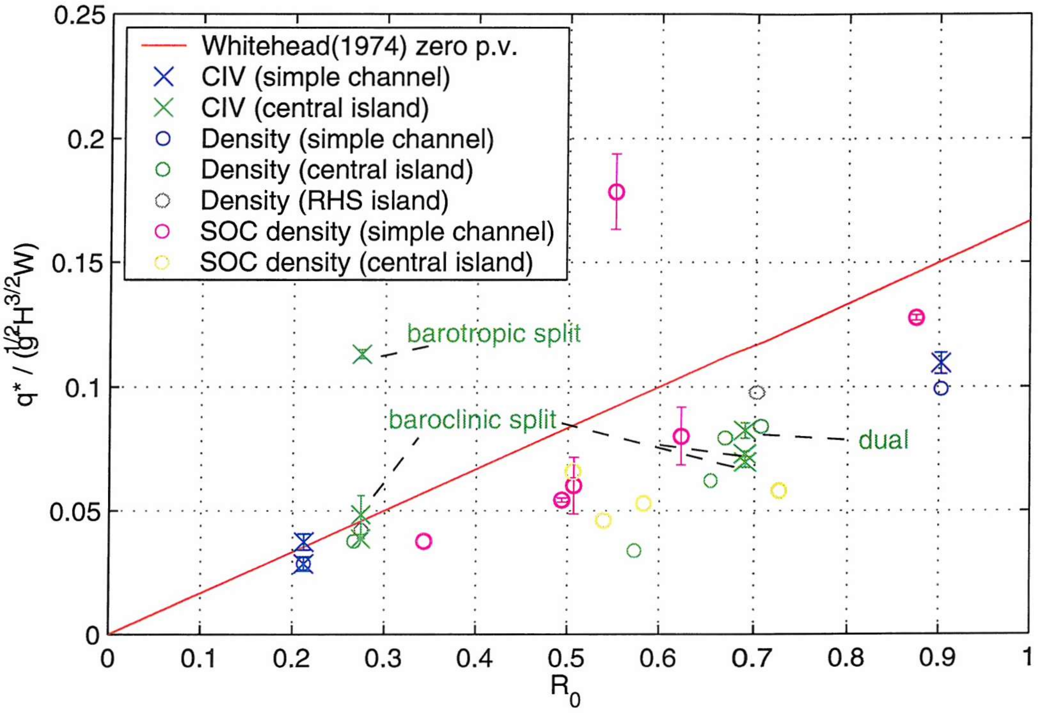

Figure 6.3: Time-averaged (non-dimensional) exchange fluxes as in figure 6.1 (p.137) but enlarging the range $R_0 < 1$. Note the distinct quasi-steady states at $R_0 \sim \{0.7; 0.3; 0.2\}$. The first set shows only small differences in flux between the "dual" regime (higher flux) and the "split" one. The second set has a flux similar to the hydraulic (zero p.v.) prediction for the baroclinically split regime but the barotropic one is associated with a more than doubled flux (barotropic split regime in experiment 5). The latter is not seen in any distinguishable regime in the simple channel case at slightly lower R_0.

6.1.2 Two separate baroclinic exchange flows?

Now that we have analysed the influence of channel geometry and rotation on fluxes, the question remains whether the flows on each island side are independent of each other. This can be tested by considering the theoretical flux as given in equations 2.2 and 2.3 (p.30) for each of the channel sides, i.e.

$$q^*_{side} = q^*_{whiteheadside} = \left\{ \begin{array}{r} \frac{1}{2}\sqrt{g'}H^{\frac{3}{2}}\frac{\frac{W_i}{2}}{2}(1 - \frac{1}{3}\frac{(\frac{W_i}{2})^2}{R^2})\ forR_{0side} > 1 \\ \frac{1}{6}\frac{g'H^2}{f}\ forR_{0side} < 1 \end{array} \right. , \qquad (6.2)$$

where $R_{0side} = 2R_0$. The width of one side-channel, if it was a completely separate simple channel connection between the reservoirs, is represented by $\frac{W_i}{2}$. Note the appropriate value here is not $\frac{W_s}{2}$, as each side-channel is considered independently. If the channels are indeed independent this flux should agree with the real exchange flux in each channel half in a similar way as the fluxes over the whole cross-section are close to the theoretical estimate as presented in section 6.1.1 (p.133). Such comparison is shown in figure 6.4 (p.142) for all the island cases, where the non-rotating value of $q_{rhs} = q_{lhs} = 50\%$. Note the difference in q_{rhs} and q_{lhs} is of similar order as the net flux across the whole section, i.e. a measure of the error in the exchange fluxes, and is always within $\sim \pm 10\%$ of half the measured total exchange flux, $\frac{q^*}{2}$. All values are given as a fraction of the total theoretical exchange flux, $q_{whitehead}$, as given in equation 6.1 (p.134). It is evident that the q^*_{side} ($q_{(rhs,lhs)}$) are close to the theoretical estimate ($q_{whiteheadside}$) for values of $R_0 > 1$ and indeed to half the theoretical estimate for the whole channel ($\frac{q_{whitehead}}{2}$), which is due to the fact that fluxes for $R_0 > 1$ are almost entirely proportional to W. However, $q_{whiteheadside}$ increasingly deviates from $q_{(rhs,lhs)}$ as R_0 decreases.The barotropic split regime does show $q_(rhs, lhs)$ actually higher than $q_{whiteheadside}$, but the net flux here and in the other split regimes is so great that the measure of exchange flux, i.e. the mean between absolute fluxes in both layers, no longer seems appropriate.

These results demonstrate that each channel half is not an independent exchange flow in the dual baroclinic regimes occurring for $R_0 \sim 1$, as the theoretical simple-channel prediction for each island side is significantly larger than the measured flux. The split regimes, on the other hand, pose the question if the overall flow can still be viewed as an exchange flow: if so, then the channels halves are also not likely to be independent, since the flow on one island side must somehow communicate to the other that a certain flux occurs. This means no net flux is overall possible, by definition, so that the flux on one island side cannot differ from that on the other; c.f. hydraulic control in section 6.3, p.150. The other possibility is that single reduced gravity layer flow on each island side somehow leads in and out of each reservoir, which slowly adjust their volume to effectively lead to an exchange, albeit no longer in the layered sense. However, if reservoir conditions were the same as for the simple channel, the flux would be given by Whitehead *et al.* (1974)'s theoretical prediction for a hydraulically controlled single reduced gravity layer flow, which is three times the value predicted in equation 6.2 (p.140) for $R_{0side} < 1$, i.e. $3q^*_{whiteheadside}$. This is clearly not the case, however, not even in the barotropic split regime, where the flux of just one layer one each island side gives $q_{side}* \sim 2q^*_{whiteheadside}$. In other words, $q^*_{side} > q^*_{whiteheadside}$, as shown in figure 6.4 (p.142).

Another way to test the independence of each side-channel is to calculate the net flux in each channel half and see if this is larger than the net flux over the whole channel width, i.e. the measure of error used in section 6.1.1 (p.133). Assuming the error is the same across the whole channel, this would show that each side-channel is not likely to represent an independent exchange flow as the net flux in a lock-exchange flow is zero, by definition. Thus each side-channel would be part of one large exchange over the whole channel.

Figure 6.5 shows the net flux for each of the channel halves as well as the net flux over the whole channel. The latter is representative of the overall error of our exchange flow measurement, as it is by definition zero in a lock-exchange. It can be seen that the net flux increases as $R_0 \rightarrow 1$, representing the influence of the Coriolis force, pushing part of the flow in each layer into the side-channel to its right, with respect to flow direction, as was seen in the interface slopes presented in section 5.2.1 (p.108). This again emphasises the interdependent nature of the side-channels as part of one overall exchange. The net flux in the split regimes is just representative of the split nature of the flow. However, the increase in net flux as R_0 decreases is not seen to the same extent in the dual regime for $R_0 \sim 0.7$. Actually for $R_0 \sim 0.7$ there is less net-flux than the cases with $R_0 \sim 1.2$, which indicates that the nature of the baroclinic exchange is more independent in each side-channel here. This is also indicated by the separated nature of the flow during the dual regime.

Overall the flux results indicate that none of the values of R_0 under study lead to separate exchange flows on each side of the island, except possibly the dual regime with $R_0 \sim 0.7$. The interdependence of both channel halves in the island cases is discussed in more detail in section 7.1 (p.168) in the light of further results from section 6.3 (p.150).

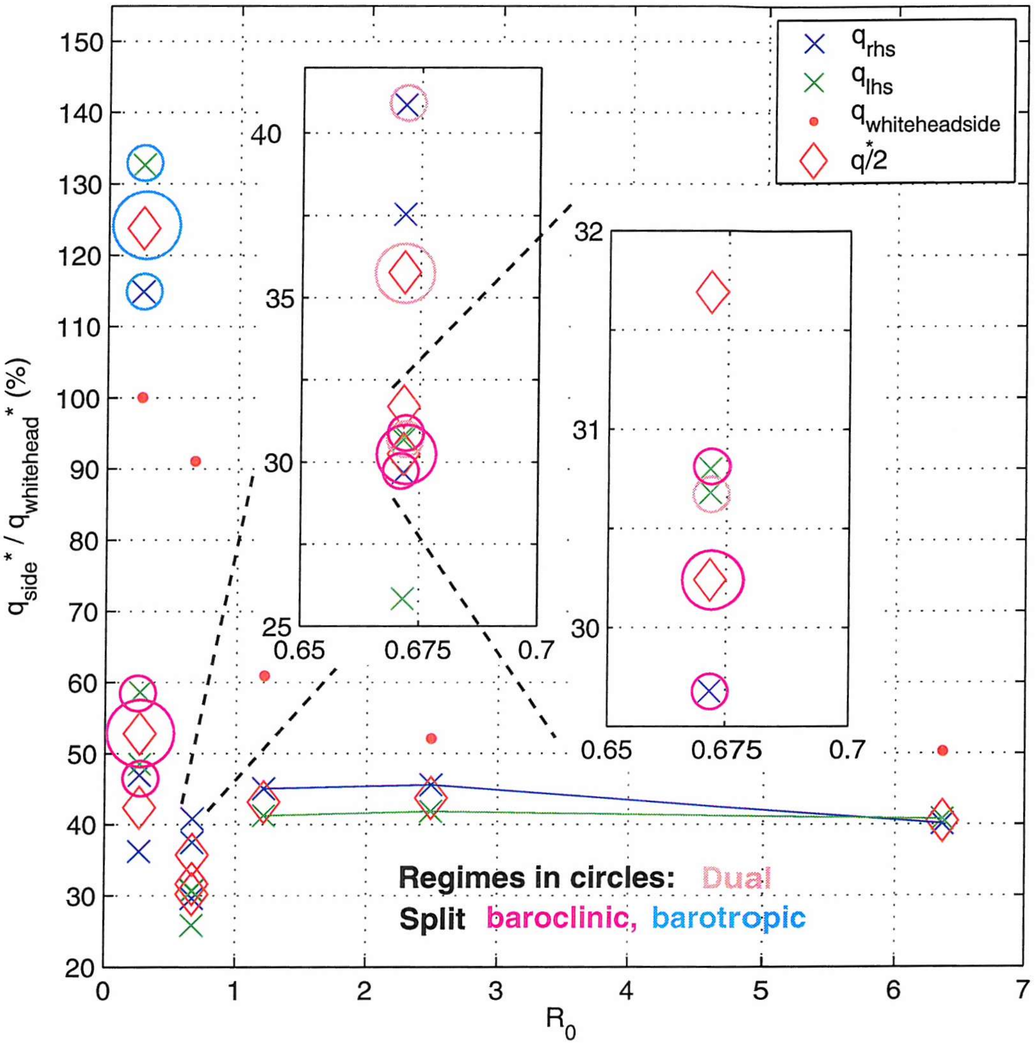

Figure 6.4: Along-channel flux on each island side, $q_{side}*$, in % of the theoretical total flux, $q_{whitehead}*$, vs. R_0. In this non-dimensional representation, a value of 50% represents half the theoretical simple channel exchange flux through the narrows section. Regimes for $R_0 < 1$ are circled as shown. Theoretical estimate for each side-channel, as given in equation 6.2 (p.140), is also shown ($q_{whiteheadside}*$). Note the relatively small difference in fluxes on either island side for $R_0 >> 1$, increasing slightly as $R_0 \rightarrow 1$, with a much lower theoretical flux throughout this range. Only for $R_0 < 1$ is a difference between both side-channels evident and theoretical estimates are closer to the measured values. In particular for the barotropic split regime the theoretical estimate is very close to the measured flux in each channel half; c.f. section 6.1.1, p.133, where the measured $\bar{q}$ is much higher than the theoretical one.

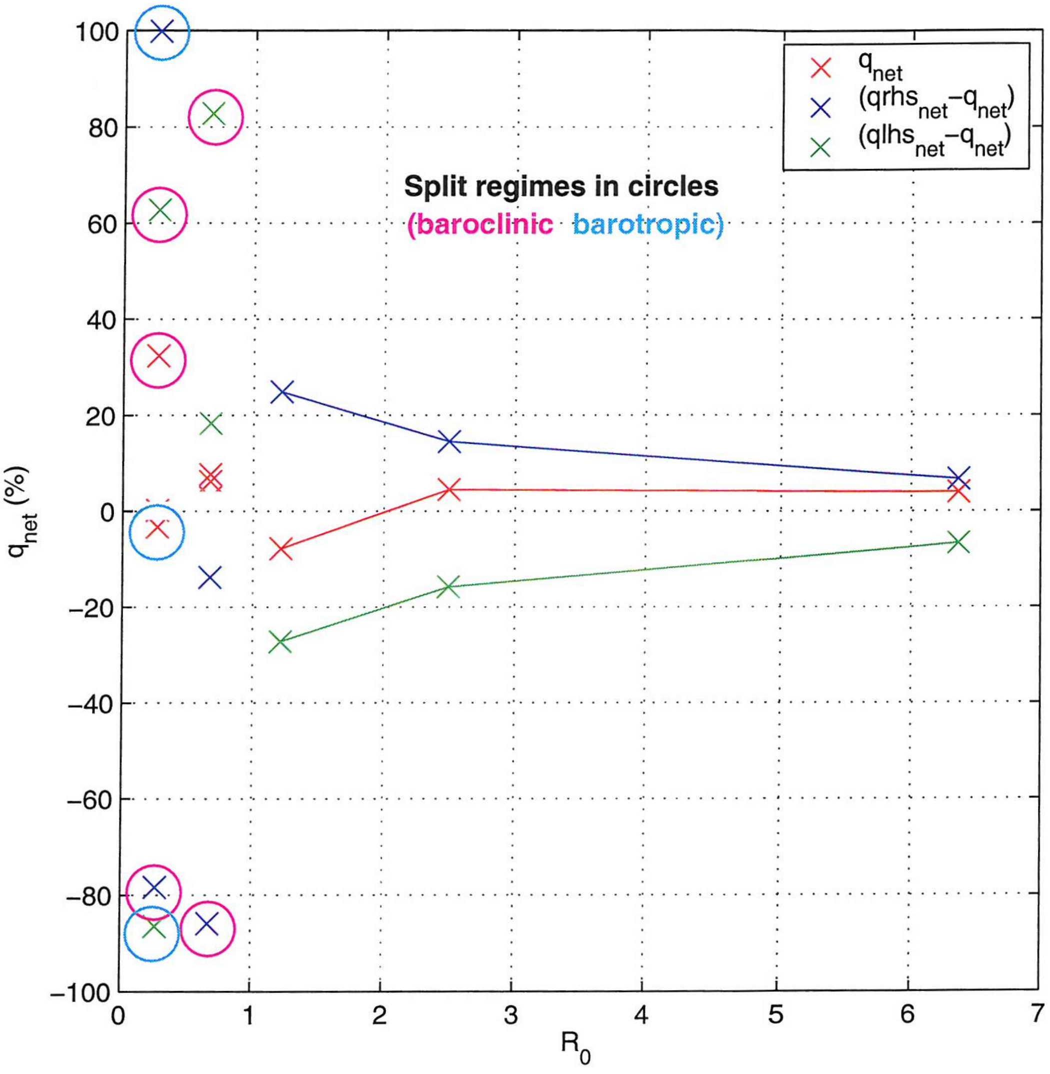

Figure 6.5: Net along-channel flux vs. R_0. The net flux is given relative to the exchange flux in the channel over which it is calculated, i.e. is divided by q^*_{side} as presented above (blue and green marks), or the whole-channel one (red marks). The value over the whole channel is representative of the percentage error in the exchange flux over the whole channel cross-section, whereas the values for each channel half are generally larger and represent true net flux through each half cross-section. Note the generally smaller net fluxes in each channel half for $R_0 > 1$ and the extremely large (absolute) values for the split barotropic regime at $R_0 \sim 0.3$.

6.2 Continuity

6.2.1 Velocity extrapolation

When looking at representative velocity profiles in experiments with $R_0 \geq 1$, we can see that a region approximately $\frac{1}{5}H$ thick is sheared. This cannot be neglected, as it has significant influence on the mean velocity in each layer, in particular where the interface is near the surface or bottom boundaries. When fluxes were presented in the preceding sections, they were calculated at the narrows section, where both layer thicknesses are of similar magnitude. This means that significant shear only occurs around the middle of most velocity profiles at the narrows. Thus the assumption of constant velocity toward the surface and bottom boundaries is approximately correct. For calculation of quantities from layer mean velocities throughout the whole channel this may no longer be correct, since the interpolated velocity profiles used to calculate the mean may show significant shear near the surface or bottom. Therefore, in addition to an interpolation of our vertical levels we require a boundary approximation at both ends of such profiles.

We use the same interpolation as presented in section 3.3.5 (p.69), where we calculated the layer depth from maximal shear. For the extrapolation a linear gradient at the surface and bottom of the profiles was chosen respectively. This is valid insofar as the 'real' boundary layers are limited by Ekman layer thickness, which is $o(1cm)$ or less in all experiments (see section 3.4, p.73), i.e. much smaller than H. When either layer depth has the minimum value ($6cm$ in dimensional units) in the highest R_0 experiments, the error would be $< 18\%$. Furthermore, in the rotating exchange, the fastest velocities and thus the majority of the flux in a layer are concentrated in the thickest region at any channel cross-section, so that we can expect a much smaller error when averaging quantities across the channel. The accuracy of linearly extrapolating the near-boundary velocities, is represented by the non-dimensional Ekman layer thicknesses in figure 3.15 (p.74).

A representative example is shown for the non-rotating case in figure 6.6 where the continuous line represents the interpolated and extrapolated data based on the CIV data (crosses) at different along-channel positions (sections at other y are similar). The extrapolation appears largely consistent except where the shear interface is close to the surface or bottom boundaries. The rotating flows show similarly shaped profiles but varying in addition across the channel.

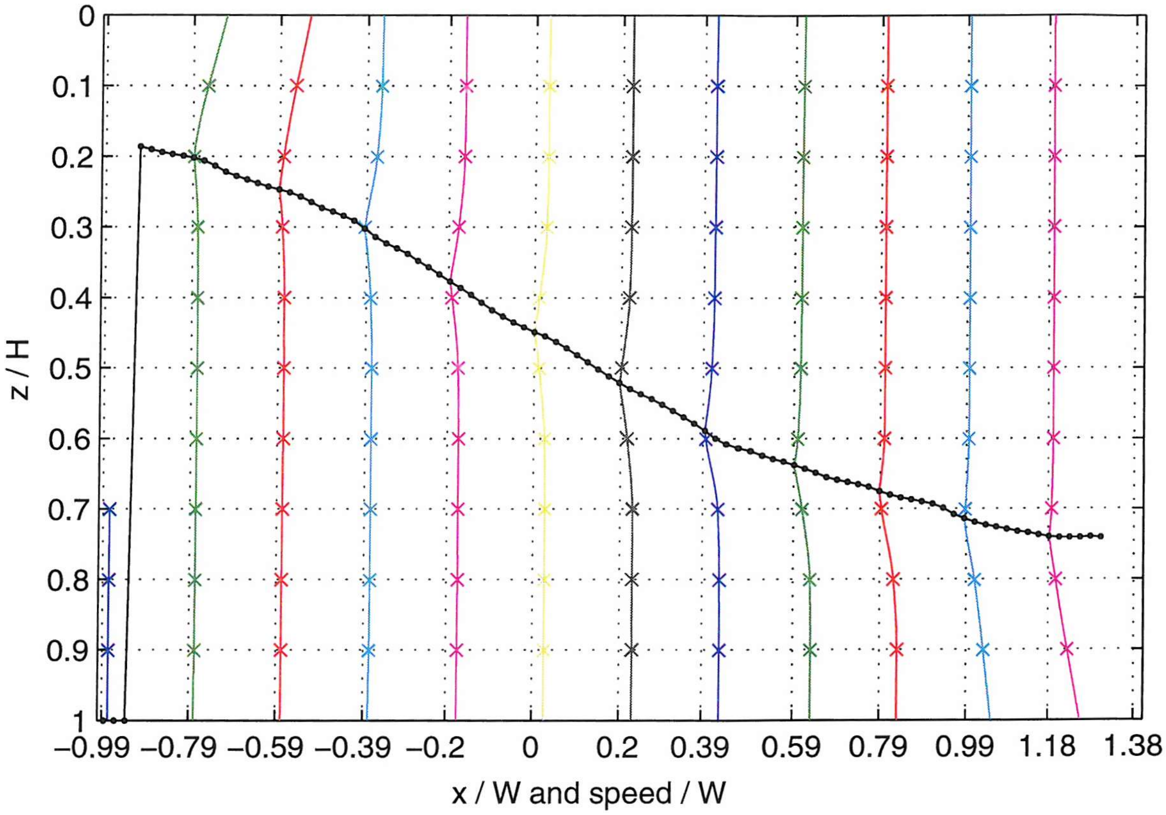

Figure 6.6: Interpolated horizontal absolute velocity (speed) at different along-channel positions for the non-rotating experiment (14); CIV data values also shown (crosses). Colours are used to distinguish consecutive profiles. Magnitudes of speed is relative to dashed grid-lines (divided by W); note that this representation is not strictly dimensionless but illustrates the shape of different speed profiles within the same experiment. Also shown is the position of the zero velocity interface (black line), which shows the vertical offset noted before. Extrapolation at surface/bottom of profiles was done using the respective linear gradients at each available endpoint. This works well at the narrows but leads to an overestimate of layer velocity in regions where the interface is close to the surface or bottom boundaries.

6.2.2 Layer flux divergence

Continuity in a steady non-linear shallow water layer satisfies the following:

$$\underline{\nabla} \cdot (\underline{u}h) = 0 \Rightarrow \frac{\partial(uh)}{\partial x} + \frac{\partial(vh)}{\partial y} = 0, \qquad (6.3)$$

where h is the layer depth, assumed to vary significantly in each direction so that the equation cannot be linearised. We can plot this equation for each of our layers to see how valid the two-layer assumption is. In a non-rotating exchange flow, we would expect some entrainment into the corresponding thinner layer near each reservoir as shown in figure 6.7 (p.147). This means that the shear interface is coincident with the density interface at the narrows but nearer mid-depth near the reservoirs (Hogg *et al.*, 2001a; Stenström, 2003). As density measurements are not available, the shear interface (h) is used to distinguish both layers in the partially viscous exchange. This is consistent with the concept of inviscid two-layer exchange flows (Stenström, 2003; Winters and Seim, 2000). If there is significant mixing between the layers, local fluxes will be significantly divergent due to entrainment across the density interface and corresponding change in the position of the shear interface.

This method does not detect if a single velocity profile contains any shear, but instead determines if this profile changes in a divergent manner between grid points. Neither does it detect uniform mixing between layers, where mass is exchanged but no volume is gained or lost by each layer. This means that only if volume, in the two-layer sense, is not conserved within each layer, divergence will be non-zero. Thus this method can detect entrainment, i.e. non-uniform mixing, near the reservoirs.

As errors in the CIV velocities become significant when evaluating difference quantities, it is useful to use the cross-channel mean volume conservation along the channel. This reduces not only the random, but also the mean-bias error due to "peaklocking" (section 3.3.3, p.58) for the rotating experiments, as u-velocity values and thus error vary across the channel. For this analysis the cross-section average of equation 6.3 (p.146) is multiplied by the channel width to get an actual flux, comparable to the horizontal exchange flux. Non-dimensionalised by the latter this is

$$q_{div} = q^{-1*} \int_{y=\frac{-W(x)}{2}}^{\frac{W(x)}{2}} \nabla \cdot (\underline{u}(x,y)h(x,y))dy, \qquad (6.4)$$

where $W(x)$ is the width of the channel at different along-channel locations. Note that all quantities here are dimensional, except q_{div}.

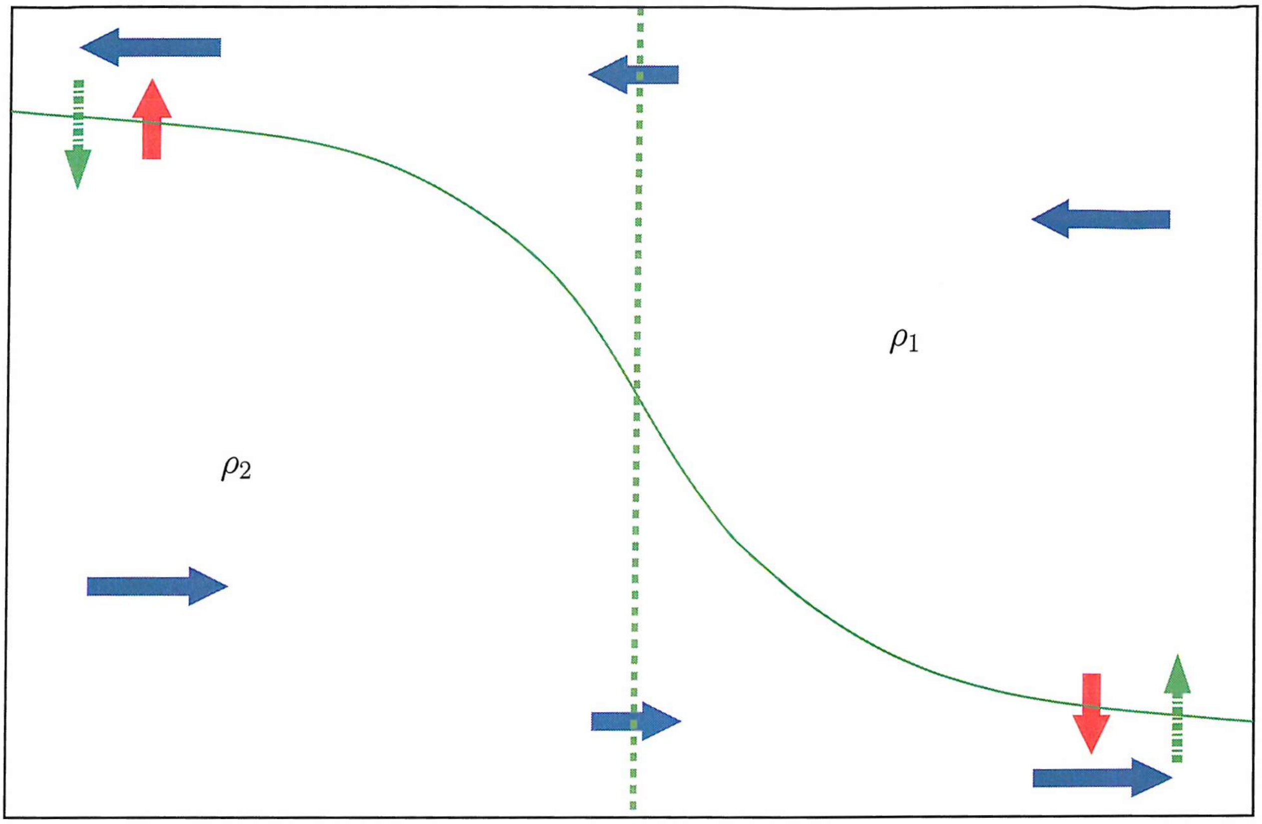

Figure 6.7: Schematic of a partially viscous exchange (fluxes represented by blue arrows) with entrainment (red arrows) at either end of the channel. The respective thinner layer will gain volume and thus displace the shear interface (green line) toward mid-depth, as shown by the green arrows (see also Hogg *et al.*, 2001a; Stenström, 2003).

All data was extrapolated as explained in section 6.2.1 (p.144), which leads to an overestimate of velocity in regions where one layer is very thin when the shear interface is close to $0.1H$ from the surface or bottom boundary. Therefore divergent fluxes are overestimated near the ends of the field of view in the layer that is very thin, i.e. the lower layer (2) near the light reservoir ($x > 0$) and the upper layer (1) near the dense reservoir ($x < 0$). Therefore it is more reliable to consider the corresponding thicker layer in those regions. In the vicinity of the narrows both layers should be equally reliable.

An alternative way to measure the entrainment is to consider continuity of horizontal fluxes along the channel. This can be expressed in a similar way as equation 6.5 (p.147):

$$\frac{q(x)*}{q*} = q^{-1*} \int_{y=\frac{-W(x)}{2}}^{\frac{W(x)}{2}} u(x,y)h(x,y)dy, \tag{6.5}$$

where the integral represents the horizontal along-channel flux through one layer at each cross-section and $q*$ the dimensional along-channel exchange flux at the narrows. Note that again all quantities are dimensional, so * have been omitted. Equation 6.5 (p.147) is deemed to give better results than equation 6.4 (p.146) as the latter contains additional errors due to differencing of the CIV velocities and also v-velocity.

The non-rotating experiment (14) shows values of $\frac{\overline{q}(x)^{*}-\overline{q}^{*}}{\overline{q}^{*}}$ that are mostly positive for $x << 1$ and negative for $x >> 1$. This indicates that the the lower layer (2) gains volume from the narrows toward the light reservoir and the upper one (1) gains flowing from the narrows in the other direction. This is consistent with the expected behaviour due to entrainment in a partially-mixed non-rotating exchange flow (see schematic in figure 6.7, p.147). The rotating experiments largely follow this behaviour near the light reservoir ($x \sim 1$) but not necessarily near the dense one. The discrepancy in some experiments for $x < 1$ could be explained if part of the flow that is missed due to the lack of data near the walls and the island in this region changes the value of $q(x)^{*}$, i.e. important flow features are contained within these regions.

Generally, the signal at $x \sim 1$ weakens as $R_0 \rightarrow 1$ for the island experiments, which could be due to the presence of separation regions near the tip or near the walls, which grow with decreasing R_0 (see section 5.4, p.125). In those regions, h is difficult to determine and could therefore induce an error in $q(x)^{*}$. However, it could also be a sign of reduced mixing as R_0 decreases. Among the other factors mentioned in section 6.1.1 (p.133), viscous effects and mixing at the interface could thus be partly responsible for the difference in fluxes from the theoretical, inviscid estimate. Indeed figure 6.1 (p.137) shows differences of $\sim 20\%$ for $R_0 >> 1$ and decreasing differences from the theoretical estimate as $R_0 \rightarrow 1$.

Overall volume entrainment does appear to be measurable in the exchange flows under study for $R_0 > 1$ but appears to be significantly reduced relative to the non-rotating case. Therefore the assumption of an approximately two layer flow is justified. This will be discussed further in section 7.3 (p.174) in the light of previous studies on frictionally influenced non-rotating exchange flows.

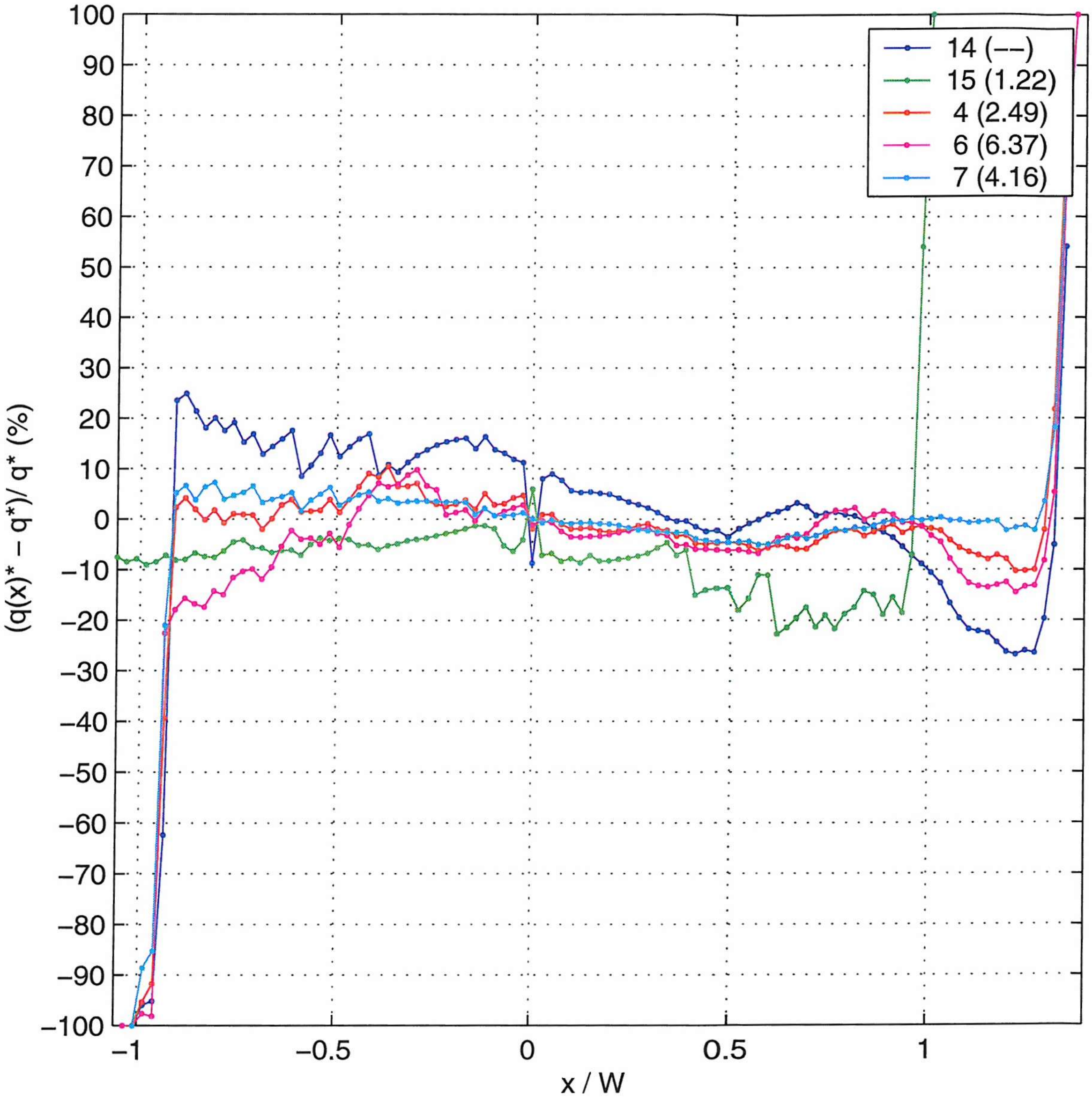

Figure 6.8: Along-channel horizontal flux as a fraction of narrows exchange flux (q^*) for different x. Experiments and R_0 as given. Note that the narrows exchange flux is also subtracted, so that a flux of 0% represents the same along-channel flux as at the narrows. This is representative of the cumulative, from the narrows outward, divergent vertical/diapycnal flux with respect to the upper layer (1), $\frac{q(x)^*-q^*}{q^*}$. Note that $q^* \equiv q(0)^*$, as used throughout this thesis. Data shown for *Coriolis* experiments with $R_0 > 1$. Only the locally thicker layer is used so that divergence values are corresponding to those of layer 1 for $x > 0$ and the negative ones of layer 2 for $x < 0$ (i.e. positive values mean layer 1 gains).

6.3 Hydraulic control

6.3.1 Non-rotating case

To test if the exchange is controlled in the hydraulic sense, the method for inviscid hydraulically controlled exchange (Armi, 1986) is applied to the non-rotating experiment (14). As reviewed in section 2.1.2 (p.25), the idea of control in such flows is represented by velocity and interface variations. Small changes in each of the layers can propagate on the interface by long, internal gravity waves. If we assume that the geometry associated with baroclinically controlling the flow is located somewhere within the channel, the flow is fully hydraulically controlled if no change in either of the reservoirs can propagate into this region. This condition can be expressed by the Froude number for each layer and combined to a composite Froude number as in equation 2.1 (p.25): $G^2 = F_1^2 + F_2^2 = \frac{U_1^2}{g'h_1} + \frac{U_2^2}{g'h_2}$, where U_i is the layer mean velocity and h_i the thickness, as before. The flow is controlled where $G^2 = 1$. If the flow is fully controlled, we expect this to occur around the narrows with $G^2 > 1$ toward either reservoir, i.e. super-critical flow, with hydraulic jumps near the channel ends to join to the sub-critical flow within the reservoirs. If both reservoir conditions during the steady period are approximately the same as near the beginning of the experiment, we expect the flow to be fully controlled.

This condition is based on an inviscid, purely two-layer model. In our flow, we actually see a considerable shear interface, spanning as much as 0.2 times the total depth (see figure 6.6, p.145). Previous studies, such as Stenström (2003), assumed the zero-isotach interface to be most representative of the hydraulic nature of the exchange. Thus the same interface depth fields, h_1, as calculated in section 3.3.5 (p.69) and presented in chapter 5 (p.105) will be used, where a rigid lid assumption, $h_2 = H - h_1$, is made as before.

The results of the calculation outlined above using the time-mean velocity field in the non-rotating experiment is given in figure 6.9 (p.151). The G^2 is approximately the same across the channel with variations along the y-axis, which can be seen more easily in the cross-channel average, $\overline{G^2}$. A control region around the narrows can clearly be seen with super-critical conditions on either side. Peaks in $\overline{G^2}$ can be seen near either channel end, indicating the location of hydraulic jumps. There are no sub-critical regions visible inside the field of view, and they are likely located nearer the reservoirs. The control region is spread around the narrows and offset toward the light reservoir. This may be caused by internal friction and mixing around the shear interface, both of which are found to separate the inviscid measure of topographic and virtual control symmetrically by reducing the values of G^2 overall in a pure lock-exchange without net flux (see Winters and Seim, 2000). Therefore each of the two

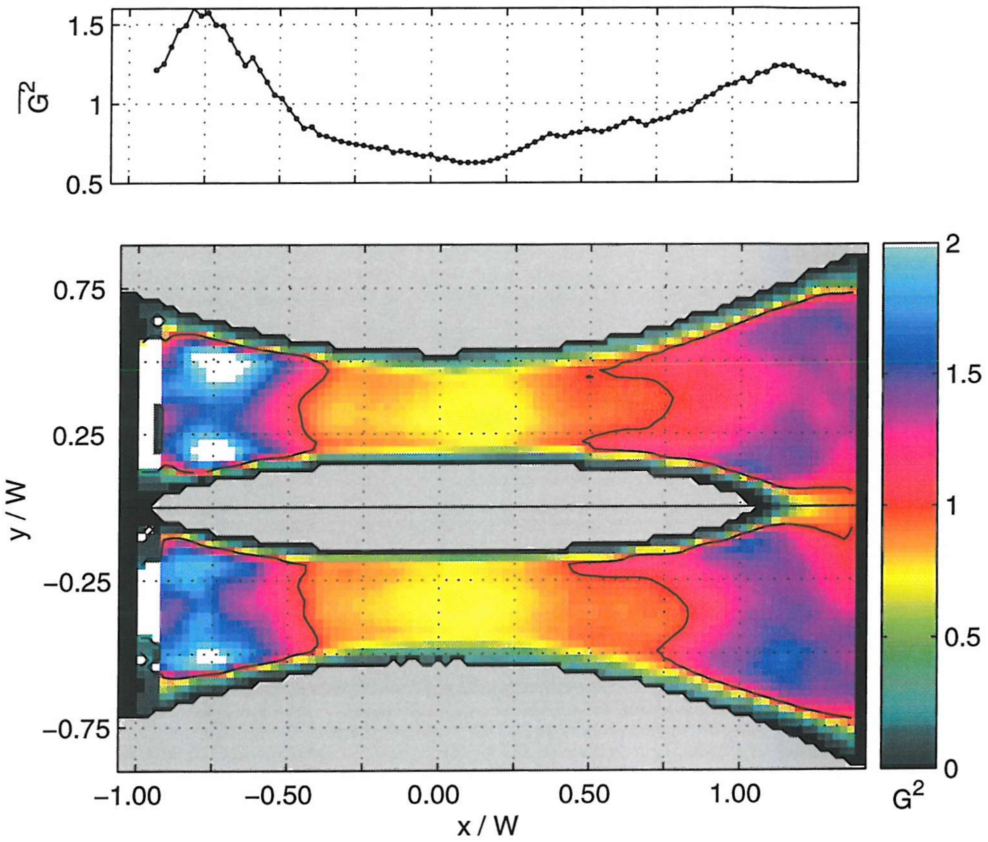

Figure 6.9: Composite Froude number (G^2) for the non-rotating experiment (14). Both the 2-d field over whole channel and the cross-channel average ($\overline{G^2}$) are shown. The values of U_i used in calculating G^2 are from vertically interpolated and extrapolated velocity profiles (see section 6.2.1, p.144). Note conditions around the narrows are sub-critical (control region), bounded by super-critical regions toward the two reservoirs, in agreement with previous work on exchange with some influence of interfacial friction and mixing. The control regions are centred near the narrows, on the light reservoir side, which agrees with the offset in h_1 due to bottom friction (section 5.1, p.105). Accordingly, G^2 is slightly lower near the light reservoir than the other end, representing increase in h_2 and reduction in U_2 there.

internal gravity wave speeds is arrested at a different location near the narrows (Hogg *et al.*, 2001a). In addition, the top and bottom boundaries differ in the experiments under study: the channel surface is a nearly free-slip boundary, only influenced by wind-drag, while the channel floor is a no-slip boundary, where the flow is expected to exert drag. A numerical model study by Zaremba *et al.* (2003) shows that the sub-critical region bounded by the controls shifts downstream with respect to the lower layer if friction at the bottom is much larger than at the surface. The shift observed in experiment 14 is small relative to the channel length $\sim 0.2W = 0.08L$, which agrees with Zaremba *et al.* (2003)'s modelling results and the shift in interface depth described in section 5.1 (p.105).

The diffuse nature of the interface may give rise to other modes of internal wave propagation, as outlined in Hogg *et al.* (2001b). However, such analysis would require knowledge of the density field which we do not have inside the field of view.

The distribution of G^2 is the same as that associated with a fully hydraulically controlled maximal exchange flow with small friction in previous studies (Zaremba *et al.*, 2003; Hogg *et al.*, 2001a; Winters and Seim, 2000).

6.3.2 Rotating control

To my knowledge, no general criteria to determine hydraulic control in real rotating exchange flows have yet been proposed without making further limiting assumptions, such as semi-geostrophy and zero potential vorticity.

Applying the non-rotating condition to the rotating experiments is only partially useful, as h_1 and thus G^2 varies across the channel, which can be seen for the simple channel experiment with $R_0 \sim 4$ (figure 6.10(a), p.153). Regions of super-critical flow are confined to the corners of the field of view where one of the two layers is very thin. This leads to a sub-critical region skewed relative to the non-rotating case, still located around the narrows but now extending toward the reservoirs. Overall it is found that this region around the narrows widens in the along-channel direction with decreasing R_0, which could be due to viscous effects at the interface similar to non-rotating flows. The interface generally spans a greater range of x in the simple channel cases as compared with the island cases. This may be explained by the ratio of the horizontal channel dimensions leading to more elongated channels and flow in the simple channel cases (c.f. separation in section 5.4, p.125). Nevertheless, the G^2 approach cannot lead to conclusive judgement about the existence and nature of hydraulic control in the rotating exchanges.

One approach to detect the location of hydraulic control is to consider the speed of internal waves at several locations within the channel. Information about the baroclinic flow

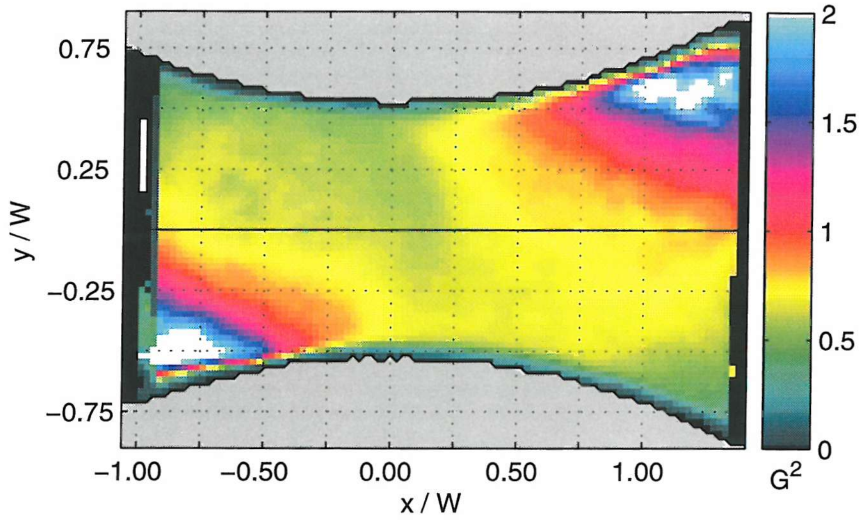

(a) Experiment 7 ($R_0 = 4.16$, simple channel)

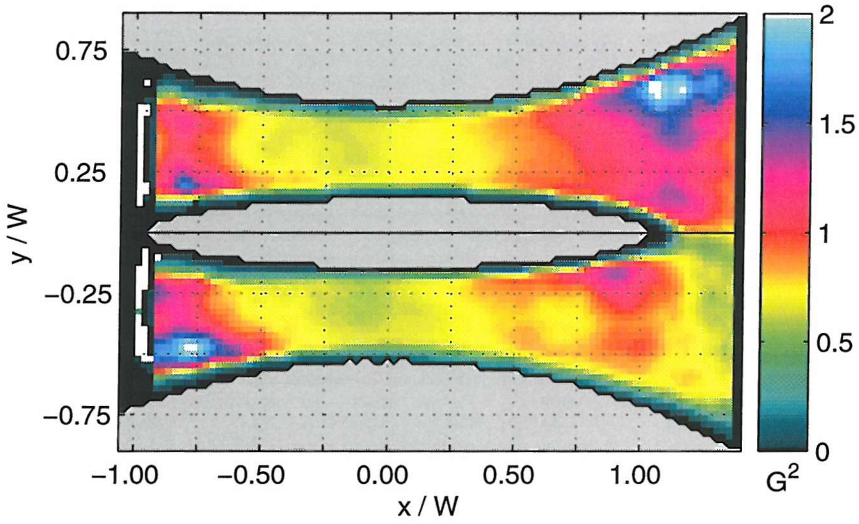

(b) Experiment 6 ($R_0 = 6.37$, island)

Figure 6.10: Composite Froude number (G^2) field as in figure 6.9 (p.151) for $R_0 >> 1$. Note the flow is locally super-critical near either reservoir where one layer is very thin, e.g. h_2 is very low on LHS near light reservoir, but sub-critical elsewhere. The along-channel offset of the super-critical regions toward the light reservoir can still be noticed. In the simple channel case, nowhere is a whole cross-section occupied by super-critical regions. Thus such a distribution says little about the propagation of rotating internal gravity (Kelvin) waves, as these have uniform speed across the channel. The island case shows super-critical conditions on the LHS near the light reservoir island tip, which could prevent waves entering this side of the channel from this reservoir end.

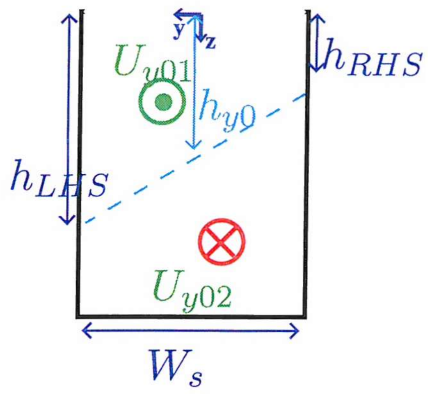

Figure 6.11: Schematic of the semi-geostrophic flow cross-section used for the hydraulic control problem. All variables, U_i and h_1 are essentially reduced to the cross-channel mean. In this sense it is similar to the non-rotating Froude number approach, where only one value of G^2 is used for each cross-section.

cannot propagate past the point where such waves are arrested. The speeds of such waves (c_i) can be calculated by considering the system of equations governing the flow, such as the semi-geostrophic equations of motion, and perturbing these. A wave-like solution to the perturbed equations, such as a Kelvin wave with constant along-channel speed in y but varying amplitude, can then be used to get an eigenvalue problem, which can be solved to obtain c_i, represented by the eigenvalues, at different locations within the channel. However, the results of such an analysis are generally difficult to interpret as one ends up with a large number of c_i and thus choice of those relevant to the hydraulic control problem is not obvious. Nevertheless, this type of analysis has been successfully applied to rotating hydraulic theory (Riemenschneider, 2004) but was found to be more difficult to interpret for more complicated flow solutions, such as numerical models of rotating exchange flows. The type of eigenvalue problem suggested for analysis would also require the calculation of velocity differences (vorticity). In the cases under study in this thesis there is a problem with CIV velocity error for such quantities, so that no such analysis is attempted here. However, a simpler approach may be used, as described below.

Pratt and Helfrich (2003) propose a method to determine hydraulic control in single or reduced gravity layer flows using energy and flux conservation along the channel. They divided channel cross-sections into a set of boxes laterally delimited by the streamlines of the flow. Both the Bernoulli energy as well as the volume flux should be conserved in an inviscid, semi-geostrophic flow along the channel. This is used together with Gill (1977)'s functional condition for hydraulic control to formulate an eigenvalue problem, which can be used to determine the location of hydraulic control points.

Extending this method to two-layer flows is not straight-forward, however, as streamlines differ in both layers and thus the boxes above and below the interface do not coincide laterally. Therefore, we consider the simplest system in which the streamlines used are located at the side wall boundaries, i.e. the box is now as wide as the channel at any x location. The boxes in both layers are of the same width, $W_s(x)$, and the along-channel flux within each box is conserved. This case is illustrated in the schematic in figure 6.11 (p.154), where the along-channel flow is geostrophically balanced by the cross-channel slope in interface depth ($\frac{\partial h_1}{\partial y}$). This means that the interface depth at the walls (h_{LHS} and h_{RHS}) can be related to the cross-channel mean along-channel velocity (U_{y0i}) in layer i, as follows:

$$h_{LHS} = h_{RHS} - 2W_s(x)\frac{\partial h_1}{\partial y} = h_{RHS} - W_s(x)\frac{f}{2g'}(U_{y01} - U_{y02})$$

For practical purposes, it is useful to use the interface depth at $y = 0$, h_{y0}, which can be related to h_{RHS}:

$$h_{y0} = \frac{h_{RHS} + h_{LHS}}{2} \Rightarrow h_{RHS} = h_{y0} + \frac{f}{4g'}W_s(x)(U_{y01} - U_{y02})$$

Pratt and Helfrich (2003) use the hydraulic functional condition to establish the location of hydraulic controls by solving

$$|m| = |\frac{\partial M}{\partial \gamma}| = 0, \tag{6.6}$$

where M is a vector of a conserved quantity and γ a vector variable. The conserved quantities in the two-layer case are the difference in Bernoulli potential between the two layers (ΔB) and the along-channel fluxes (q_i) in each layer, where

$$\Delta B = \frac{1}{2}(U_{y01}^2 - U_{y02}^2) + g'h_{y0} \tag{6.7}$$

$$q_1 = U_{y01}h_{y0}W_s(x)\ ;\ q_2 = U_{y02}(H - h_{y0})W_s(x). \tag{6.8}$$

We now have a system of three equations per along-channel location (cross-section) which can be entirely described by three variables: h_{y0}, U_{y01} and U_{y02}. The quantity $|m|$ in equation 6.6 (p.155) is the Jacobian of the vector function M and is given by

$$m = \begin{pmatrix} \frac{\partial \Delta B}{\partial U_{y01}} & \frac{\partial \Delta B}{\partial U_{y02}} & \frac{\partial \Delta B}{\partial h_{y0}} \\ \frac{\partial \Delta q_1}{\partial U_{y01}} & \frac{\partial \Delta q_1}{\partial U_{y02}} & \frac{\partial \Delta q_1}{\partial h_{y0}} \\ \frac{\partial \Delta q_2}{\partial U_{y01}} & \frac{\partial \Delta q_2}{\partial U_{y02}} & \frac{\partial \Delta q_2}{\partial h_{y0}} \end{pmatrix}, \tag{6.9}$$

where the partial derivatives refer to the variation in the along-channel (x) direction. Solving equation 6.6 (p.155) then gives values of x where the functional vanishes and hydraulic control occurs. It is also possible to look for x where at least one of the eigenvalues of $|m|$ is zero, meaning that internal waves are arrested at such x.

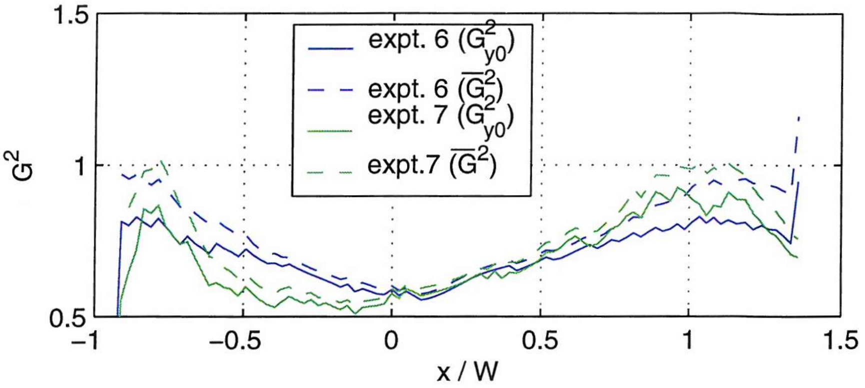

Figure 6.12: Composite Froude number from semi-geostrophic variables, G_{y0}^2, and the cross-channel mean of the G^2 fields in figure 6.10 (p.153), $\overline{G^2}$. Note the sudden drop-off near high and low values of x are due to bad interface depth data. Experiments with $R_0 >> 1$ shown for the the island (expt. 6) and simple channel (expt. 7) case, experiments 7 and 6, respectively. $\overline{G^2}$ is just critical near $x = \{-0.8; 1\}W$, i.e. the island tips. G_{y0}^2 shows generally lower values, likely caused by a departure from the semi-geostrophic assumption, i.e. non-linearities in the flow.

Using equations 6.7 (p.155) and 6.8 (p.155) with equation 6.6 (p.155) reduces to the simple equation

$$\frac{u_{y01}^2}{g'h_{yo}} + \frac{u_{y02}^2}{g'(H - h_{y0})} = G_{y0}^2 = 1, \tag{6.10}$$

which is similar to the non-rotating condition but uses a Froude number, G_{y0}^2, based on the variable averages for the whole cross-section, $u_{y0(1,2)}$ and h_{y0}. This is shown in figure 6.12 (p.156) for $R_0 >> 1$ together with the cross-channel average of the local Froude number, $\overline{G^2}$. It can be seen that the conditions are critical at two locations between the narrows and either reservoir, which agrees with the findings in the previous section. However, we found that such an approach breaks down for lower R_0, likely due to the deviation from the semi-geostrophic assumption, i.e. non-linearity in the y-component of the momentum equations. This is also represented in the difference between $\overline{G^2}$ and G_{y0}^2, which would be equal if non-linear effects were not present.

In the following section we will put hydraulic control in the context of flow features around the island tips. Further discussion of hydraulic control can be found in section 7.2 (p.172).

6.3.3 Island tip circulation

To look at the separation from the island, the focus will be on the island-tip region, the width of the two joining currents and the extent of the separation region. This is important as it represents the conditions of joining between the two currents from either island side (flowing in the same directions) and the conditions at the discontinuity of the tip. This region represents the link between both channel sides and is thus important with respect of the independence of both channel halves when an island is present, e.g. with respect to hydraulic control by the propagation of small amplitude baroclinic gravity waves in a rotating fluid (e.g. Kelvin waves).

The separation is to some extent evident in the h fields (e.g. figure 5.10(b), p.121) where the interface height is locally higher and not as smoothly varying near the island tip as elsewhere. It highlights the separation where there is an almost stagnant region present near the bottom in between the two currents joining nearer the reservoir. Because of this it was found difficult to determine a clear shear interface in this region, which is why mainly velocity fields will be considered in this section.

A close inspection of the island-tip region on level 9 (level 1 for experiment 15) is shown in figure 6.13 (p.158) for each *Coriolis* experiment, highlighting the change in the separation region between the currents from either island side as R_0 is decreased. Note that for experiment 15 reservoir densities were reversed so that level 1 is shown. For high R_0 (figure 6.13(a), p.158) we see only a very small region between the currents that is weakened but not yet entirely separated. The currents gradually join after passing the island tip. As $R_0 \rightarrow 1$, however, the joining region of the currents extends toward the reservoir downstream with respect to the currents (figure 6.13(b), p.158 for $R_0 = 1.22$). A clear separation region is noticeable. It is located toward the narrows on the RHS, next to the island, and shows some recirculation, even in the time averaged velocity field, so that it is not due to a moving vortex. For $R_0 = 1.22$ it extends to $z \sim 0.4H$ below which velocity is generally in the other along-channel direction near the tip.

Separation in the lee of obstacles has been investigated by Blanchonette (1998). He modelled the two-layer, unidirectional flow past a cylinder in an otherwise unbounded space. Vertical shear was found to increase the size of the separation regions. However, the study used a Rossby number scaling based on the mean flow velocity in both layers and the cylinder radius, which means that higher R_0 actually increases the separation. Note that he assumed $R_0 << 1$, i.e. geostrophic flow within each layer. The separation region was also found to be much smaller in the faster moving layer, which is attributed to a β-effect due to the sloping interface. Blanchonette (1998) also found that the separation region in the slower layer is stretched, thinner and longer toward the downstream direction, by an increase in the inverse of our R_0. Using the cylinder diameter as the horizontal length scale he termed this a "Froude number" and explained the results by the advection of vorticity generated near the obstacle by long Rossby waves. In our experiments, the layers are flowing in opposite

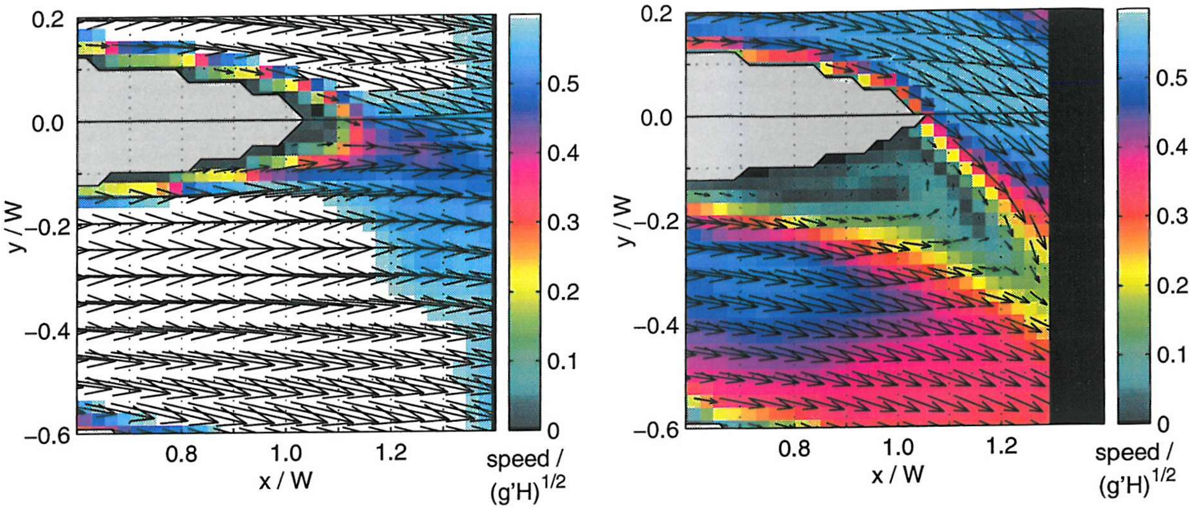

(a) Experiment 6 ($R_0 = 6.37, 9f^{-1} < t < 22f^{-1}$)

(b) Experiment 15 ($R_0 = 1.22$, $108f^{-1} < t < 140f^{-1}$)

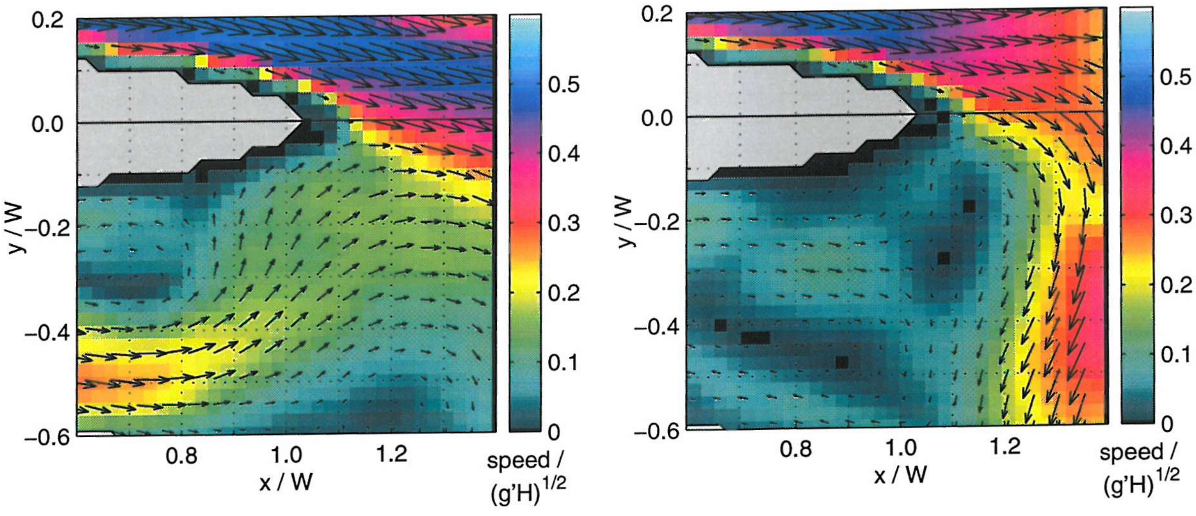

(c) Experiment 3 ($R_0 = 0.67$, dual regime, , $114f^{-1} < t < 148f^{-1}$)

(d) Experiment 3 ($R_0 = 0.67$, split regime, $272f^{-1} < t < 307f^{-1}$)

Figure 6.13: Local horizontal velocity field in plan view on near-bottom level 9 in the vicinity of the island tip ($x \sim 1$). Note near-surface level 1 is shown for experiment 15 as reservoir densities are reversed. The white areas represent speed above $5cms^{-1}$. The very small zero-velocity (black) area that surrounds the island tip was hidden from camera view by the island; however, we do expect velocity there if the surrounding region does not show separation. Note that with increasing R_0 the joining of both currents from either island side is moved toward the reservoir and the separation region becomes wider and moves toward the RHS. Such a region does not exist in the simple channel cases.

directions, so that the separation regions are at opposite ends of the island. Furthermore, the island is different to the cylinder geometry and the flow is overall forced by buoyancy and likely to be hydraulically controlled and forced by geometry to cross the channel. Nevertheless, it is interesting to note that the decrease in R_0 itself, an increase in Blanchonette (1998)'s Froude number, could be one reason why the separation region at the tip stretches toward the reservoir. Note the interfacial shear actually decreases with decreasing R_0, which may be due to the fact that the horizontal component of this shear increases relative to the purely vertical shear. However, for $R_0 \sim 0.7$ such a separation region is no longer obvious and other processes must occur guiding the flow near the tip.

Figure 6.13(c) (p.158) shows experiment 3 ($R_0 = 0.67$) during the dual regime. We see that the separation region near the bottom is no longer present and the slow current from the RHS is joining the faster one from the LHS at the tip. However, the deep current in the RHS part of the channel is separated from the island away from the tip toward $x < 0$, as noted before (figure 5.11, p.122). The turning of the current toward the left would intuitively be opposite to the expected direction due to Coriolis. However, the thinning of the lower layer, possibly forced by the upper layer via the interface, may lead to a β-effect, that would reduce the relative vorticity in the lower layer. For potential vorticity conservation, the lower layer loses relative vorticity with decreasing layer thickness. Such forcing may only occur at this location ($x \sim 1$) as for other x in the lower layer the RHS has stagnant fluid above. It is also conceivable that the upper layer current, while it crosses near the light reservoir island tip, 'drags' the lower layer in the direction of the island and thus toward the current from the other side-channel through shear. This would agree with the recirculation of the lower layer found near mid-depth on the RHS of the tip. Another possibility is that the deep current path during the quasi-steady state is to some extent dependent on the preceding transients; for example, the current crossing could be due to the way the advancing RHS current meets the one already flowing from the LHS past the island tip. The separation from the RHS could be due to the meandering common in flows with $R_0 < 1$, but as the RHS current meets the LHS one near the tip, it is redirected toward the RHS wall.

During the dual regime the deeper flow from the RHS is turning around mid-depth and below in the direction of the lighter near-surface flow (figure 6.13(d), p.158). The recirculated water flows in the same direction as the overlying water, so velocity data alone makes it difficult to distinguish the light and dense water due to the lack of a shear interface. To see the extent of the dense layer and thus indicate the position of the density interface fluorescene dye was used in one experiment on the *Coriolis* platform, not otherwise presented in this thesis. The recirculated water is found to belong to the lower layer in a repeat run of experiment 3, which agrees with dense water being present on both island sides during the dual regime. The fluorescence results are also in agreement with a flow from the LHS turning around the island tip to enter the RHS and flow in a similar manner below the upper layer; however, the velocity fields in experiment 3 did not support this in either of the two regimes, so that such water is likely to move only sluggishly if at all, instead of actively circulating around the tip. Such recirculation has implications for hydraulic control of the flow in the sense that unidirectional flow in two overlying density layers would allow the propagation of baroclinic waves in the direction of the flow, regardless of the Froude number, since only waves travelling in the opposite direction could be arrested by the flow.

The split regime (figure 6.13(d), p.158) shows a fairly abrupt crossing of the (LHS) bottom current toward the RHS wall at $x \sim 1$, leaving a stagnant region at the island tip. This represents the tendency of the flow around a cape, represented by the island tip (Serra *et al.*, 2002; Sadoux *et al.*, 2000; Cenedese and Whitehead, 2000), to reattach to the other side of the tip. This means the flow would circumvent the tip and reattach to the island inside the RHS channel. Note that this does not occur during the dual regime. The exchanging nature of the flow due to buoyancy forcing presumably causes the flow to turn instead to the light reservoir direction as it reaches the RHS wall. This is visible at the surface near the same island tip but on the LHS. The upper layer there flows toward the side-channel but then recirculates in a vortex and does not reach the narrows. The nature of hydraulic control in the split case is evidently more complicated as the baroclinic flow is separated by the island at the location where the channel-crossing occurs. In these cases the location of the crossing is near the narrows as opposed to the tips during the dual regime.

6.4 Viscous effects, boundaries and initial conditions

The results of this and the previous chapter show that for $R_0 > 1$ fluxes and the interface slope at the narrows show good overall agreement with theoretical predictions, with differences attributable to known factors, such as viscous effects. Some asymmetries in the interface and the current structure could be observed and will be treated in this section with respect to viscous effects at the boundaries and the fluid interior. Viscous boundary layers are not only relevant in the laboratory but are also important in the ocean (Johnson and Ohlsen, 1994), although they occur in a way different to the rectangular channel case. Thus asymmetry in layer depth may depend on the Ekman number (Ek), which differs on both platforms, as shown in appendix C, figure D.1 (p.202). This number determines the scale and dynamics of both Ekman and Stewartson boundary layers, as explained in section 3.4 (p.73). Note that the effects of internal friction and mixing, represented by the partially sheared interface and seen in section 6.2 (p.144) will be discussed in section 7.3 (p.174). It is also possible that asymmetry is dependent upon the initial conditions.

Interface offset

A vertical offset of the interface toward the surface, mentioned in section 5.1 (p.105), is evident throughout most experiments. This offset is 0.025 to $0.05H$ in the *Coriolis* experiments with $R_0 > 1$ and it is slightly less and more symmetric with a straighter interface in the island cases than in the simple channel; an exception is the $R_0 \sim 6$ case with an island, which has a very shallow cross-channel slope and no offset is evident. In comparison, experiment 712 from the *SOC* platform shows a similar offset. However, experiments 710, 715 and 713 (figure 5.4, p.111) exhibit a higher vertical offset in the interface, $\sim 0.15H$ toward the surface, than the *Coriolis* experiments. Similarly, for $R_0 \sim 1$ there is an overall vertical offset of $\sim 0.1H$ both without and with an island, for example experiment 807 (red line in figure 5.5(a) (p.112)).

If the upper boundary is assumed to be approximately free-slip, we can neglect boundary layer effects there. Thus the Ekman layer at the bottom boundary will cause the interface to be offset toward the surface (Zaremba *et al.*, 2003). This is due to the fact that the boundary layers are sheared with a non-zero mean velocity and we assume that velocities in the inviscid parts of each layer are similar, so that volume conservation requires the layer with a greater boundary layer to be deeper than the other layer. The offset of the interface toward the surface is thus $\lesssim EkH = \delta_{Ek}$, i.e. of the order of the Ekman boundary layer thickness. The values for δ_{Ek} shown in table 3.15 (p.74) for $R_0 \sim 1$ are only slightly larger than the offsets observed on the *Coriolis* platform. However, for $R_0 >> 1$, the δ_{Ek} is much larger than the observed dz, suggesting that the boundary layers are not yet fully developed in the time-averaged velocity fields. This agrees with the previously mentioned fact that the spin-up time, T_s is longer than the experiment running time. It is interesting to note that in the case of reversed reservoir densities, such as experiment 15 (figure5.2(b), p.109), the vertical offset is similar to the corresponding case with the standard reservoir densities, i.e. experiment 2. Therefore we can assume that the vertical offset is due to the difference in bottom and surface boundary conditions and not the reservoir conditions. It is also noticeable that the interface depth offset toward the surface reduces slightly as $R_0 \to 1$ (figure 5.2.1, p.108). This may be due to the nature of the bottom boundary layer, which, unlike the non-rotating case, is not influenced by the channel length in the rotating exchange but is limited in depth by $Ek^{\frac{1}{2}}H$.

Comparison to previous laboratory experiments

The most recent work on rotating two-layer exchange flows through a simple constant depth channel is by D88 and Dalziel (1990). The theory, based largely on constant or zero potential vorticity, has already been used to analyse the cross-section slope and exchange fluxes at the narrows in sections 5.2.1 (p.108) and 6.1.1 (p.133), respectively. Here experimental data by D88 is compared to the experiments under study in this thesis. One important difference to note is the assumption in D88's work that the upper and lower boundaries are solid with no-slip conditions in the experiments. Thus boundary layers are expected near the wall, the surface, the bottom and the interface. Figure 6.14 (p.163) shows the experimental and theoretical density interface cross-sections at the narrows taken from D88's work. His experiments were carried out using a constant depth, horizontally narrowing, submerged channel with rigid surface and bottom boundaries, both equidistant to the reservoir surface and floor, respectively.

D88 found best agreement between the theoretical and measured interface positions for high R_0, whereas for $R_0 \sim 0.9$ there was a considerably shallower cross-channel slope than expected, even when theory takes the Stewartson sidewall boundary layers into account in the form of a reduced 'effective' channel width . D88 suggested that Ekman layer flow is responsible for this thickening of the corresponding thinner layer near the walls. He found the Ekman flux to be even more evident for $R_0 \sim 0.4$ where the region to the left of the upper layer current at the narrows showed a virtually flat interface whereas the other channel half contained the active part (figure 5.2.1, p.108). This was also found in experiments by Whitehead *et al.* (1974), who did not observe the separation of the interfaces from the sidewalls and intersection with the channel floor even for low R_0. This was also observed in the *SOC* experiments, as dye was used to mark the extent of the layers. The *Coriolis* platform did not give us this information, apart from one experiment. However, we could see that for low R_0, there were stagnant or recirculating areas, which could have slowly been filled by Ekman transport with the same density water as the active part adjacent at the same depth. For $R_0 \sim 0.9$, D88's experiments did not show the vertical asymmetry found in our experiments which suggests at first that the difference in top and bottom boundary conditions is responsible for this asymmetry in our case. Frictional boundary layers can also be important in the real ocean, as observations of secondary Ekman circulation in the Faeroe Bank Channel by Johnson and Sanford (1992) showed. This was examined further in laboratory experiments with a semi-circular cross-section, relatively long channel based on the conditions in the Faeroe Bank Channel (Johnson and Ohlsen, 1994).

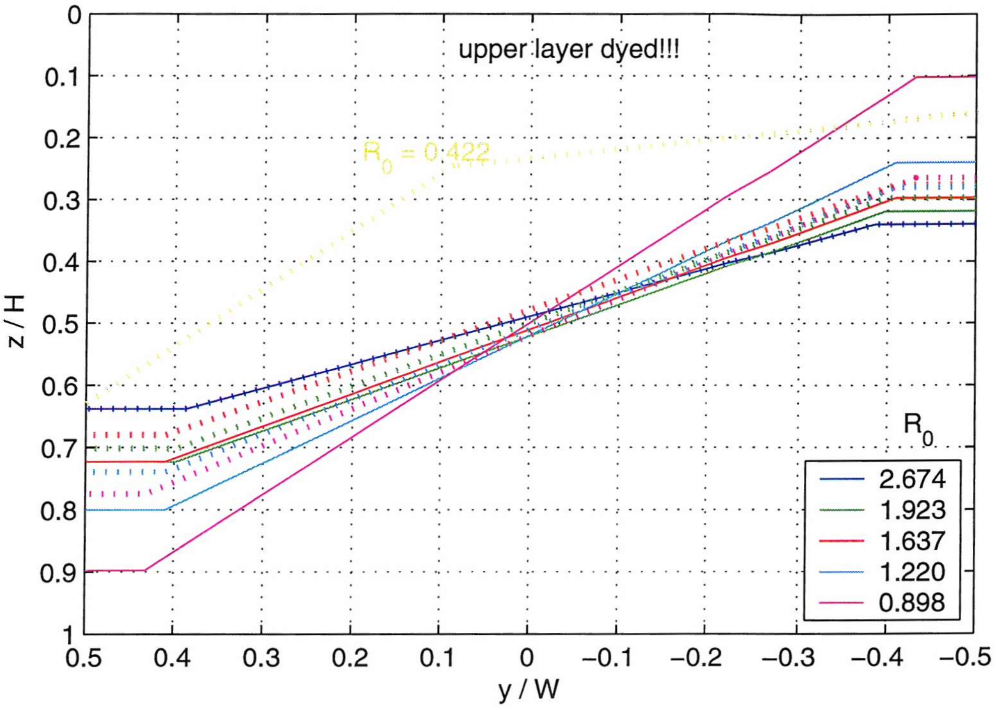

Figure 6.14: Experimental (dotted) and theoretical (solid) interface depth estimates at the narrows reproduced from D88. Data and theoretical prediction is for a constant depth, horizontally-contracting channel with rigid top and bottom boundaries. D88's laboratory experiments used fluorescene dye in upper layer to visualise the interface, and the theory used the semi-geostrophic assumption. The latter also includes a viscous correction incorporating the Stewartson sidewall boundary layers effectively reducing the channel width available to the inviscid flow. Note that despite this the theory does not agree with the experimental interface depth which was proposed by D88 to be due to Ekman transport from the centre of the interface toward the walls. This can be seen in the $R_0 \sim 0.4$ example, where only part of the cross-section is sloping and the other almost flat, likely stagnant with slow supply of fluid by Ekman transport.

Asymmetry and initial conditions

Experiment 1 with $R_0 = 0.9$ shows a distinctly asymmetric velocity distribution (figure 5.2(f) (p.109)). The lower layer is banked up on the RHS and only occupies $\sim \frac{1}{3}$ of the cross-section, while the upper layer occupies all of the channel within 0.3 of the surface. The exact value has some uncertainty because only three depth levels were sampled in this experiment. The vertical offset is actually opposite to the other experiments with the lower layer less wide and deep than expected. In the corresponding *SOC* experiment (708) the lower layer is of width $\sim R_0$ as expected. Therefore viscous effects are not likely to be responsible for the asymmetry seen in experiment 1 which may be due to the influence of the initial conditions on the quasi-steady flow. This has implications for hydraulic control, which would normally lead to a flow more centred around the narrows. However despite the asymmetry in experiment 1 at the narrows, to balance the exchange flux in both layers it is necessary to consider the whole cross-section, which is more likely to show stagnation for part of the section if R_0 is lower, for example in experiment 708. It is interesting to note that the current cores in experiment 7 with $R_0 = 4.16$ also show that the crossing is centred around the location of the lock-gate rather than the narrows, although there are no stagnant regions. The crossing in the island cases usually occurs around the narrows, which is likely due to the fact that the narrows constrict the channel more than in the simple channel cases.

For $R_0 < 1$ there is no a-priori reason for the crossing to occur around the narrows in an inviscid flow. D88 suggests that viscosity may act through the boundary layers moving the crossing toward the narrows in cases with $R_0 < 1$. Therefore, even if initial conditions set the crossing around the barrier, viscosity may still centre the flow around the narrows. It is evident that the crossing does occur around the narrows at times in experiment 8 ($R_0 << 1$). This does not happen in experiment 1, even though the boundary layers should be fully developed during the quasi-steady period, which is set around the spin-up time (T_s). The latter is also true for experiments 701 and 703, where the barrier is at opposite ends, representative of different initial conditions, and the quasi-steady interface at the narrows is found to differ in both experiments. Therefore, initial conditions do appear to have an effect on the quasi-steady state for simple channel exchange with $R_0 \lesssim 1$.

Fluxes

Figure 6.1 (p.137) shows that flux values are generally below Whitehead *et al.* (1974)'s inviscid prediction, down to a fraction of $\sim \frac{4}{5}\bar{q}_{whitehead}$ for $R_0 >> 1$, which is higher than the study on frictionally modified rotating exchange by Johnson and Ohlsen (1994). They found that a combination of friction and rotation had a greater effect on the two-layer exchange than each of these separately and attributed their findings to the effects of a secondary circulation (see also Johnson and Sanford, 1992). The influence of the latter is likely to differ in the rectangular channel geometry used in this study to the semi-circular cross-section geometry by Johnson and Ohlsen (1994). However, that secondary circulation is likely to occur even in rectangular channel geometries was shown by D88's results in figure 6.14 (p.163).

Summary

The role of boundary layers is difficult to determine because CIV is often unable to calculate velocity close to the boundary. CIV velocities have to some extent been smoothed so that some of the gradient near the boundary may not actually be a boundary layer. Therefore no attempt is made to adapt existing theory to include viscous sidewall boundary layers and the reader is instead referred to the discussion of oceanic boundary layers in section 7.4.1 (p.177) and inter-facial friction and entrainment in section 7.3 (p.174). This section does show that the behaviour of the flow and fluxes is in qualitative agreement with the viscous influence on rotating exchange flows found in previous studies. In particular, bottom friction acting on the lower layer deepens that layer and shifts the control sections away from the narrows. Furthermore, it is found that initial conditions can influence the location of the crossing of the flow in simple channel cases with $R_0 \lesssim 1$. In the island cases, this may not occur to the same extent due to the additional constriction in the channel centre. However, the 'dual' regime in experiment 3 ($R_0 = 0.7$) shows that the currents are attached to only one boundary in each side-channel at the narrows and that the current-crossings do not always occur at the narrows but can instead be located near the island tips.

6.5 Summary

Volume exchange fluxes from reservoir density and CIV velocity measurements at the narrows cross-section were presented in this chapter. Good agreement was found between all measurements with differences attributable largely to the inclusion of the initial adjustment and changing reservoir conditions over the course of each experiment. CIV velocity estimates for quasi-steady flow regimes agreed well with existing simple channel, zero potential vorticity theory except for viscous effects and CIV measurement errors near the side walls. The R_0 parameter, R_{0i} with an island and R_{0s} in the simple channel cases, is found to be suitable for describing the influence of channel width and rotation on the exchange fluxes, as was found for the cross-channel slope at the narrows in the previous chapter. It is important to note that the fluxes in the island cases would be wrongly estimated by simple channel theory if the channel width was not adjusted by the island width, i.e. W_s used instead of W_i. In the non-dimensional sense this estimate would be higher or lower than the theoretical prediction, depending on the value of R_0.

Viscous effects and entrainment near the interface may be responsible for some of the difference in theoretical and measured fluxes, which is evidenced by partially sheared velocity profiles throughout the channel and comparison to previous work. However, even though entrainment effects are measurable they are very small in the rotating cases. The results agree with previous studies on frictionally modified exchange flows. Overall, it is likely that all frictional effects, at the interface as well as at the side-wall boundaries, contribute to the reduction in exchange fluxes relative to the theoretical prediction. This is so as even small interfacial mixing has been found to influence the exchange significantly (Hogg *et al.*, 2001a). Non-zero potential vorticity is not likely to be responsible to the same extent, at least not for

$R_0 > 1$, where the effect on fluxes is found to be small in simple channels (D88, Dalziel, 1990).

Dimensional fluxes are found to be increased with an island for $R_{0s} \sim 1$, so that the simple channel estimate here would be lower, although there are only three measurements made for such R_{0s}. This is not the trend expected from a simple channel of width W_i, as such reduction in width is expected to decrease the dimensional flux given in equation 2.2 (p.30) for $R_{0s} \gtrsim 1$. In such a case, a decreased cross-sectional area, due to the island, would require an increase in the velocity difference between both layers and thus an increase in cross-channel slope in each side-channel, provided the flow is approximately semi-geostrophic. This is the observed behaviour found in the previous chapter, where the slope in each side-channel is steeper than the overall slope across the whole channel. This does not explain the vertical offset in the attachment points of the interface at the island, but such offset is in agreement with the flow direction around the island tip, for example for the lower layer flow toward the right where the interface is lower.

The island scaling can improve flux estimates to a degree that is important in the light of oceanic exchange flows, as will be discussed further in section 7.4.1 (p.177). The unexpectedly high flux during the barotropic split regime found only in the island case for $R_0 \sim 0.3$ is also likely to be important for such flux estimates.

Hydraulic control is found to occur in the non-rotating case and agrees with previous modelling studies on hydraulically controlled flows under the influence of small friction, where the composite Froude number, G^2 is found to give two critical sections bounding a subcritical region around the narrows. For the rotating exchange flows analysis shows that hydraulic control is also likely to occur, although the position of such control is difficult to determine using hydraulics theory, such as Gill (1977)'s functional approach, with our data. Noteworthy is also the simple channel case with $R_0 = 0.9$, where the channel-crossing of the lower layer current does not occur at the narrows but near the location of the initial adjustment. This shows that initial conditions can influence the steady state in some cases for $R_0 \leq 1$ and is interesting in particular as hydraulic control in flows for such R_0 is thought to be linked to the channel-crossing (D88, Dalziel, 1990).

An analysis of the fluxes and net fluxes in each channel half indicates that each island side-channel for $R_0 > 1$ is not likely to be an independent exchange flow. For lower R_0 the separation and the split flow regimes give rise to more unidirectional flow and therefore not an independent "exchange" on each island side. For all R_0, it is clear that each of the side-channels show much lower fluxes than would be expected from simple channel theory if they were completely separate. This confirms that there are important interactions between the island and the flow, as seen in the qualitative observations in chapter 5 (p.105) and section

6.3.3 (p.156). Further discussion of hydraulic control and the independence of the two island side-channels is given in the following chapter.

Chapter 7

Discussion

The flow path and flux results in this thesis so far show that the simple channel experiments agree with the previous theoretical and laboratory work bar viscous effects and other second order effects. The introduction of an island adds an additional boundary in the channel centre which can be accounted for by considering the reduced width at the narrows for cases with $R_0 > 1$. However, for lower R_0, more complicated flows develop, not seen in the simple channel cases. These findings will be used in conjunction with the evidence of hydraulic control and the conditions near the island tips to determine the nature of the exchange, in particular if an island separates the channel flow into independent parts. Further, viscous effects at the interface and mixing will be discussed in the context of previous work. Finally, the relevance of our experimental findings with respect to real ocean exchange flows is discussed in the light of flux measurements and bathymetry.

7.1 How does the island separate the flow inside the channel?

7.1.1 Two separate baroclinic exchange flows?

When an island is placed in the channel, can the flow in each of the two passages be considered as two entirely independent exchange flows or does the whole channel over the length of the island need to be considered to sufficiently describe the exchange? This section discusses this question for $R_0 \gtrsim 1$.

The flux analysis in section 6.1.2 (p.140) suggests that the flows on each island side are not independent, as they do not show fluxes in agreement with simple channel theory applied to just one side-channel. A similar test can be done using the narrows cross-sections in section

5.2 (p.108). There the slope across the whole channel is shown to be a function of R_0 (see equation 5.2, p.110), taking into consideration a reduced W ($= W_i$) in the island cases. In a similar manner, the depth spanned by the interface in only one channel half (RHS or LHS) of the island can be considered, for example in experiment 4 $dz = 0.15$. Taking the size of that part of the channel to be $W_{side} = \frac{W_i}{2} = 0.35$ we get $dz_W \sim 0.43$, implying a Rossby number for just this channel $R_{0side} = \frac{R}{\frac{W_i}{2}} = 2.3$. From the measured R we actually have a significantly different value, however, $R_{0side} = 4.98$. Therefore, while the overall slope is in agreement with equation 5.2, p.110, the slope on either island side alone is not. This is similar to saying that a simple channel exchange flow is not the same as the flow through one side-channel if both have the same R_0 and R_{0side}, respectively. Therefore this argument supports the idea of the flow on both island sides being part of a larger exchange flow.

The slope being larger than expected from simple channel theory applied to one island side-channel also implies that the island width has an influence on this: with a flat-plate island, the interface would be at the same depth in the channel centre on either island side, as in the simple channel case, indicating that the island width increases the vertical offset of the interface on either side and thus increases the slope on each side. The vertical interface offset is also consistent with the jet turning around the island tip from the left to the right, with respect to flow direction.

Other indications about the independence of flow in either side-channel can be obtained from conditions of the joining of the flows meeting near the island tips. This means the flow on either island side could be separated in the sense that small amplitude, interfacial waves could not be transmitted between both channels unless they grew to finite amplitude, e.g. in the form of an internal bore. For example, if there is a hydraulic jump near the island tips, between both joining currents, this could isolate the side-channels from each other, although not from each current's relative upstream reservoir. As the island leads to a more rapidly widening cross-section than the simple channel cases and to separation regions near the walls closer to the narrows in the island than the simple channel cases with the same R_0, a hydraulic jump may be expected near the tips. However, we have seen in sections 5.4.2 (p.130) and 6.3.3 (p.156) that there is no significant ($\sim 1H$) interface depth change near the island tip so that a real 'shock', in the non-rotating sense, does not occur (e.g. Wood and Simpson, 1984). Indeed, such was not observed in the non-rotating experiment as shown in figure 5.1(b) (p.106). Note that slightly super-critical, close to critical, flow can still lead to a weak, undular jump, which may only be a small fraction of the channel depth, not measurable in our experiments. Furthermore, any non-rotating hydraulic jump requires super-critical upstream conditions. This should be indicated by the local Froude number in the two-layer fluid, G^2, as presented in sections 6.3.1, p.150 and 6.3.2, p.152. Figure 6.10(b) (p.153) shows that such conditions approximately exist in the vicinity of the island tip around $x = 1W$, where super-critical flow is present, $G^2 > 1$, but turns into sub-critical toward the light reservoir, at the edge of the field of view. Such high values of G^2 were not observed for lower R_0. This may be due to the differing nature of rotating jumps that often show a more lateral change in the interface with respect to upstream flow direction as was studied, for example, by Pratt (1987) for single layer flows over a sill. This is relevant in particular at low local Rossby number, meaning the Rossby radius is locally much smaller than the channel width. Pratt (1987) showed that such jumps, even if separated upstream, can still occur if the fluid downstream attaches to a wall on its left. For entirely separated flows Nof (1984) showed that stationary jumps are not possible, but only one layer was considered active in his study. In the experiments in this work, there are two active layers in the vicinity of the island tips, at least for $R_0 \gtrsim 1$. Fedorov and Melville (1996) suggests that hydraulic jumps of such 3-dimensional nature could be stationary along a boundary, such as an island, if two geostrophic currents met flowing in opposite directions along this boundary. This could then prevent internal Kelvin waves if they scale with R, that may propagate toward the narrows along the wall to their right, to split at the island tip, which is on their left. In other words, this could prevent a similar disturbance to enter into the channel to the right of their direction of propagation.

If the conditions near the island tips are indeed super-critical, then no disturbances can enter either side-channel from the reservoirs and consequently the flow on either island side cannot communicate via linear disturbances. This would imply that if geometric conditions, such as depth or width, were different on either side, they would influence the flow only on the side they are located. This would imply independent exchange flows. However, the analysis of flux and cross-channel interface slope shows that the flows do not lead to two simple channel exchange flows in either side-channel using the same reservoir conditions. Therefore the only other way to satisfy this would be to have differing reservoir conditions for either side-channel. This would agree with the narrows velocity cross-sections in section 5.2 (p.108), which intuitively indicate that there are indeed two separate exchange flows, but with either a net flux or differing reservoir conditions on either side. Note the 'channels' on each side of the island are similar at the narrows in the sense that inverting the z- and y-coordinates as well as reversing velocity in one half of the channel would give approximately the same image as the other half. However, this again poses the question about the joining of the exchange flow inside the channel and the reservoir, which is beyond the scope of this study.

This discussion shows that for $R_0 \gtrsim 1$ there are several indications that the two island side-channels are not independent but rather part of one large exchange flow. However, we note that a rotating lateral hydraulic jump, separating the two sides, could exist near the island tips, despite the fact that large interface depth variations were not observed there. However, we note that it is difficult to detect the existence of such lateral jumps in the lateral variations due to the geometric forcing, i.e. curvature of the island and the walls, on our exchange flows. The next section considers the independence of both island side-channels relative to each other for $R_0 \lesssim 1$ as well as the occurrence of any lateral splitting of the flow in each direction in the simple channel cases.

Overall, this discussion tries to solve the case under study in this thesis, where the island is longer than the channel width at the narrows but shorter than the strait. This case can be considered intermediate to the two following extremes: with an infinitely long island, i.e. much longer than R and the strait length, the two parallel channels would be expected to lead to two separate exchange flows with hydraulic jumps located inside each island side-channel. In the other extreme a very small island would still reduce the width at the narrows available to the flow, but any hydraulic jumps would be likely located away from it, closer to the reservoirs. Thus, the intermediate case is likely to allow both independent and joined exchange flows in each island side-channel, depending on the value of R_0. This will be illustrated in the next section.

7.1.2 Stagnant zones and flow separation

The last section showed that the flow at $R_0 \gtrsim 1$ is not likely to represent two independent exchange flows in the cases considered in this study. This section investigates this for lower R_0, in particular with respect to the unique occurrence of the 'dual' and 'split' regimes, such as in experiment 3, figures 5.11 (p.122) and 5.12 (p.123), that are not observed in the simple channel experiments.

Similar to the flows with $R_0 > 1$ the dual regime with $R_0 \sim 0.7$ (experiment 3) shows baroclinic coupling at the narrows. However, the possibility of hydraulic jumps near the island tips, as discussed in the previous section, suggests that the flow in each of the side-channels could be independent, in particular as the deep flow on the RHS shows a strong change in current direction before joining the one coming from the LHS (figures 5.11, p.122 and 6.13(c), p.158). For the split baroclinic ($R_0 \sim \{0.7; 0.3\}$) or barotropic ($R_0 \sim 0.3$) regimes it is actually somewhat easier to see the isolation between the two island sides as there is no obvious baroclinic coupling between the currents in both directions, at least not within the field of view. However, the question remains how such single, reduced gravity layer flows are limited in terms of having approximately the equal and opposite flux on both sides. It is conceivable that such currents, if not entirely barotropic but bound above or below by an interface to a quasi-stagnant region, would allow disturbances to travel on this interface. Killworth *et al.* (1984) showed that such an active layer forming a front in an otherwise stagnant fluid is prone to instability on the interface. The isolation of the currents suggest that the flow mechanism in this regime is still an exchange but appears different to the baroclinic exchange prominent at higher R_0, for example being closer to two single layer flows with a practically stagnant, thin, layer above or below. The reservoirs would then be practically infinite basins that only slowly need to adjust their volume. Unfortunately we cannot verify this, as the measurements in this study were confined to the channel itself. Indeed the joining of the flow in the channel and the reservoirs is a subject of ongoing study, which has been attempted for single layer strait flows, such as the numerical model study by Helfrich and Pratt (2003), but is still very much unclear for the two-layer case. There is some suggestion that the flow through the strait is fed by a localised or cross-basin uniform overturning in the reservoirs or fed by an inflow source flowing along the boundaries toward the strait joining the reservoir. Helfrich and Pratt (2003) showed in their shallow-water numerical model study that all of these cases can occur in deep overflows, but that the strait flow itself is fairly independent of the nature of this circulation. Instead they emphasised the importance of monitoring the actual strait entrance, where reservoir and strait join, instead of just the basin conditions. This region has also generally been found important in cases where time variability is significant, such as internal tides in the Strait of Gibraltar (e.g. Brandt *et al.*, 2004; Helfrich, 1995; Armi and Farmer, 1988).

7.2 Hydraulic control in Rotating Exchanges

The results in chapters 5 (p.105) and sections 6.3.3 (p.156) and 6.1.2 (p.140) show several features in the flow that indicate where hydraulic control could be located and gives some reasons why this may occur. This discussion attempts to judge the likelihood of hydraulic control occurring in the experimental setups in the light of oceanic exchange flows and emphasises the differences between the flow regimes found in the flows under study.

In the experiments with $R_0 > 1$ the conditions are approximately baroclinic everywhere, except in separation regions near the side walls and close to the island tip, allowing the propagation of baroclinic waves on the interface. Therefore, hydraulic control is expected to take place in these exchanges, in particular as the flow at the narrows is generally similar to previous studies of fully hydraulically controlled flows, such as D88. The exact nature of hydraulic control could not be discerned due to problems with CIV velocity errors when calculating differences. However, composite Froude numbers G^2 do show regions of super-critical and others of sub-critical flow, indicating that waves are arrested at some cross-sections. Section 7.1 (p.168) showed that any control is likely to govern the exchange across the whole channel, leading to one coupled instead of two independent exchanges.

It is less clear how baroclinic waves may propagate in the dual regime with $R_0 \sim 0,7$ (experiment 3). Figure 5.11, p.122 shows that the near the island tips the shear interface is much less strong and the current cores are more horizontally separated than at the narrows, in particular on the RHS of the channel. However, this does not necessarily mean that the layers are not strongly coupled, as mixing may have caused a diffuse interface here which would still allow this (e.g. see Hogg *et al.*, 2001b). Furthermore, some of the lower layer flow in the RHS part of the channel actually turns in the direction of the near-surface flow at around mid-depth. As shown in section 6.3.3 (p.156), the findings from another experiment with similar R_0 suggest that some of this water is actually dense, flowing underneath the light upper layer. Thus the two layers would have contact via this density interface, which allows the propagation of baroclinic waves, at least in the direction of the flow, toward the narrows in both layers. This would make hydraulic control at the narrows unlikely, as information could propagate toward there. However, at the narrows the currents in either layer are separated from the wall to their left, with respect to flow direction. Separation at the narrows is also found in D88's experiments, even though semi-geostrophic theory cannot predict details of such flows. In such cases, Dalziel (1990) shows that a Froude number, to determine baroclinic information propagation and thus hydraulic control, can no longer be determined. In his study the Froude number is defined using the hydraulic functional. Dalziel (1990) suggests that the channel crossing of a separated two-layer region of the exchanging currents takes on the role of the control with frontal waves communicating baroclinic information on the interface. In the dual regime case, the occurrence of two such controls is suggested by the location of the channel crossing near the island tips (section 5.4.2, p.130). In this case wave propagation within the sub-critical region around the narrows would not affect hydraulic control.

For the simple channel case with $R_0 << 1$ the flow may be controlled by frontal waves in much the same manner outlined above. This is supported by the close agreement of exchange fluxes with theory in section 6.1.1 (p.133).

In some of the split regimes the channel crossing occurs in the vicinity of the narrows. Therefore, hydraulic control may also be expected there. As only one layer is present in each channel half, waves could travel on the interface to the stagnant layer, presumably of different density, above or below (Killworth *et al.*, 1984). However, these could then only be limited by the flow in the active layer, i.e. only downstream from the narrows could waves be prevented from travelling toward the narrows. This would suggest the flow is partially controlled, i.e. the exchange flux is not maximal. However, this is certainly not the case with $R_0 \sim 0.3$, where fluxes are found to be similar to or larger than the two-layer inviscid theoretical flux (section 6.1.1, p.133). For $R_0 \sim 0.7$ fluxes are noticeably lower than the theoretical prediction but the maximality of the exchange is difficult to verify due to the presence of viscous effects. Another location for hydraulic control could be the island tips. For example, during the baroclinic split regime with $R_0 \sim 0.7$ one of the currents crosses toward the wall there, e.g. from the LHS channel around the tip to the RHS wall near the light reservoir. However, as mentioned in section 7.1.2 (p.171) there is no obvious baroclinic coupling of the current near the surface and bottom via an interface at the tip. With rotation the Taylor-Proudman theorem predicts that motion in a uniform density layer becomes vertically homogeneous. Thus, if the water in between the two layers were of approximately homogeneous density, they may communicate change in interface depths adjacent to each current core. This cannot be answered fully due to the lack of density measurements. However, if the fluid in between the layers was stratified, control mechanisms such as presented by Hogg *et al.* (2001b) for non-rotating flows may occur via the mid-density isopycnal.

It is important to remember that this thesis studies cases where the island is longer than the channel width at the narrows but shorter than the strait. This can be considered intermediate to the two following extremes: with an island much longer than R and the strait length the two parallel channels would be expected to lead to two separate exchange flows with hydraulic jumps located inside each island side-channel. In the other extreme a very small island would still reduce the width at the narrows available to the flow, but any hydraulic jumps would be likely located away from it. Thus, the intermediate case is likely to allow both split and dual / baroclinic exchange flows in each island side-channel, depending on the value of R_0. This has been shown in the experimental results, and there are values of R_0 where both can occur at different times during the experiment. This consideration can also be seen in the context of oceanic examples in section 7.4 (p.177).

7.3 Validity of the two-layer assumption

In an inviscid lock exchange flow between two uniformly mixed reservoirs we assume two approximately uniform layers separated by an infinitely thin interface. This is a common assumption made in hydraulics style theories, as the exchange can be described entirely by the depth and the depth-mean velocity of each layer. However, representative velocity profiles in experiments with $R_0 \geq 1$, show that a region of approximately $\frac{1}{5}H$ is sheared (see figure 6.6, p.145). This cannot be neglected, as it has a significant influence on the mean velocity in each layer, in particular where the interface is near the surface or bottom boundaries.

A partially sheared and mixed interface has been investigated by Hogg *et al.* (2001b) with respect to internal wave propagation in non-rotating exchange flows and is likely to be not only significant for hydraulic control of the baroclinic flow but also for potential vorticity and energy. The latter may dissipate in the form of such internal friction. The shear profile Hogg *et al.* (2001b) used as an example case is similar to the ones occurring in our experiments.

The first question that arises is whether this shear profile is accompanied by a similarly shaped density profile caused by internal friction induced mixing around the strongest vertical density gradient. Hogg *et al.* (2001a) found in numerical simulations of non-rotating exchange flows that the mid-density isopycnal actually stays fairly constant unless mixing is significantly increased relative to the horizontal exchange flux. On the contrary, the level of zero velocity is overall flatter along the channel, i.e. the shear interface is nearer mid-depth at both ends of the channel but coincident with the density interface around the narrows. This means that the volume flux will be reduced relative to the inviscid case, as some of the water entering the channel from the reservoirs turns around again in the other direction. The mass flux is similarly reduced, though more so as the layers are no longer of uniform density. In other words, the reduced volume flux now carries less (more) dense water in the upper (lower) layer, i.e. the respective layer mean density is now closer to the mean density between both layers.

If interfacial mixing leads to entrainment, as shown in section 6.2.2 (p.146), the regions near either end show a greater flux than at the narrows if we define our layers by the shear interface. The latter is denoted by the zero-velocity isotach and has generally been considered to be more consistent when studying viscous effects with respect to inviscid two-layer non-rotating exchange flows (Hogg *et al.*, 2001a; Stenström, 2003). Furthermore, in these same studies the density interface is generally not changed nearly as much by small degrees of mixing as the shear interface near the reservoirs. Thus, the tracer flux is reduced even further than the volume flux. It is also noteworthy that the divergent flux is very small around the narrows, so that our exchange flow estimates there are likely to be reliable, if the density interface is at the same location. We expect this from non-rotating exchange flows (Hogg *et al.*, 2001a). However, in rotating flows, the density interface at the narrows is sloping across the channel, so that the interface there is also close to the surface or bottom for parts of the cross-section. The question immediately arises, if this leads to a similar offset of the shear interface relative to the density interface as is found near the reservoirs. If entrainment is caused by interfacial friction/viscosity in the thinner layer, it would not hold at the narrows, as rotation not only tilts the interface, but also confines highest velocity to the thicker region. As viscous action / friction is dependent on velocity, we can expect less friction and thus less shear interface offset due to entrainment at the narrows than in the accelerated layers of similar thickness near the reservoirs

Even if it is not possible to accurately quantify entrainment near the reservoirs, an idea of the total mixing/entrainment along the channel can be obtained by using the same methods as Hogg *et al.* (2001a) and calculate their parameter, $G_{rT}A^2$ (see also section 2.1.2). From this it is possible to infer the expected volume flux and the deviation from hydraulic theory, at least for the non-rotating experiment:

$$G_{rT}A^2 = \frac{g'H^3}{k_\nu}\frac{H}{L}, \tag{7.1}$$

where k_ν is the viscosity and L the length along the channel over which mixing occurs. First, we use the value for molecular kinematic viscosity, $k_\nu = \nu$, g' and H from experiment 14, assuming a laminar flow. This should give an upper bound on G_{rT}, as any turbulence in our flow would increases the value of k_ν. We also assume that if any mixing takes place, it will be over the whole length of the channel, i.e. $L = 5m$, as we have no other scale available to estimate this. With this we have $\nu = 10^{-6}m^2s^{-1}$, $g' = 6 \cdot 10^{-3}ms^{-2}$ and $H = 0.6m$. Therefore, $G_{rT}A^2 \approx 10^6$. On the other hand, we can use Hogg *et al.* (2001a)'s empirical relationship between interface thickness, h_t, and $G_{rT}A^2 = (\frac{h_t}{3.4})^{-4}$. We use $h_t = 0.3$ which gives us $G_{rT}A^2 \approx 10^4$. The second approach appears more believable as it is valid for a range of values of A and does not include errors made in estimating L or k_ν. It would suggest that our volume is approximately 0.85 times the inviscid hydraulic solution. Looking at the results in section 6.1, we can see that this is close to the non-rotating fluxes calculated from our velocity measurements, $\sim 0.225q_{nr}$, i.e. 0.9 times the inviscid, non-rotating limit. Thus a similar fractional reduction in total volume flux can be expected to occur in the rotating experiments due to entrainment near the reservoirs. However, it is shown in section 6.2.2 (p.146) for $R_0 > 1$ that this is actually slightly less in the rotating cases. This may be due to the limiting nature of rotation on the boundary layers, which inject spun-down, partially mixed fluid into the free-stream, inviscid part of the flow and whose influence does not increase with channel length, as opposed to the non-rotating case where viscous effects act over this length (see also Johnson and Ohlsen, 1994). The process of entrainment in the rotating case is more likely to be due to instability at the interface. However, we cannot determined this by, for example, a Richardson number and stability analysis due to the lack of density measurements. The results of section 6.1.1 (p.133) can therefore be viewed with respect to the effect of interfacial mixing in addition to the effect of viscous sidewall boundary layers.

7.4 Relevance of laboratory cases to real ocean exchanges

So far we have discussed various effects an island has on the exchange flows studied in an idealised laboratory setting. This showed that the island changes not only the exchange flux and interface position in relation to a simple channel but is also likely to influence information propagation and hydraulic control of the flow. In real oceanic strait flows the question then arises if the influence of an island is noticeable with respect to the accuracy of fluxes inferred from hydrography and other observations. It is also of interest to compare such measurements with theoretical estimates and the arguments used in this study in relation to information propagation and independence of each side-channel formed by the island.

7.4.1 Laboratory fluxes and accuracy

One question that arises out of the results in this thesis is if the scaling of the channel width and thus R_0 by taking into account the width actually available to the flow in the island case could be useful in improving estimates of flux and interface depth through oceanic passages. The latter may be relevant if long-term monitoring at a single location, such as moored current meter, is used to infer time series of fluxes and the state of the exchange. It is clear from sections 5.2.1 (p.108) and 6.1.1 (p.133) that for a given R_0, using the whole width of the channel in the island cases would overestimate the cross-channel slope and give a wrong estimate of the fluxes. A shown before, this requires R_{0i} and the reduced width W_i to be used in the island cases instead of R_{0s} and W_s. This would then also apply to flux estimates from oceanic measurements.

In quantitative terms the theoretical estimate of non-dimensional fluxes given in equation 6.1, p.134 for a simple channel would be associated with an error of

$$\epsilon_q \sim \begin{cases} \frac{n^2-1}{3*R_0^2-n^2} \, for R_0 > 1 \\ (n-1)\bar{q}_{island} \, for R_0 < 1 \end{cases} \tag{7.2}$$

with respect to the island case, if an island is present but ignored. n is the fraction of the total channel width not occupied by the island and thus available to the flow. Note that there is a range of R_0 where the error is in between both estimates, i.e. the simple channel falls into the fast rotating and the island case into the slowly rotating range. For the cross-channel slope, an error of

$$\epsilon_{dz_W} = (\frac{1}{n} - 1) * dz_{Wisland} \tag{7.3}$$

is expected. $dz_{W_{island}}$ is the cross-channel slope with an island. If an island covers $\sim \frac{1}{3}$ the strait width at the narrows, as in the *Coriolis* experiments, $\epsilon_{dz_W} = -2 * dz_{W_{island}}$ or -200%. Similarly, using equation 7.2 (p.177) gives $\epsilon_q \sim -66\%$ of the island flux for $R_0 \lesssim 1$ and reducing for $R_0 \gtrsim 1$ (e.g. $\epsilon_q \sim -0.71\%$ for $R_0 = 5$). The R_0 limit should be seen with respect to the island case. Further inaccuracy in theoretical estimates may arise if reliable bathymetric data to correctly estimate the depth at the narrows or a sill is not available. This is, for example the case in the complex system of straits in the Cretan Arc, where simple non-rotating hydraulic control models have been used (Tsimplis *et al.*, 1999).

In comparison to the steady theoretical estimate, fluxes inferred from oceanic measurements in strait exchanges and overflows can vary by up to several 100% (e.g. Strait of Sicily Astraldi *et al.*, 1996, 1999). This is because they are not only limited by the accuracy of finite horizontal spacing of measurement stations but also time variability, such as tides. Therefore the effects of an island, represented by the error from just using a simple channel approach, ϵ_q, are expected to be only significant if the island covers a good fraction of the strait width and ϵ_q is similar to the error in flux estimates from oceanic measurements. Furthermore, with the advancement of measurement and modelling techniques, better theoretical estimates are required, so that the increased accuracy by considering an island within a strait is likely to gain even more relevance in the future.

With respect to oceanic measurements, there is also the issue of the path the flow takes and the best position to measure an exchange flow in a strait. Even in separated flows with $R_0 << 1$, the velocity core may still meander and not be banked on the wall to its right (with respect to flow direction), as the experimental results in this thesis show. Thus, the whole strait width may be important. Recirculating regions near the island tips may also require fine-resolution measurements, in particular if the island is angled to the along-strait axis and/or offset from the simple channel narrows. Such a situation is found in the Strait of Sicily, where a recirculating deep current jet circumvents the tip of a submerged ridge to ultimately enter the current on the other island side (Stansfield *et al.*, 2001, 2003). The issue of sampling location is also common in any Strait with complex bottom topography, such as the Denmark Strait, where detailed Strait-specific process modelling has been used to improve the choice of location for long-term monitoring (see Käse *et al.*, 2003).

From the discussion in section 7.3 (p.174) it is evident that the best estimate of the exchange flux is from the narrows region, provided the flow is hydraulically controlled there and the density interface coincident with the shear interface at approximately mid-depth (constant depth strait). This is likely to occur in the vicinity of the narrows but comparison of interface position would be a good indicator, as the mid-depth mid-isopycnal may be offset vertically due to bottom friction and thus the hydraulic control shifted along the channel

(Zaremba *et al.*, 2003, and also sections 5.1, p.105 and 6.3.1, p.150). An exception may be posed in the dual regime, where the flow in both layers is separated and banked up on opposite sides at the narrows. There the flow may also have to be monitored in the vicinity of the island tips, in particular with respect to current crossing, to determine the state of the flow, such as hydraulic control. An estimate of the cross-channel slope as mentioned above may also be useful, even at the narrows, as any vertical profiles measuring quantities that can be associated with one layer could otherwise miss the lower layer if a large cross-channel slope is present. This can to some extent be appreciated when considering the velocity extrapolation near the surface and bottom of the channels in this study, where the shear interface is at times located just on the near-surface (near-bottom) level and thus information about the layer above (below) is not sufficient to give velocity with as much certainty as when the interface is closer to mid-depth. In hydrographic measurements this problem is known from calculating the "bottom triangles" in regions of varying topography.

7.4.2 Strait bathymetry and the island case

There are many complex straits and passage systems with two-layer flows in the ocean where the island case may be applicable. Some examples are mentioned in section 2.2.2 (p.35).

Here we will present a simple calculation of the outflow in the Straits of Hormuz and discuss the results in the context of topographic variations and observed time-dependence in the straits. This calculation can be seen in the context of the analysis and discussion of the independence of each island side-channel in sections 6.1.2 (p.140) and 7.1 (p.168). Johns *et al.* (2003) presented hydrographic and current meter observations, giving transport estimates for the deep outflow and surface inflow in the Straits of Hormuz throughout an annual cycle. One particular location is interesting with respect to the channels with an island under study in this thesis. This is located in the north of the strait, as shown in the topographic map in figure 7.1(a) (p.182). Although the strait is generally fairly wide, the dense outflow is largely confined to a deep channel in this region. The channel is separated by an island, as can be seen in the cross-section in figure 7.1(b) (p.182).

If we use a very much simplified (rectangular) channel geometry, as shown in figure 7.1(c) (p.182), the maximal exchange flux can be calculated for this cross-section, as given by equation 6.1 (p.134). A section to the West of the region of interest (see Johns *et al.*, 2003) can be used as the "upstream" (with respect to the lower layer) conditions, giving a Rossby radius of $R = 16km$ ($g' \sim 0.02ms^{-2}$, $f \sim 6.4 \cdot 10^{-5}s^{-1}$ at 26^oN and $h_2 \sim 50m$, the lower layer depth). This leads to a scaling velocity of $\sqrt{g'h_2} \sim 1ms^{-1}$, which is larger than the observed values upstream of $\sim 0.6ms^{-1}$; however, similar reduction in velocity was observed in the experimental flows in this thesis. Parts of the simplified cross-section has widths $W_R \sim 10km$, $W_L \sim 30km$, $W_i = W_R + W_L \sim 40km$ and a simple channel width (ignoring the island) of $W_s = W_i + w_{island} \sim 50km$, where w_{island} is the width of the island itself. This leads to Rossby numbers for each channel half and the whole cross-section: $R_{0R} = \frac{R}{W_R} = 1.6$ and similarly $R_{0L} \sim 0.5$, $R_{0i} \sim 0.4$ and $R_{0s} \sim 0.3$. This then leads to the following dimensional theoretical fluxes: $q_{whiteheadR} = 1.1 \cdot 10^5 m^3 s^{-1} = 0.11 Sv$ and $q_{whiteheadL} = q_{whiteheadwhole} = 0.14 Sv$, where $q_{whiteheadwhole}$ is the flux for the whole channel, equal to that on the LHS, as both corresponding Rossby numbers are less than unity. The single (reduced gravity) layer prediction would be three times $q_{whiteheadwhole}$. In comparison, the mean outflow transport is found to be $0.15Sv$ (Johns *et al.*, 2003), which is close to the prediction for the whole channel, if it is treated as a two-layer flow. If we used each channel individually (i.e. $q_{whiteheadR} + q_{whiteheadL}$) or the single active layer prediction, the observed flux would be much lower than the prediction. Thus the system is likely to be, at least for part of the year, a two-layer exchange flow with both island sides not independent of each other.

Effects responsible for reducing the observed flux may be friction and mixing, a net-flux into the evaporative Straits basin, a centrifugal effect due to topographic steering, such as observed in Oresund between Denmark and Sweden (Nielsen, 106), and time-dependence, as the region is found to be strongly tidal. As the water is directed around the North tip of a peninsula centrifugal effects of the topographic bend act against the Coriolis acceleration for the outflow, which may lead to an effectively larger Rossby radius and thus higher R_0 and higher flux. In terms of time variability, the moored current meter data in Johns *et al.* (2003) shows that at times the tides arrest the deep outflow and even reverse the near-surface inflow. The tides are found to be predominantly barotropic and aligned along the deep topographic channel, which is equivalent to imposing a temporarily increased net-flux to the exchange. However, time-variability in hydraulically controlled exchange flows is still very much a topic of ongoing research with progress to date only made for the non-rotating case (Helfrich, 1995). In addition to tides, the surface layer is found to be seasonally variable and actually reverse to an outflow above the deep one during long periods in the year. However, this water could be recirculating back into the inflow further toward the mouth of the strait (Johns *et al.*, 2003).

Figure 7.1(b) (p.182) also shows a sketch of the approximate density interface location from various SeaSoar (towed undulating platform) surveys during the cruise mentioned in Johns *et al.* (2003). It is clearly visible that the current is banking up on the South side (RHS, if seen from the lower layer flow direction) with a markedly more inclined interface in the larger half of the channel. The intersection of the interface with the channel floor on the

LHS is slightly further away from the RHS wall than the distance $R + w_{island}$, which can be attributed to the upward sloping channel floor there. This is likely to cause the interface to rise due to volume conservation.

The choice of flow path in the Straits of Hormuz may also show similar change in flow regimes as in our island experiments for $R_0 < 1$. Such may be initiated by the tidal or seasonal variability found in Johns *et al.* (2003)'s data. Since the island is relatively short, the flow, already influenced by the constricting bottom topography, has more opportunity to cross the channel before reaching the island and being confined to one channel half. Nevertheless, as the surface flow has a much larger cross-section than the deep flow, a type of split regime may also occur. It is conceivable that most of the outflow would pass through the RHS of the island, close to the peninsula, with the surface inflow largely confined to the slowly shallowing LHS of the cross-section. However, the surface flow is found to recirculate, as mentioned above, which could prevent the occurrence of a split regime. Regardless of the regime occurring due to time-variability the theoretical flux estimate shown above agrees remarkably well with the observed annual mean flux.

The Sicily channel, as mentioned in section 2.2.2 (p.35), also shows seasonal variability in the paths of the overflow. The overall flow is a two-layer exchange between the Eastern and Western Mediterranean, with near-surface water of mainly Atlantic origin and deeper water(s) originating in the Eastern Mediterranean. However, the deep flow is more likely to be representative of a single-layer flow, as the upper layer occupies a much larger area in the strait cross-section at the sills and is dominated by mesoscale processes, some of which are associated with shelf topography (Gasparini *et al.*, 2004; Napolitano *et al.*, 2003). Nevertheless, it highlights the complexity that may occur, for example due to local topographic deeps or the angle of the ridge to the shelf boundary to its right. These two examples are likely to be responsible for the return flow of the jet into the channel on the right, as shown in the hydrographic section in figure 2.2, p.38, and represents an example of flow around a cape (Serra *et al.*, 2002; Sadoux *et al.*, 2000; Cenedese and Whitehead, 2000). This circumvention of the tip by the deep flow does not occur to the same extent in our experiments, as the island was symmetrically aligned with the channel walls. This and the existence of shallow shelfs to either channel side would be an interesting extension to this work for the future.

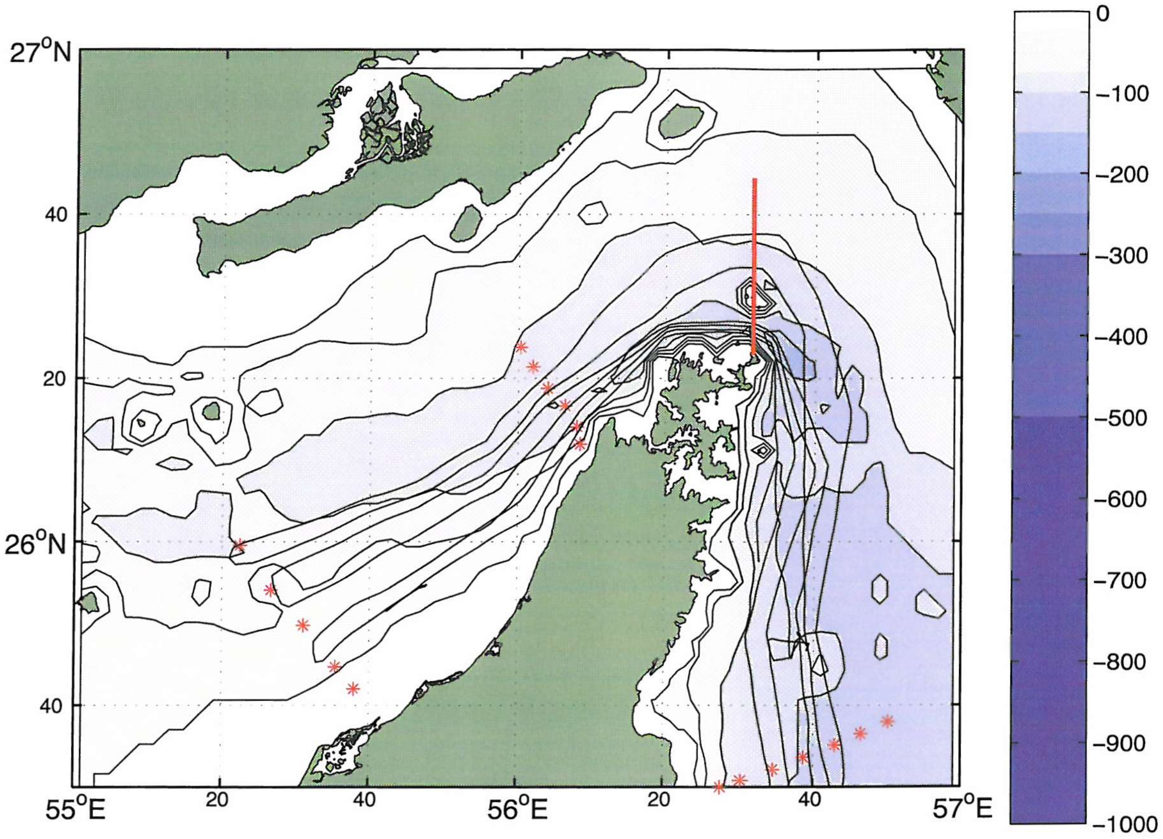

(a) Whole strait (depth in m).

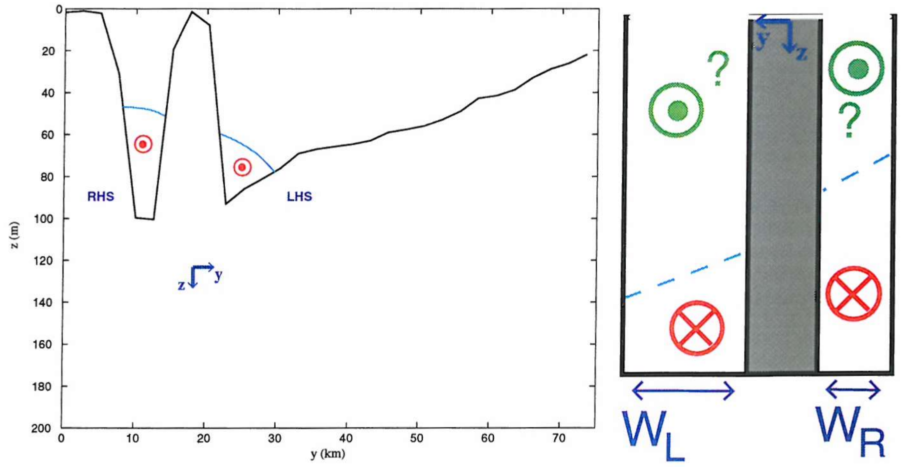

(b) Peninsula tip cross-section.

(c) Sketch of simplified cross section.

Figure 7.1: Latitude-longitude plot of bathymetry in the North-eastern part of the Straits of Hormuz region (depth given in m). The region of interest is located at the tip of the Southern peninsula. A cross-section there, marked as a red line, has an island separating the deep outflow in two parts. Both the real and simplified rectangular cross-sections are shown. The latter has the y-axis in the way used throughout the rest of this thesis. The plot of bathymetry and the interface location are courtesy of David Smeed.

Chapter 8

Conclusion and future work

8.1 Conclusions

- For the first time rotating exchange flows were modelled on a large lab platform with measurements of horizontal velocity fields. An island was introduced as this situation has been seen to lead to distinct flow features in oceanic exchange flows. Additional experiments to measure density fluxes and interface depth were carried out on a small platform.

- A quasi-steady regime is identified for $R_0 > 1$, where the flow is generally attached to both walls at the narrows and leads to baroclinic flow across the channel, both in simple channel cases and with an island: there, flow fields and fluxes behave approximately as predicted by previous simple-channel theory (D88, Dalziel, 1990; Whitehead *et al.*, 1974). The introduction of an island showed similar behaviour only if a reduction in channel width is accounted for. Analysis of narrows fluxes and interface slope in each channel half for $R_0 > 1$ shows that the flows on either island side are part of one whole exchange flow instead of independent ones, despite the separation of the channel into two halves by the island. Such flows are found to be most likely hydraulically controlled in the vicinity of the narrows, as indicated by the depth of the interface over the whole channel. An exception may be some simple channel cases with $R_0 \leq 0.9$, where initial conditions may determine the position of the current-crossing and hydraulic control.

- For $R_0 < 1$ the flows are found to be unsteady but some distinct flow regimes could be identified: quasi-steady regimes are found for $R_0 \sim 0.7$, where both 'dual' (baroclinic flow across whole channel) and 'split' (uni-directional but baroclinic on each island side) flow occurred. The former is separated at the narrows and crosses near the island tips, indicating it may actually form separate exchange flows on each island side. Further reduction in R_0 leads to flow separation and vortices: the simple channel case shows an exchange flow, crossing at the narrows at certain times in the experiment. The island case shows further unique split regimes, with unidirectional flow on each island side: one baroclinic and one almost barotropic on each island side.

- Despite much variability, flows with $R_0 < 1$ still show fluxes generally in agreement with the simple channel theory mentioned above. The exception is the barotropic split regime that is associated with a much higher flux than theoretically predicted, although still less than the theoretical value for a single-layer (reduced) gravity flow through each channel half. Such flow could not easily be categorised but it is noted that hydraulic control for any of the split regimes observed is still likely to occur in the vicinity of the narrows, where the current crosses the channel. However, this type of flow may require additional controls, such as at the island tips, to be isolated from both reservoirs with respect to baroclinic waves.
- Viscous effects are found to be measurable and can be identified by comparison to previous studies, including oceanic example cases where frictional effects are important. However, conditions are still such that a close-to-inviscid, hydraulically controlled exchange is indicated.
- Boundary layer separation could be found at the island tip, which may play a role in the choice of current paths during the regimes identified, in particular when recirculation within such regions occurs for $R_0 << 1$.
- The results are found to be relevant to oceanic cases with respect to the accuracy of hydrographic exchange flux estimates and the correction of channel width in the island cases proposed in this study.

8.2 Future work

- The length and width of the island is likely to be a factor affecting the independence of the passages on each island side and hydraulic control, represented by the propagation of internal waves. Investigation of the latter would require simultaneous density and velocity measurements, in particular in the vicinity of the island tip.
- Reservoir joining conditions, viscous effects with rotation, such as mixing and entrainment, wave propagation. Numerical model experiments would be useful to find

interesting parameter ranges that could then be studied in the laboratory.

- Time-variability, including the establishment of the quasi-steady exchange flow and vortex propagation for $R_0 << 1$, is another unresolved problem and will be the focus of further study of the data presented in this thesis and of the associated experiments not yet presented.

Appendix A

CIV peak-locking error

For time averaged fields the uvmat utility allows to calculate an estimate the peak-locking error by taking a time average histogram of all vectors, regardless of position but binned by their actual displacement values, D_a (see Fincham and Delerce, 2000). Such a histogram, or probability density function (pdf), for the u-component of the displacement vector can be found in figure A.1 (p.187), binned at 0.1 pixel intervals (D_{real}) and normalised in a way that the total integral under the curve is equal to unity. Here 117 vector fields all at the same laser level have been used, giving a total of $6 \cdot 10^5$ displacement values for each vector component. Also shown is a 1 pixel mean pdf (D_{hist}), centred on each integer displacement. This should contain no mean-bias or peak-locking error as the peak-locking error varies regularly with period 1 pixel (Fincham and Spedding, 1997; Fincham and Delerce, 2000). The mean pdf can be interpolated using a spline under the condition that the integral over each 1 pixel bin is conserved. Therefore, this splined curve (D_{spline}) is also free of mean-bias. By comparing D_{spline} and D_{hist} one can estimate the peak-locking error in pixels for different pixel displacements (Joel Sommeria, pers. comm.). No significant RMS error is expected, as we have a large number of samples. The peak-locking error is not eliminated by time-averaging, as it is dependent on the actual displacement value. Therefore, this method works because it utilises a large number of independent samples. Figure A.2 (p.188) shows that the error is generally ~ 0.1 pixels.

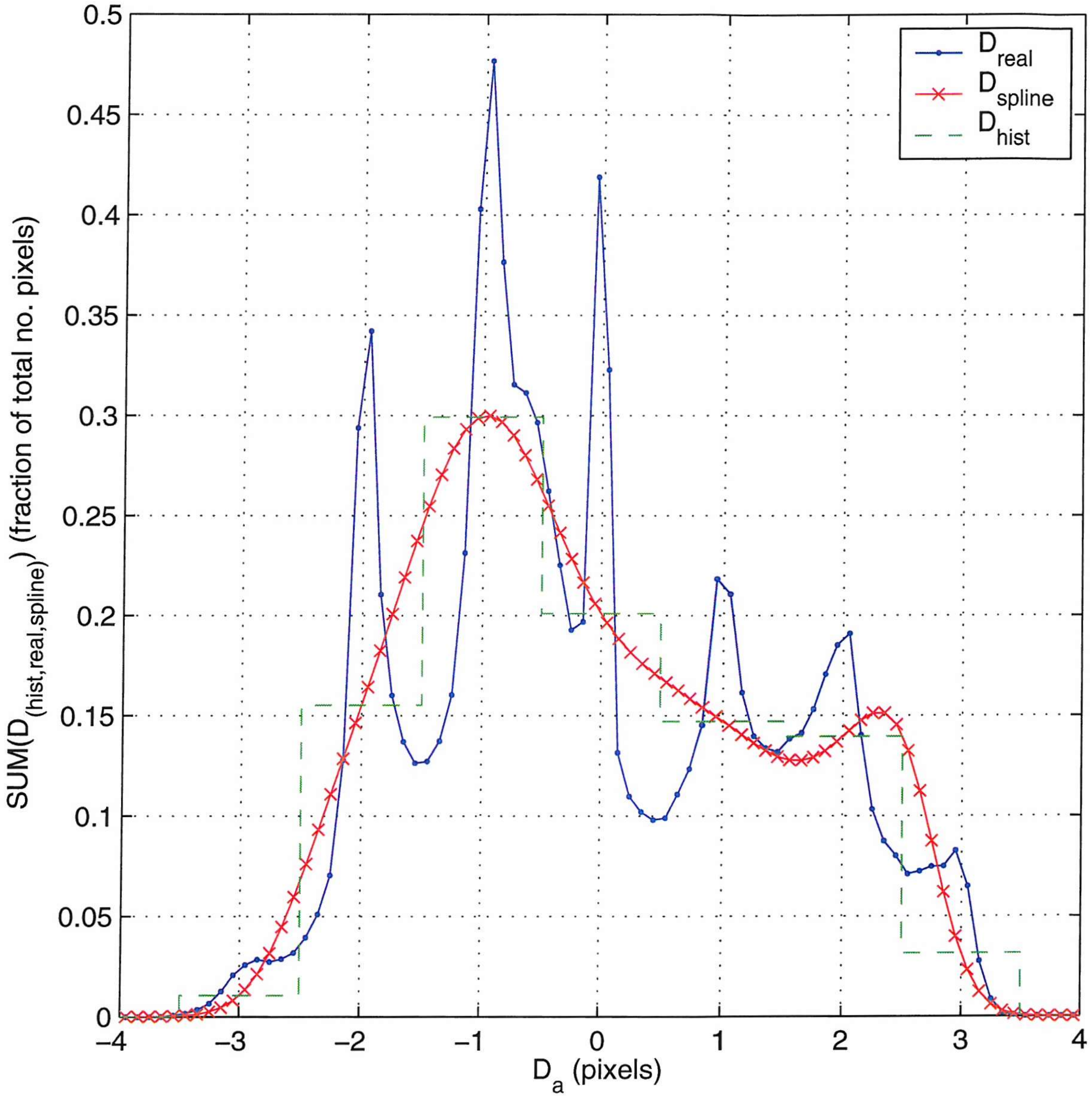

Figure A.1: Probability density function (pdf) for the u-component of a time series of displacement vector fields (experiment 15 is chosen as an example). Note the histogram bars (binned pdf, D_{hist}) and the splined mean pdf (D_{spline}) both have the same integral over a 1-pixel bin, which eliminates any peak-locking (mean-bias) error. The real pdf (D_{real}) includes this error. The total integral over the whole pixel range is conserved for all pdf's.

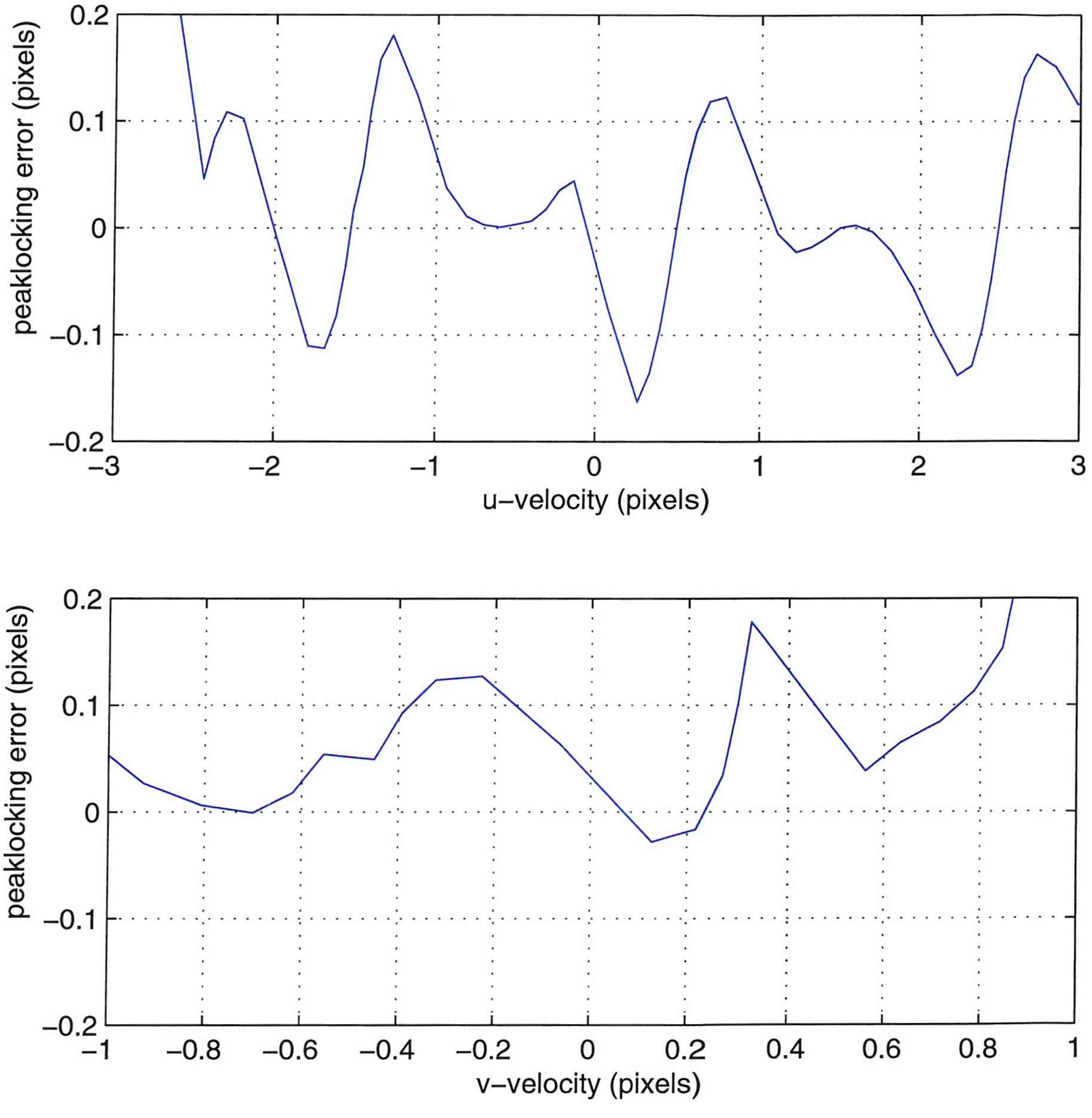

Figure A.2: Peak-locking (mean-bias) error from comparison of splined mean pdf and real pdf in figure A.1 (p.187). Note the period of approximately one pixel in error variability with pixel displacement. Values are generally ~ 0.1, with some peaks ~ 0.15.

Appendix B

Time-series of fluxes and interface depth

The time series shown here are generally similar to the ones in section 4.2.1 (p.85). Notable is the non-rotating case with an island in figure B.1 (p.190). Note that $t = 0$ starts when the barrier just leaves the water, so that some dense flow is able to propagate toward the narrows beforehand. A rapid initial adjustment within $t \sim T_L^{-1}$ can be seen, which signifies the passing of the gravity current. This process is approximately 2-dimensional with little variability in the y-direction, so that no fronts are following the gravity current here as in the rotating cases.

After some fast oscillations near the beginning, the fluxes are more or less varying around a mean value after $t \sim 7.5T_L^{-1}$. Near the end a noticeable increase can be seen which may be a returning gravity current or bore reflected within one of the reservoirs. This agrees with visual observations near the end of the experiment where particle streaks on the dense reservoir floor near the channel end were found to be disturbed, likely by a passing (turbulent) internal bore. The overall variability of $\bar{q}$ is similar to the high R_0 cases (experiments 6 and 7 shown in figures B.3, p.193 and 4.1, p.86, respectively), except that the final decrease in fluxes is not recorded. Experiment 14 has a much lower g' and thus q_{nr} than the rotating experiments.

The flux on each island side, also shown in figure B.1 (p.190), indicates some non-uniformity in the cross-channel direction. However, when compared with the flux errors of the exchange through the whole cross-section (blue line), the differences are generally small. The variability is likely caused by strong shear and errors due to the finite number of vertical laser levels. Note that the measured net flux along the channel, represented by the error bars, is not only due to the finite spacing of our vertical laser sheets and the CIV algorithm, but also to potential mixing and entrainment from one layer to the other (see section 6.2.2, p.146). However, the error magnitude is generally around 10% of $\bar{q}$ which is similar to the predicted accuracy

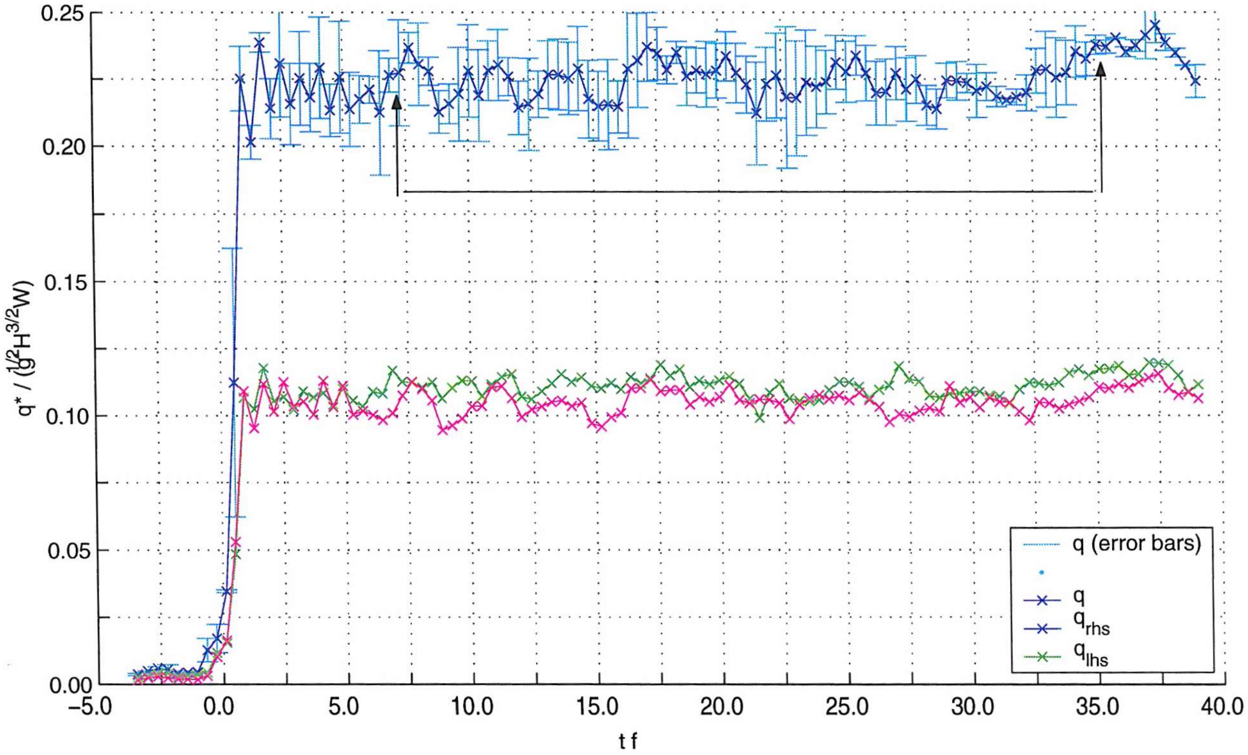

Figure B.1: Time series of narrows exchange flux ($\bar{q}$) for experiment 14 (island, non-rotating). Error bars represent the difference between the flux in each layer (in each along-channel direction), so that the ends of the bars represent $\frac{1}{2}$ the flux in each layer and the crosses the mean exchange flux. Also shown are the exchange fluxes within each island side-channel, both of which add up to the total exchange flux. Fluxes are non-dimensionalised as described in section 3.2.1 (p.45). In this non-rotating example, time units are non-dimensionalised by the time it takes the gravity current to pass half the channel (t is multiplied by $T_L^{-1} = \frac{2\cdot\sqrt{g'H}}{L}$). The initial rise of fluxes occurs within $t \sim 1$, i.e. T_L, and show fairly steady fluxes afterwards with some oscillations of similar order as the error bars. Note the fluxes in each island side-channel are almost the same, differences being within the margin of the error in the total exchange flux.

in table 3.3 (p.77).

These findings suggest that an average over most of the experiment, after the initial adjustment but before the return of any internal bores, is likely to give the best estimate of the quasi-steady two-layer exchange flow. The existence of such steadiness for the majority of the non-rotating experiment is indeed encouraging. We showed that the same applies to the rotating experiments with $R_0 \gtrsim 1$.

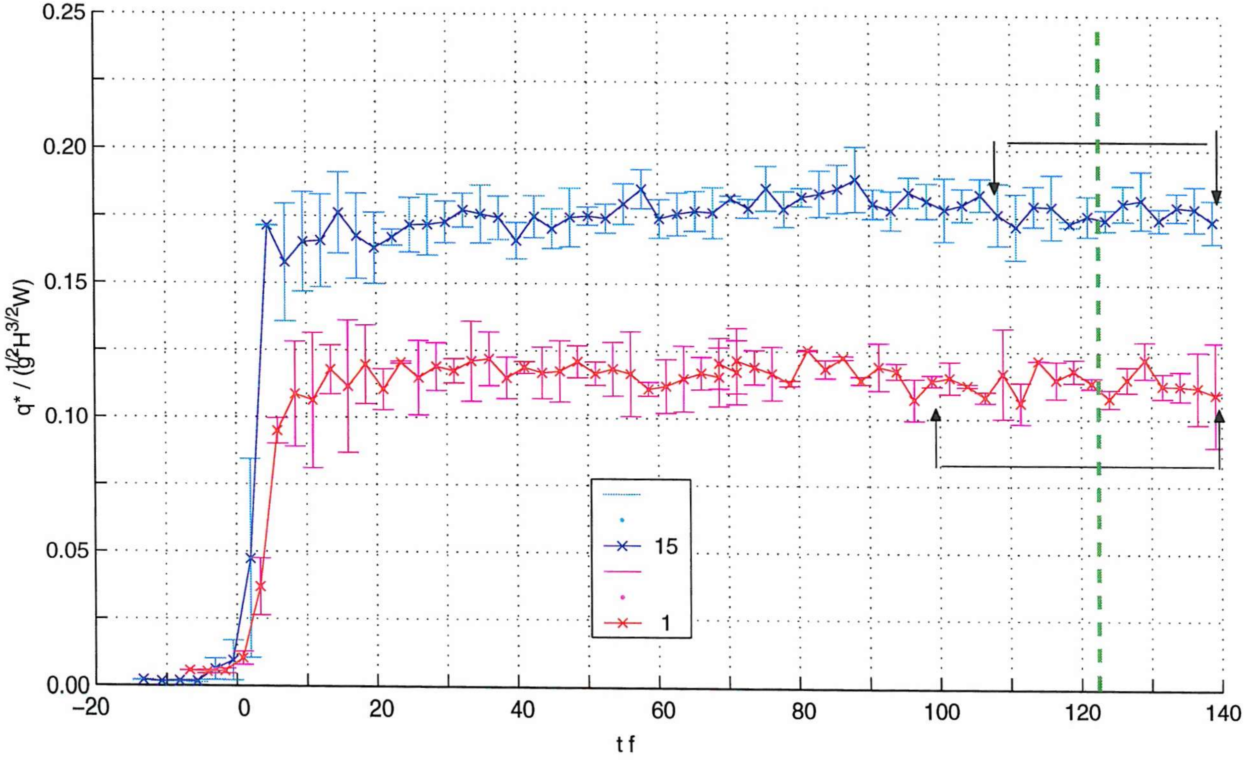

Figure B.2: Time series of $\bar{q}$ as in figure 4.1 (p.86) for experiments 1 and 15 (simple channel, $R_0 = 0.90$ and island $R_0 = 1.22$, respectively). Note the similarity in the variability of $\bar{q}$, despite the difference in channel geometry (i.e. presence of the island); differences in $\bar{q}$ are found when analysing the time-mean fluxes in section 6.1 (p.133). In both experiments, the initial adjustment is less rapid than in the higher R_0 cases and missing the initial strong peak. Conditions are quasi-steady toward the end, which gives an averaging time period (as marked by the arrows) around the spin-up time, so that any boundary layers should be fully developed.

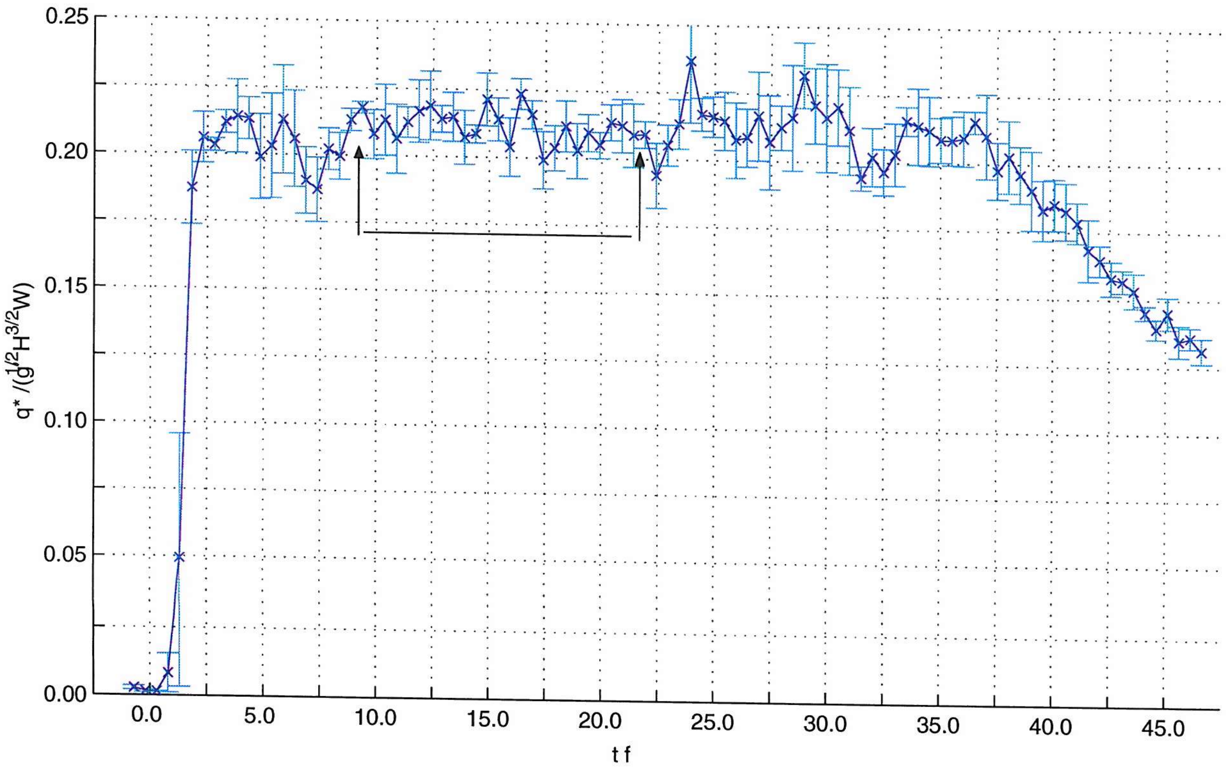

Figure B.3: Time series of $\bar{q}$ as in figure 4.1 (p.86) for experiment 6 (island $R_0 = 6.37$, respectively).

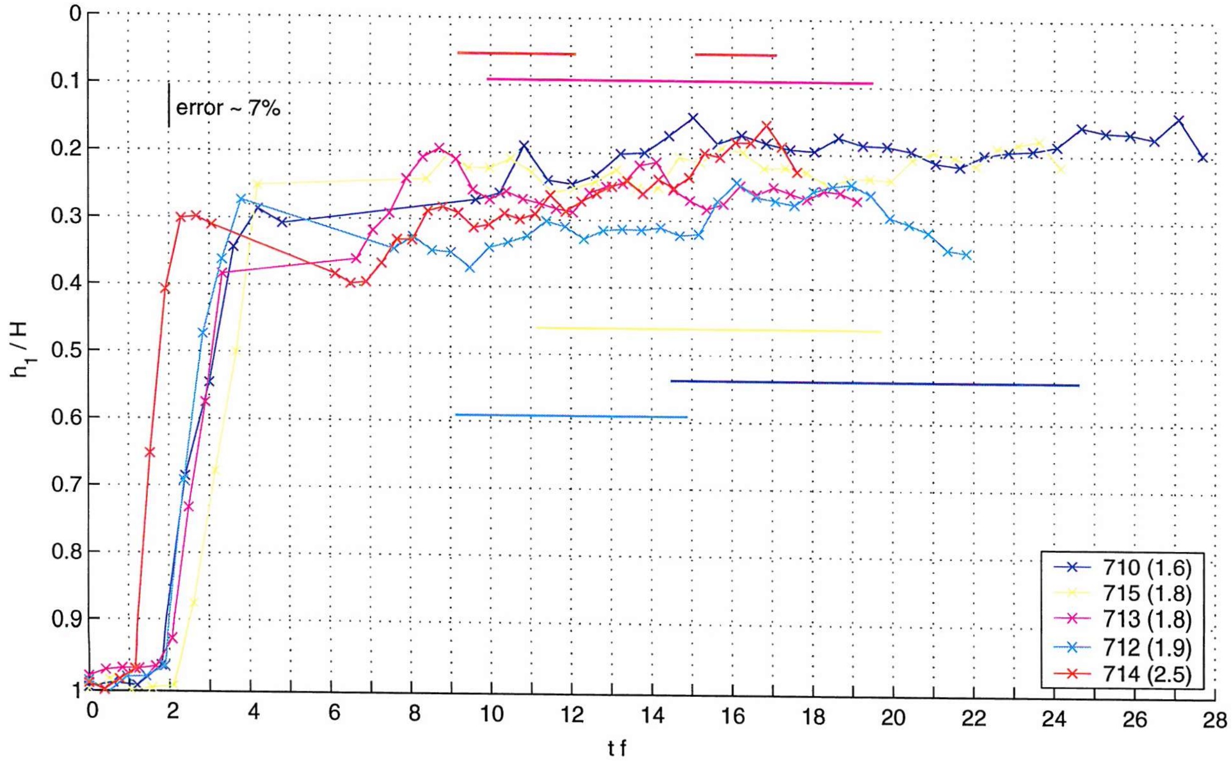

Figure B.4: Time series of interface height on RHS near narrows for experiments 710 and 712 through to 715. Corresponding Rossby numbers are given. Measurement error is 7% as shown. Also shown are the times chosen for averaging (solid horizontal lines corresponding to experiment time series of same colour)

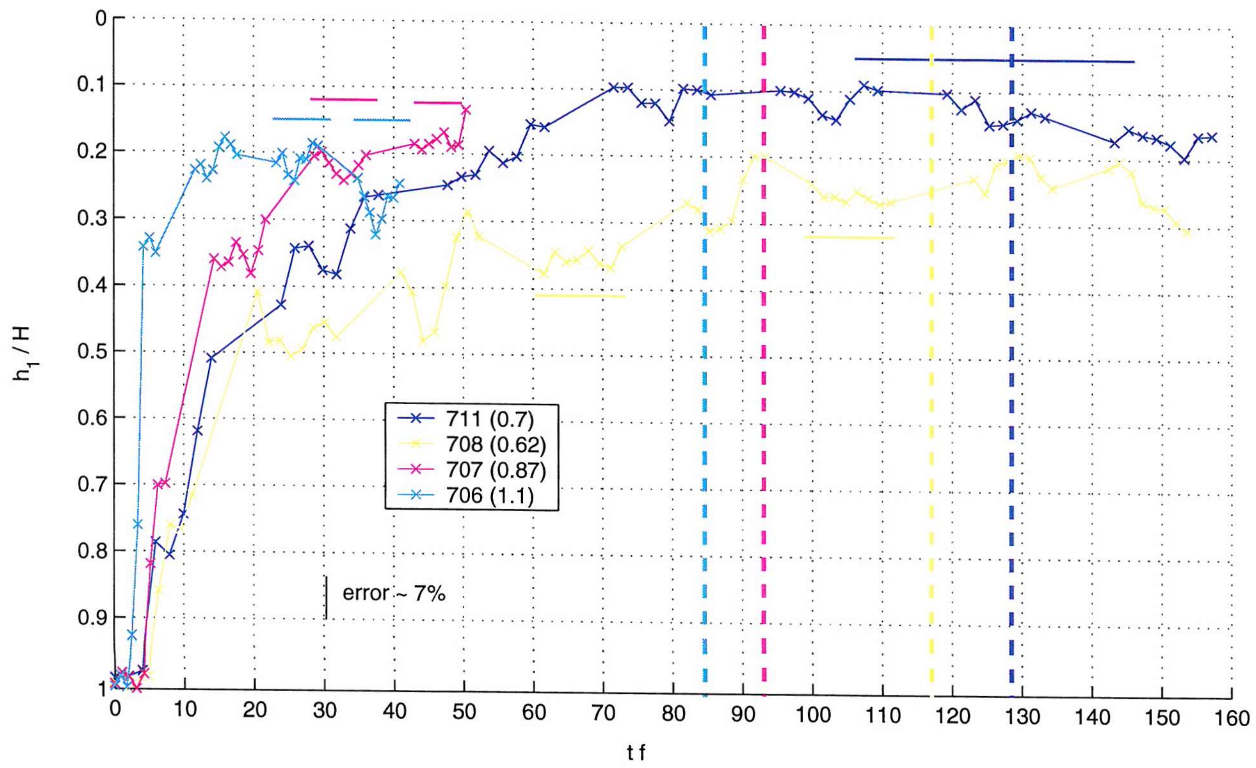

Figure B.5: Time series of interface height on RHS near narrows for experiments 711, 708, 707 and 706. Corresponding Rossby numbers are given. Measurement error is 7% as shown. Also shown are the times chosen for averaging (solid horizontal lines corresponding to experiment time series of same colour)

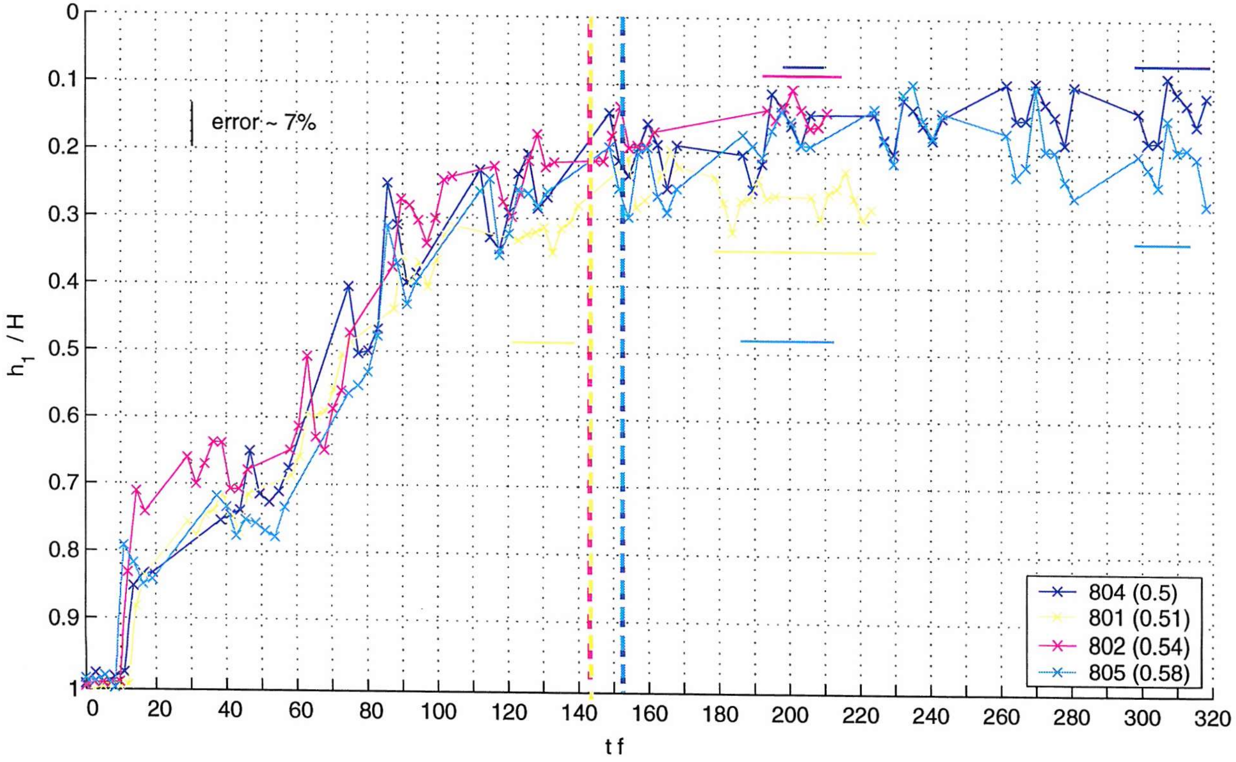

Figure B.6: Time series of $h_R(T)$ on RHS near narrows for experiments 801, 802, 804 and 805 with corresponding Rossby numbers given. Measurement error is 7% as shown. Also shown are the times chosen for averaging (solid horizontal lines corresponding to experiment time series of same colour). Note the very gradual initial adjustment but the fairly constant $h_R(t)$ toward the end, similar to the simple channel cases with $R_0 > 1.5$ (figure B.4, p.194.

Appendix C

Time-averaged flow fields

This Appendix shows some of the flow fields not presented in chapter 5 (p.105). Noteworthy is the increase in cross-channel slope of the interface throughout the channel as R_0 decreases from $\sim$ 6 to $\sim$ 2.5 (figures C.1, p.198 and C.2, p.199). The first regime in experiment 3 ($R_0 \sim 0.7$) represents a partly-dual and partly-split regime and is shown in figure C.3 (p.200). The flow on each side is mostly uni-directional with a slow but measurable return current above (below) the dense (light) current.

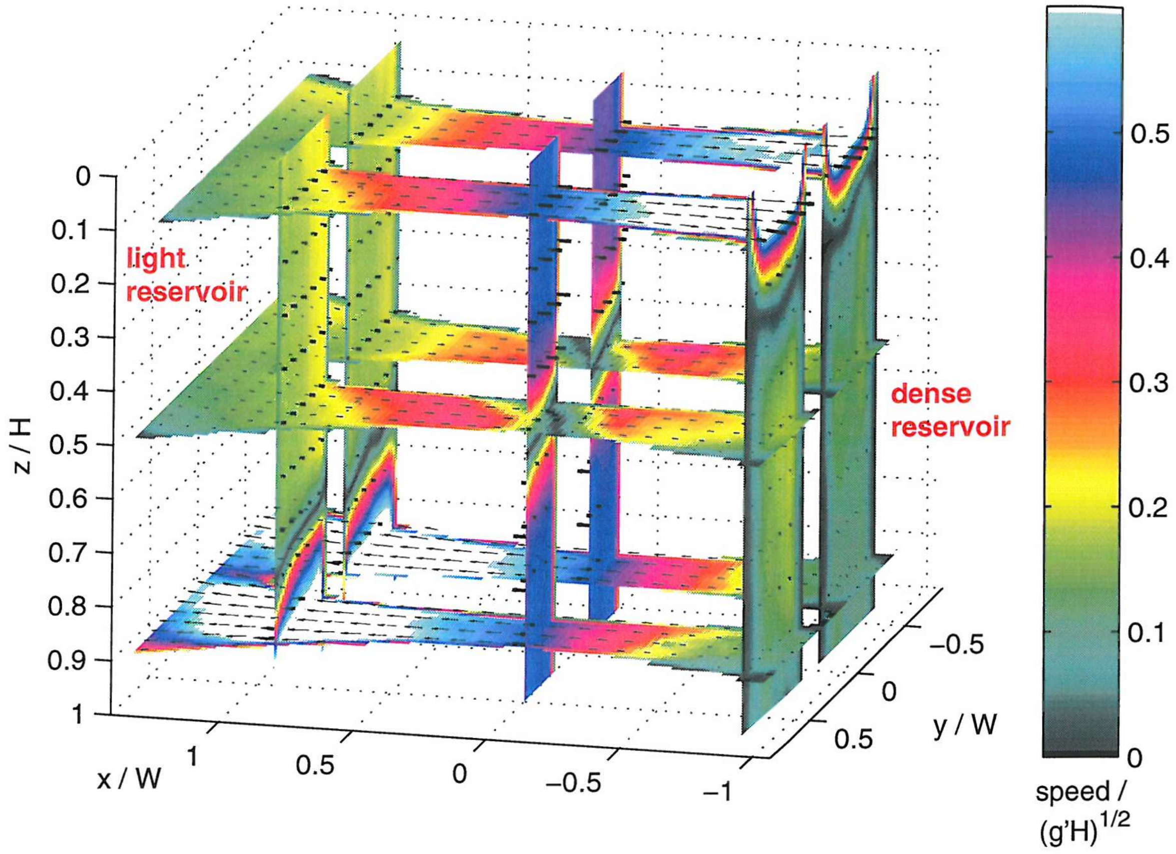

(a) Velocity vectors and speed

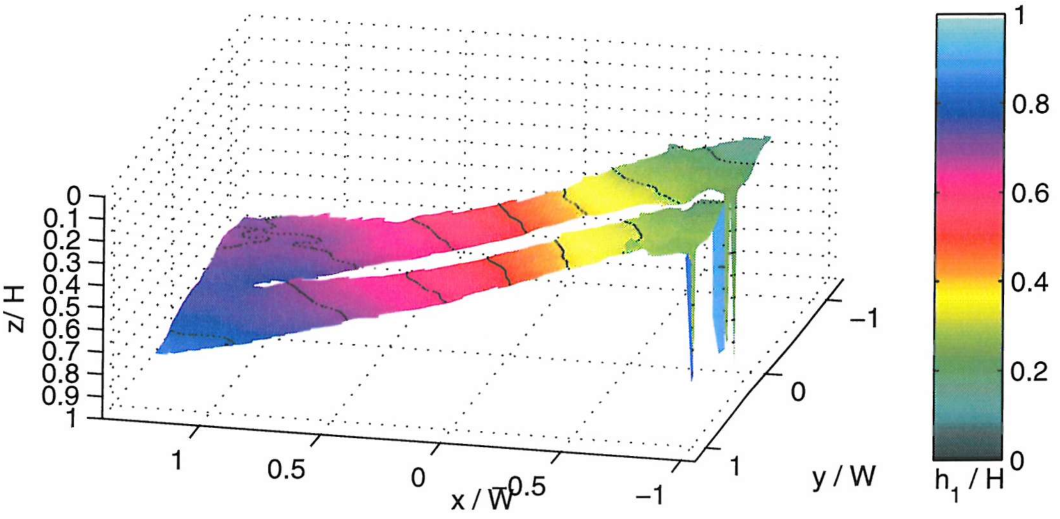

(b) Interface depth

Figure C.1: Horizontal velocity vectors, speed and shear interface position as in figure 5.9 for experiment 6 ($R_0 = 6.37$, island) during the quasi-steady period. The no-data area in the channel centre represents the island. Note the shallow cross-channel slope and the velocity mostly steered by channel geometry. A vertical offset, not occurring in the simple channel case, is evident in the shear interface attaching on both island sides.

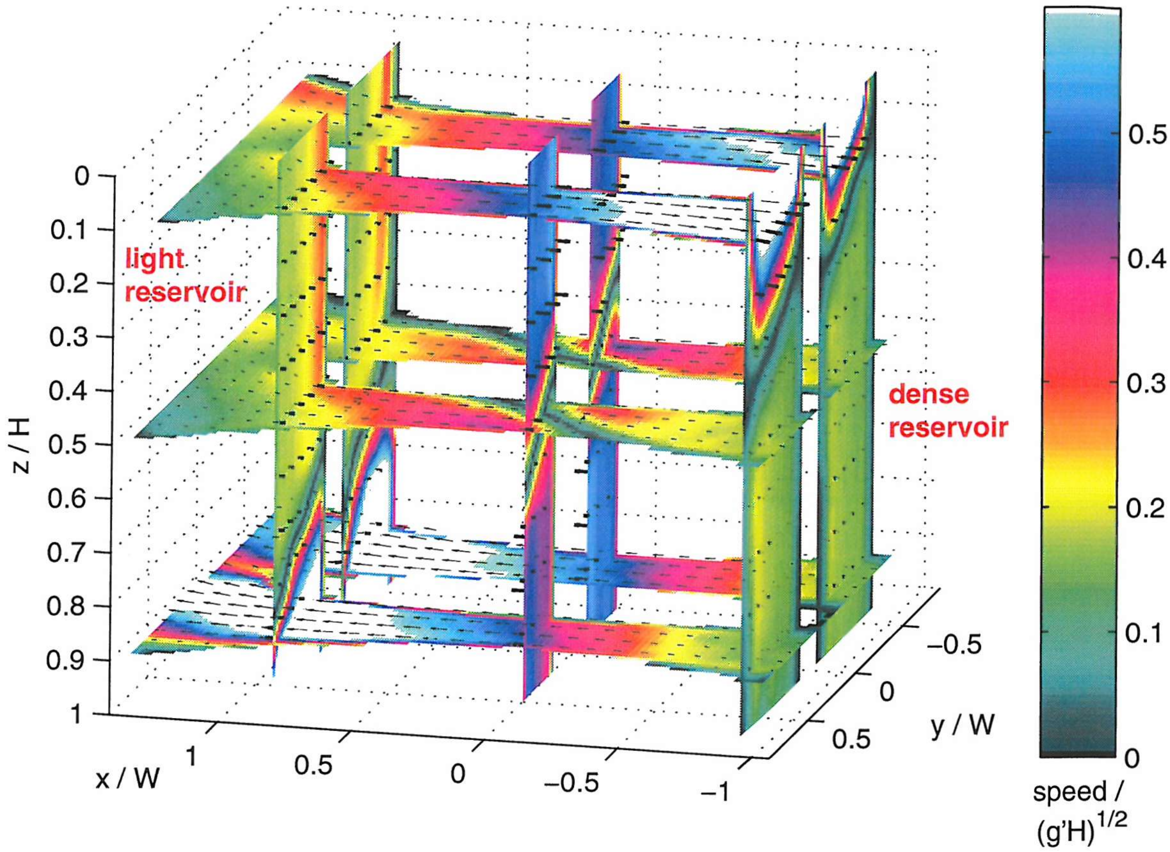

(a) Velocity

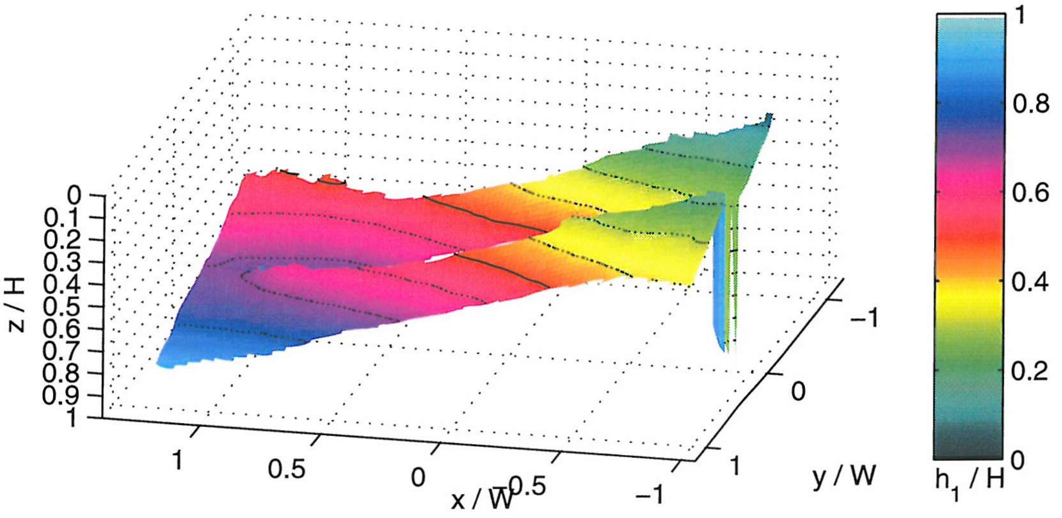

(b) Interface depth

Figure C.2: Horizontal velocity vectors, speed and shear interface position as in figure 5.9 for experiment 4 ($R_0 = 2.49$, island) during the quasi-steady period. No separation regions can be seen near the sidewalls, although on the LHS near the light reservoir at $z = 0.9$ we can see a region of very low velocity which extends beyond the badly lit area there. This is likely due to the outward curvature of the wall, the separation of the current from the island tip and the turning of the current toward the RHS due to the Coriolis force. The vertical offset in h between both island side channels is greater than in experiment 6 (figure C.1 (p.198)).

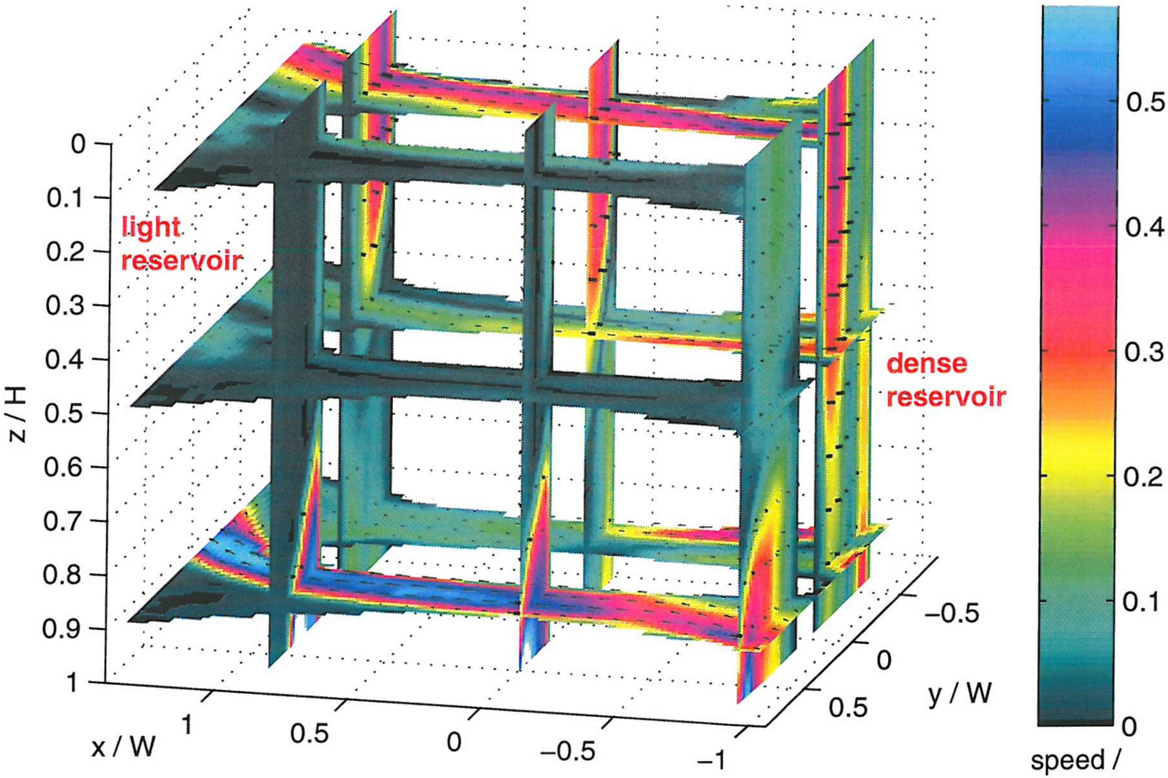

Figure C.3: Horizontal velocity vectors and speed as in figure 5.9 for experiment 3 ($R_0 = 0.67$, island) during the first quasi-steady period (table D.2, p.202). The shear interface not visible throughout most of the channel, except one the RHS at the narrows, and the exchange flow is almost 'split' between both channels. This may be considered intermediate to the fully 'split' and 'dual' regimes shown in figures 5.12 (p.123) and 5.11 (p.122), respectively.

Appendix D

Additional figures

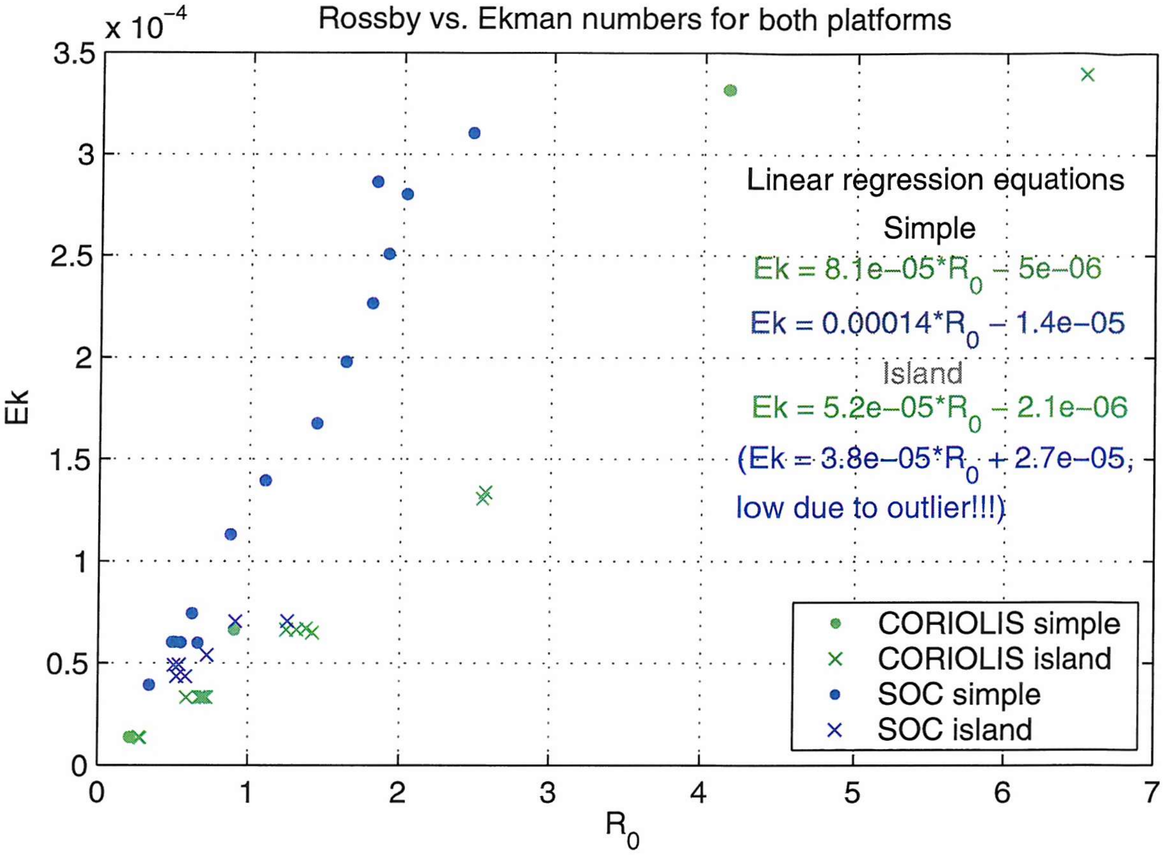

Figure D.1: Ekman numbers (Ek) on both platforms for different R_0. Island and simple channel cases are separated as f and thus Ek is different for the same R_0. The slope for the *Coriolis* platform, shown in the linear regression equations, is almost half of that for the *SOC* platform.

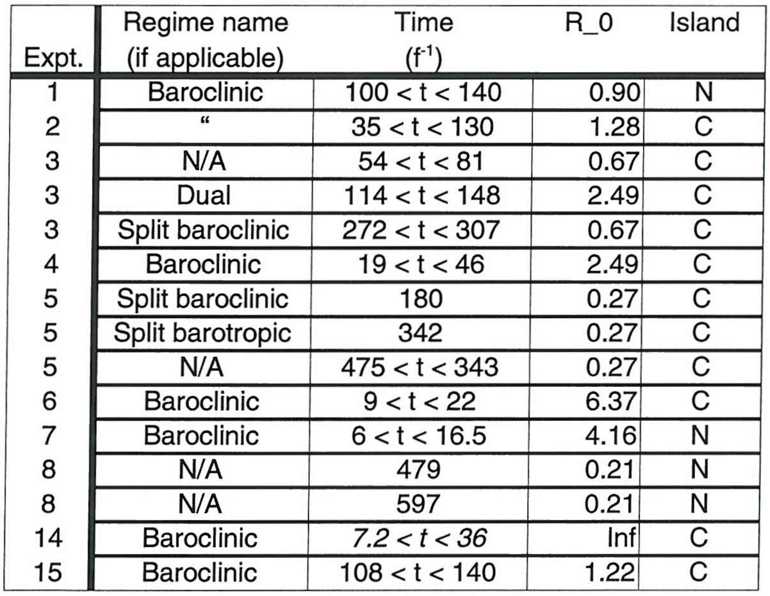

Expt.	Regime name (if applicable)	Time (f^{-1})	R_0	Island
1	Baroclinic	100 < t < 140	0.90	N
2	“	35 < t < 130	1.28	C
3	N/A	54 < t < 81	0.67	C
3	Dual	114 < t < 148	2.49	C
3	Split baroclinic	272 < t < 307	0.67	C
4	Baroclinic	19 < t < 46	2.49	C
5	Split baroclinic	180	0.27	C
5	Split barotropic	342	0.27	C
5	N/A	475 < t < 343	0.27	C
6	Baroclinic	9 < t < 22	6.37	C
7	Baroclinic	6 < t < 16.5	4.16	N
8	N/A	479	0.21	N
8	N/A	597	0.21	N
14	Baroclinic	*7.2 < t < 36*	Inf	C
15	Baroclinic	108 < t < 140	1.22	C

Figure D.2: Averaging times for *Coriolis* experiments, as marked in the figures in section 4.2.1 (p.85) and this appendix. In the case of multiple averaging times, a descriptive regime name is also given.

	Dz		R_0		%-difference	b.l. Thickness
Expt.	Measured	Inferred	Measured	Inferred	(inferred-measured)	(%W)
6	0.10	0.11	6.37	7.0	11	23.2
7	0.20	0.24	4.16	5.0	20	16.0
4	0.25	0.28	2.49	2.8	13	18.5
714(2)	0.35	0.41	2.46	2.9	16	
712	0.45	0.52	1.91	2.2	16	
713	0.45	0.55	1.83	2.2	21	
715	0.40	0.56	1.80	2.5	39	
710	0.55	0.61	1.63	1.8	12	
807(1)	*0.60*	*0.53*	1.30	1.2	-11	
2	0.50	0.55	1.28	1.4	10	15.6
15	0.55	0.58	1.22	1.3	5	15.6
706	0.60	0.91	1.10	1.7	52	
806	0.95	*0.77*	0.90	*0.7*	*-19*	
707	0.80	*1.15*	0.87	*1.3*	*44*	

Table D.1: Expected (inferred) cross-channel slope, $dz_W = \frac{dz}{W}$, from measured R_0, using equation 5.2 (p.110). The calculation was also reversed, using the dz_W from the figures in section 5.2.1 (p.108). This inferred R_0 gives an idea of the effect viscous processes near the walls have on the exchange in effectively narrowing the channel (increasing R_0 or decreasing dz_W).

Appendix E

Typical experimental procedure at *Coriolis*

Two-layer Rotating Exchange Experiments at 'Coriolis' / LEGI (Grenoble, France)
Summary Report for visit from 20/10 to 22/11/2002

Project Participants:

Dalziel, Stuart
Lane-Serff, Gregory
Rabe, Benjamin
Smeed, David

Typical Experimental Procedure

1. Modify reservoir densities by adding salt/fresh-water and start mixers (min. 1h)
2. Switch off mixers / Start Spin-up (min. 2h total)
3.a Sweep tank bottom and walk around in tank to suspend particles and mix water
3.b Clear laser glass window off bubbles and clean top of salt, if necessary
(steps 2 and 3 have sometimes been reversed, but it was later found that sweeping nearer the experiment resulted in better particle suspension / less settling)
4. Measure density / sample, often take hand-held thermometer readings (mercury and electronic)
5. Leave to settle (min. 1h)
(in cases where 4 and 5 were reversed, care was taken not to create much motion)
6. Turn on temp. probes, laser (also cooling water), cameras and motor power
7. Start probes and profiling
8. Set up SMD and PULNIX and start acquisition (this is where the stopwatch starts!!!; however, experiment running times have been corrected for this)
9. Raise barrier appr. 2 mins. after SMD acquisition start (takes appr. 20s from bottom to water surface) and swing out of SMD view; record stopwatch time
10 Run experiments for 30 to 90 minutes (depending on rotation etc.); PULNIX only at intervals; sometimes stop/restart SMD to take some constant laser level images

11. Stop SMD (shutter on!) and then probes
12. Switch on lights, put barrier in place and lower; switch off all motors, cameras, laser and temperature probes (BUT leave other probes powered on)
13. Mixers on and spin down
14. Measure final densities and take samples

Bibliography

Alessio, S., Briatore, L., Ferrero, E., Longhetto, A., Giraud, C., and Morra, O. (1992). Interaction between atmospheric flows and obstacles: experiments in a rotating channel. *Boundary-Layer Meteorology*, pages 235–241.

Anati, D., Assaf, G., and Thompson, R. (1977). Laboratory models of sea straits. *Journal of Fluid Mechanics*, 81:341–351.

Apel, J. (1987). *Principles of ocean physics*, volume 38 of *International Geophysics Series*. Academic Press: London.

Armi, L. (1986). The hydraulics of two flowing layers with different densities. *Journal of Fluid Mechanics*, 163:27–58.

Armi, L. and Farmer, D. (1988). The flow of Mediterranean water through the Strait of Gibraltar. *Progress in Oceanography*, 21:1–105.

Astraldi, M., Balopoulos, S., Candela, J., Font, J., Gacic, M., Gasparini, G., Manca, B., Theocharis, A., and Tintore, J. (1999). The role of straits and channels in udnerstanding the characteristics of Mediterranean Circulation. *Progress in Oceanography*, 44:65–108.

Astraldi, M., Gasparini, G., Sparnocchia, S., Moretti, M., and Sansone, E. (1996). The characteristics of the water masses and the water transport in the Sicily Strait at long time scale. In *Bulleting de l'Institut oceanographique, Monaco*, number special 17 in CIESM Science Series no. 2, pages 95–115. Institut oceanographique, Monaco.

Bigg, G., Jickells, T., Liss, P., and Osborn, T. (2003). The role of the oceans in climate. *International Journal of Climatology*, 23(10):1127–1159.

Blanchonette, P. (1998). Two-layer flows past a cylinder in a rotating frame. *Journal of Fluid Mechanics*, 371:301–318.

Borenas, K. and Lundberg, P. (1988). On the deep water flow through the Faeroe Bank Channel. *Journal of Geophysical Research*, 93(C2):1281–1292.

Borenas, K. and Lundberg, P. (1990). Some questions arising from the application of hydraulic theory to the Faeroe Bank Channel deep-water flow. *PAGEOPH*, 133(4):573–585.

Borenäs, K. and Whitehead, J. (1998). Upstream separation in a rotating channel flow. *Journal of Geophysical Research*, 103(C4):7567–7578.

Boyer, D. and Davies, P. (2000). Laboratory studies of orographic effects in rotating and stratified flows. *Annual Review of Fluid Mechanics*, pages 165–202.

Brandt, P., Rubinno, A., Sein, D., Baschek, B., Izquierdo, A., and Backhaus, J. (2004). Sea level variations in the western Mediterranean studied by a numerical tidal model of the Strait of Gibraltar. *Journal of Physical Oceanography*, 34(2):433–443.

Bryden, H. and Kinder, T. (1991). Steady two-layer exchange through the Strait of Gibraltar. *Deep Sea Research*, 38:S445–S463.

Cenedese, C. and Whitehead, J. (2000). Eddy shedding from a boundary current around a cape over a sloping bottom. *Journal of Physical Oceanography*, 30:1514–1531.

Dalziel, S. (1988). *Two-layer hydraulics: maximal exchange flows*. PhD thesis, Department of Applied Mathematics and Theoretical Physics, University of Cambridge.

Dalziel, S. (1990). Rotating two-layer sill flows. In Pratt, L., editor, *The Physical Oceanography of Sea Straits*, pages 343–371. Kluwer Academic.

Dalziel, S. (1991). Two-layer hydraulics: a functional approach. *Journal of Fluid Mechanics*, 223:135–163.

Dickson, B., Meincke, J., Vassie, I., Jugclaus, J., and Osterhus, S. (1999). Possible predictability in overflow from the Denmark Strait. *Nature*, 397(6716):243–246.

Farmer, D. and Armi, L. (1986). Maximal 2-layer exchange over a sill and through the combination of a sill and contraction with barotropic flow. *Journal of Fluid Mechanics*, 164:53–76.

Fedorov, A. and Melville, W. (1996). Hydraulic jumps at boundaries in rotating fluids. *Journal of Fluid Mechanics*, 324:55–82.

Fincham, A. and Delerce, G. (2000). Advanced optimization of correlation imaging velocimetry algorithms. *Experiments in Fluids*, pages S13–S22.

Fincham, A. and Spedding, G. (1997). Low cost, high resolution DPIV for measurement of turbulent fluid flow. *Experiments in Fluids*, 23:449–462.

Fritsch, F. and Carlson, R. (1980). Monotone piecewise cubic interpolation. *SIAM Journal of Numerical Analysis*, 17:238–246.

Garrett, C. (1996). The role of the Strait of Gibraltar in the evolution of Mediterranean water, properties and circulation. *Bulleting de l'Institut oceanographique, Monaco (CIESM Series No. 2)*, (17):1–19. CIESM Series No. 2, Briand, F.(ed.).

Garrett, C. and Gerdes, F. (2003). Hydraulic cotnrol of homogenous shear flows. *Journal of Fluid Mechanics*, 475:163–172.

Gasparini, G., Smeed, D., Alderson, S., Sparnocchia, S., Vetrano, A., and Mazzola, S. (2004). Tidal and subtidal currents in the Strait of Sicily. *Journal of Geophysical Research*, 109(C2):C02011.

Gill, A. (1976). Adjustment under gravity in a rotating channel. *Journal of Fluid Mechanics*, 77(3):603–627.

Gill, A. (1977). The hydraulics of rotating-channel flow. *Journal of Fluid Mechanics*, 80:641–671.

Gordon, A., Giulivi, C., and Ilahude, A. (2003). Deep topographic barriers within the Indonesian seas. *DRS-II*, 50:2205–2228.

Greenspan, H. (1968). *The theory of rotating fluids*. Cambridge University Press.

Gregg, M. and Özsoy, E. (2002). Flow, water mass changes, and hydraulics in the Bosporus. *Journal of Geophysical Research*, 107(C3). 10.1029/2000JC000485.

Grimm, T. and Maxworthy, T. (1999). Buoyancy-driven mean flow in a long channel with a hydraulically constrained exit condition. *Journal of Fluid Mechanics*, 398:155–180.

Hacker, J. and Linden, P. (2002). Gravity currents in rotating channels. Part1. Steady-state theory. *Journal of Fluid Mechanics*, 457:295–324.

Hart, D. (1998). The elimination of correlation error in PIC processing. In *9th International Symposium on Applications of Laser Techniques to Fluid Mechanics, 13-16 July, Lisbon.*

Harzallah, A., C. D. and Crepon, M. (1993). Possible forcing effects of net evaporation, atmospheric pressure and transients on water transports in the Mediterranean Sea. *Journal of Geophysical Research*, 98(C7):12341–12350.

Helfrich, K. (1995). Time-dependent two-layer exchange flows. *Journal of Physical Oceanography*, 25:359–373.

Helfrich, K., Kuo, A., and Pratt, L. (1999). Nonlinear Rossby adjustment in a channel. *Journal of Fluid Mechanics*, 390:187–222.

Helfrich, K. and Pratt, L. (2003). Rotating hydraulics and upstream basin circulation. *Journal of Physical Oceanography*, 33:1651–1663.

Henderson, F. (1966). *Open channel flow*. Collier Macmillan.

Hermann, A., Rhines, R., and Johnson, E. (1989). Nonlinear Rossby adjustment in a channel: beyond Kelvin waves. *Journal of Fluid Mechanics*, 205:469–502.

Hogg, A., Ivey, G., and Winters, K. (2001a). Hydraulics and mixing in controlled exchange flows. *Journal of Geophysical Research*, 106(C1):959–972.

Hogg, A., Winters, K., and Ivey, G. (2001b). Linear internal waves and the control of stratified exchange flows. *Journal of Fluid Mechanics*, 447:357–375.

Holford, J. and Dalziel, S. (1996). Measurements of layer depth in a two-layer flow. *Applied Scientific Research*, 56(2-3):191–207.

Johns, W., Yao, F., Olson, D., Josey, S., Grist, J., and Smeed, D. (2003). Observations of seasonal exchange through the Straits of Hormuz and the inferred headn and freshwater budgets of the Persian Gulf. *Journal of Geophysical Research*, 108(C12):3391.

Johnson, G. and Ohlsen, D. (1994). Frictionally modified rotating hydraulic channel exchange and ocean outflows. *Journal of Physical Oceanography*, 24:66–78.

Johnson, G. and Sanford, T. (1992). Secondary circulation in the Faroe Bank Channel Outflow. *Journal of Physical Oceanography*, 22:927–933.

Kahaner, D., Moler, C., and Nash, S. (1988). *Numerical methods and software.* Prentice Hall.

Killworth, P. (1995). Hydraulic control and maximal flow in rotating stratified hydraulics. *Deep Sea Research I*, 42(6):859–871.

Killworth, P. and McDonald, N. (1993). Maximal reduced-gravity flux in rotating hydraulics. *Geophysical Astrophys. Fluid Dynamics*, 70:31–40.

Killworth, P., Paldor, N., and Stern, M. (1984). Wave propagation and growth on a surface front in a two-layer geostrophic current. *Journal of Marine Research*, 42:761–785.

Käse, R., Girton, J., and Sanford, T. (2003). Structure and variability of the Denmark Strait overflow: model and observations. *Journal of Geophysical Research*, 108(C6):art. 3181.

Laanearu, J. and Lundberg, P. (2000). Topographic control of rotating deep water flow through the combination of a sill and a horizontal constriction. *Journal of Geophysical Research*, 105(C12):28663–28669.

Lane-Serff, G. (2004). Adjustment and transient phenomena in rotating exchange flows. in preparation.

Lane-Serff, G., Beal, L., and Hadfield, T. (1995). Gravity current flow over obstacles. *Journal of Fluid Mechanics*, 292:39–53.

Lane-Serff, G., Smeed, D., and Postlethwaite, C. (2000). Multi-layer hydraulic exchange flows. *Journal of Fluid Mechanics*, 416:269–296.

Lane-Serff, G. and Woodward, M. (2001). Internal bores in two-layer exchange flows over sills. *Deep Sea Research I*, 48:63–78.

Long, R. (1956). Waves in a two-fluid system. *Journal of Meteorology*, 13:70–74.

Long, R. (1970). Blocking effects in flow over obstacles. *Tellus*, 22:471–480.

Long, R. (1974). Some experimental observations of upstream disturbances in a two-fluid system. *Tellus*, 23:313–317.

Longhetto, A., Hieres, G., Briatore, L., Didelle, H., Ferrero, E., and Giraud, C. (1996). A Laboratory experiments on the development of cyclogenesis in the lee of a mountain. *NuovoCimento Della Societa Italiana di Fisica C - Geophysics and Space Physics*, 19(4):561–578.

Munday, D. (2000). Effects of rotation on internal bores. University of Southampton SOES Honour Research Project Dissertation.

Napolitano, E., Gianmaria, S., Artale, V., and Marullo, S. (2003). Modeling the baroclinic circulation in the area of the Sicily channel: The role of stratification and energy diagnostics. *Journal of Geophysical Research*, 108(C7):3230.

Nielsen, J. (1912). Hydrography of the Mediterranean and adjacent waters. *Report on the Danish Oceanographical Expeditions*, 1:77–191.

Nielsen, M. (106). Evidence for internal hydraulic control in the northern Oresund. *Journal of Geophysical Research*, 106(C7):14055–14068.

Nof, D. (1984). Shock waves in currents and outflows. *Journal of Physical Oceanography*, 14:1683–1702.

Nof, D. (1986). Geostrophic shock waves. *Journal of Physical Oceanography*, 16:886–901.

Nof, D. (1995). Choked flows from the pacific to the Indian ocean. *Journal of Physical Oceanography*, 25:1369–1383.

Potemra, J., Hautala, S., and Sprintall, J. (2003). Vertical structure of Indonesian throughflow in a large-scale model. *Deep Sea Research-II*, 50:2143–2161.

Pratt, L. (1986). Hydraulic control of sill flow with bottom friction. *Journal of Physical Oceanography*, pages 1970–1980.

Pratt, L. (1987). Rotating shocks in a separated laboratory channel flow. *Journal of Physical Oceanography*, 17:483–491.

Pratt, L. and Armi, L. (1990). Two-layer rotating hydraulics: strangulation, remote and virtual controls. *PAGEOPH*, 133(4):587–617.

Pratt, L. and Helfrich, K. (2003). Generalized conditions for hydraulic criticality in oceanic overflows. in preparation.

Pratt, L., Helfrich, K., and Chassignet, E. (2000). Hydraulic adjustment to an obstacle in a rotating channel. *Journal of Fluid Mechanics*, 404:117–149.

Rabe, B. and Smeed, D. (2002). Rotating exchange flows through straits with multiple channels: Preliminary results of laboratory studies. In *Proceedings of the 2nd Meeting on the Physical Oceanography of Sea Straits, Villefranche, 15th-19th April 2002*, pages 185–188.

Rabe, B., Smeed, D., Lane-Serff, G., and Dalziel, S. (2003). Rotating exchange flows through staits with multiple channels. In *Proceedings of the International Conference: Towards a Balanced Methodology in European Hydraulic Research in Budapest, 22-23 May, 2003*. http://www.vituki.hu/publikacio/ic/table_of_content.htm.

Riemenschneider, U. (2004). *The dynamics of rotating two-layer exchange flows - an analytical and numerical modelling study*. PhD thesis, School of Ocean and Earth Science, University of Southampton.

Sadoux, S., Baey, J., Fincham, A., and Renouard, D. (2000). Experimental study of the stability of an intermediate current and its interaction with a cape. *Dynamics of Atmospheres* *and Oceans*, 31:165–192.

Serra, N., Sadoux, S., Ambar, I., and Renouard, D. (2002). Observations and laboratory modeling of meddy generation at Cape St. Vincent. *Journal of Physical Oceanography*, 32:3–25.

Shen, C. (1981). The rotating hydraulics of the open-channel flow between two basins. *Journal of Fluid Mechanics*, 112:161–188.

Siddall, M., Smeed, D.A., M. S., and Rohling, E. (2002). Modelling the seasonal cycle of the exchange flow in Bab El Mandab (Red Sea). *Deep Sea Research I*, 49(9):1551–1569.

Smeed, D. (1988). Baroclinic instability of 3-layer flows. 2. Experiments with eddies. *Journal of Fluid Mechanics*, 194:233–259.

Smeed, D. (2000). Hydraulic control in three-layer exchange flows and application to the Bab al Mandab. *Journal of Physical Oceanography*, 30(10):2574–2588.

Smeed, D. (2004). Exchange flow through multiple straits of different width. in preparation.

Spedding, G. and Rignot, E. (1993). Performance analysis and application of grid interpolation techniques for fluid flows. *Experiments in fluids*, 15:417–430.

Stansfield, K., Gasparini, G., and Smeed, D. (2003). High-resolution observations of the path of the overflow from the Strait of Sicily. *Deep Sea Research*, 50:1129–1149.

Stansfield, K., Smeed, D., Gasparini, G., McPhail, S., Millard, N., Tevenson, P., Webb, A., Vetrano, A., and Rabe, B. (2001). Deep-sea, high-resolution, hydrography and current measurements using an autonomous underwater vehicle: the overflow from the Strait of Sicily. *Geophysical Research Letters*, 28(13):2645–2648.

Stenström, P. (2003). Mixing and recirculation in two-layer exchange flows. *Journal of Geophysical Research*, 108(C8).

Stommel, H. and Farmer, H. (1953). Control of salinity in an estuary by a transition. *Journal of Marine Research*, 12:13–20.

Theocharis, A., Balopoulos, E., Kioroglou, S., Kontoyiannis, H., and Iona, A. (1999). A synthesis of the circulation and hydrography of the South Aegean Sea and the straits of the Cretan Arc (March 1994 to Jannuary 1995). *Progress in Oceanography*, 44(4):469–509.

Tipler, P. (1991). *Physics for scientists and engineers.* Worth Publishers: New York, 3 edition.

Toulany, B. and Garrett, C. (1984). Geostrophic control of fluctuating barotropic flow through straits. *Journal of Physical Oceanography*, 14(4):649–655.

Tritton, D. (1988). *Physical fluid dynamics.* Clarendon Press, 2nd edition.

Tsimplis, M., Velegrakis, A., Drakopoulos, P., Theocharis, A., and Collins, M. (1999). Cretan deep water outflow into the Eastern Mediterranean. *Progress in Oceanography*, 44:531–551.

Whitehead, J. (2002). Hydraulically controlled rotating flow - complexities from passage shape. In *Proceedings of the 2nd Meeting on the Physical Oceanography of Sea Straits, Villefranche, 15th-19th April 2002*, pages 229–232.

Whitehead, J., Leetmaa, A., and Knox, R. (1974). Rotating hydraulics of strait and sill flows. *Geophysical Fluid Dynamics*, 6:101–125.

Winters, K. and Seim, H. (2000). The role of dissipation and mixing in exchange flow through a contracting channel. *Journal of Fluid Mechanics*, 407:265–290.

Wood, I. and Simpson, J. (1984). Jumps in layered miscible fluids. *Journal of Fluid Mechanics*, 140:329–342.

Zaremba, L., Lawrence, G., and Pieters, R. (2003). Frictional two-layer exchange flow. *Journal of Fluid Mechanics*, 474:339–354.